INVESTIGATION OF BREAST TUMOR HEMODYNAMICS BY NEAR INFRARED SPECTROSCOPY: APPLICATIONS TO CANCER THERAPY MONITORING

by

JAE GWAN KIM

Presented to the Faculty of the Graduate School of

The University of Texas at Arlington and

The University of Texas Southwestern Medical Center at Dallas

in Partial Fulfillment of the Requirements

for the Degree of

DOCTOR OF PHILOSOPHY

THE UNIVERSITY OF TEXAS AT ARLINGTON

DECEMBER 2005

DEDICATION

To my wife SooJung, my children HyunJae, HyunJin,

and to my parents and parents-in-law

ACKNOWLEDGEMENTS

I first want to give my deepest gratitude to my mentor, Dr. Hanli Liu for introducing me into the biomedical optics research. Since 2000 summer, I became very lucky to be influenced by her enthusiasm about the research, knowledge in biomedical optics, love to her children, and the way to treat her students as collaborators.

I'm also very fortunate to have Dr. Ralph P. Mason as a co-adviser. Without his support and abundant knowledge in cancer, I couldn't come to this stage. I am deeply indebted to Dr. Dawen Zhao for his strong support in animal studies and also friendship. I am very grateful as well to Drs. Robert C. Eberhart and Ohwofiemu Nwariaku for serving as my dissertation defense committee members and their valuable suggestions to this work. I also need to thank all faculties in my department who have shared their knowledge in their classes. To the all members in biomedical optics laboratory, I owe your friendship and sharing of your knowledge and experiences.

Finally, I deeply appreciate my parents, parents-in-laws, wife and children for their love, and sacrifices over the years. This work was supported by DOD breast cancer research grant DAMD 17-03-1-0353 (Jae G. Kim), DAMD17-03-1-0363 (Dawen Zhao), DAMD17-00-1-0459 (Hanli Liu), NIH 1R21CA101098-01 (Hanli Liu) and NIH/NCI P20 CA086354 (Ralph P. Mason).

November 18, 2005

ABSTRACT

INVESTIGATION OF BREAST TUMOR HEMODYNAMICS BY NEAR INFRARED SPECTROSCOPY: APPLICATIONS TO CANCER THERAPY MONITORING

Publication No. _____

Jae Gwan Kim, Ph. D.

The University of Texas Southwestern Medical Center at Dallas
and
The University of Texas at Arlington, 2005

Supervising Professor: Hanli Liu, Ph. D.

Hyperoxic gas interventions using carbogen (95% O_2 and 5% CO_2) or oxygen has been tried to increase the tumor oxygenation since it will enhance the therapeutic effects on the tumors. Others in the laboratory had previously applied near infrared spectroscopy (NIRS) to monitor the changes in tumor blood oxygenation during hyperoxic gas intervention and found that oxyhemoglobin concentration changes ($\Delta[HbO_2]$) during gas intervention can be fitted by a two-exponential equation containing two time constants.

Based on the model, they formed a hypothesis that changes in oxygenated hemoglobin concentration result from well perfused and poorly perfused regions of an animal tumor to explain why there are two different time constants in the $\Delta[HbO_2]$ data. In this study, the aims were 1) to modify and refine the algorithm for obtaining vascular hemoglobin concentration by near infrared spectroscopy (NIRS), 2) to understand the bi-phasic feature of tumor hemodynamics during hyperoxic gas interventions, and 3) to apply a bi-exponential model to investigate tumor physiology, such as vascular heterogeneity, and to monitor tumor responses to cancer therapy.

For aim 1, blood phantom experiments were performed, and the algorithm was modified empirically. Possible differences in calculated hemoglobin concentration induced by the discrepancy in hemoglobin extinction coefficients were also estimated. For aim 2, a dynamic vascular phantom simulating blood vessels was developed, and the finite element method (FEM) was applied to support the dynamic phantom experiments. To accomplish aim 3, multi-channel NIRS was utilized to observe the heterogeneity in tumor oxygen dynamics during hyperoxic gas intervention. For therapy monitoring, two chemotherapeutic drugs, a conventional chemotherapeutic agent and a vascular disrupting agent, were administered in tumor-bearing rats. The responses of tumors during oxygen intervention were compared between pre- and post- treatment.

The dynamic vascular phantom experiments and FEM simulations support the previous hypothesis on the bi-phasic feature of tumor hemodynamics, and that the bi-phasic features of NIRS taken during hyperoxic intervention can be an effective tool to monitor tumor responses to cancer therapy.

TABLE OF CONTENTS

ACKNOWLEDGEMENTS iv

ABSTRACT v

LIST OF ILLUSTRATIONS xiv

LIST OF TABLES xx

LIST OF ABBREVIATIONS xxi

Chapter

1. INTRODUCTION 1

1.1 Background 1

1.2 Tumor Hypoxia 2

1.3 Overview of Dissertation 5

2. REFINEMENT AND MODIFICATION OF EQUATIONS FOR OBTAINING HEMOGLOBIN DERIVATIVE CONCENTRATIONS BASED ON BEER-LAMBERT'S LAW 8

2.1 Introduction 8

2.2 Modification of Algorithm for a Single Channel Frequency Domain System 10

2.3 Importance of a Factor 4 14

2.4 Importance of Correct Values of Hemoglobin Extinction Coefficient 15

2.4.1 Background 15

2.4.2 Derivation of Equations for Error Estimation 18

2.4.3 Results of Error Estimation 22

2.4.4 Discussion and Conclusion..... 30

2.5 Calibration of Broadband, CCD-based NIRS System..... 38

2.6 Comparison of Algorithms Using
Two Wavelengths vs. Six Wavelengths 44

2.7 Summary..... 48

3. INVESTIGATION OF BI-PHASIC TUMOR OXYGEN
DYNAMICS INDUCED BY HYPEROXIC GAS INTERVENTION:
THE DYNAMIC PHANTOM APPROACH 50

3.1 Introduction..... 50

3.2 Materials and Methods 53

3.2.1 Review of the Mathematical Model of
Tumor Vascular Oxygenation..... 53

3.2.2 Design and Implementation of
the Dynamic Vascular Phantom..... 56

3.2.3 Multi-Channel NIR Spectroscopy 58

3.2.4 Experimental Setup and Procedures of
Dynamic Phantom Measurements..... 59

3.3 Results..... 62

3.3.1 NIR Measurements Taken from Dynamic
Tumor Vascular Phantom 1 62

3.3.2 NIR Measurements Taken from Dynamic
Tumor Vascular Phantom 2 70

3.4 Discussion and Conclusion..... 73

4. INVESTIGATION OF BI-PHASIC TUMOR OXYGEN DYNAMICS INDUCED BY HYPEROXIC GAS INTERVENTION: A NUMERICAL STUDY 79

4.1 Introduction 79

4.2 Review of Our Mathematical Model for Tumor Vascular Oxygenation 81

4.3 Computer Simulations Using the Finite Element Method 83

4.4 Results 88

4.5 Discussion and Conclusion 93

5. INTERPLAY OF TUMOR VASCULAR OXYGENATION AND TUMOR pO_2 OBSERVED USING NIRS, OXYGEN NEEDLE ELECTRODE, AND ^{19}F MR pO_2 MAPPING 100

5.1 Introduction 100

5.2 Algorithms Development 102

5.2.1 Relationship among Normalized $\Delta[HbO_2]$, sO_2 and Blood pO_2 102

5.2.2 Relationship Between Normalized $\Delta[HbO_2]$ and Tissue/Tumor pO_2 105

5.3 Materials and Methods 106

5.3.1 Tumor Model 106

5.3.2 NIRS and pO_2 Needle Electrode Measurements 107

5.3.3 Tissue Phantom Solution Model 109

5.3.4 MRI Instrumentation and Procedure 110

5.4 Results 112

5.4.1 Tumor Study 112

5.4.2 Tissue Phantom Study 116

5.4.3 Correlation between pO_2 and Normalized $\Delta[HbO_2]$ 117

5.4.3.1 Tissue Phantoms Study 117

5.4.3.2 Tumor Study 119

5.5 Discussion and Conclusion 120

6. ACUTE EFFECTS OF COMBRETASTATIN A4 PHOSPHATE ON BREAST TUMOR HEMODYNAMICS MONITORED BY NIRS 125

6.1 Introduction 125

6.2 Material and Methods 128

6.2.1 Animal and Tumor Model 128

6.2.2 Drug Preparation and Dose 128

6.2.3 Near-Infared Spectroscopy 128

6.2.4 Experimental Design 131

6.2.5 Estimation of Percent Changes in Tumor Blood Volume 132

6.2.6 Statistical Analysis 136

6.3 Results 137

6.3.1 Control Group 137

6.3.2 CA4P Treated Group 138

6.3.3 Comparison of Tumor Response Between Control and CA4P Treated Groups 140

6.3.4 Changes in Hemodynamics After CA4P Treatment 141

6.3.4.1 Changes in bi-phasic amplitudes of $[HbO_2]$ after CA4P treatment 144

6.3.4.2 Changes in bi-phasic time constants of $[HbO_2]$ after CA4P treatment 147

6.3.4.3 Changes in bi-phasic perfusion rates of tumors after CA4P treatment 149

6.3.4.4 Changes in A_1/A_2, τ_1/τ_2, and f_1/f_2 after CA4P treatment 151

6.3.5 Changes in Blood Volume and $[HbO_2]$ 2 hours After CA4P Administration 153

6.4 Discussion and Conclusion 157

7. NON-UNIFORM TUMOR VASCULAR OXYGEN DYNAMICS MONITORED BY MULTI-CHANNEL NIRS 164

7.1 Introduction 164

7.2 Material and Methods 166

7.2.1 Tumor Model and Measurement 166

7.2.2 Multi-Channel NIR Spectroscopy 168

7.3 Results 171

7.3.1 Three Channel NIRS Experiments 171

7.3.2 Four Channel NIRS Experiments 178

7.4 Discussion and Conclusion 181

8. CHEMOTHERAPEUTIC (CYCLOPHOSPHAMIDE) EFFECTS ON RAT BREAST TUMOR HEMODYNAMICS MONITORED BY MULTI-CHANNEL NIRS 186

8.1 Introduction 186

8.2 Materials and Methods 188

8.2.1 Tumor Model and Experimental Procedure 188

8.2.2 Measurement System 191

8.3 Results 192

8.3.1 Body Weight and Tumor Volume Changes During Chemotherapy 192

8.3.2 Vascular Hemodynamics Changes From Control Group 194

8.3.3 Vascular Hemodynamics Changes From Metronomic Low Dose CTX Treated Group 197

8.3.4 Vascular Hemodynamics Changes From Single High Dose CTX Treated Group 199

8.3.5 Intratumoral Heterogeneity in Tumor Response to CTX Treatment 200

8.3.6 Intertumoral Heterogeneity in Tumor Response to CTX Treatment 202

8.3.7 Changes in Fitted Parameters Before and After Chemotherapy 204

8.3.8 Correlations between tumor volume regressions and fitted parameters 209

8.4 Discussion and Conclusion 211

9. CONCLUSIONS AND FUTURE SUGGESTIONS 217

9.1 Conclusions 217

9.3 Future suggestions 221

Appendix

A. THE SUMMARIZED EXTINCTION COEFFICIENT VALUES OF HUMAN HEMOGLOBIN FROM LITERATURES 224

REFERENCES 245

BIOGRAPHICAL INFORMATION 261

LIST OF ILLUSTRATIONS

Figure

1.1 (a) Relationship between radiosensitivity and oxygen concentration of a tumor (b) the effect of oxygen in radiotherapy shown by percent DNA degradation 4

2.1 Simultaneous dynamic changes of $\Delta[HbO_2]$, $\Delta[Hb]$, and $\Delta[Hb_{total}]$ in the phantom solution measured using NIRS with Eqs. (2.8) and (2.9) 12

2.2 Replotted Fig. 2.1 with empirically modified Eqs. (2.10) and (2.11) 13

2.3 Hemoglobin near IR absorption spectra from Cope, Prahl, and Zijlstra *et al* 24

2.4 Differences in hemoglobin absorption spectra among Cope, Prahl and Zijlstra *et al* 26

2.5 A setup for the calibration experiment 40

2.6 Raw intensity changes at six wavelengths (650, 700, 730, 750, 803, 830 nm) during air or nitrogen flow 41

2.7 Replotted from Fig. 2.6 to show the raw intensity changes at 803 nm and 830 nm during air or nitrogen flow 41

2.8 Optical density changes at six wavelengths (650, 700, 730, 750, 803, 830 nm) during air or nitrogen flow 42

2.9 The changes of [Hb], $[HbO_2]$ and $[Hb_{total}]$ during a phantom experiment by using Eqs. (2.45)-(2.47) 43

2.10 The changes of [Hb], $[HbO_2]$ and $[Hb_{total}]$ during a phantom experiment by using Eqs. (2.51)-(2.53) 46

2.11 Absolute differences of Δ[Hb], Δ[HbO_2] and Δ[Hb_{total}] between Figs. 2.9 and 2.10 47

2.12 Changes of [Hb], [HbO_2] and [Hb_{total}] during a phantom experiment obtained by using 2 wavelengths at 700 and 750 nm (a) or at 803 and 830 nm (b) 48

3.1 Time course of tumor vascular Δ[HbO_2], Δ[Hb], and Δ[Hb_{total}] for a representative 13762NF breast tumor with the inhaled gas under the sequence of air-oxygen-air. 52

3.2 A schematic diagram of light transmitting patterns in tumor when tumor has two distinct perfusion regions. 55

3.3 A schematic diagram for one vascular modeling device (VMD)..... 56

3.4 An experimental setup for the tumor dynamic phantom study 60

3.5 Absorption changes measured from the dynamic tumor vascular phantom with increasing a flow rate from (a) 1 to 10 ml/hr and (b) 15 to 60 ml/hr..... 62

3.6 A correlation (a) between time constants and flow rates and (b) ink flow velocities and ink flow rates..... 64

3.7 (a) Three temporal profiles of 3-channel NIRS measurements result from D1, D2, and D3 on dynamic phantom 1 (b) Absorption changes obtained from D1, D2, and D3 during step 3 at Fig. 3.7(a). 66

3.8 (a) Three temporal profiles of 3-channel NIRS measurements result from D1, D2, and D3 on dynamic phantom 2 (b) Absorption changes obtained from D1, D2, and D3 during step 4 at Fig. 3.8(a). 71

4.1 A representative hemodynamic changes of rat breast tumor obtained with the NIRS measurement..... 80

4.2 A schematic diagram of light transmitting patterns in a tumor with two distinct perfusion regions..... 82

4.3 The geometry used in FEM simulations for a simplified tumor vascular model. 84

4.4 Light distribution inside of a simplified tumor vascular model simulated by FEM with the increase of R1 and R2 87

4.5 Simulated light distributions of a simplified tumor vascular model with varying flow rates 90

4.6 Simulated light distributions of a simplified tumor vascular model with changes in position of the light source 92

5.1 Schematic experimental setup of one channel, near infrared, frequency domain IQ instrument for tumor investigation *in vivo*. 108

5.2 Experimental setup for phantom study..... 110

5.3 Simultaneous dynamic changes of $\Delta[HbO_2]$ and pO_2 in R3327-HI rat prostate tumors using NIRS and pO_2 needle electrode..... 113

5.4 Dynamic changes of $\Delta[HbO_2]$ and pO_2 in two R3327-AT1 rat prostate tumors measured sequentially using NIRS and ^{19}F MR pO_2 mapping..... 115

5.5 A simultaneous measurement of $\Delta[HbO_2]$, $\Delta[Hb]_{total}$ and pO_2 in the phantom solution using NIRS and pO_2 needle electrode.. 117

5.6 Changes of tissue pO_2 with normalized $\Delta[HbO_2]$ in the phantom solution using NIRS and pO_2 needle electrode 118

5.7 Changes of tissue pO_2 with normalized $\Delta[HbO_2]$ in tumors measured with NIRS, pO_2 needle electrode, and ^{19}F MR pO_2 mapping. 120

6.1 A schematic diagram of experimental setup 129

6.2 A representative data of tumor vascular $\Delta[HbO_2]$, $\Delta[Hb]$, and $\Delta[Hb_{total}]$ from a control group 137

6.3 A representative data of tumor vascular $\Delta[HbO_2]$, $\Delta[Hb]$, and $\Delta[Hb_{total}]$ from a CA4P treated group..... 139

6.4 Differences of $\Delta[HbO_2]$, $\Delta[Hb]$, and $\Delta[Hb_{total}]$ between 2 wavelengths algorithm and 6 wavelengths algorithm 140

6.5 Changes in $\Delta[HbO_2]$, $\Delta[Hb]$, and $\Delta[Hb_{total}]$ from breast tumors shown in Fig. 6.2 and 6.3 at 1 day after saline (a) and CA4P (b) administration 141

6.6 Dynamic changes of $\Delta[HbO_2]$ from rat breast tumors during oxygen intervention before and after administration of CA4P 142

6.7 Changes of $\Delta[HbO_2]$ during oxygen intervention before (a) and after (b, c, d) CA4P administration 143

6.8 Summary of two fitted parameters, A_1 (a) and A_2 (b) 145

6.9 DCE-MRI performed before, 2 h, and 24 h after treatment with CA4P (30 mg/kg). 145

6.10 The maximal enhancing rim sizes versus time after CA4P, measured using T1-weighted MR images 146

6.11 Summary of two fitted parameters, $1/\tau_1$ (a) and $1/\tau_1$ (b) 148

6.12 The relationship between pre- and post- CA4P administration measurements of tumor perfusion (a) 30 minutes and (b) 24 hours after drug administration 148

6.13 Summary of two fitted parameters, f_1 (a) and f_2 (b) 150

6.14 The effect of 10 mg/kg CA4P on blood flow to peripheral (a) and central (b) regions of the tumor 150

6.15 Summary of two fitted parameters: A_1/A_2 (a), τ_1/τ_2 (b), and f_1/f_2 (c) 153

6.16 The averaged value of percent changes in blood volume (a) and $\Delta[HbO_2]$ (b) after CA4P administration 154

6.17 Relative changes of red blood cell velocity (a) and nonfunctioning vessel number (b) after CA4P administration 155

6.18 (a) Percentage of changes in $\Delta[HbO_2]$ during oxygen intervention before and after administration of saline and CA4P. (b) Changes in $\Delta[HbO_2]$ and $\Delta[Hb_{total}]$ during 2 hours after administration of saline and CA4P 157

7.1 (a) A schematic experimental setup of animal experiment, (b)A top view of three channel NIRS and (c) four channel NIRS measurements. 167

7.2 Dynamic changes of [HbO_2] from three detectors in tumor A 172

7.3 Gross view of a histological section of a tumor 173

7.4 Dynamic changes of [HbO_2] from three detectors in tumor B 176

7.5 Dynamic changes of [HbO_2] from four detectors in tumor C 178

7.6 Fitted Δ[HbO_2] from four locations in tumor C 179

8.1 (a) A schematic experimental setup of animal experiment, (b) A top view of four channel NIRS measurements. 190

8.2 Normalized changes in rat body weight (a) and tumor volume (b) during the saline and CTX treatments 194

8.3 Changes of Δ[HbO_2] before and after saline administration 195

8.4 Changes of Δ[HbO_2] before and after administration of metronomic low dose of CTX (20 mg/kg for 10 days) 198

8.5 Changes of Δ[HbO_2] before and after administration of A single high dose of CTX (200 mg/kg) 200

8.6 Dynamic changes of [HbO_2] taken at 4 locations from a rat breast tumor before and after a single high dose of CTX treatments 201

8.7 Dynamic changes of [HbO_2] from 4 different tumors before and after a single high dose of CTX treatments 203

8.8 Summary of fitted parameters, A_1 (a) and A_2 (b) 204

8.9 Summary of fitted parameters, τ_1 (a) and τ_2 (b) 205

8.10 Summary of fitted parameters, f_1 (a) and f_2 (b) 207

8.11 Summary of fitted parameters, A_1/A_2 (a), τ_1/τ_2 (b), and f_1/f_2 (c) 208

8.12 Correlations between the normalized tumor volume changes and normalized $\Delta[HbO_2]_{max}$ (a) and normalized A_1 values (b) during oxygen intervention after a CTX treatment. 210

LIST OF TABLES

Table

2.1 Deoxyhemoglobin ε from three different groups 23

2.2 Oxyhemoglobin ε from three different groups 24

2.3 Differences in hemoglobin ε values among three different groups 25

2.4 The relative errors caused by discrepancies of hemoglobin ε value 29

2.5 Absolute differences in hemoglobin extinction coefficients between human and other species 37

3.1 Summary of fitted parameters obtained at the three detectors in Fig. 3.7(b) 69

3.2 Summary of fitted parameters obtained at the three detectors in Fig. 3.8(b) 73

7.1 Summary of vascular oxygen dynamics determined at the three detectors from Figure 7.3 for Tumor A 174

7.2 Summary of vascular oxygen dynamics determined at the three detectors from Figure 7.5 for Tumor B 177

7.3 Summary of vascular oxygen dynamics determined at the four detectors from Figure 7.6 for Tumor C 181

8.1 Summary of vascular oxygen dynamics determined at location #1 from the control tumor shown in Fig. 8.3 196

8.2 Summary of vascular oxygen dynamics determined at location #1 from the low dose CTX treated tumor shown in Fig. 8.4 198

8.3 Summary of vascular oxygen dynamics determined at location #1 from the single high dose CTX treated tumor shown in Fig. 8.5 200

LIST OF ABBREVIATIONS

ANOVA	Analysis of variance
CA4P	Combretastatin A4 phosphate
CT	Computed tomography
CTX	Cyclophosphamide
CW	Continuous wave
DAC	Data acquisition
DCE	Dynamic contrast enhanced
DPF	Differential pathlength factor
ε	Extinction coefficient
ε_{Hb}	Extinction coefficient of deoxyhemoglobin
ε_{HbO2}	Extinction coefficient of oxyhemoglobin
ε_{Hbi}	Extinction coefficient of methemoglobin
EPI	Echo planar imaging
EPR	Electron paramagnetic resonance
FREDOM	Fluorocarbon relaxometry using echo planar imaging for dynamic oxygen mapping
Gd-DTPA	Gadolinium (III) diethyltriaminepentaacetic acid
Hb	Deoxyhemoglobin
HbO_2	Oxyhemoglobin
Hb_{total}	Total hemoglobin
HFB	Hexafluorobenzene
I.P.	Intra-Peritoneal
I.V.	Intr-Venous
I&Q	In-phase and quadrature-phase
MRI	Magnetic resonance imaging

MRS	Magnetic resonance spectroscopy
NIRS	Near-infrared spectroscopy
NMR	Nuclear magnetic resonance
PET	Positron emission tomography
PMT	Photo multiplier tube
pO_2	Partial oxygen pressure
rCBF	Regional cerebral blood flow
RF	Radio frequency
SD	Standard deviation
SE	Standard error
sO_2	Percent oxyhemoglobin saturation
TFA	Trifluoroacetic acid
VEGF	Vascular endothelial growth factor
VDA	Vascular disrupting agent
VMA	Vascular modifying agent
VMD	Vascular modeling device
VTA	Vascular targeting agent

CHAPTER 1

INTRODUCTION

1.1 Background

According to the American Cancer Society, cancer is defined as "a group of diseases characterized by uncontrolled growth and spread of abnormal cells" [1]. Based on this definition, we expect that most tumor characteristics can be used as optical signals for tumor detection and prognosis. For examples, due to their uncontrolled growth, tumors normally have higher blood volume and also are very active in their metabolism, which can be seen by their lower concentration of oxyhemoglobin in comparison to adjacent tissues.

Breast cancer is a type of cancer that has the highest incidence rate and the second highest death rate for women in the U.S. According to the data from the American Cancer Society [1], 662,870 cases of cancer are estimated from women in 2005. Among those cases, 33% (i.e., 218,747 cases) is from breast cancer, being the largest number among all other types of cancer in women. One fortunate thing about breast cancer is that it shows the highest survival rate 5 years after diagnosis.

Traditionally, mammography has been a common tool to detect breast tumors from the surrounding normal breast tissues. In recent years, several groups of researchers have tried to use near infrared (NIR) light (700~900nm) to detect breast

cancer [2] [3] [4]. Even though most light is absorbed by hemoglobin, water, and lipid, tissues are relatively transparent to the light in the NIR range. NIR light can transmit through tissues about a few centimeters, depending on the separation between the light source and detector. By detecting the light intensity changes at two or more wavelengths in the NIR region, the changes in concentrations of deoxygenated hemoglobin, [Hb], oxygenated hemoglobin, [HbO_2], and total hemoglobin, [Hb_{total}] of deep tissues can be estimated by using either the diffusion approximation or modified Beer-Lambert's law. For the formal approach, it requires a rigorous mathematical boundary condition and an assumption that the measured sample/organ is relatively homogeneous and large [5] [6] [7]. The latter approach, on the other hand, measures relative changes in [Hb], [HbO_2], and [Hb_{total}] with respect to a baseline condition. It is feasible to obtain accurate measures for relatively small and heterogeneous samples or organs. Thus, modified Beer-Lambert's law is more appropriate for my study since most of my experimental work, both in laboratory and animal measurements, highly involves large heterogeneity and small sizes of tumors.

1.2 Tumor hypoxia

Tumor cells are proliferating much faster than normal cells; endothelial cells, a main component of blood vessels, in tumor can be grown irregularly with leaky vessel walls, blind ends and temporary occlusions. Hypoxia often occurs in the region of tumors that is far away from blood vessels. Moreover, there are several bad consequences when tumors become hypoxic [8]. Firstly, a hypoxic tumor promotes

metastasis of cancer by selecting cells with a more malignant phenotype. Secondly, a hypoxic tumor is one of the possible causes for the release of vascular endothelial growth factor (VEGF). VEGF is much needed for tumor cells because they need to obtain supplies of oxygen and nutrients to survive through blood vessels. Interestingly, the receptors for VEGF are expressed on the endothelium of tumor vasculature, while they are virtually absent in the adjoining tissues. Thirdly, tumor hypoxia also makes release of the factor, hypoxia inducible factor 1 (HIF-1), which again induces the transcription of VEGF. Tumor hypoxia and VEGF interact with the angiopoietin system to dedifferentiate vasculature and to prevent its maturation, which can be one of the reasons that the tumor vasculature is leaky.

In terms of the relationship between tumor hypoxia and therapeutic efficacy, it has long been known that hypoxic tumor cells are more resistant to radiation therapy than well-oxygenated tumor cells [9]. As seen in Fig. 1.1(a), when the pO_2 value of a tumor is near zero, the tumor shows nearly three times more resistance to radiotherapy than a well-oxygenated tumor [10]. It is also seen that given the same dose of radiotherapy, there is more percentage of DNA degraded by radiotherapy when oxygen gas is provided to flow around the tumor cells during therapy than that with nitrogen flowing environment (Fig. 1.1(b)). Similarly, hypoxic tumor cells show poor responses to photodynamic therapy [11] and to some forms of chemotherapeutic agents [12]. This is because hypoxic cells are physically far away from blood vessels, and thus chemotherapeutic agents can hardly reach the hypoxic region of tumors through blood

vessels. Therefore, it is important to elevate the oxygen level in tumors in order to have better treatment efficacy.

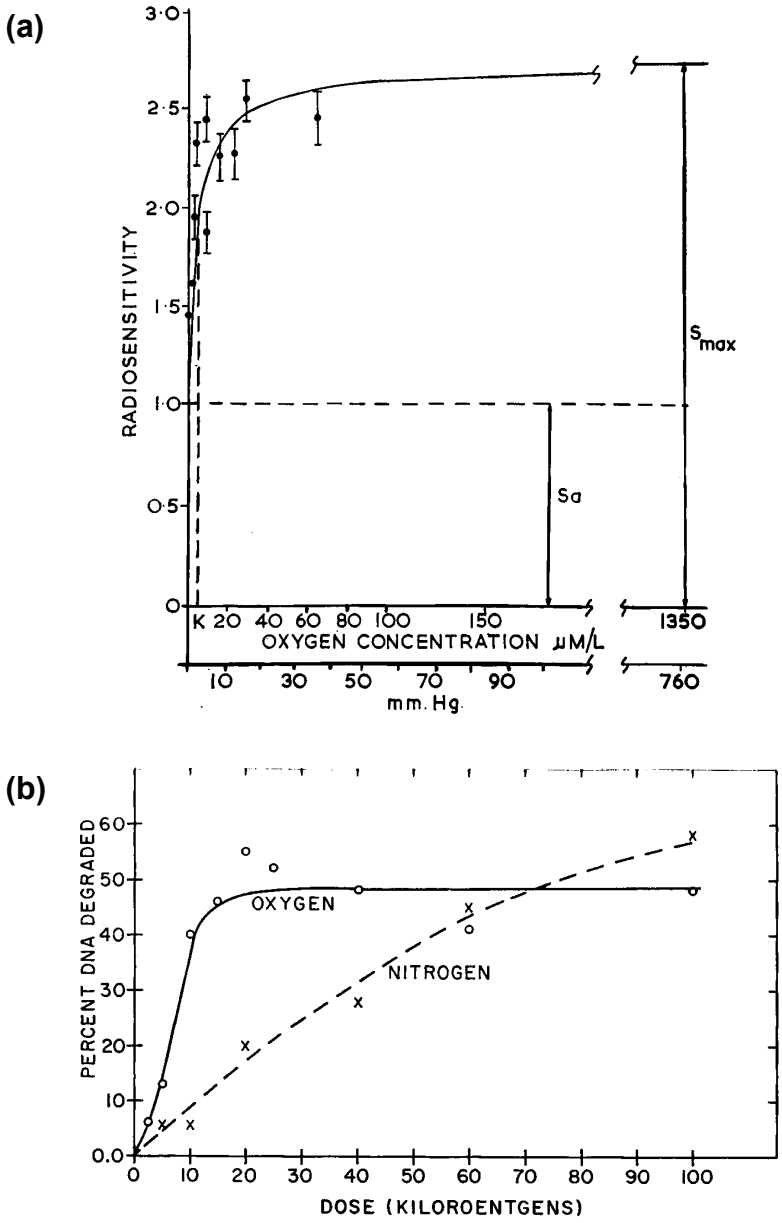

Fig. 1.1 (a) Relationship between radiosensitivity and oxygen concentration of a tumor and (b) the effect of oxygen in radiotherapy shown by percent DNA degradation (Reprinted from Ref. 10)

As one example, breathing pure oxygen (100%) or carbogen (95% O_2, 5% CO_2) has been used during therapy for an attempt to improve tumor oxygenation [13] [14]. To monitor tumor tissue oxygen tension [15], i.e., tumor pO_2, and its dynamic changes under respiratory interventions, various methods have been utilized, including fiber optic sensors [16], oxygen electrodes [17], electron spin resonance [18], and magnetic resonance imaging (MRI) [19]. In comparison, MRI has a particular advantage of providing dynamic maps of tumor pO_2 so that tumor heterogeneity can be revealed [20]. While NIR spectroscopy (NIRS) does not quantify tumor pO_2, on the other hand, it allows determination of dynamic changes in tumor vascular oxygenation and has advantages of being entirely non-invasive, providing real-time measurements, and being cost effective and portable [21]. Therefore, NIRS is a very important tool to be explored for monitoring changes in tumor oxygenation during tumor therapeutic intervention or treatment. This is the main research topic of my dissertation; namely, in the next 7 chapters, I **investigate breast tumor hemodynamics using NIRS for applications to cancer therapy monitoring**. The outline of my dissertation is given in the next section.

1.3 Overview of Dissertation

The overall objectives of my Ph. D. project are 1) to prove the hypothesis that the bi-phasic increase of $\Delta[HbO_2]$ during oxygen/carbogen inhalation is due to two different perfusion rates in tumor, using both laboratory phantoms and computational simulations, and 2) to demonstrate that NIRS can be an effective means for monitoring

tumor responses to therapeutic intervention and to cancer therapies, using animal models. Two hypotheses are proposed for this project, and accordingly I had seven specific aims planned to achieve, as listed below.

Hypothesis 1: The experimentally observed bi-phasic feature of $\Delta[HbO_2]$ increase in rat breast tumors during hyperoxic gas interventions is highly associated with two different perfusion rates within the tumor.

Aim 1: to modify and refine algorithms for accurate determination of oxygenated and deoxygenated hemoglobin concentrations in tumors. (Chapter 2)

Aim 2: to develop a tumor vascular dynamic phantom to prove that the bi-phasic feature of $\Delta[HbO_2]$ increase in tumor during oxygen intervention is highly associated with two different perfusion rates within the tumor. (Chapter 3)

Aim 3: to support the tumor vascular dynamic phantom experiments by numerically simulating bi-phasic tumor oxygen dynamics using the steady state Finite Element Method with variable levels of perfusion. (Chapter 4)

Hypothesis 2: NIRS is complementary with other techniques used to measure tumor oxygenation and can monitor cancer therapy effects by detecting changes in tumor vascular hemodynamics during respiratory challenges.

Aim 4: to demonstrate the consistency and correlation of NIRS results with those taken from needle pO_2 electrodes and MRI pO_2 readings. (Chapter 5)

Aim 5: to monitor and investigate tumor vascular responses before and after administration of a vascular disrupting agent using NIRS. (Chapter 6)

Aim 6: to monitor and quantify the heterogeneity of tumor vasculature using a multi-channel NIRS system with the proved mathematical model. (Chapter 7)

Aim 7: to monitor responses of tumors before and after cyclophosphamide treatment and to understand the therapeutic effects on tumor vasculatures. (Chapter 8)

CHAPTER 2

REFINEMENT AND MODIFICATION OF EQUATIONS FOR OBTAINING HEMOGLOBIN DERIVATIVE CONCENTRATIONS BASED ON BEER-LAMBERT'S LAW

2.1 Introduction

Hemoglobin is a molecule in the red blood cells that has a role of delivering oxygen to tissue cells. Hemoglobin is composed of four heme groups and a protein group, known as a globin. Historically, for spectrophotometric experiments, biological chemists and biochemists utilized Beer-Lambert's law and developed the notation of absorbance to express light absorption as a function of hemoglobin concentration as given [22] [23] [24] [25]:

$$OD = \text{Log}(I_0/I) = \varepsilon c L, \tag{2.1}$$

where OD is the optical density, I_0 is the light intensity of incident light, I is the light intensity of transmitted light, ε is the extinction coefficient of hemoblogin, c is the concentration of hemoglobin, and L is the length of light path through solution.

When the measured sample has a mixture of oxygenated and deoxygenated hemoglobin, Eq. (2.1) can be further expanded as [24] [25],

$$OD^{\lambda} = \{\varepsilon_{Hb}{}^{\lambda} [Hb] + \varepsilon_{HbO2}{}^{\lambda} [HbO_2]\} L, \tag{2.2}$$

where OD^{λ} is the optical density or absorbance at wavelength λ, $\varepsilon_{Hb}(\lambda)$ and $\varepsilon_{HbO2}(\lambda)$ are the extinction coefficients at wavelength λ for molar concentrations of deoxygenated hemoglobin ([Hb]) and oxygenated hemoglobin ([HbO_2]), respectively, assuming ferrihemoglobin is minimal. In some references, the light path, *L*, was taken as 1 cm without mentioning each time [24] [26]. By employing two wavelengths in Eq. (2.2), both of [HbO_2] and [Hb] can be solved and determined by measuring the light absorbance at the two specific wavelengths, provided that the values for $\varepsilon_{Hb}(\lambda)$ and $\varepsilon_{HbO2}(\lambda)$ are known, as expressed below:

$$[HbO_2] = \frac{\varepsilon_{Hb}{}^{\lambda_2} OD^{\lambda_1} - \varepsilon_{Hb}{}^{\lambda 1} OD^{\lambda_2}}{L\left(\varepsilon_{Hb}{}^{\lambda_2}\varepsilon_{HbO2}{}^{\lambda_1} - \varepsilon_{Hb}{}^{\lambda_1}\varepsilon_{HbO2}{}^{\lambda_2}\right)}, \tag{2.3}$$

$$[Hb] = \frac{\varepsilon_{HbO2}{}^{\lambda_2} OD^{\lambda_1} - \varepsilon_{HbO2}{}^{\lambda 1} OD^{\lambda_2}}{L\left(\varepsilon_{Hb}{}^{\lambda_1}\varepsilon_{HbO2}{}^{\lambda_2} - \varepsilon_{Hb}{}^{\lambda_2}\varepsilon_{HbO2}{}^{\lambda_1}\right)}. \tag{2.4}$$

It follows that changes in [Hb] and [HbO_2] can be consequently given as:

$$\Delta[HbO_2] = \frac{\varepsilon_{Hb}{}^{\lambda_2} \Delta OD^{\lambda_1} - \varepsilon_{Hb}{}^{\lambda 1} \Delta OD^{\lambda_2}}{L\left(\varepsilon_{Hb}{}^{\lambda_2}\varepsilon_{HbO2}{}^{\lambda_1} - \varepsilon_{Hb}{}^{\lambda_1}\varepsilon_{HbO2}{}^{\lambda_2}\right)}, \tag{2.5}$$

$$\Delta[Hb] = \frac{\varepsilon_{HbO2}{}^{\lambda_2} \Delta OD^{\lambda_1} - \varepsilon_{HbO2}{}^{\lambda 1} \Delta OD^{\lambda_2}}{L\left(\varepsilon_{Hb}{}^{\lambda_1}\varepsilon_{HbO2}{}^{\lambda_2} - \varepsilon_{Hb}{}^{\lambda_2}\varepsilon_{HbO2}{}^{\lambda_1}\right)}, \tag{2.6}$$

$$\Delta[Hb_{total}] = \Delta[Hb] + \Delta[HbO_2], \quad (2.7)$$

where ΔOD^{λ} represents a change in optical density at the specific wavelength, λ, and equals $\log(A_B/A_T)$. A_B and A_T correspond to light intensities measured under the baseline and transient conditions. Equations (2.5) – (2.7) are the fundamental equations that have been used in my Ph.D. studies to obtain changes of [Hb], [HbO_2], and [Hb_{total}].

In this chapter, I will first describe the calibration and modification of algorithms that were used for a single-channel, frequency-domain system in section 2.2. In section 2.3, the importance of a factor of 4 in extinction coefficients will be discussed briefly. In section 2.4 of this chapter, the importance of correct values of extinction coefficients will be extensively investigated when one calculates the changes of [Hb], [HbO_2], and [Hb_{total}] using NIRS. In section 2.5, I will report the calibration experiments for a broadband NIRS system that has been used for the study to monitor acute effects of a vascular disrupting agent on breast tumor hemodynamics, which will be investigated in Chapter 6. In section 2.6, finally, I will examine the accuracy of Δ[Hb], Δ[HbO_2], and Δ[Hb_{total}] calculated by using two wavelengths versus six wavelengths.

2.2 Modification of Algorithm for a Single-Channel, Frequency-Domain System

A single-channel, frequency-domain system was the first NIRS device that I used for obtaining tumor blood oxygenation changes during hyperoxic gas intervention,

starting summer 2000. The system had two laser diodes at wavelengths of 758 nm and 785 nm. Therefore, equations to calculate $\Delta[HbO_2]$, $\Delta[Hb]$, and $\Delta[Hb_{total}]$ were derived by entering the hemoglobin extinction coefficient values at 758 and 785 nm [27] into Eqs. (2.5) and (2.6) and obtained the following expressions:

$$\Delta[HbO_2] = \{-11.73 * \log(A_B / A_T)^{758} + 14.97 * \log(A_B / A_T)^{785}\}/L, \quad (2.8)$$

$$\Delta[Hb] = \{8.09 * \log(A_B / A_T)^{758} - 6.73 * \log(A_B / A_T)^{785}\}/L. \quad (2.9)$$

However, when I did blood phantom experiments to calibrate the NIRS system, I found a significant error in $\Delta[Hb_{total}]$ during a blood oxygenation cycle, as shown in Fig. 2.1. For this phantom experiment, I used 2 liters of 0.01M phosphate buffered saline (P-3813, Sigma, St Louis, MO) and 1% Intralipid (Intralipid® 20%, Baxter Healthcare Corp., Deerfield, IL) with pH = 7.4 at 25 ^{o}C. 14 g of baking yeast was dissolved in the phantom solution to deoxygenate the solution, and pure oxygen gas was used to oxygenate the solution. After the yeast was well mixed in the solution, 3 ml of human blood was added into the solution twice. When the blood was fully deoxygenated, pure oxygen was introduced in the solution to oxygenate the blood. After the blood was fully oxygenated, oxygen blowing was stopped in order to deoxygenate the solution with yeast again.

Since the solution was confined within a beaker during deoxygenation and oxygenation process, the total hemoglobin concentration should be maintained constant. However, as seen in Fig. 2.1, large unexpected and erroneous fluctuation of $\Delta[Hb_{total}]$ was shown during the oxygenation and deoxygenation cycles. This error in $\Delta[Hb_{total}]$ became an important issue and needed to be solved in order to trust the algorithms for monitoring blood oxygenation in tumors during hyperoxic gas interventions.

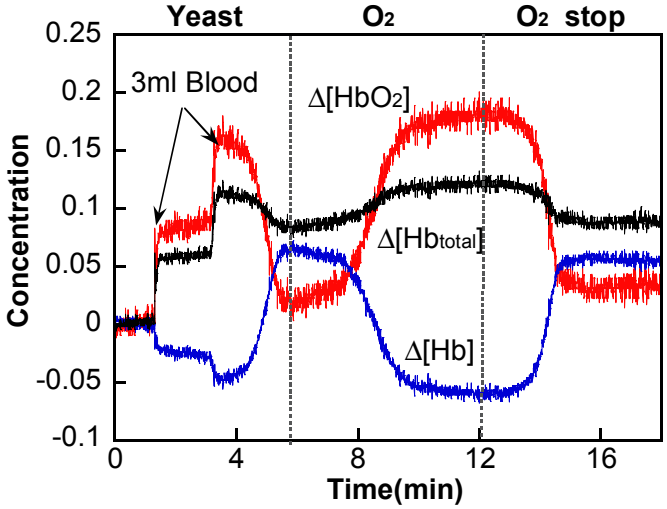

Fig. 2.1 Simultaneous dynamic changes of $\Delta[HbO_2]$, $\Delta[Hb]$, and $\Delta[Hb_{total}]$ in the phantom solution measured using NIRS with Eqs. (2.8) and (2.9), showing results with "old" hemoglobin coefficients.

To solve this calibration problem, I first tested a system at Dr. Britton Chance's lab in the University of Pennsylvania. I did a few more blood phantom experiments and tested the system for a crosstalk between amplitude and phase. Even after I found the proper range of amplitude to be used for experiments, it did not solve the calibration

problem. I finally decided to empirically calibrate Eqs. (2.8) and (2.9) to have stable signals in $\Delta[Hb_{total}]$ during the oxygenation and deoxygenation process.

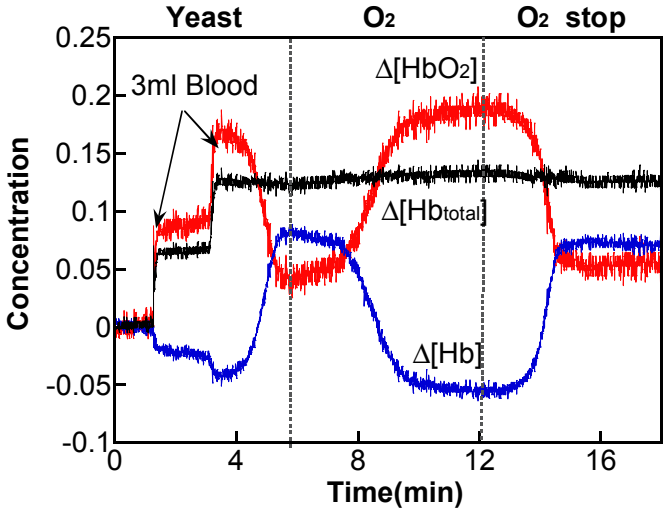

Fig. 2.2 Simultaneous dynamic changes of $\Delta[HbO_2]$, $\Delta[Hb]$, and $\Delta[Hb_{total}]$ in the phantom solution measured using the single-channel, frequency-domain NIRS system. $\Delta[HbO_2]$, $\Delta[Hb]$, and $\Delta[Hb_{total}]$ were recalculated from Fig. 2.1 by using empirically modified equations (Eqs. 2.10 and 2.11).

For empirical calibration, I divided $\log(A_B / A_T)^{758}$ in Eq. (2.8) by a factor of 1.08 and also multiplied $\log(A_B / A_T)^{758}$ in Eq. (2.9) with a factor of 1.08, resulting in Eqs. (2.10) and (2.11):

$$\Delta[HbO_2] = [-11.73 * \log(A_B / A_T)^{758} /1.08 + 14.97 * \log(A_B / A_T)^{785}] / L$$

$$= [-10.86 * \log(A_B / A_T)^{758} + 14.97 * \log(A_B / A_T)^{785}] / L, \quad (2.10)$$

$$\Delta[\mathrm{Hb}] = [8.09 * \log(A_B / A_T)^{758} * 1.08 - 6.73 * \log(A_B / A_T)^{785}] / \mathrm{L}$$

$$= [8.74 * \log(A_B / A_T)^{758} - 6.73 * \log(A_B / A_T)^{785}] / \mathrm{L}. \quad (2.11)$$

These empirically modified equations were reapplied to Fig. 2.1 and now $\Delta[\mathrm{Hb_{total}}]$ remained constant during the oxygenation and deoxygenation cycles as it should be (Fig. 2.2).

2.3 Importance of a Factor of 4

The spectrophotometric calculations shown in section 2.1 seem straight forward mathematically and have been used for several decades by biochemists to quantify [Hb] and [HbO_2] in the laboratory measurements. However, close attention needs to be paid to the definition and accuracy of ε since biochemical details in obtaining ε values give rise to different quantification of hemoglobin concentration. In early publications on spectrophotometry of hemoglobin [24], it was clearly stated that all extinction coefficients were expressed on a heme basis, using a term of equivalence, where per equivalent of hemoglobin was assumed to be 66,800/4 or 16,700 gm, i.e., one-quarter of the molecular weight of the hemoglobin molecule [28].

While spectroscopic absorption measurements became a popular methodology for biochemists to quantify [Hb] and [HbO_2] in laboratories [25] [28] [29], the notation of extinction coefficients being based on one heme group (or per equivalent) was gradually not mentioned and has become a conventional understanding for biological chemists for last 2-3 decades. It gradually becomes clear that for NIRS of hemoglobin

quantification, a factor of 4 needs to be multiplied by the ε values that were published by the conventional biochemistry methods. This is a conversion factor to account for 4 hemes per hemoglobin molecule, which has been demonstrated by Mark Cope [30]. In this way, more meaningful results for concentrations of [Hb] and [HbO_2] can be arrived from the NIR absorption measurements. In earlier publications [31] [33] [34], this factor of 4 was not considered for the calculations of Δ[Hb], Δ[HbO_2], and Δ[Hb_{total}]. However, the conclusions remain the same since the relative changes in Δ[Hb], Δ[HbO_2], and Δ[Hb_{total}] were monitored and a constant factor would not affect the dynamic behaviors of hemodynamics.

2.4 Importance of Correct Values of Hemoglobin Extinction Coefficient

2.4.1 Background

After I developed empirically modified equations for Δ[HbO_2], Δ[Hb], and Δ[Hb_{total}], I found that there is another source of hemoglobin extinction coefficients provided by the dissertation of Mark Cope [30]. Before Cope's dissertation, I had references for hemoglobin extinction coefficients only from Zijlstra's group [27] [32]. The drawback of Zijlstra's reports is that they provide only a few discrete values of hemoglobin extinction coefficient values in the near infrared range in tabular form. That is the reason that Dr. Liu's group had to estimate the values of extinction coefficients of Hb and HbO_2 by interpolating adjacent values in their earlier publications [31] [33] [34]. For examples, the values of Hb and HbO_2 extinction coefficients at 758 nm were estimated by interpolating the values between 750 and 775 nm, and also the values of

Hb and HbO_2 extinction coefficients at 785 nm were estimated by interpolating the values between 775 and 800 nm. Later, I found that this estimation of εHb and εHbO_2 at 758 and 785 nm, which deviated greatly from the correct ones at 758 and 785 nm, was the main reason why $\Delta[Hb_{total}]$ was not stable during oxy- or deoxygenation process, as previously shown in Fig. 2.1. Therefore, I started to compile all the possible references that contain the tabular form of hemoglobin extinction coefficients and compared the possible differences in $\Delta[HbO_2]$, $\Delta[Hb]$, and $\Delta[Hb_{total}]$ calculated by using different values of hemoglobin extinction coefficients. This section reports my detailed study in this regard.

Tabular forms of hemoglobin extinction coefficients are available mainly from three research groups, namely Zijlstra *et al.* [25] [27] [29] [32] [23] [35] [36], Delpy *et al.* (Wray *et al.* [37], Cope [30], Matcher *et al.* [38]), and Prahl [39]. Zijlstra's group has extensively reported human hemoglobin extinction coefficients and also reported hemoglobin extinction coefficients from various species [36]. However, they showed only a few discrete extinction coefficient values of hemoglobin derivatives in the NIR region while Cope [30] provided extinction coefficients of human blood in every single unit (nm) of wavelength from 650 nm to beyond 1 μm. Cope measured human extinction coefficients with their own experiments, compared with other previous reports, and found that the isobestic point of hemoglobin in the NIR region was shifted to 798 ± 1.5 nm from 800 nm [22], 805 nm [40] and 815 nm [41]. The hemoglobin extinction coefficient values from Prahl [39] are only available in the website, not as a published reference. However, his values were adopted in this study to be compared

with other groups' extinction coefficients, since his extinction coefficients have been widely used by different groups of researchers [42] [43] [44].

There are several sources which can cause variations in hemoglobin extinction coefficients. Firstly, the extinction coefficient values of hemoglobin derivatives impose experimental errors when they were obtained. Secondly, the central peaks of laser diodes or LEDs used as light sources in NIRS can deviate from the known centre peaks that the manufacturers originally provided. The wavelength of a laser diode or LED can be shifted by changes of temperature or driving current during experiments. For example, according to the specification of a laser diode from Hitachi (HL7851G, http://www.has.hitachi.com.sg/databook/Hitachi/ Optoelec/ HL7851G.pdf), temperature changes from 20 to 30 ^{o}C can cause a shift of wavelength from 784 nm to 787 nm, and an operation current change from 140 mA to 170 mA can cause a shift of wavelength from 785 nm to 795 nm. Thirdly, when one uses human hemoglobin extinction coefficients to calculate hemoglobin concentrations from animal experiments, there can be an error in determination of hemoglobin concentration due to discrepancies of hemoglobin extinction coefficients between human and animals. According to Zijlstra *et al.* [32], three human hemoglobin extinction coefficients at 750 nm, 775 nm, and 800 nm were off by 0.01 (cm^{-1} mM^{-1}) from rat hemoglobin extinction coefficients. In addition, temperature, pH and sensitivity of detectors can have influences on the accuracy of determinations in oxyhemoglobin, [HbO_2], deoxyhemoglobin, [Hb] and total hemoglobin, [Hb_{total}], concentrations.

The objective of this section is to demonstrate that even small variation of hemoglobin extinction coefficients can cause notable errors in determination of hemoglobin concentration.

2.4.2 Derivation of Equations for Error Estimation

By replacing ΔO.D. with log (A_B/A_T) and also reformatting into matrix form, Eqs. (2.5) and (2.6) in section 2.1 can be combined and expressed as Eq. (2.12)

$$\begin{pmatrix} \Delta[Hb] \\ \Delta[HbO_2] \end{pmatrix} = \frac{1}{d \cdot DPF} \cdot \frac{1}{\varepsilon_{Hb}^{\lambda 2}\varepsilon_{HbO_2}^{\lambda 1} - \varepsilon_{Hb}^{\lambda 1}\varepsilon_{HbO_2}^{\lambda 2}} \begin{pmatrix} -\varepsilon_{HbO_2}^{\lambda 2} & \varepsilon_{HbO_2}^{\lambda 1} \\ \varepsilon_{Hb}^{\lambda 2} & -\varepsilon_{Hb}^{\lambda 1} \end{pmatrix} \begin{pmatrix} \log\left(\frac{A_B}{A_T}\right)^{\lambda 1} \\ \log\left(\frac{A_B}{A_T}\right)^{\lambda 2} \end{pmatrix}. \qquad (2.12)$$

The error in Δ[Hb], Δ[HbO_2] and Δ[Hb_{total}] caused by the variations in ε can be estimated in the following way. Since $\varepsilon_{Hb}^{\lambda 1}$, $\varepsilon_{Hb}^{\lambda 2}$, $\varepsilon_{HbO_2}^{\lambda 1}$ and $\varepsilon_{HbO_2}^{\lambda 2}$ are independent from each other, the errors in Δ[Hb], Δ[HbO_2] and Δ[Hb_{total}] caused by the variations in all of $\varepsilon_{Hb}^{\lambda 1}$, $\varepsilon_{Hb}^{\lambda 2}$, $\varepsilon_{HbO_2}^{\lambda 1}$ and $\varepsilon_{HbO_2}^{\lambda 2}$ can be estimated using the following error propagation principle [45]:

$$\Delta\{\Delta[Hb]\} = \pm\left\{\left(\Delta\varepsilon_{Hb}^{\lambda 1}\cdot\frac{\partial\{\Delta[Hb]\}}{\partial\varepsilon_{Hb}^{\lambda 1}}\right)^2+\left(\Delta\varepsilon_{Hb}^{\lambda 2}\cdot\frac{\partial\{\Delta[Hb]\}}{\partial\varepsilon_{Hb}^{\lambda 2}}\right)^2\right.$$

$$\left.+\left(\Delta\varepsilon_{HbO_2}^{\lambda 1}\cdot\frac{\partial\{\Delta[Hb]\}}{\partial\varepsilon_{HbO_2}^{\lambda 1}}\right)^2+\left(\Delta\varepsilon_{HbO_2}^{\lambda 2}\cdot\frac{\partial\{\Delta[Hb]\}}{\partial\varepsilon_{HbO_2}^{\lambda 2}}\right)^2\right\}^{1/2} \tag{2.13}$$

$$\Delta\{\Delta[HbO_2]\} = \pm\left\{\left(\Delta\varepsilon_{Hb}^{\lambda 1}\cdot\frac{\partial\{\Delta[HbO_2]\}}{\partial\varepsilon_{Hb}^{\lambda 1}}\right)^2+\left(\Delta\varepsilon_{Hb}^{\lambda 2}\cdot\frac{\partial\{\Delta[HbO_2]\}}{\partial\varepsilon_{Hb}^{\lambda 2}}\right)^2\right.$$

$$\left.+\left(\Delta\varepsilon_{HbO_2}^{\lambda 1}\cdot\frac{\partial\{\Delta[HbO_2]\}}{\partial\varepsilon_{HbO_2}^{\lambda 1}}\right)^2+\left(\Delta\varepsilon_{HbO_2}^{\lambda 2}\cdot\frac{\partial\{\Delta[HbO_2]\}}{\partial\varepsilon_{HbO_2}^{\lambda 2}}\right)^2\right\}^{1/2} \tag{2.14}$$

$$\Delta\{\Delta[Hb_{total}]\} = \pm\left\{\left(\Delta\varepsilon_{Hb}^{\lambda 1}\cdot\frac{\partial\{\Delta[Hb_{total}]\}}{\partial\varepsilon_{Hb}^{\lambda 1}}\right)^2+\left(\Delta\varepsilon_{Hb}^{\lambda 2}\cdot\frac{\partial\{\Delta[Hb_{total}]\}}{\partial\varepsilon_{Hb}^{\lambda 2}}\right)^2\right.$$

$$\left.+\left(\Delta\varepsilon_{HbO_2}^{\lambda 1}\cdot\frac{\partial\{\Delta[Hb_{total}]\}}{\partial\varepsilon_{HbO_2}^{\lambda 1}}\right)^2+\left(\Delta\varepsilon_{HbO_2}^{\lambda 2}\cdot\frac{\partial\{\Delta[Hb_{total}]\}}{\partial\varepsilon_{HbO_2}^{\lambda 2}}\right)^2\right\}^{1/2} \tag{2.15}$$

where $\Delta\varepsilon_{Hb}^{\lambda 1}$, $\Delta\varepsilon_{Hb}^{\lambda 2}$, $\Delta\varepsilon_{HbO_2}^{\lambda 1}$ and $\Delta\varepsilon_{HbO_2}^{\lambda 2}$ are the uncertainties in $\varepsilon_{Hb}^{\lambda 1}$, $\varepsilon_{Hb}^{\lambda 2}$, $\varepsilon_{HbO_2}^{\lambda 1}$ and $\varepsilon_{HbO_2}^{\lambda 2}$, respectively. To facilitate the computation, the following parameters are defined:

$$C1 = \log\left(\frac{A_B}{A_T}\right)^{\lambda 1},\ C2 = \log\left(\frac{A_B}{A_T}\right)^{\lambda 2}, \text{ and} \tag{2.16}$$

$$D = \varepsilon_{Hb}^{\lambda 2}\varepsilon_{HbO_2}^{\lambda 1} - \varepsilon_{Hb}^{\lambda 1}\varepsilon_{HbO_2}^{\lambda 2}, \tag{2.17}$$

After substituting Eqs. (2.16) and (2.17) into Eqs. (2.12) and (2.7), $\Delta[Hb]$, $\Delta[HbO_2]$ and $\Delta[Hb_{total}]$ can be expressed as

$$\Delta[Hb] = \frac{1}{d}\frac{\left(-\varepsilon_{HbO_2}^{\lambda 2}\cdot C1 + \varepsilon_{HbO_2}^{\lambda 1}\cdot C2\right)}{D}, \tag{2.18}$$

$$\Delta[HbO_2] = \frac{1}{d}\frac{\left(\varepsilon_{Hb}^{\lambda 2}\cdot C1 - \varepsilon_{Hb}^{\lambda 1}\cdot C2\right)}{D}, \tag{2.19}$$

$$\Delta[Hb_{total}] = \frac{1}{d}\frac{\left[\left(\varepsilon_{Hb}^{\lambda 2} - \varepsilon_{HbO_2}^{\lambda 2}\right)\cdot C1 + \left(\varepsilon_{HbO_2}^{\lambda 1} - \varepsilon_{Hb}^{\lambda 1}\right)\cdot C2\right]}{D}, \tag{2.20}$$

Note that the factor of *DPF* has been included in the unit as mM/*DPF*. Then, the respective derivative terms in Eqs. (2.13)-(2.15) are derived and expressed as

$$\frac{\partial\{\Delta[Hb]\}}{\partial\varepsilon_{Hb}^{\lambda 1}} = \frac{\varepsilon_{HbO_2}^{\lambda 2}}{d}\frac{\left(-\varepsilon_{HbO_2}^{\lambda 2}\cdot C1 + \varepsilon_{HbO_2}^{\lambda 1}\cdot C2\right)}{D^2}, \tag{2.21}$$

$$\frac{\partial\{\Delta[Hb]\}}{\partial\varepsilon_{Hb}^{\lambda 2}}=\frac{-\varepsilon_{HbO_2}^{\lambda 1}}{d}\frac{(-\varepsilon_{HbO_2}^{\lambda 2}\cdot C1+\varepsilon_{HbO_2}^{\lambda 1}\cdot C2)}{D^2}, \tag{2.22}$$

$$\frac{\partial\{\Delta[Hb]\}}{\partial\varepsilon_{HbO_2}^{\lambda 1}}=\frac{\varepsilon_{HbO_2}^{\lambda 2}}{d}\frac{\left(\varepsilon_{Hb}^{\lambda 2}\cdot C1-\varepsilon_{Hb}^{\lambda 1}\cdot C2\right)}{D^2}, \tag{2.23}$$

$$\frac{\partial\{\Delta[Hb]\}}{\partial\varepsilon_{HbO_2}^{\lambda 2}}=\frac{-\varepsilon_{HbO_2}^{\lambda 1}}{d}\frac{\left(\varepsilon_{Hb}^{\lambda 2}\cdot C1-\varepsilon_{Hb}^{\lambda 1}\cdot C2\right)}{D^2}. \tag{2.24}$$

$$\frac{\partial\{\Delta[HbO_2]\}}{\partial\varepsilon_{Hb}^{\lambda 1}}=\frac{\varepsilon_{Hb}^{\lambda 2}}{d}\frac{(\varepsilon_{HbO_2}^{\lambda 2}\cdot C1-\varepsilon_{HbO_2}^{\lambda 1}\cdot C2)}{D^2}, \tag{2.25}$$

$$\frac{\partial\{\Delta[HbO_2]\}}{\partial\varepsilon_{Hb}^{\lambda 2}}=\frac{-\varepsilon_{Hb}^{\lambda 1}}{d}\frac{(\varepsilon_{HbO_2}^{\lambda 2}\cdot C1-\varepsilon_{HbO_2}^{\lambda 1}\cdot C2)}{D^2}, \tag{2.26}$$

$$\frac{\partial\{\Delta[HbO_2]\}}{\partial\varepsilon_{HbO_2}^{\lambda 1}}=\frac{\varepsilon_{Hb}^{\lambda 2}}{d}\frac{\left(-\varepsilon_{Hb}^{\lambda 2}\cdot C1+\varepsilon_{Hb}^{\lambda 1}\cdot C2\right)}{D^2}, \tag{2.27}$$

$$\frac{\partial\{\Delta[HbO_2]\}}{\partial\varepsilon_{HbO_2}^{\lambda 2}}=\frac{-\varepsilon_{Hb}^{\lambda 1}}{d}\frac{\left(-\varepsilon_{Hb}^{\lambda 2}\cdot C1+\varepsilon_{Hb}^{\lambda 1}\cdot C2\right)}{D^2}. \tag{2.28}$$

$$\frac{\partial\{\Delta[Hb_{total}]\}}{\partial\varepsilon_{Hb}^{\lambda 1}}=\frac{\left(\varepsilon_{Hb}^{\lambda 2}-\varepsilon_{HbO_2}^{\lambda 2}\right)}{d}\cdot\frac{\left(\varepsilon_{HbO_2}^{\lambda 2}\cdot C1-\varepsilon_{HbO_2}^{\lambda 1}\cdot C2\right)}{D^2}, \tag{2.29}$$

$$\frac{\partial\{\Delta[Hb_{total}]\}}{\partial\varepsilon_{Hb}^{\lambda 2}}=\frac{\left(\varepsilon_{HbO_2}^{\lambda 1}-\varepsilon_{Hb}^{\lambda 1}\right)}{d}\cdot\frac{\left(\varepsilon_{HbO_2}^{\lambda 2}\cdot C1-\varepsilon_{HbO_2}^{\lambda 1}\cdot C2\right)}{D^2}, \tag{2.30}$$

$$\frac{\partial\{\Delta[Hb_{total}]\}}{\partial\varepsilon_{HbO_2}^{\lambda 1}}=\frac{\left(\varepsilon_{HbO2}^{\lambda 2}-\varepsilon_{Hb}^{\lambda 2}\right)}{d}\cdot\frac{\left(\varepsilon_{Hb}^{\lambda 2}\cdot C1-\varepsilon_{Hb}^{\lambda 1}\cdot C2\right)}{D^2}, \tag{2.31}$$

$$\frac{\partial\{\Delta[Hb_{total}]\}}{\partial\varepsilon_{HbO_2}^{\lambda 2}}=\frac{\left(\varepsilon_{Hb}^{\lambda 1}-\varepsilon_{HbO_2}^{\lambda 1}\right)}{d}\cdot\frac{\left(\varepsilon_{Hb}^{\lambda 2}\cdot C1-\varepsilon_{Hb}^{\lambda 1}\cdot C2\right)}{D^2}. \tag{2.32}$$

By substituting Eqs. (2.21)-(2.32) into Eqs. (2.13)-(2.15), errors of $\Delta[Hb]$, $\Delta[HbO_2]$ and $\Delta[Hb_{total}]$ caused by $\Delta\varepsilon_{Hb}^{\lambda 1}$, $\Delta\varepsilon_{Hb}^{\lambda 2}$, $\Delta\varepsilon_{HbO_2}^{\lambda 1}$ and $\Delta\varepsilon_{HbO_2}^{\lambda 2}$ can be quantified.

2.4.3 Results of Error Estimation

Since the wavelengths of the light sources used in the homodyne, frequency-domain NIRS system were 758 and 785 nm, I have obtained hemoglobin extinction coefficient values at these two specific wavelengths from three different groups (Table 2.1 and 2.2). Extinction coefficients given in the left three columns of ε_{Hb} and ε_{HbO_2} in Table 2.1 and 2.2 are from Zijlstra *et al*'s reports [27] [32] [36], and the ones in the fourth and fifth column of ε_{Hb} and ε_{HbO_2} are from Cope [30] and Prahl [39], respectively.

Since the tabular form of extinction coefficients from Zijlstra *et al.* [32] does not have ε values of Hb and HbO_2 at 758 and 785 nm, the values listed were obtained by linear interpolation between 750 and 775 nm and between 775 and 800 nm, respectively. In a similar way, ε values of Hb and HbO_2 at 775 and 785 nm from Prahl [39] and Zijlstra [36] were obtained by linear interpolation between 774 and 776 nm and between 784 and 786 nm, respectively. The hemoglobin extinction coefficients, ε, from Zijlstra are "per equivalent" or "per heme" values, and thus they were multiplied by 4 to be considered as four hemes per hemoglobin so that they can be compared to the ε values given by Cope [30] and Prahl [39]. To be more complete, the hemoglobin extinction coefficients in the NIR range (700 to 900 nm) from Cope, Prahl, and Zijlstra *et al.* [36] were plotted in Fig. 2.3.

Table 2.1 Deoxyhemoglobin extinction coefficients from three different groups.*

Wave length (nm)	ε_{Hb} ($mM^{-1}\cdot cm^{-1}$)				
	Zijlstra (1991)	Zijlstra (1994)	Zijlstra (2000)	Cope (1991)	Prahl (1998)
750	1.56	1.48	1.552	1.5458	1.4052
758		1.416	1.668	1.6820	1.5605
775	1.16	1.28	1.226	1.2481	1.1883
785		1.104	0.996	0.9975	0.9770
800	0.80	0.84	0.86	0.8399	0.7617

* Errors of these coefficients were not provided from the references.

Table 2.2 Oxyhemoglobin extinction coefficients from three different groups. *

Wave length (nm)	ε_{HbO_2} ($mM^{-1}\cdot cm^{-1}$)				
	Zijlstra (1991)	Zijlstra (1994)	Zijlstra (2000)	Cope (1991)	Prahl (1998)
750	0.56	0.6	0.592	0.5495	0.5180
758		0.6384	0.628	0.5974	0.5740
775	0.68	0.72	0.706	0.7038	0.6832
785		0.768	0.756	0.7681	0.7354
800	0.80	0.84	0.832	0.8653	0.8160

* Errors of these coefficients were not provided from the references.

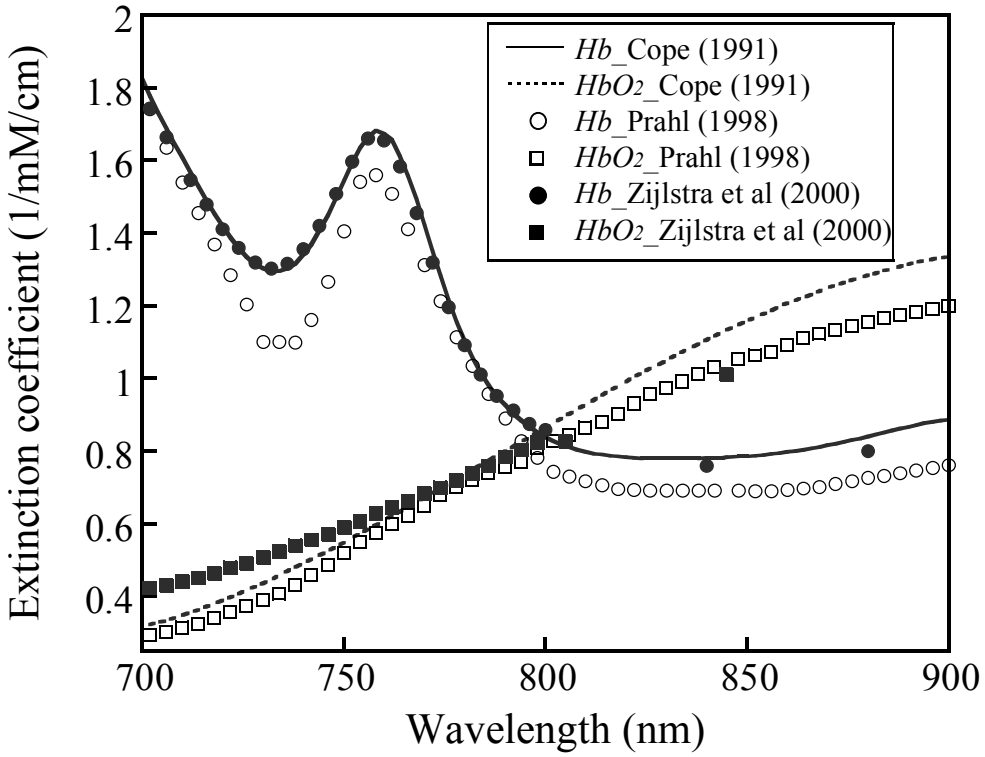

Fig. 2.3 Hemoglobin near IR absorption spectra from Cope [30], Prahl [39], and Zijlstra *et al.* [36].

As shown in Fig. 2.3, the spectra of ε_{Hb} and ε_{HbO_2} given by the three respective groups are similar but with notable differences from one another. To determine how much deviations in $\Delta[HbO_2]$, $\Delta[Hb]$, and $\Delta[Hb_{total}]$ can be resulted from the discrepancies in hemoglobin extinction values among the groups, I first obtained the differences of hemoglobin ε values among the three groups as shown in Table 2.3. Figure 2.4 shows the spectral differences of hemoglobin ε values among Cope [30], Prahl [39] and Zijlstra *et al.* [36] within the NIR range (700 nm to 900 nm). Note that there are only a few points available from 800 nm to 900 nm between Zijlstra *et al.* [36] versus Cope [30] and Zijlstra *et al.* [36] versus Prahl [39] since Zijlstra *et al.* [36] has published only four ε values of *Hb* and HbO_2 in this wavelength range.

Table 2.3 Differences in hemoglobin ε values among three different groups.

Wave length (nm)	$\Delta\varepsilon_{Hb}$ ($mM^{-1}\cdot cm^{-1}$)				$\Delta\varepsilon_{HbO_2}$ ($mM^{-1}\cdot cm^{-1}$)			
	Zijlstra (1994) vs. 2000	Zijlstra (2000) vs. Cope	Zijlstra (2000) vs. Prahl	Cope vs. Prahl	Zijlstra (1994) vs. 2000	Zijlstra (2000) vs. Cope	Zijlstra (2000) vs. Prahl	Cope vs. Prahl
750	0.072	0.0062	0.1468	0.1406	0.008	0.0425	0.074	0.0315
758	0.252	0.014	0.1075	0.1215	0.0104	0.0306	0.054	0.0234
775	0.054	0.0221	0.0377	0.0598	0.014	0.0022	0.0228	0.0206
785	0.108	0.0015	0.019	0.0205	0.012	0.0121	0.0206	0.0327
800	0.02	0.0201	0.0983	0.0782	0.008	0.0333	0.016	0.0493

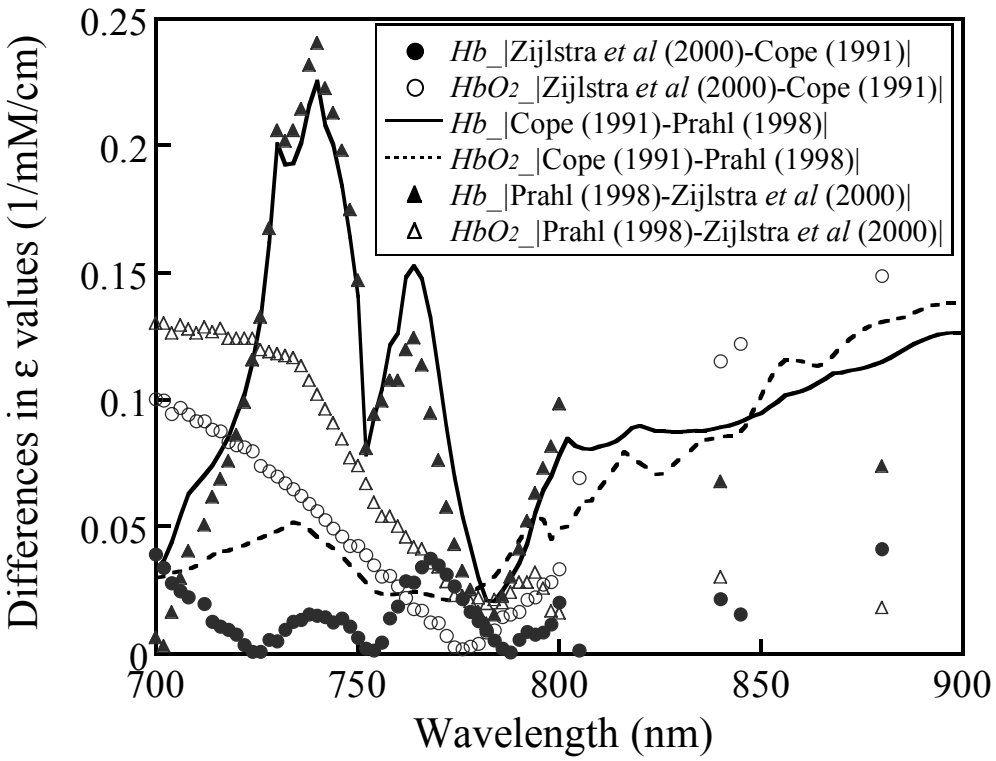

Fig. 2.4 Differences in hemoglobin absorption spectra among Cope [30], Prahl [39] and Zijlstra *et al.* [36].

Once I obtained the differences of hemoglobin extinction coefficients at 758 and 785 nm among the three groups, the values of $\Delta\varepsilon_{Hb}^{\lambda 1}$, $\Delta\varepsilon_{Hb}^{\lambda 2}$, $\Delta\varepsilon_{HbO_2}^{\lambda 1}$ and $\Delta\varepsilon_{HbO_2}^{\lambda 2}$ are available for error calculations using Eqs. (2.13) to (2.15). The needed respective derivative terms in Eqs. (2.13) and (2.15) are given through Eqs. (2.21) to (2.32) with the definitions of $C1=\log\left(\frac{I_B}{I_T}\right)^{\lambda 1}$, $C2=\log\left(\frac{I_B}{I_T}\right)^{\lambda 2}$, and $D=\varepsilon_{Hb}^{\lambda 2}\varepsilon_{HbO_2}^{\lambda 1}-\varepsilon_{Hb}^{\lambda 1}\varepsilon_{HbO_2}^{\lambda 2}$. Specifically, I utilized a set of amplitudes at $\lambda 1$=758 nm and $\lambda 2$=785 nm taken during the deoxygenated state (1 min before oxygen intervention) from the tissue phantom experiment shown in Figs. 2.1 and 2.2 with the following readings:

$$C1 = \log\left(\frac{I_b}{I_t}\right)^{\lambda 1} = \log\left(\frac{297}{264}\right)^{758} = 0.0512\,,\ C2 = \log\left(\frac{I_b}{I_t}\right)^{\lambda 2} = \log\left(\frac{148}{134}\right)^{785} = 0.0432\,. \qquad (2.33)$$

Substituting Eq. (2.33) and the hemoglobin ε values at 758 nm and 785 nm given by Zijlstra *et al.* [32] into Eqs. (2.13) to (2.15) leads to values of $\Delta[Hb]$, $\Delta[HbO_2]$, and $\Delta[Hb_{total}]$ as follows:

$$\Delta[Hb] = 15.33\ (\mu M/DPF), \qquad (2.34)$$

$$\Delta[HbO_2] = 6.06\ (\mu M/DPF), \qquad (2.35)$$

$$\Delta[Hb_{total}] = 21.39\ (\mu M/DPF). \qquad (2.36)$$

Based on Table 2.3, I further obtained $\Delta\varepsilon_{Hb}^{758} = 0.252\ mM^{-1}cm^{-1}$, $\Delta\varepsilon_{Hb}^{785} = 0.108\ mM^{-1}cm^{-1}$, $\Delta\varepsilon_{HbO_2}^{758} = 0.0104\ mM^{-1}cm^{-1}$, and $\Delta\varepsilon_{HbO_2}^{785} = 0.012\ mM^{-1}cm^{-1}$, as the variation or uncertainty of hemoglobin extinction coefficients between Zijlstra *et al.* [32] and [36]. The corresponding relative deviations in $\Delta[Hb]$, $\Delta[HbO_2]$ and $\Delta[Hb_{total}]$ are calculated using Eqs. (2.13) to (2.15) with respect to Eqs. (2.34) to (2.36):

$$\frac{\Delta\{\Delta[Hb]\}}{\Delta[Hb]} = \frac{8.3}{15.33}\cdot 100\% = 54.1\%\,, \qquad (2.37)$$

$$\frac{\Delta\{\Delta[HbO_2]\}}{\Delta[HbO_2]} = \frac{12.7}{6.06} \cdot 100\% = 209.6\%\,, \tag{2.38}$$

$$\frac{\Delta\{\Delta[Hb_{total}]\}}{\Delta[Hb_{total}]} = \frac{6.1}{21.39} \cdot 100\% = 28.5\%\,. \tag{2.39}$$

To more completely compare the calculated uncertainties of $\Delta[Hb]$, $\Delta[HbO_2]$, and $\Delta[Hb_{total}]$ using different groups of hemoglobin ε values, I have calculated relative deviations in four cases with different comparative combinations, as shown in Table 2.4. All of the calculations for $\Delta\{\Delta[Hb]\}$, $\Delta\{\Delta[HbO_2]\}$, and $\Delta\{\Delta[Hb_{total}]\}$ in this table were obtained using the amplitude values shown in Eq. (2.33), d = 2 cm, and hemoglobin extinction coefficient values from Zijlstra *et al.* (1994) (Case 1), Zijlstra *et al.* (2000) (Case 2), Cope (1991) (Case 3), and Prahl (1998) (Case 4). This table clearly shows that the minimum deviation in calculated hemoglobin derivative concentrations is obtained between using Zijlstra *et al*'s (2000) and Cope's (1991) hemoglobin ε values (Case 2), with less than 15% relative deviations. The greatest deviation occurred between using the ε values given by Zijlstra *et al.* (1994) and Zijlstra *et al.* (2000).

In these calculations, the extinction coefficients of *Hb* and HbO_2 at 758 nm and 785 nm given by Zijlstra *et al.* (1994) [32] were obtained by a linear interpolation between values at 750 nm, 775 nm, and 800 nm. This linear interpolation obviously is the source of big deviation in ε values in comparison with those from Zijlstra *et al.* (2000) [36], and thus the largest deviation in $\Delta[Hb]$, $\Delta[HbO_2]$, and $\Delta[Hb_{total}]$ occurred

Table 2.4 The relative errors caused by discrepancies of hemoglobin ε values.

Case 1: Zijlstra *et al.* (1994) vs. Zijlstra *et al.* (2000) ($\Delta\varepsilon_{Hb}^{758}$=0.252, $\Delta\varepsilon_{Hb}^{785}$=0.108, $\Delta\varepsilon_{HbO_2}^{758}$=0.0104, and $\Delta\varepsilon_{HbO_2}^{785}$=0.012; all in $mM^{-1}cm^{-1}$)			
Concentration (μM/*DPF*)	A:Calculated by using ε from Zijlstra (1994)	B: Deviation (=Δ{Δ[Hb derivatives]})	Relative deviation to A (=100*B/A) (%)
Δ[*Hb*]	15.33	8.32	54.3
Δ[HbO_2]	6.06	12.72	209.9
Δ[Hb_{total}]	21.39	6.07	28.4
Case 2: Zijlstra *et al.* (2000) vs. Cope (1991) ($\Delta\varepsilon_{Hb}^{758}$=0.014, $\Delta\varepsilon_{Hb}^{785}$=0.0015, $\Delta\varepsilon_{HbO_2}^{758}$=0.0306, and $\Delta\varepsilon_{HbO_2}^{785}$=0.0121; all in $mM^{-1}cm^{-1}$)			
Concentration (μM/*DPF*)	A:Calculated by using ε from Zijlstra (2000)	B: Deviation (=Δ{Δ[Hb derivatives]})	Relative deviation to A (=100*B/A) (%)
Δ[*Hb*]	9.10	1.26	13.8
Δ[HbO_2]	16.55	0.97	5.9
Δ[Hb_{total}]	25.65	1.93	7.5
Case 3: Cope (1991) vs. Prahl (1998) ($\Delta\varepsilon_{Hb}^{758}$=0.1215, $\Delta\varepsilon_{Hb}^{785}$=0.0205, $\Delta\varepsilon_{HbO_2}^{758}$=0.0234, $\Delta\varepsilon_{HbO_2}^{785}$=0.0327; all in $mM^{-1}cm^{-1}$)			
Concentration (μM/*DPF*)	A:Calculated by using ε from Cope (1991)	B: Deviation (=Δ{Δ[Hb derivatives]})	Relative deviation to A (=100*B/A) (%)
Δ[*Hb*]	9.70	2.23	23.0
Δ[HbO_2]	15.49	2.20	14.2
Δ[Hb_{total}]	25.20	4.55	18.1
Case 4: Prahl (1998) vs. Zijlstra *et al.* (2000) ($\Delta\varepsilon_{Hb}^{758}$=0.1075, $\Delta\varepsilon_{Hb}^{785}$=0.019, $\Delta\varepsilon_{HbO_2}^{758}$=0.054 and $\Delta\varepsilon_{HbO_2}^{785}$=0.0206; all in $mM^{-1}cm^{-1}$)			
Concentration (μM/*DPF*)	A:Calculated by using ε from Prahl (1998)	B: Deviation (=Δ{Δ[Hb derivatives]})	Relative deviation to A (=100*B/A) (%)
Δ[*Hb*]	10.95	2.48	22.6
Δ[HbO_2]	14.80	2.31	15.6
Δ[Hb_{total}]	25.75	3.31	12.9

between the two cases of using the ε values by Zijlstra *et al.* [32] and [36]. Another notable point shown in Table 2.4 is that the values of $\Delta\{\Delta[Hb_{total}]\}$ due to discrepancies in hemoglobin extinction coefficients are not always the largest in comparison with those of $\Delta\{\Delta[Hb]\}$ and $\Delta\{\Delta[HbO_2]\}$. This point will be discussed in the following subsection.

2.4.4 Discussion and Conclusion

To quantify concentrations of hemoglobin derivatives, the extinction coefficient values of HbO_2 and Hb have to be employed. However, little report has shown how small deviation in extinction coefficients could cause errors in quantifying the concentrations of hemoglobin derivatives. In this section, I derived equations to estimate deviations or errors of hemoglobin derivatives caused by variation of hemoglobin extinction coefficients. To support my error analysis, I applied the data from my blood phantom experiment (Figs. 2.1 and 2.2), which was shown in section 2.2. The error calculation has shown that even small variation (0.01 $cm^{-1}mM^{-1}$) in extinction coefficients can produce significant deviations in quantification of $\Delta[HbO_2]$, $\Delta[Hb]$, and $\Delta[Hb_{total}]$. This study clearly demonstrates that it is important to be aware of any variation in hemoglobin extinction coefficients, which could highly affect the accuracy of $\Delta[HbO_2]$, $\Delta[Hb]$, and $\Delta[Hb_{total}]$ from *in vivo* tissue measurements.

The hemoglobin extinction coefficients have been studied for more than 5 decades by biochemists or clinical chemists to quantify $[Hb]$ and $[HbO_2]$ in laboratory measurements. For convenient comparison, representative tabulated values of

hemoglobin extinction coefficients from several references [22] [23] [24] [25] [26] [27] [30] [32] [35] [36] [37] [38] [39] [41] are compiled in Appendix D in this dissertation with a unit of 0.25 mM^{-1} cm^{-1} which represents the "per heme" values.

Although my error analysis focuses on the accuracy for changes in [Hb], [HbO_2] and [Hb_{total}], all the mathematical derivations given in Eqs. (2.13) to (2.15) and (2.21) to (2.32) can be readily used in error analysis for absolute calculations of [Hb], [HbO_2] and [Hb_{total}]. It is known that the expresions for [Hb] and [HbO_2] can be expressed as [46] [47]:

$$\begin{pmatrix} [Hb] \\ [HbO_2] \end{pmatrix} = \frac{1}{2.3} \cdot \frac{1}{\varepsilon_{Hb}^{\lambda 2}\varepsilon_{HbO_2}^{\lambda 1} - \varepsilon_{Hb}^{\lambda 1}\varepsilon_{HbO_2}^{\lambda 2}} \begin{pmatrix} -\varepsilon_{HbO_2}^{\lambda 2} & \varepsilon_{HbO_2}^{\lambda 1} \\ \varepsilon_{Hb}^{\lambda 2} & -\varepsilon_{Hb}^{\lambda 1} \end{pmatrix} \begin{pmatrix} \mu_a^{\lambda 1} \\ \mu_a^{\lambda 2} \end{pmatrix}. \tag{2.40}$$

The similarity between equations (2.12) and (2.40) warrants the validation of the analysis methodology for [Hb], [HbO_2] and [Hb_{total}].

Previously, Fantini *et al.* [48] studied the uncertainties in [Hb], [HbO_2] and [Hb_{total}] due to propagation of uncertainties in μ_a and μ_s'. In their report, they have shown an equation for the uncertainty in [Hb_{total}] caused by the standard deviation in μ_a and μ_s' as follows:

$$\sigma([Hb_{total}]) = \sqrt{\{\sigma([Hb])\}^2 + \{\sigma([HbO_2])\}^2}\ . \tag{2.41}$$

This equation basically implies that the variation of [Hb_{total}] caused by uncertainties in μ_a and μ_s' is always larger than those of [Hb] or [HbO_2]. In this study, however, it is seen that the deviation in $\Delta[Hb_{total}]$ is not always larger than those of $\Delta[Hb]$ or $\Delta[HbO_2]$ (Case 1 in Table 2.4 and Eqs. (2.42)-(2.44)). The disagreement between this study and Fantini *et al*'s report can be interpreted as follows. Equation (2.41) would be valid with the assumption that [Hb_{total}] is a dependent variable and [Hb] and [HbO_2] are two independent variables. However, with a close inspection on [Hb], [HbO_2], and [Hb_{total}], one can realize that the actual independent variables should be hemoglobin extinction coefficients and OD (or μ_a in Eq. (2.40)), not [Hb] and [HbO_2]. Therefore, Eq. (2.15) should give an accurate estimation of uncertainties in $\Delta[Hb_{total}]$ induced by the uncertainties from discrepancies in hemoglobin extinction coefficients between the reported data.

Temperature can be another important factor that could affect calculations of $\Delta[Hb]$, $\Delta[HbO_2]$ and $\Delta[Hb_{total}]$ measured by NIRS since temperature alters hemoglobin extinction coefficients. Studies have shown that the optical absorbance spectra of hemoglobin derivatives vary with temperature [49] [50] [51]. The extinction coefficients used in this study were determined *in vitro* at ambient temperature (20-24^{o}C) [27] [30] [32] [36]. However, the temperature during *in vivo* measurements from human or animal tissues is often ~ 37^{o}C and is significantly higher than that from *in vitro* measurements.

The results reported by Steinke and Shepherd [50] showed the effect of temperature changes from 20 to 40^{o}C on hemoglobin extinction coefficients within 480

nm to 650 nm, excluding the NIR range. Their report indicated that temperature had the most pronounced effect on both deoxyhemoglobin and oxyhemoglobin extinction coefficients in the wavelength range of 500 ~ 610 nm and also showed that oxyhemoglobin extinction coefficients are more sensitive to changes in temperature than carboxy- or deoxyhemoglobin extinction coefficients. In this range of wavelength, changes in extinction coefficients ranged from 0.4 to 2.8 $mM^{-1}cm^{-1}$ when temperature changed from 20 to 40 ^{o}C.

The report from Cordone *et al.* [49] showed the effect of temperature on extinction coefficients from 650 to 1350 nm, with temperature changes from 25 to –253 ^{o}C. In their report, there was an approximate increase of 0.22 $mM^{-1}cm^{-1}$ in deoxyhemoglobin extinction coefficient at 758 nm when the temperature dropped from 25 to –73 ^{o}C, which can be approximately estimated as a 0.022 $mM^{-1}cm^{-1}$ increase per $10^{o}C$ temperature drop. In 1997 Sfareni *et al.* [51] reported the changes of NIR absorption spectra of hemoglobin in the temperature range 20 to 40 ^{o}C. It was reported that the deoxyhemoglobin ε at 758 nm was increased ~0.036 $mM^{-1}cm^{-1}$ when the temperature was dropped from 40 to $20^{o}C$, and that the oxyhemoglobin ε decreased around 0.008 $mM^{-1}cm^{-1}$ with an decrease in temperature. The deoxyhemoglobin ε at 785 nm was roughly decreased 0.032 $mM^{-1}cm^{-1}$ by an decrease of temperature from 40 to 20 ^{o}C, while oxyhemoglobin ε showed an increase of around 0.004 $mM^{-1}cm^{-1}$.

Here I demonstrate the possible errors of $\Delta[Hb]$, $\Delta[HbO_2]$ and $\Delta[Hb_{total}]$ due to temperature changes from 20 to 40 ^{o}C. Using the hemoglobin ε values given by Zijlstra

et al. [36], I obtain deviations in ε values due to temperature as $\Delta\varepsilon_{Hb}^{758}$ = 0.036, $\Delta\varepsilon_{Hb}^{785}$ = 0.032, $\Delta\varepsilon_{HbO_2}^{758}$ = 0.008, and $\Delta\varepsilon_{HbO_2}^{785}$ = 0.004, all in $cm^{-1}mM^{-1}$. With the same parameters as those used to calculate Eqs. (2.37) - (2.39), the relative errors of $\Delta[Hb]$, $\Delta[HbO_2]$ and $\Delta[Hb_{total}]$ induced by temperature changes are quantified as follows:

$$\frac{\Delta\{\Delta[Hb]\}}{\Delta[Hb]} = \frac{0.6}{9.10}\cdot 100\% = 6.6\%, \tag{2.42}$$

$$\frac{\Delta\{\Delta[HbO_2]\}}{\Delta[HbO_2]} = \frac{0.96}{16.55}\cdot 100\% = 5.8\%, \tag{2.43}$$

$$\frac{\Delta\{\Delta[Hb_{total}]\}}{\Delta[Hb_{total}]} = \frac{0.80}{25.65}\cdot 100\% = 3.1\%. \tag{2.44}$$

While the relative errors caused by temperature variation from 20 to 40^{o}C are less than 10%, they are noticeable and need to be considered as possible error sources. On the other hand, such errors can be minimized by choosing proper wavelengths. Around 735, 770 and 800 nm, deoxyhemoglobin extinction coefficients have little changes as temperature varies. In the range from 750 nm to 810 nm, the changes of oxyhemoglobin extinction coefficients due to temperature variation from 20 to 40 ^{o}C are less than 0.008 $cm^{-1}mM^{-1}$. These facts suggest that with the proper selection of

wavelengths, the errors of [Hb], [HbO_2] and [Hb_{total}] determinations induced by temperature variations may be reduced.

After close inspection of the published literature, I have noticed that the hemoglobin extinction coefficients, reported from the same group at different times, can vary within a certain degree. For instances, the hemoglobin ε values from Zijlstra *et al.* [27] [32] [36] are not the same, as shown in Table 2.1 and 2.2. Although such variation seems to be small, it introduces appreciable uncertainty in calculations of Δ[Hb], Δ[HbO_2] and Δ[Hb_{total}]. Similarly, Wray *et al.* [37] and Cope [30] provided different values of hemoglobin extinction coefficients. Their deoxyhemoglobin extinction coefficients are similar to each other, while their oxyhemoglobin extinction values show discrepancies. These facts basically show an existing challenge for biochemists to more accurately quantify hemoglobin extinction coefficients. Whether or not these ε values have already reached their limit of experimental accuracy remains to be seen. On the other hand, for biomedical physicists and engineers, it is important to be aware of uncertainties and errors in [Hb], [HbO_2] and [Hb_{total}] caused by variation of hemoglobin extinction coefficients.

Animals such as mice, rats, rabbits, dogs and pigs are often used as animal models in experiments for testing a new drug, understanding physiology, or investigating a specific disease. NIRS also has been applied to various animal experiments to monitor hemodynamics or to measure concentrations of hemoglobin derivatives. It has been a common practice to utilize human hemoglobin extinction coefficients to quantify concentrations of [Hb], [HbO_2] and [Hb_{total}] in animals, for

example, rats [52], pigs [53], and sheep [54]. Zijlstra *et al.* have compared the hemoglobin extinction coefficients from dogs [35] and rats [32] to the values from humans. The studies have shown that hemoglobin absorptivities of dogs and humans in visible region do not differ significantly, while those of rats and humans are significantly different from each other. A tabulated list of hemoglobin extinction coefficients is available for cows, pigs, horses, and sheep from 450 nm to 800 nm (in every 2 nm) and a few points between 800 nm to 1000 nm [36]. In the same reference, the hemoglobin ε values for dogs were given in the range of 450 nm to 610-690 nm, while the rat hemoglobin ε values were tabulated only from 450 nm to 800 nm. For comparison, I have summarized the differences in ε values between humans and other species in Table 2.5. This table is obtained after multiplying the original ε values given by Zijlstra *et al.* [36] by a factor of 4. It is seen that the differences become smaller when wavelengths are longer than 700 nm. Thus, it is more accurate and preferable to utilize the hemoglobin extinction coefficients of corresponding animals for animal experiments. Especially, I suggest avoiding the use of human hemoglobin ε values for sheep measurements or for sheep blood since the relative differences of ε values between human and sheep are up to 7% to 50 %, possibly leading to hidden but significant errors in calculations of hemoglobin derivative concentrations.

The effect of pH changes on methemoglobin extinction coefficients (ε_{Hi}) have been reported by Benesch *et al.* [26] and Zijlstra *et al.* [32]. Benesch *et al.* reported changes of ε_{Hi} values at 540, 560, 570, 576, and 630 nm when the pH values changed

Table 2.5 Absolute differences in hemoglobin extinction coefficients between human and other species. (Unit: $mM^{-1}cm^{-1}$, four hemes values)

Wave length	Human vs. Rat		Human vs. Horse		Human vs. Pig		Human vs. Cow		Human vs. Sheep	
(nm)	$\Delta\varepsilon_{Hb}$	$\Delta\varepsilon_{HbO_2}$	$\Delta\varepsilon_{Hb}$	$\Delta\varepsilon_{HbO_2}$	$\Delta\varepsilon_{Hb}$	$\Delta\varepsilon_{HbO_2}$	$\Delta\varepsilon_{Hb}$	$\Delta\varepsilon_{HbO_2}$	$\Delta\varepsilon_{Hb}$	$\Delta\varepsilon_{HbO_2}$
630	0.272	0.324	0.156	0.136	0.396	0.292	0.264	0.184	0.48	0.376
660	0.048	0.092	0.088	0.076	0.104	0.044	0.108	0.032	0.268	0.256
700	0.016	0.016	0.076	0.02	0.112	0.016	0.1	0.012	0.244	0.204
750	0.064	0.012	0.008	0.012	0.036	0.004	0.012	0.016	0.12	0.16
800	0.008	0.02	0.048	0	0.06	0.016	0.044	0.008	0.12	0.124
805			0.032	0.024	0.028	0.028	0.044	0.016	0.08	0.1
840			0.02	0.036	0.06	0.028	0.032	0.028	0.064	0.092
845			0.008	0.032	0.048	0.028	0.02	0.028	0.052	0.092
880			0.028	0.036	0.052	0.032	0.028	0.036	0.052	0.084

from 6.2 to 8.8. Specifically, as pH increased from 6.2 to 8.8, ε_{Hi} at 630 nm increased more than 50% of its value at pH=6.2, while ε_{Hi} at other wavelengths (540, 560, 570. 576 nm) were decreased more than 50% from its value at pH=6.2. Zijlstra *et al.* [32] also reported the effect of pH changes on ε_{Hi} of humans and rats in the wavelength range of 450 nm to 700 nm. They found that the pH-dependence of rat ε_{Hi} was limited within pH=6.42 and 6.9, but that human ε_{Hi} were greatly affected by pH changes from 520 to 620 nm within pH=6.01 and 7.34. For the effect of pH on Hb and HbO_2 extinction coefficients in the NIR region, Helledie and Rolfe [55] have reported that there is little pH effect on ε_{Hb} and ε_{HbO2}.

In conclusion, I have reported in this section that there could be a significant error in determination of hemoglobin derivative concentrations using NIRS when the

values of hemoglobin extinction coefficients have variations or uncertainties. The variations in ε values can result from the wavelength shift during the measurements, temperature deviation, and different literature sources given for the hemoglobin extinction coefficients. The mathematical calculations in combination with the blood phantom experiments demonstrated that even small discrepancies in hemoglobin extinction coefficients between different sources can cause 5-25% relative errors in quantification of hemoglobin concentrations. This study has found that among changes in $\Delta[Hb]$, $\Delta[HbO_2]$ and $\Delta[Hb_{total}]$, the error in $\Delta[Hb_{total}]$ caused by discrepancies of hemoglobin extinction coefficients is not always larger than errors of $\Delta[Hb]$ or $\Delta[HbO_2]$. Although these derivations have been developed to obtain error analysis for $\Delta[Hb]$, $\Delta[HbO_2]$ and $\Delta[Hb_{total}]$, the analysis is also valid for estimating errors in absolute concentrations of $[Hb]$, $[HbO_2]$ and $[Hb_{total}]$. I also discussed the variations in ε values due to temperature changes and possible errors induced by using human ε values for animals. I wish to suggest the readers to process the raw animal data with the corresponding animal hemoglobin extinction coefficients in order to obtain accurate values of $[Hb]$, $[HbO_2]$ and $[Hb_{total}]$ taken from animals. Otherwise, an alternate method is to use the closest extinction coefficients from other species available.

2.5 Calibration of a Broadband, CCD-Based NIRS system

Besides the single-channel, frequency-domain NIRS system, a broadband, CCD-based, NIRS system has been utilized for my tumor study to be presented in Chapter 6; thus, a calibration procedure and analysis for the new system had to be performed. The

new system used for Chapter 6 consists of a tungsten-halogen white light source (HL2000-HP, Ocean Optics, Inc., Dunedin, FL), a CCD spectrometer (USB2000, Ocean Optics Inc., Dunedin, FL), and two 3-mm optical fiber bundles. The light transmitted through the tumor/phantom is collected through one of the fiber bundles and sent to the CCD spectrometer, which converts photons in the 350-1100 nm range to electrical signals. An interface (OEM) software provided from the company (OOIBASE32, Ocean Optics, Dunedin, FL) allows to save each spectrum during the measurements and also allows the spectral output to be tabulated in an MS Excel format at six selectable wavelengths for further data processing.

For the calibration experiment, a phosphate buffered saline (P-3813, Sigma, St Louis, MO) solution of 300 mL containing 1% Intralipid (Intralipid® 20%, Baxter Healthcare Corp., Deerfield, IL) was used. A photo of the experiment setup is shown in Fig. 2.5. Before the baseline measurement, 2 mL of defibrinated horse blood (HemoStat Laboratories, Dixon, CA) was added in the solution, and air was bubbled within the solution to oxygenate the solution. When a stable baseline was obtained, the bubbling gas was switched from air to nitrogen to deoxygenate the solution. During this experiment, the solution was thoroughly stirred by using a magnetic stirrer (PC-220, Corning, Acton, MA) placed under the solution container, and the signals at 6 selected wavelengths (650, 700, 730, 750, 803, and 830 nm) were recorded by OOIBASE32 software, and $\Delta[Hb]$, $\Delta[HbO_2]$ and $\Delta[Hb_{total}]$ were calculated using two wavelengths at 750 nm and 830 nm. I used horse blood rather than other species blood because 1) it can be easily ordered through a company compared to human or rat blood, and 2)

hemoglobin extinction coefficients of horse blood are very similar to those of rat or human blood.

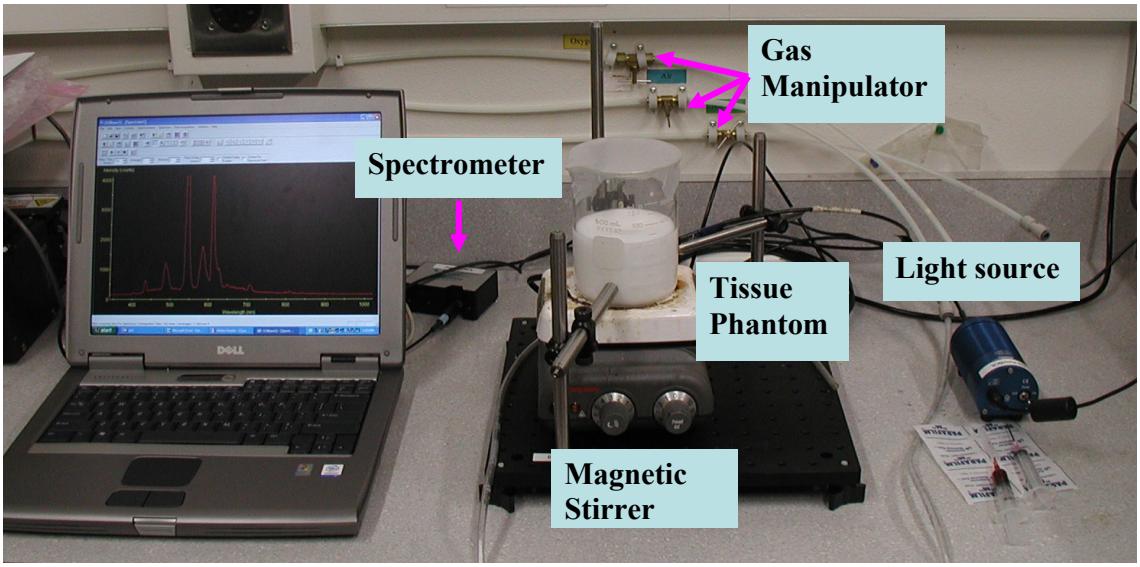

Fig. 2.5 A setup for the calibration experiment. A light source fiber and a detector fiber are placed in semi-reflectance geometry, and the separation was 4 cm. Gas was switched between air and nitrogen to oxygenate and deoxygenate the blood tissue phantom solution, respectively.

The raw light intensity measured from the blood phantom is shown in Fig. 2.6. As shown in Fig. 2.3, deoxyhemoglobin has more light absorption than oxyhemoglobin when the wavelength is below 800 nm. Therefore, during the nitrogen gas flow, oxyhemoglobin is converted to deoxyhemoglobin as a process of deoxygenation, and thus the raw intensities detected at 650, 700, 730, 750 nm are decreasing due to increased light absorption of deoxyhemoglobin. (Fig. 2.6) For the absorption at 830 nm, deoxyhemoglobin has lower absorption than oxyhemoglobin. Therefore, slight increase in raw intensity at 830 nm can be seen. (Fig. 2.7) The raw intensity at 803 nm is near

the isobestic point of hemoglobin absorption spectra; therefore, it shows a minimal change in raw intensity during the oxygenation and deoxygenation process. (Fig. 2.7)

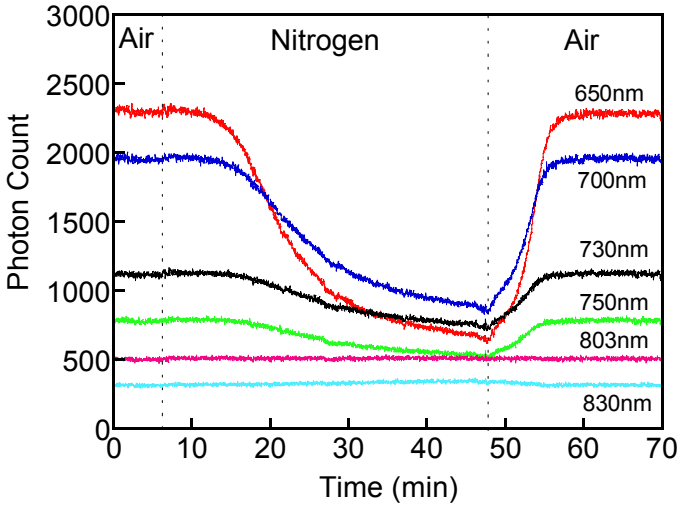

Fig. 2.6 Raw intensity changes at six wavelengths (650, 700, 730, 750, 803, 830 nm) during air or nitrogen flow.

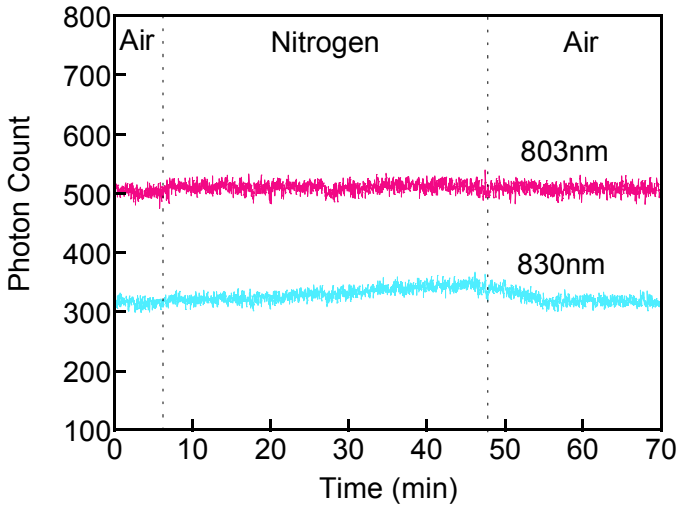

Fig. 2.7 Replotted from Fig. 2.6 to show the raw intensity changes at 803 nm and 830 nm during air or nitrogen flow.

After obtaining raw light intensity values, changes in optical density (ΔO.D.) were calculated and are shown in Fig. 2.8. Since ΔO.D. is equal to $\log(A_B/A_T)$, it increases when the raw intensity decreases from the baseline. Here, A_B and A_T correspond to light intensities measured under the baseline and transient conditions, respectively. Therefore, decreases in light intensities at 650, 700, 730, 750 nm shown in Fig. 2.6 now lead to increases of ΔO.D. at the respective wavelengths. Following the same principle, an increase in light intensity at 830 nm gives rise to a decrease in ΔO.D. After obtaining ΔO.D. from 6 wavelengths, $\Delta[Hb]$, $\Delta[HbO_2]$ and $\Delta[Hb_{total}]$ were calculated by using two wavelengths.

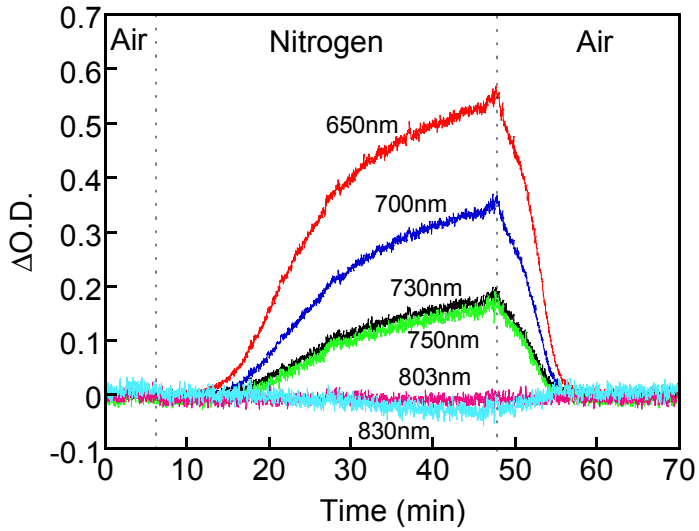

Fig. 2.8 Optical density changes at six wavelengths (650, 700, 730, 750, 803, 830 nm) during air or nitrogen flow.

Figure 2.9 shows the results of $\Delta[Hb]$, $\Delta[HbO_2]$ and $\Delta[Hb_{total}]$ calculated from Eqs. (2.45) and (2.46) using two wavelengths of 750 and 830 nm.

$$\Delta[HbO_2] = \{-0.653 * \log(A_B / A_T)^{750} + 1.293 * \log(A_B / A_T)^{830}\}/L, \quad (2.45)$$

$$\Delta[Hb] = \{0.879 * \log(A_B / A_T)^{750} - 0.460 * \log(A_B / A_T)^{830}\}/L, \quad (2.46)$$

$$\Delta[Hb_{total}] = \Delta[HbO_2] + \Delta[Hb]. \quad (2.47)$$

When nitrogen gas flows into the solution, Δ[Hb] is agreed to increase and Δ[HbO_2] to decrease, as expected. Meanwhile, Δ[Hb_{total}], representing the total blood volume in the solution, maintained constant during the deoxygenation process as required. This result clearly proves that Eqs. (2.45) - (2.47) can be used accurately to monitor Δ[Hb], Δ[HbO_2] and Δ[Hb_{total}] in tumors during hyperoxic gas interventions.

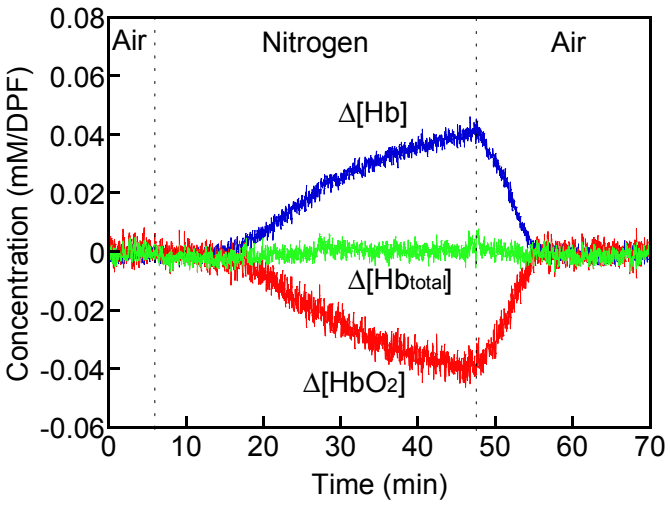

Fig. 2.9 The changes of [Hb], [HbO_2] and [Hb_{total}] during a phantom experiment by using Eqs. (2.45)-(2.47). The coefficients in the equations were calculated by using Cope's human hemoglobin ε values [30] at 750 and 830 nm.

2.6 Comparison of Algorithms Using Two Wavelengths vs. Six Wavelengths

Since this new broadband, CCD-based NIRS system can trace a maximum of 6 wavelengths during the measurements, I have tried to utilize all of the 6 wavelengths to obtain $\Delta[Hb]$, $\Delta[HbO_2]$ and $\Delta[Hb_{total}]$ based on the phantom experiment. Equation (2.2) can be expanded to Eq. (2.48) if one obtains ΔO.D. values from 6 wavelengths:

$$\begin{pmatrix} \Delta OD^{650} \\ \Delta OD^{700} \\ \Delta OD^{730} \\ \Delta OD^{750} \\ \Delta OD^{803} \\ \Delta OD^{830} \end{pmatrix} = \begin{pmatrix} \varepsilon_{Hb}^{650} & \varepsilon_{HbO_2}^{650} \\ \varepsilon_{Hb}^{700} & \varepsilon_{HbO_2}^{700} \\ \varepsilon_{Hb}^{730} & \varepsilon_{HbO_2}^{730} \\ \varepsilon_{Hb}^{750} & \varepsilon_{HbO_2}^{750} \\ \varepsilon_{Hb}^{803} & \varepsilon_{HbO_2}^{803} \\ \varepsilon_{Hb}^{830} & \varepsilon_{HbO_2}^{830} \end{pmatrix} \begin{pmatrix} \Delta[Hb] \\ \Delta[HbO_2] \end{pmatrix} L, \qquad (2.48)$$

where L = d·DPF as described earlier.

Mathematically, Eq. (2.48) is a matrix and can be inversed and written as Eq. (2.49). This gives a mathematical means to solve $\Delta[Hb]$ and $\Delta[HbO_2]$ using six wavelengths.

$$\begin{pmatrix} \Delta[Hb] \\ \Delta[HbO_2] \end{pmatrix} = \frac{1}{d \cdot DPF} \begin{pmatrix} \varepsilon_{Hb}^{650} & \varepsilon_{HbO_2}^{650} \\ \varepsilon_{Hb}^{700} & \varepsilon_{HbO_2}^{700} \\ \varepsilon_{Hb}^{730} & \varepsilon_{HbO_2}^{730} \\ \varepsilon_{Hb}^{750} & \varepsilon_{HbO_2}^{750} \\ \varepsilon_{Hb}^{803} & \varepsilon_{HbO_2}^{803} \\ \varepsilon_{Hb}^{830} & \varepsilon_{HbO_2}^{830} \end{pmatrix}^{-1} \begin{pmatrix} \Delta OD^{650} \\ \Delta OD^{700} \\ \Delta OD^{730} \\ \Delta OD^{750} \\ \Delta OD^{803} \\ \Delta OD^{830} \end{pmatrix}. \quad (2.49)$$

However, since the matrix of ε is not a square matrix, Moor-Penrose inverse method [56] was applied to obtain pseudoinverse matrix of ε as shown in Eq. (2.50).

$$\Delta C=(\varepsilon^T \cdot \varepsilon)^{-1} \cdot \varepsilon^T \cdot \Delta OD, \quad (2.50)$$

where ΔC is a matrix of Δ[Hb] and Δ[HbO_2] and ε^T is a transposed matrix of ε matrix. After detailed matrix calculations, final equations for Δ[Hb] and Δ[HbO_2] derived from Eq. 2.50 are given as follows.

$$\begin{aligned} \Delta[HbO_2] = \{&-0.286 * \log(A_B / A_T)^{650} - 0.054 * \log(A_B / A_T)^{700} \\ &+ 0.099 * \log(A_B / A_T)^{730} + 0.136 * \log(A_B / A_T)^{750} \\ &+ 0.459 * \log(A_B / A_T)^{803} + 0.574 * \log(A_B / A_T)^{830}, \end{aligned} \quad (2.51)$$

$$\Delta[\mathrm{Hb}] = \{0.228 * \log(A_B / A_T)^{650} + 0.093 * \log(A_B / A_T)^{700}$$
$$+ 0.036 * \log(A_B / A_T)^{730} + 0.038 * \log(A_B / A_T)^{750}$$
$$- 0.065 * \log(A_B / A_T)^{803} - 0.092 * \log(A_B / A_T)^{830}, \quad (2.52)$$

$$\Delta[\mathrm{Hb_{total}}] = \Delta[\mathrm{HbO_2}] + \Delta[\mathrm{Hb}]. \quad (2.53)$$

Figure 2.10 replotted the phantom experiment results, which were shown in Fig. 2.9, using Eqs. (2.51)-(2.53). By using six wavelengths, the noise level is clearly reduced, especially for Δ[Hb] trace, but the overall traces and values in Δ[HbO_2], Δ[Hb], and Δ[Hb_{total}] remain the same as those shown in Fig. 2.9.

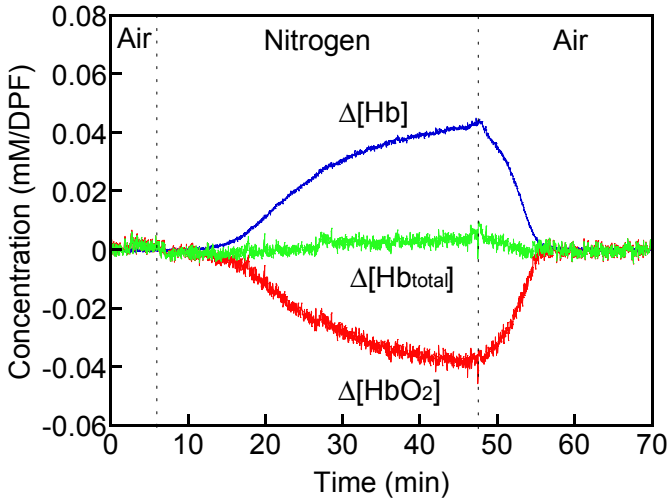

Fig. 2.10 Changes of [Hb], [HbO_2] and [Hb_{total}] during a cycle of deoxygenation and oxygenation taken from a phantom experiment using Eqs. (2.51)-(2.53). The coefficients of Δ[Hb], Δ[HbO_2] and Δ[Hb_{total}] equations were calculated by using 6 wavelengths from Mark Cope's human hemoglobin extinction coefficients.

The absolute differences of Δ[Hb], Δ[HbO_2] and Δ[Hb_{total}] between Figs. 2.9 and 2.10 are further calculated and shown in Fig. 2.11. To estimate the error of Δ[Hb_{total}], standard deviation of the baseline from Fig. 2.9 is obtained (=0.0021 mM/DPF), and the maximum difference of Δ[Hb_{total}] is less than 0.004 mM/DPF, which is less than 2 standard deviations. The relative maximum differences of Δ[Hb] and Δ[HbO_2] between Figs. 2.9 and 2.10 during the deoxygenation-oxygenation cycle are about 10%. Therefore, the differences between the algorithms using 2 wavelengths versus 6 wavelengths are within the systematic error range, and thus a simple 2-wavelengths algorithm can be used throughout this dissertation to monitor tumor responses to hyperoxic gas interventions and chemotherapeutic treatments

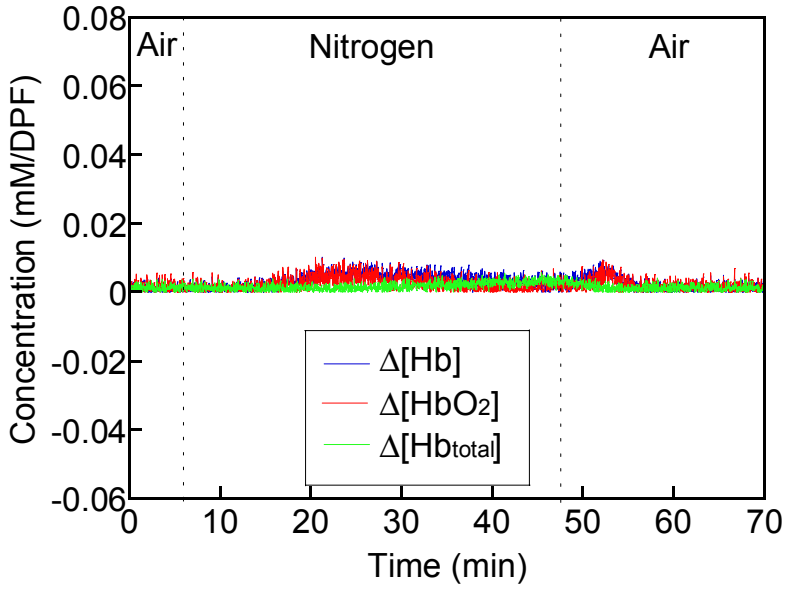

Fig. 2.11 Absolute differences of Δ[Hb], Δ[HbO_2] and Δ[Hb_{total}] between Figs. 2.9 and 2.10.

For comparison, I calculated $\Delta[Hb]$, $\Delta[HbO_2]$ and $\Delta[Hb_{total}]$ by selecting two wavelengths from either below 800 nm or above 800 nm, as shown in Figs. 2.12(a) and 2.12(b). These results exhibit significant differences when compared to Figs 2.9 and 2.10. Therefore, the proper selection of two wavelengths is essential for this system to be used to monitor hemodynamic changes in either tissue or phantom.

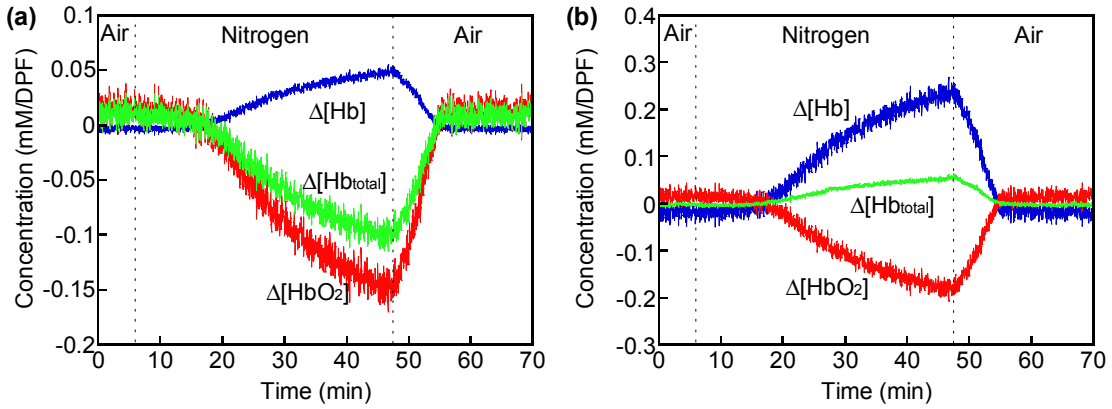

Fig. 2.12 Changes of [Hb], $[HbO_2]$ and $[Hb_{total}]$ during a phantom experiment obtained by using 2 wavelengths at 700 and 750 nm (a) or at 803 and 830 nm (b).

2.7 Summary

In this chapter, I have described the refinement and modification of the existing algorithm, which had been used for a single-channel, frequency-domain system. The empirically developed equations were also better understood later in section 2.4. During the process of refining the algorithms, I noticed how important it is to use correct values of hemoglobin extinction coefficients and further estimated possible errors from discrepancies in hemoglobin extinction coefficient values. For a new broadband, CCD-based, NIR spectroscopic system that was used for the work to be presented in Chapter

6, I performed laboratory calibration experiments and proved the reliability of broadband system. Moreover, comparative results have been obtained from the phantom experiment using 2 wavelengths versus 6 wavelengths. My conclusion is that using two wavelengths at 750 and 830 nm produces the results as well as those with 6 wavelengths. However, caution is required for selecting the two wavelengths to calculate $\Delta[Hb]$, $\Delta[HbO_2]$ and $\Delta[Hb_{total}]$. Significant errors could occur when utilizing the two-wavelength algorithm in comparison to the results obtained with the 6-wavelength algorithm without a calibration procedure.

* Section 2.3 and part of Section 2.4 are published in IEEE Engineering in Medicine and Biology Magazine in 2005. Section 2.4 was prepared for a manuscript and submitted to the journal, Physics in Medicine and Biology, and is currently under review process.

Jae G. Kim, Mengna Xia, Hanli Liu, "Extinction coefficients of hemoglobin for near-infrared spectroscopy of tissue", *IEEE Eng. in Med.Biol. Magazine*, **24(2)**, 118-121 (2005).

CHAPTER 3

INVESTIGATION OF BI-PHASIC TUMOR OXYGEN DYNAMICS INDUCED BY HYPEROXIC GAS INTERVENTION: THE DYNAMIC PHANTOM APPROACH

3.1 Introduction

Solid tumors are known to exhibit heterogeneous blood flow distribution [57] [58], and various methods have been used to study tumor perfusion heterogeneity, such as Doppler ultrasound [59], dynamic contrast MRI [60], diffuse correlation spectroscopy [61] and the use of tumors grown in window chambers [62]. Intensive studies using ^{19}F Magnetic Resonance FREDOM (Fluorocarbon Relaxometry using Echo planar imaging for Dynamic Oxygen Mapping) by Mason *et al.* have revealed intratumoral heterogeneities of tumor pO_2 and their heterogeneous responses to hyperoxic gas breathing [16] [20] [63]. The severe pO_2 heterogeneity in tumors can be attributed to the heterogeneous distribution of blood flow, since tissue pO_2 level is determined by a balance between the supply of oxygen from blood vessels and the oxygen consumption rate of tissue cells [64]. Unlike FREDOM, near-infrared spectroscopy (NIRS) techniques measure hemoglobin oxygenation and concentration *in vivo*, providing possible quantification and monitoring of vascular oxygenation *in vivo*

of the measured sample/organ non-invasively. This is why in recent years, NIRS has been widely utilized to investigate hemoglobin oxygenations of muscles [65] [66] [67], the brain [68] [69] [70], and animal tumors [31] [33] [71].

The heterogeneity of blood perfusion in tumors also results in the development of regions of hypoxia during tumor growth. It is well known that in comparison to well oxygenated tumor cells, hypoxic cells in tumor are highly resistant to radiation therapy [10] [72], photodynamic therapy [11], and some forms of chemotherapy [12]. A number of clinical studies have shown that the tumor oxygenation level affects greatly the survival probability of cancer patients, as measured either by tumor regression or by local control [73]. Therefore, tumor oxygenation needs to be increased during therapy to improve the efficacy of cancer treatments. As a mean of improving tumor oxygenation, breathing a hyperoxic gas, such as carbogen (95% O_2 and 5% CO_2) or 100% oxygen, has been used to enhance the cancer treatment [74] [75]. However, oxygen delivery from blood vessels to tumor cells in the hypoxic region can be prohibited by the poor vascular perfusion in tumors. Thus, measurements of local vascular oxygenation and perfusion in tumors can be important for tumor treatment planning and for evaluation of methods designed to modulate tumor oxygenation.

Previous studies in Dr. Liu's lab demonstrated that improvement of tumor vascular oxygenation during hyperoxic gas intervention could be monitored by NIRS [21] [31] [33] [34]. A bi-phasic feature that has a rapid increase, followed by a gradual but significant further increase, in response to carbogen or pure oxygen intervention was repeatedly observed from the changes of oxyhemoglobin concentration ($\Delta[HbO_2]$)

in tumor vasculature (Fig. 3.1). Liu *et al.* established a mathematical model based on Kety's approach [76] to explain this biphasic behavior of tumor hemodynamics in their earlier publication [31]. In that study, they formed a hypothesis that tumor vasculature was comprised of a well-perfused and poorly perfused region that could be detected with the two time constants through $\Delta[HbO_2]$ readings derived from the NIRS. The mathematical model basically allowed them to associate the bi-phasic $\Delta[HbO_2]$ amplitudes and time constants with the ratio of vascular coefficients and vascular perfusion rates in the two different regions [31].

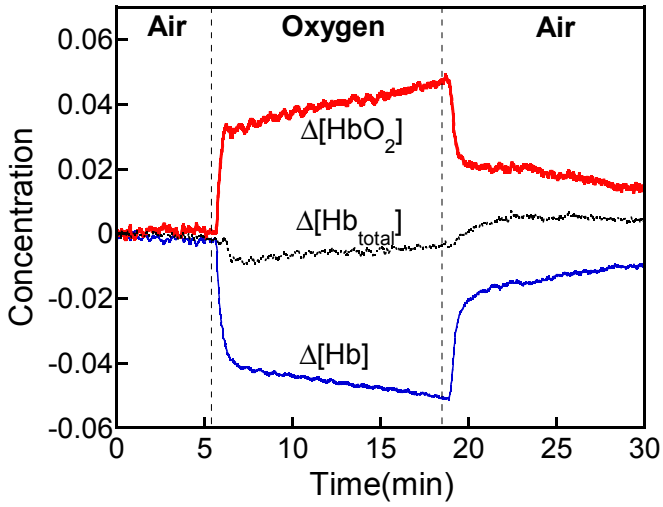

Fig. 3.1 Time course of tumor vascular $\Delta[HbO_2]$, $\Delta[Hb]$, and $\Delta[Hb_{total}]$ for a representative 13762NF breast tumor with the inhaled gas under the sequence of air-oxygen-air. It clearly shows the bi-phasic increase of $\Delta[HbO_2]$ during oxygen intervention.

Even though the developed mathematical model was useful for interpretation of tumor hemodynamics and physiological parameters, there was lack of any proof or

confirmation of validity. To provide solid support for this model and to further investigate heterogeneities of tumor vasculature, I have developed dynamic tumor vascular phantoms and have performed three-channel NIRS experiments on the dynamic phantoms. In this chapter, I will report 1) the design and implementation for the dynamic vascular phantoms, 2) the experimental setup and measurements for the NIRS readings from the dynamic phantoms, 3) the relationship between the NIRS time constants and flow velocities passing through the phantoms, and 4) the evidence to support Liu's mathematical model. The results from this chapter show clearly that the two time constants observed in tumor oxygenation dynamics *in vivo* can result from two different perfusion rates or two different blood velocities. It is concluded that with the bi-phasic mathematical model, tumor vascular dynamics can be determined and monitored non-invasively using NIRS, while a perturbation of hyperoxic gas intervention is given.

3. 2 Materials and Methods

3.2.1 Review of the Mathematical Model of Tumor Vascular Oxygenation

In 1951, Kety developed a model to quantify regional cerebral blood flow (rCBF) with diffusible radiotracers [76]. In a previous report by Liu *et al.* [21], a similar mathematical model for interpreting NIRS readings from animal tumors under hyperoxic intervention was adapted following Kety's approach. I give a brief review here: by applying Fick's principle and defining γ as the ratio of $\Delta[HbO_2]$ in the vascular

bed to that in veins, $\Delta[HbO_2]$ that was induced by hyperoxic gas intervention in tumor vasculature could be mathematically modeled as Eq. (3.1):

$$\Delta[HbO_2]^{vasculature}(t) = \gamma H_o[1-\exp(-ft/\gamma)] = A[1-\exp(-t/\tau)], \quad (3.1)$$

where γ was defined as the vasculature coefficient of the tumor ($=\Delta[HbO_2]^{vasculature}/\Delta[HbO_2]^{vein}$), H_o was the arterial oxygenation input function, f represented the blood perfusion rate, τ was the time constant with $A=\gamma H_o$ and $\tau=\gamma/f$. The measured signal, $\Delta HbO_2{}^{vasculature}(t)$, is the change of $[HbO_2]$ in vasculature within the light interrogated tissue volume per unit time, and perfusion rate, f, is defined as the rate of total blood flow per unit mass or volume of tissue, which has a unit of ml/min/100g or ml/min/cm^3, while blood flow rate is the rate of blood flow within the blood vessels (ml/min).

If a tumor has two distinct perfusion regions, and the measured NIRS signals result from both regions (Figure 3.2), then it is reasonable to include two different blood perfusion rates, f_1 and f_2, and two different vasculature coefficients, γ_1 and γ_2, in the model. Eq. (3.1) then becomes Eq. (3.2) to count for the double exponential feature observed in the NIRS experiments:

$$\begin{aligned}\Delta HbO_2{}^{vasculature}(t) &= \gamma_1 H_o[1-\exp(-f_1 t/\gamma_1)] + \gamma_2 H_o[1-\exp(-f_2 t/\gamma_2)] \\ &= A_1[1-\exp(-t/\tau_1)] + A_2[1-\exp(-t/\tau_2)], \quad (3.2)\end{aligned}$$

where f_1 and γ_1 are the blood perfusion rate and vasculature coefficient in the well perfused region, respectively; f_2 and γ_2 represent the same respective meanings for the poorly perfused region, and $A_1 = \gamma_1 H_o$, $A_2 = \gamma_2 H_o$, $\tau_1 = \gamma_1 / f_1$, $\tau_2 = \gamma_2 / f_2$.

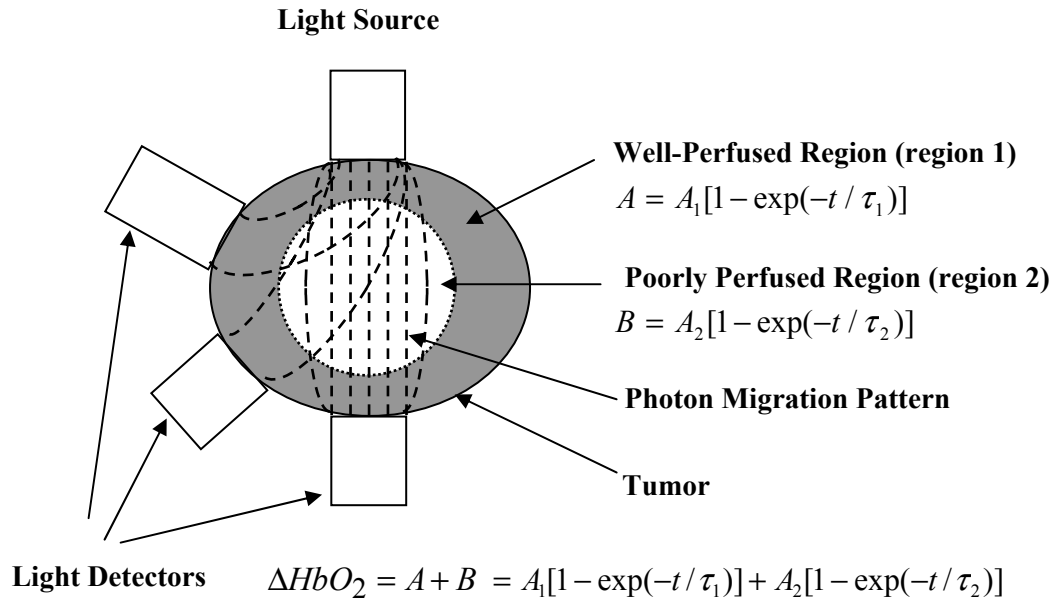

Fig. 3.2 A schematic diagram of light transmitting patterns in tumor when tumor has two distinct perfusion regions. Center of the tumor represents poorly perfused region, and the peripheral region with gray color is representing a well-perfused region.

Since A_1, A_2, τ_1, and τ_2 can be determined by fitting Eq. (3.2) with $\Delta[HbO_2]$ readings taken from the NIRS measurements, the ratios of two vasculature coefficients and the two blood perfusion rates can be obtained as:

$$\frac{\gamma_1}{\gamma_2} = \frac{A_1}{A_2}; \qquad \frac{f_1}{f_2} = \frac{A_1 / A_2}{\tau_1 / \tau_2}. \tag{3.3}$$

With these two ratios, one can understand more about tumor vascular structures and blood perfusion rates. In this chapter, I report experimental evidence to support the tumor hemodynamics model by quantifying γ_1/γ_2 and f_1/f_2 from three different locations of the tumor dynamic phantoms with the use of three-channel NIRS.

3.2.2 Design and Implementation of the Dynamic Tumor Vascular Phantom

To represent two different perfusion regions in tumors, I designed a vascular mimic device (VMD) by winding a small diameter tube around a big diameter core tube, as shown in Fig 3.3. VMD-1 was fabricated by wrapping ethyl vinyl acetate microbore tubing (0.51 mm ID) around a Tygon lab tube (14.4 mm OD), and VMD-2 was fabricated by winding polyethylene tubing (0.86 mm ID) around another piece of Tygon lab tube (14.4 mm OD) to represent two kinds of vasculature with small (0.51 mm ID) and large (0.86 mm ID) diameters of blood vessels, respectively. All tubing materials were purchased from Cole-Parmer Company (Vernon Hills, IL).

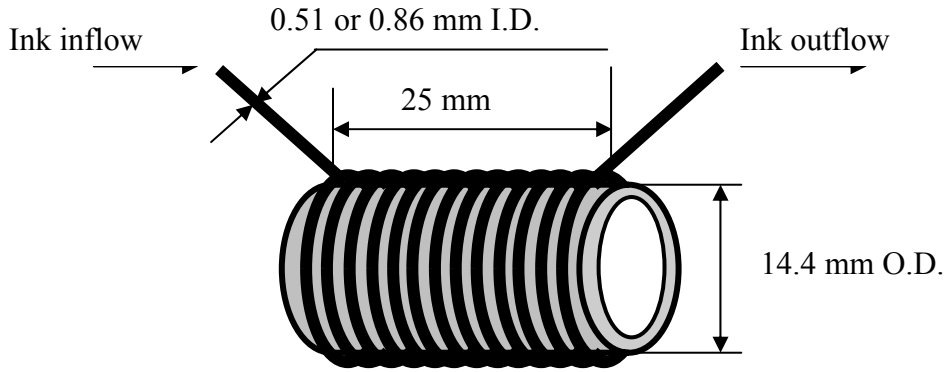

Fig. 3.3 A schematic diagram for one vascular modeling device (VMD). Two different inner diameter (I.D.) sizes of tubing have been used to wind outside of core tubing to simulate different blood vessel diameters within a breast tumor.

The dynamic tumor vascular phantom was fabricated by embedding the two VMD's into a cylindrical soft gelatin, which represented non-vascular tissues. Specifically, the tissue mimic gelatin was prepared by mixing 50 g of gelatin powder (Sigma, Gelatin Type A, St. Louis, MO) with 350 ml of boiling water, and the solution was stirred thoroughly until the gelatin powder was dissolved completely. When the solution was cooled down to around 50^{o}C, 200 ml of 20% Intralipid solution (Intralipid® 20%, Baxter Healthcare Corp., Deerfield, IL) was added and mixed thoroughly to simulate light scattering in tumor tissues. Just before the solution started to solidify, it was poured into a cylindrical container (diameter=4.5 cm, height=3.5 cm) containing the two VMD's and also into a box-shaped container (length=15 cm, width=15 cm, and height= 5 cm). After completely being cooled down, the solution became a soft gelatin phantom with the two VMD's embedded inside. The optical properties of gelatin phantoms were measured from the gelatin phantom in the box-shaped large container (15 × 15 × 7.5 cm) using an NIR tissue oximeter (model: 96208, ISS Inc., Champaign, IL), and those values were close to tissue optical properties with μ_a= 0.032 cm^{-1} and μ_s'=9.2 cm^{-1} at 750 nm.

Two kinds of dynamic tumor vascular phantoms were fabricated: Phantom 1 contained one VMD-1 and one VMD-2, while phantom 2 had two of VMD-1's. A stream of diluted black ink solution with μ_a=1.5 cm^{-1} at 730 nm (measured by a regular spectrophotometer) was used to go through the VMD's to simulate a blood flow through tumor vasculature. By pumping the ink solution through VMD-1 and VMD-2 with the same flow rate in phantom 1, I could simulate the effects of different sizes of

blood vessels on the bi-phasic behavior of changes in NIRS signals. Meanwhile, by injecting the ink solution through the two VMD-1's in phantom 2 with two different flow rates, I would be able to associate the bi-phasic feature of NIRS with the flow rate. In this way, I could mimic the dynamic fluid dependence of a breast tumor, with a hyperoxic gas inhalation, on different sizes of blood vessels and on different perfusion rates.

3.2.3 Multi-Channel NIR Spectroscopy

I used a multi-channel, continuous wave, NIRS system with one light source at 730 nm and three detectors to monitor light absorption changes from the dynamic tumor vascular phantoms in this study. Based on the modified Beer-Lambert's law [77], the data presented in this chapter were analyzed using the measured amplitudes to quantify changes in optical density (O.D.) induced by absorber concentration changes (Eq. 3.4).

$$\Delta O.D. = O.D._T - O.D._B = log\,(I_B/I_T), \tag{3.4}$$

where and I_B and I_T are baseline and transient amplitudes of the measured optical signals, respectively. Equation (3.4) was repeatedly utilized for each of the three channels for individual data analysis.

3.2.4 Experimental Setup and Procedures of Dynamic Phantom Measurements

The schematic experimental setup for dynamic phantom measurements is shown in Fig. 3.4(a). Near infrared light at 730 nm was delivered from a multi-channel NIRS system to the dynamic tumor vascular phantom, and three optical detectors were placed on the side of the cylindrical phantom to collect the NIR signals at three different locations. A diluted ink solution was injected into the VMD's using 5 ml B-D™ disposable syringes (Cole-Parmer, Vernon Hills, IL) by two syringe infusion pumps (model KDS200, KdScientific Inc., New Hope, PA), and the ink wastes were collected in a waste beaker. I used two separate syringe infusion pumps so that I could control the flow rate of each VMD independently. Figure 3.4(b) shows the close-up geometry of light source and three optical detectors around dynamic phantom 1 with the two imbedded VMD's.

The light source was placed between the two VMD's, and detector D3 was located across the light source in transmission mode so that it would detect the signal passing through both VMD's. Other two detectors (D1 and D2) were placed in the semi-reflectance geometry with respect to the light source so that D1 and D2 would get the NIR signals mostly from only VMD-1 or VMD-2, respectively. The setup was the same for dynamic phantom 2, containing two VMD-1's instead of one VMD-1 and one VMD-2.

In phantom 1 measurement, VMD-1 and VMD-2 were initially filled with water to obtain the NIR baseline readings. Next, the ink solution was injected into VMD-2

first with a flow rate of 20 ml/hr to simulate the dynamic process of blood flow, followed by a washout with water.

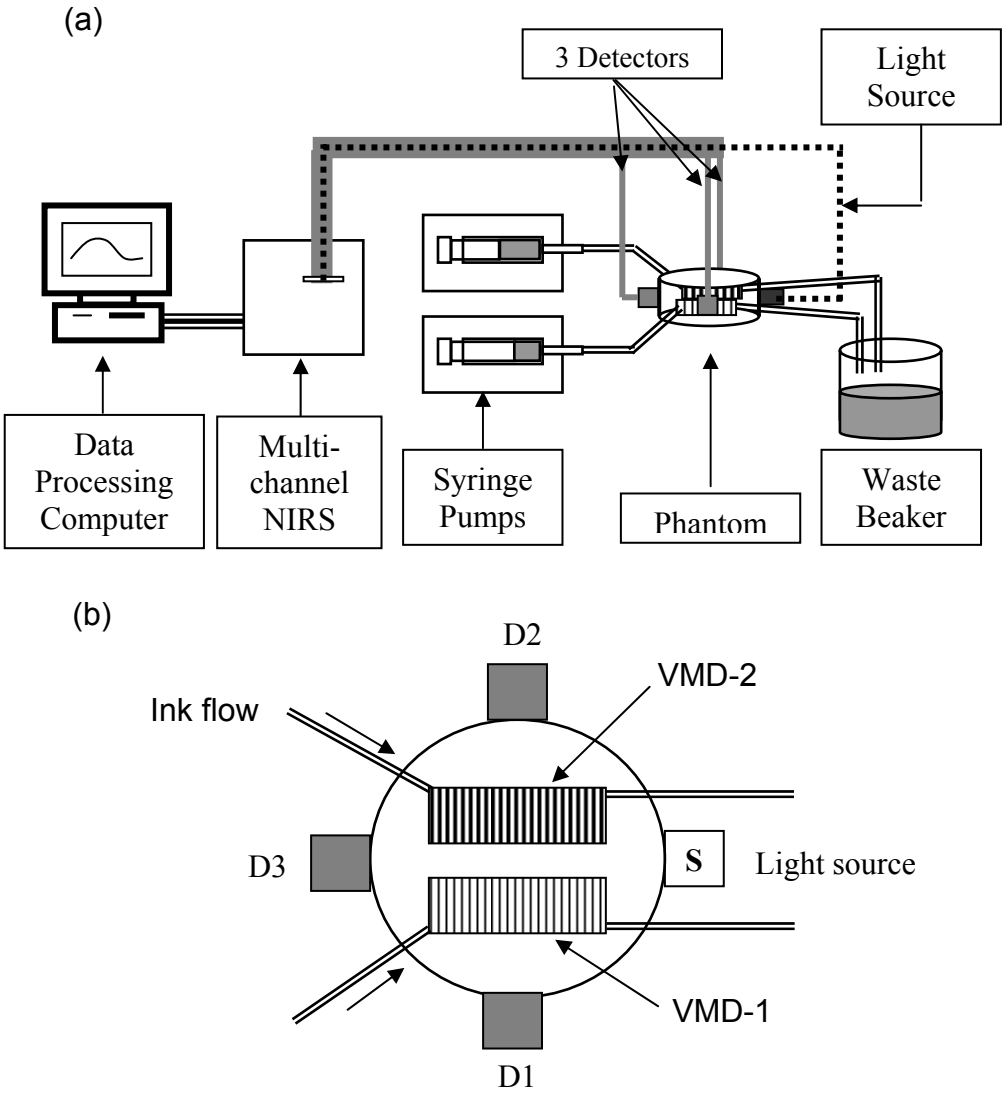

Fig. 3.4 An experimental setup for the tumor dynamic phantom study. (a) Two syringe pumps were connected to two VMD's in tumor vascular dynamic phantom individually to have different ink flow rates for each VMD. (b) Enlarged tumor vascular dynamic phantom with two embedded VMD's. Tumor phantom 1 has VMD-1 and VMD-2 as shown here, and tumor phantom 2 has two VMD-1's.

As the third step, the dynamic procedure was repeated with the ink solution injected into VMD-1 with the same flow rate. Lastly, the measurement was reproduced while the ink solution was infused simultaneously into both VMD-1 and VMD-2 with the same flow rate (20 ml/hr). The last step was planned to observe a bi-phasic increase in light absorption, which is expected due to two different perfusion velocities through VMD-1 and VMD-2 having two tube diameters, while the applied solution flow rates in both VMD's kept the same. The relationship between the ink flow average velocity, v (cm/sec), and ink flow rate, Q (cm^3/sec), is given as

$$Q = V/t = S \times v = \pi r^2 \times v, \tag{3.5}$$

where V and S are the volume and cross-section area of a tube, respectively, and r is the inner radius of simulated blood vessel or tube. Equation (3.5) shows clearly that v will be different for two vessels or tubes with different sizes if they have the same flow rate, Q.

In phantom 2 measurement, the same dynamic protocols were used to fill the two identical VMD-1's separately and simultaneously for the dynamic NIRS readings, with the same flow rate (20 ml/hr) followed by a washout of water. In addition, the ink solution was injected into the two VMD-1's with two different flow rates, i.e., 5 and 20 ml/hr for the top and bottom VMD-1, respectively, and water was used to wash out the two VMD-1's. For both of the phantom experiments, the changes in NIR light intensity were measured through the whole experiment. The time constants during the dynamic

changes were obtained by fitting Eqs. (3.1) or (3.2) to the data using Kaleidagraph (Synergy Software, Reading, PA)

3.3 Results

3.3.1 NIR Measurements Taken from Dynamic Tumor Vascular Phantom 1

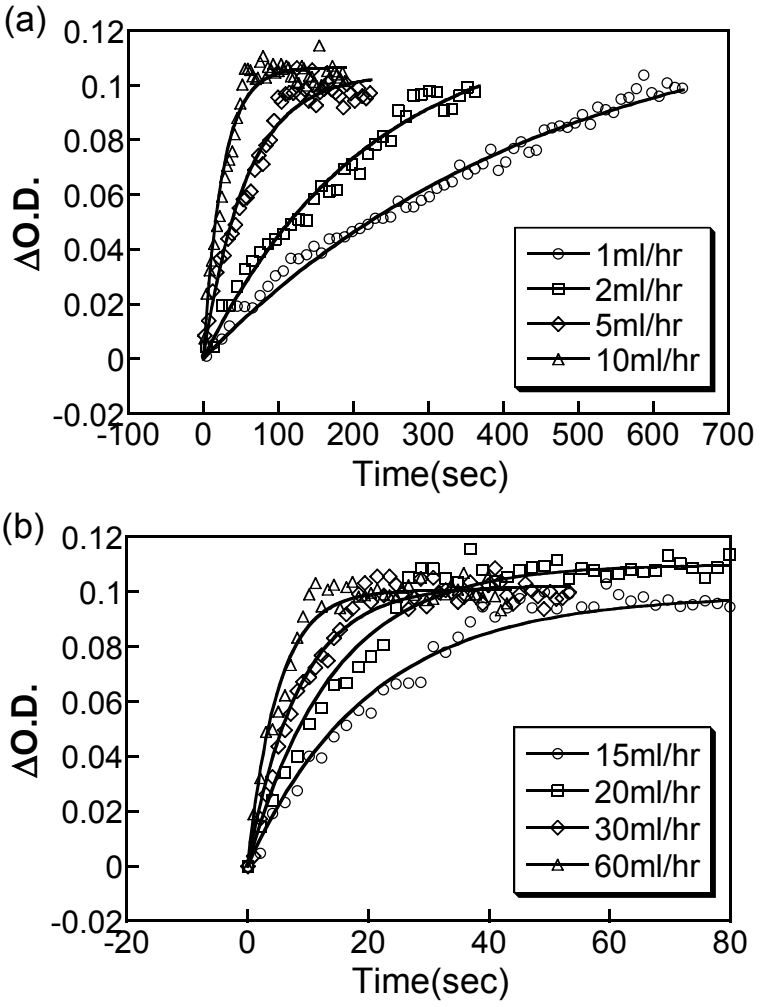

Fig. 3.5 Absorption changes measured from the dynamic tumor vascular phantom with increasing a flow rate from (a) 1 to 10 ml/hr and (b) 15 to 60 ml/hr. The symbols and curves are obtained from the phantom experiments and from one-exponential curve fitting, respectively.

To observe the correlation between the flow rate and time constant, I have utilized a flow rate range from 1 to 60 ml/hr firstly within VMD-1 and measured optical density changes (ΔO.D.) from the dynamic tumor vascular phantoms with the source and detector located at S and D3, respectively, as shown in Fig. 3.4(b). The actual ΔO.D. values were calculated based on Eq. (3.5), and a set of temporal ΔO.D. data are shown in Fig. 3.5(a). The optical density changes with flow rates from 15 to 60 ml/hr are shown in Fig. 3.5(b) separately since these curves are too close to the curve with 10 ml/hr. These figures clearly show that the detected change in light absorption occurs faster with a high flow rate, exhibiting a smaller time constant obtained with a single-exponential curve fitting using Eq. (3.1).

Figure 3.6(a) plots the relationship between the time constants and flow rates of the ink solution using both the linear (bottom and left axis) and logarithmic scale (top and right axis). It is seen here that the time constant rapidly drops as the flow rate increases, and a strong exponential correlation between them (R=0.99), as given in Eq. (3.6), is confirmed by the straight line in the logarithmic plot.

$$\tau = 419.71\, Q^{-1.13}, \tag{3.6}$$

where Q is in ml/hr, and τ is in sec.

On the other hand, the velocity of ink solution at each flow rate can be quantified by dividing the large tube length (25 mm, see Fig. 3.3) by the duration of time when the ink solution inside the small tube entered the phantom at one end and

came out at the other. I recorded this temporal duration using a stop watch for each measurement. In this way, I have calculated the average velocities of ink solutions and plotted them in Fig. 3.6(b). Furthermore, given the flow rate and diameters of the small wrapping tubes used for VMD's inside the phantom, the velocity of ink solution flow can be calculated by using Eq. (3.5) (i.e., $v = Q/(\pi r^2)$).

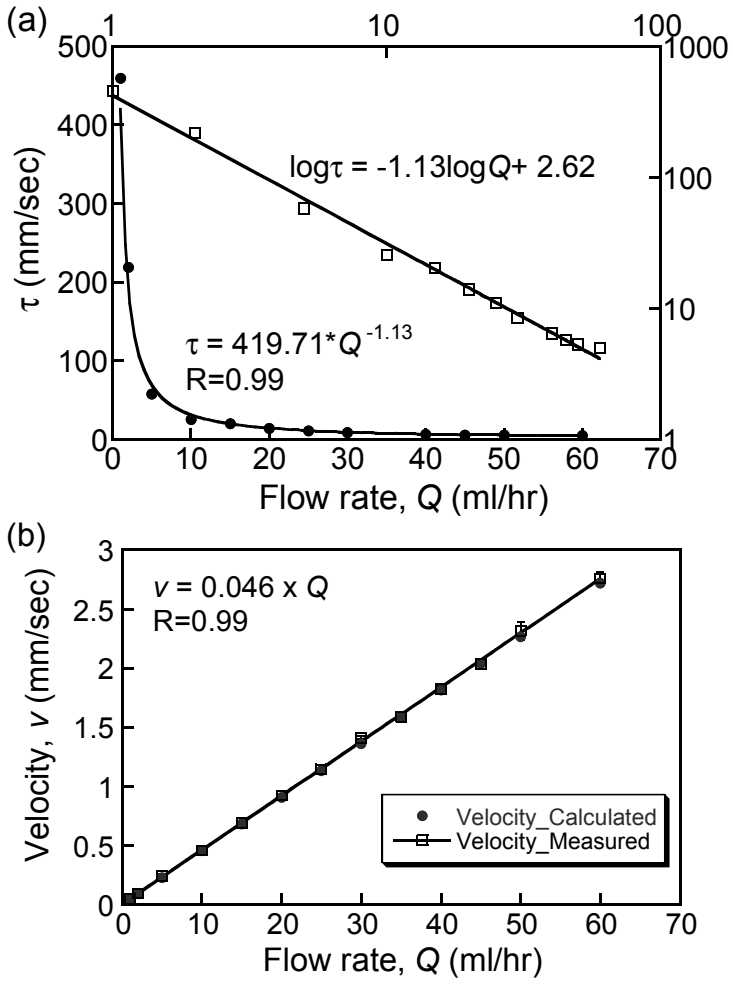

Fig. 3.6 (a) A correlation between time constants and flow rates plotted with the linear scale (left and bottom axis) and logarithmic scale (top and right axis). (b) A linear correlation between ink flow velocities and ink flow rates with a fixed diameter of tube.

For example, the velocity of ink flow at a flow rate of 10ml/hr can be obtained as follows. Since the radius of small tube is 0.255 mm, the area of tube cross section is 0.2043 mm^2 (= π*0.255^2). The flow rate of 10ml/hr is equal to 2.78 mm^3/sec after converting the unit of time from hour to second and also after converting the unit of volume from ml to mm^3. Then, the velocity of ink solution flowing inside the small tube results in 13.6 mm/sec (= 2.78 $mm^3 \cdot sec^{-1}$/0.2043 mm^2).

It is noted that D3 detector measured optical signal changes from the dynamic phantom while the ink solution flowed spirally along the large tube. Therefore, the calculated velocity of ink flow seen by D3 for the NIRS signal needs to be converted to a longitudinal velocity along the big tube (25 mm, see Fig. 3.3). Given the total length of the wrapped small tube being 750 mm, I obtained a factor of 30 (= 750 mm/25 mm = the length of small tube wrapping around the large tube/large tube length). With this conversion factor, I arrived at 0.453 mm/sec (= 13.6 $mm \cdot sec^{-1}$/30) as a final calculated velocity for the 10 ml/hr flow rate with the 0.51-mm-diameter tube. Figure 3.6(b) shows the consistency between the calculated and measured velocities using the two different approaches. It also exhibits a strong correlation between the flow rate and the velocity of ink solution measured from the dynamic tumor vascular phantom (R=0.99). It is worthy to point out that these ink flow velocities shown are within the biological range of velocities of red blood cells (i.e., 1~20 mm/sec in arterioles and 1~8 mm/sec in venules from normal mice [78]).

Figure 3.7(a) shows the optical density changes (ΔO.D. at 730 nm) at three different positions taken from dynamic vascular phantom 1 when the ink solution was

injected into the VMD's. The first step in this experiment was injecting the diluted ink into only VMD-2, having a large diameter tube (0.86 mm ID) with a flow rate of 20 ml/hr.

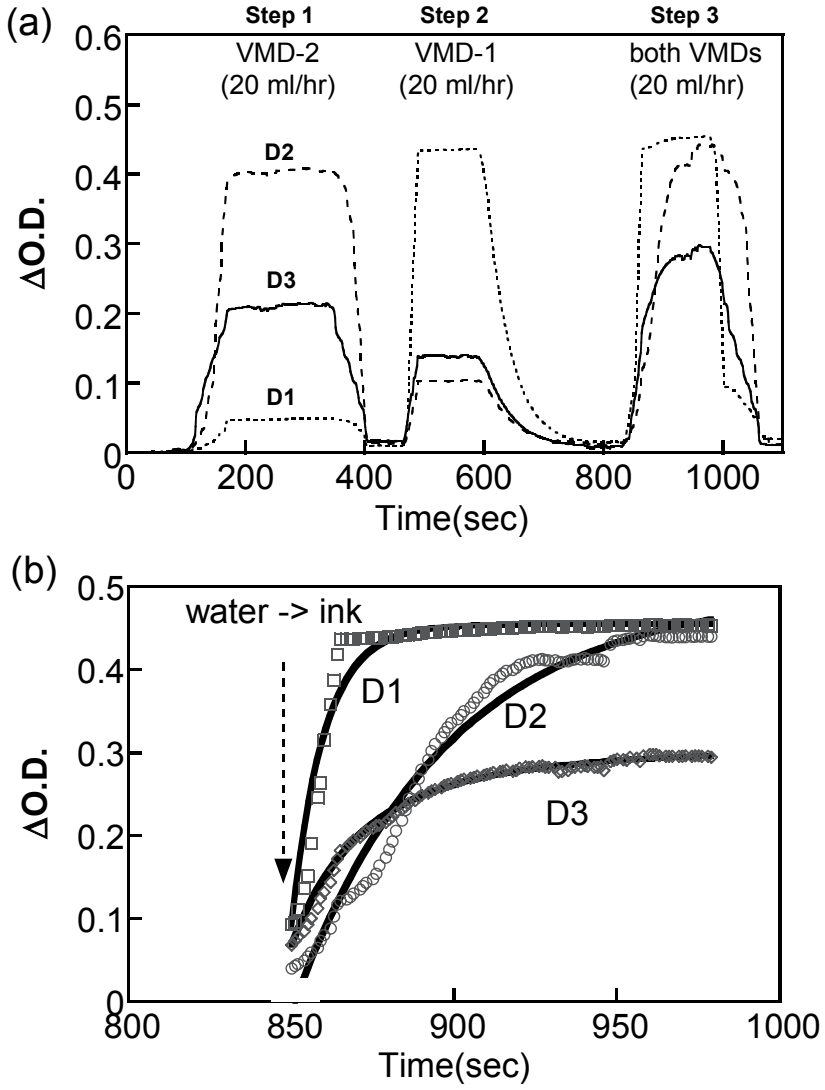

Fig. 3.7 (a) Three temporal profiles of 3-channel NIRS measurements result from D1, D2, and D3 on dynamic phantom 1 that has two different sizes of VMD's (VMD-1 and VMD-2). (b) Absorption changes obtained from D1, D2, and D3 during step 3 at Fig. 3.7(a). Open symbols represent the raw data of absorption changes, and solid lines are obtained with either mono-exponential model fitting (D1 and D2) or bi-exponential model fitting (D3).

As seen in this figure, the readings from D2 and D1 show the largest and smallest increase in Δ O.D., respectively, since the changes of O.D. in VMD-2 would be detected most sensitively by D2 and least sensitively by D1 (see Fig. 3.4(b)). The increase in ΔO.D. obtained from D3 is between those from D1 and D2, as expected.

A similar pattern is also displayed at step 2, when the diluted ink flowed only into VMD-1 (at 20 ml/hr) having a smaller diameter for the wrapping tube (0.51 mm ID). In this case, the readings at D1 offered the largest increase in ΔO.D., and D2 had a smallest ΔO.D. increase, as expected. Steps 1 and 2 clearly illustrate that an NIRS detector collects optical signals more sensitively from an adjacent VMD than from a distant one. The third step in the measurement was to inject the solution into both VMD-1 and VMD-2 simultaneously with the same flow rate as before (20 ml/hr). At this step, two features could be observed clearly: 1) the time profile taken at D1 had a faster transition time than that at D2, and 2) the time profile taken at D3 had a clear bi-phasic characteristic, similar to those often observed in animal tumor dynamic measurements [21] [33] [31].

To understand this set of results, the ink flow velocities at each tube need to be considered. Although the flow rate was kept the same in both VMD's ($Q_{VMD\text{-}1} = Q_{VMD\text{-}2}$), the velocities of ink solutions in the two VMD's were different because of the different inner diameters of wrapping tubes. Since $Q_{VMD\text{-}1} = Q_{VMD\text{-}2}$, Eq. (3.6) leads to Eq. (3.7) with $r_{VMD\text{-}1} = 0.255$ mm and $r_{VMD\text{-}2} = 0.43$ mm:

$$\frac{v_{VMD-1}}{v_{VMD-2}} = \frac{r_{VMD-2}^2}{r_{VMD-1}^2} = \frac{0.43^2}{0.255^2} = 2.84\,, \tag{3.7}$$

where $v_{VMD\text{-}1}$ and $v_{VMD\text{-}2}$ are velocities of the ink solution in VMD-1 (ID=0.51 mm) and VMD-2 (ID=0.86 mm), respectively, and $r_{VMD\text{-}1}$ and $r_{VMD\text{-}2}$ present the radii of the VMD-1 and VMD-2, respectively. This velocity difference may be the reason why the transition time in VMD-1 seen by D1 (see Fig. 3.4) is faster than that in VMD-2 detected by D2. Furthermore, since D3 was in the transmission geometry and nearly equal distanced to both of the VMD's, the signal obtained at D3 may sense the dynamic changes in light absorption within both VMD-1 and VMD-2. I expect that the bi-phasic feature recorded by D3 results from a superposition of two different dynamic transitions at VMD-1 and VMD-2.

To confirm my expectation, the ΔO.D. values detected from all three detectors at step 3 given in Fig. 3.7(a) were fitted with Eq. (3.1) or Eq. (3.2) to obtain amplitudes and time constants. The fitted values for each curve are listed in Table 3.1, and the corresponding curves are shown in Fig. 3.7(b). The results show that when the ink solution flows into both VMD-1 and VMD-2, the fast time constant (τ_1=11.7 ± 3.5 sec) and slow time constant (τ_2=35.2 ± 7.3 sec) observed at D3 are close to τ_1 (=7.3 ± 0.3 sec) obtained from D1 near VMD-1 and τ_1 (=42.8 ± 1.5 sec) obtained from D2 near VMD-2, respectively.

Table 3.1 Summary of fitted parameters obtained at the three detectors in Fig. 3.7(b).

Parameters	**Mono-Exponential fitting** $\Delta HbO_2 = A_1[1\text{-}\exp(-t/\tau_1)]$		**Double-Exponential fitting** $\Delta HbO_2 = A_1[1\text{-}\exp(-t/\tau_1)] + A_2[1\text{-}\exp(-t/\tau_2)]$
Detectors	Detector D1 (near VMD 1: I.D.=0.51 mm)	Detector D2 (near VMD 2: I.D.=0.86 mm)	Detector D3 (equal distanced between VMD 1 and VMD 2)
A_1 (mM/DPF)	0.340 ± 0.001	0.490 ± 0.007	0.092 ± 0.041
τ_1 (min)	7.3 ± 0.3	42.8 ± 1.5	11.7 ± 3.5
A_2 (mM/DPF)			0.18 ± 0.04
τ_2 (min)			35.2 ± 7.3
χ^2	0.016	0.039	0.0018
R	0.98	0.99	0.99

The ratio between the fast and slow time constants, i.e., τ_1/τ_2, is near 1/3 (≈11.7 sec/35.2 sec), almost equal to the reciprocal ratio of $\frac{v_{VMD-1}}{v_{VMD-2}} = 2.84$. This can be further expressed mathematically, using Eq. (3.7):

$$\frac{\tau_1}{\tau_2} \approx \left(\frac{v_{VMD-1}}{v_{VMD-2}} \right)^{-1} = \frac{1}{2.84} = 0.35 \tag{3.8}$$

Equation (3.8) clearly demonstrates that a fast flow velocity can give rise to a fast transient component, with a small time constant, seen by the NIRS, and a slow

transient component results from a slow flow velocity. The data taken from Phantom 1 basically demonstrate that the bi-phasic feature similar to that seen in tumor $\Delta[HbO_2]$ during carbogen/oxygen inhalation can be experimentally mimicked by utilizing two different flow velocities in two VMD's with different diameters. The knowledge learned in this study includes that: 1) the two-exponential behavior of tumor blood oxygenation during carbogen inhalation can be closely associated with two different sizes of blood vessels in tumors, and 2) the bi-phasic time constants are closely associated with the blood flow velocities in tumors, independent of sizes of tumor blood vessels.

Phantom 2 experimental results to be shown in the next subsection will also demonstrate that the bi-exponential dynamics may also result from different flow rates, given the same diameters for the two VMD's.

3.3.2 NIR Measurements Taken from Dynamic Tumor Vascular Phantom 2

Figure 3.8(a) shows the experimental results from tumor vascular dynamic phantom 2, which is different from phantom 1 by having two VMD-1's instead of one VMD-1 and one VMD-2 in tumor phantom 1. Since I now have two VMD-1's, the velocities of ink solution in VMD's will be totally depending on the ink flow rates controlled by two syringe pumps. The source and detector positions were same as those used in phantom 1 experiment, shown in details in Fig. 3.4(b).

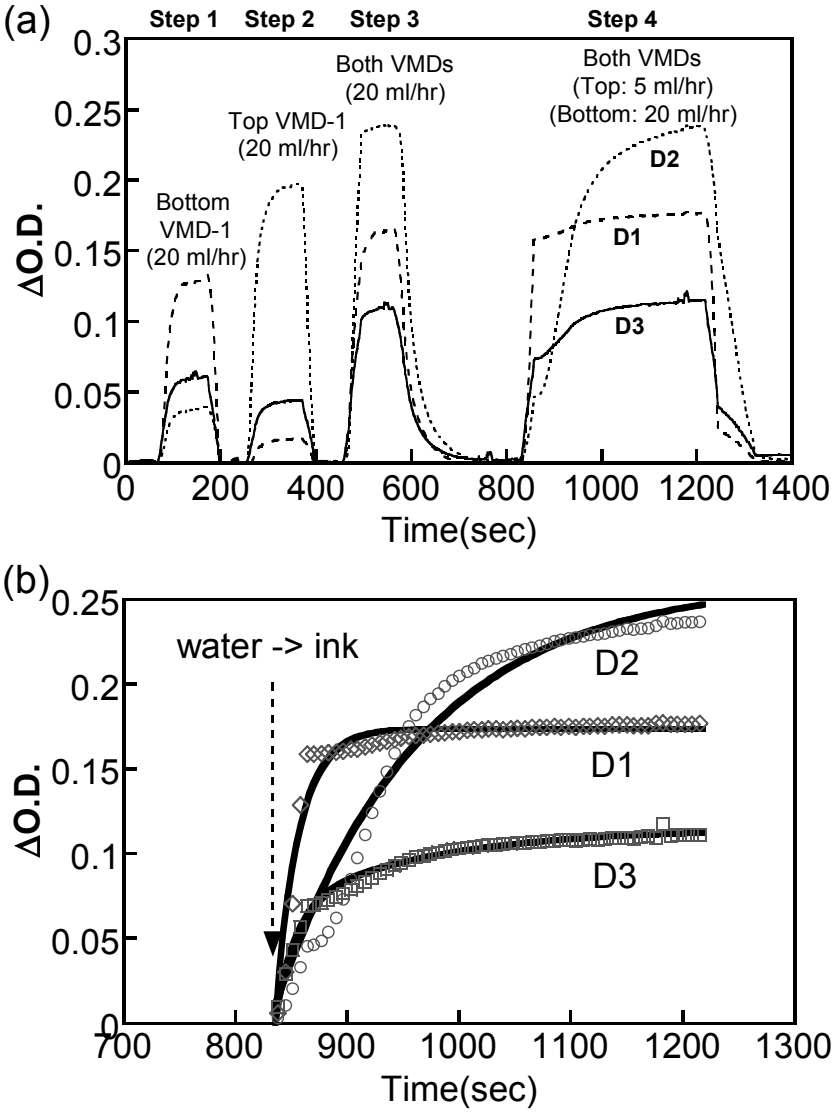

Fig. 3.8 (a) 3-channel NIRS results measured from tumor dynamic phantom 2 that has two VMD-1's. Three traces represent the readings at D3 (in transmission mode and located between the two VMD's), D2 (near the top VMD-1), and D1 (near the bottom VMD-1). (b) Temporal profiles of the NIRS measurements from D1, D2, and D3 with mono-exponential fitting (D1, and D2) and bi-exponential fitting (D3).

I observed the results similar to those shown in Fig. 3.7(a) by alternating the flow rates. The first step for this experiment was injecting the ink solution only into

bottom VMD-1 with a flow rate of 20 ml/hr. As a result, D1 showed the largest increase of ΔO.D. while D2 showed the least increase of ΔO.D. because D2 was located quite far away from bottom VMD-1. For the second step, top VMD-1 was injected with ink solution at the same flow rate of 20 ml/hr. Here, D2 showed the largest increase of ΔO.D. and D1 showed the smallest increase of ΔO.D. In both of the cases, the signals from D3 showed similar profiles as those taken from D1 and D2, without showing a clear bi-phasic feature.

Then, as the third step, the ink was injected into both top and bottom VMD-1's with the same flow rate (20 ml/hr). Similarly, I did not observe any clear two-exponential increase in ΔO.D. from D3. For the fourth step, I injected the ink solution into both of VMD-1's, but with two different flow rates: 5 ml/hr for top VMD-1 and 20 ml/hr for bottom VMD-1. Now a bi-exponential behavior appears seen by D3 since D3 detects signals from both top and bottom VMD-1's, which have two different ink flow rates.

Once again, time constant analysis was performed for the increase of ΔO.D. from three detectors at step 4, and the fitted curves are shown in Fig. 3.8(b). The analysis shows that ΔO.D. increases seen by D1 and D2 are well fitted by a mono exponential model while ΔO.D. increase detected by D3 is fitted better with a double exponential model. As seen in Table 3.2 with the values of fitted parameters, the fast (τ_1= 18.13 ± 0.87 min) and slow (τ_2= 133.66 ± 11.36 min) time constant obtained at D3 are well matched with τ_1 in D1 (20.92 ± 0.53 min) and τ_1 in D2 (131.19 ± 3.46 min). This suggests that the dynamic signals obtained from D3 with a fast and slow

component indeed result from two different ink flow rates in two VMD-1's. In addition, the components of A_1 (0.068 ± 0.0024) and A_2 (0.047 ± 0.0018) from D3 in step 4 are well matched with the values of A_1 from D3 in step 1 (A1=0.060± 0.001) and in step 2 (A1=0.043± 0.001). This consistency further shows that the ΔO.D. measured from D3 at step 4 is a summation of ΔO.D.'s observed from both of VMD-1's separately.

Table 3.2 Summary of fitted parameters obtained at three detectors given in Fig. 3.8(b)

Parameters	**Mono-Exponential fitting** $\Delta HbO_2 = A_1[1-\exp(-t/\tau_1)]$		**Double-Exponential fitting** $\Delta HbO_2 = A_1[1-\exp(-t/\tau_1)] + A_2[1-\exp(-t/\tau_2)]$
Detectors	Detector D1 (20 ml/hr)	Detector D2 (5 ml/hr)	Detector D3
A_1 (mM/DPF)	0.170 ± 0.001	0.260 ± 0.003	0.068 ± 0.003
τ_1 (min)	20.92 ± 0.53	131.2 ± 3.5	18.1 ± 0.9
A_2 (mM/DPF)			0.047 ± 0.002
τ_2 (min)			133.7 ± 11.4
χ^2	0.019	0.057	0.0018
R	0.97	0.98	0.99

3.4 Discussion and Conclusion

The results from dynamic tumor vascular phantom experiments supported previous hypothesis that the bi-phasic tumor hemodynamic feature during carbogen/oxygen inhalation results from a well-perfused and a poorly perfused region

in the tumor vasculature. Through this phantom study, I was able to find that the main cause for having a bi-phasic behavior results from different blood flow rates, or, more precisely, from different blood velocities in tumors. These differences in velocity can be induced from different blood vessel diameters with the same blood flow rate or from different blood flow rates with the same vessel diameter, both of which tumor vasculatures usually have.

The mathematical model developed by Liu *et al.* [31] actually carries this kind of information. As originally defined, $\tau = \gamma/f$, the value of time constant is affected by both γ and f (Eq. 3.1). Firstly, by assuming that f is constant, then τ will be depending on the value of γ. According to the definition of γ, it is a ratio of $\Delta[HbO_2]$ in vasculature and $\Delta[HbO_2]$ in veins. In NIRS experiments, $\Delta[HbO_2]$ in vasculature is limited to $\Delta[HbO_2]$ in microvessels within a tissue volume interrogated by the NIR light since NIRS measurement is more sensitive to small-sized blood vessels than to large blood vessels, including veins. Therefore, $\Delta[HbO_2]_{vasculature}$ can be altered by the amount of $\Delta[HbO_2]$ in microvessels, which is highly associated with the microvessel density and with the diameter of microvessels when oxygen consumption rate and arterial input function, $\Delta[HbO_2]_{artery}$, are constants, as assumed in the mathematical model. This leads one to expect that the time constant will increase when a large volume of $\Delta[HbO_2]$ exists, resulting either from a higher density of microvessels within the interrogated tissue volume or from larger-diameter microvessels in the tissue. This expectation was confirmed by my phantom 1 experiment, which shows that VMD-2 with a larger tube

diameter has a much slower time constant (42.8 min) than VMD-1 with a time constant of 7.3 min (see Table 3.1). Secondly, τ depends on the value of f if γ remains constant. It is obvious that the perfusion rate, f, is linearly proportional to blood flow rate when the microvessel density and the diameter of microvessels are unchanged. Then, τ will become smaller when the flow rate of blood increases. My phantom 2 experiment simulated such a condition and proved that one VMD-1 with a faster flow rate (20 ml/hr) has a much shorter time constant (20.92 min) than that (131.2 min) from another VMD-1 with a slower flow rate (5 ml/hr) (see Table 3.2).

Tumor blood vessels are known to be very leaky, longer in vessel lengths, and larger in vessel diameter; their local microvessel density is much more heterogeneous in comparison to normal tissues [57]. In addition, solid tumors usually develop hypoxia, which can result from poor perfusion in the central region when the tumors grow bigger. Meanwhile, the peripheral region of a tumor is normally well perfused so that it can be well provided with nutrition and oxygen. Therefore, tumor vasculature can be a mixed structure between well-perfused region and poorly perfused region, which can be observed as a bi-phasic feature of hemodynamics with respiratory challenges. I expect that a multi-channel NIRS system allows one to study dynamic heterogeneity of the tumor measured at different locations, as I will show in Chapters 7 and 8. I also expect that the tumor vasculature in the poorly perfused region (with a lower perfusion rate) can be eventually oxygenated if the two dynamic components are observed. On the other hand, if only the fast component (i.e., the mono-exponential model) can be found during tumor blood oxygenation from hyperoxic gas intervention, it may suggest that

either the perfusion rate in the poorly perfused region of the tumor is too slow to be detected, or this tumor is in its early development stage and quite homogeneously well-perfused.

As described in Section 3.2 earlier, γ_1/γ_2 may be associated with the vascular volume or density of two regions, and f_1/f_2 is related to the ratio of blood perfusion rates between region 1 and 2. The dynamic tumor vascular phantom experiments in this chapter showed that A or γ values are related to the amount of absorption changes of VMD's in dynamic vascular phantoms, and τ values are related to the flow velocity of ink solution. The intensity of absorption changes that measured from different detectors depends on the absorption coefficient of ink, the tube length and diameter in VMD, the wrapping number of the small tubing around the big tubing, and the location of the detectors. The time constant mainly depends on an ink flow velocity, which is affected by both γ and the perfusion rate, as described earlier in this section. To simulate a tumor experiment, the μ_a value of ink solution used in the phantom experiments corresponds to the level of blood oxygenation, and the VMD's in phantoms can be thought as a blood vessel network. The number of winding small tubing around the big tubing presents the vascular density in a tumor, affecting the values of both γ and f.

Previous measurements of animal tumors were performed in a transmittance mode by one channel NIRS, which could obtain only a global measurement of tumor hemodynamics. Therefore, those results could not show intratumoral or intertumoral spatial heterogeneities of tumor vasculature. However, multi-channel NIRS, by comparing γ_1/γ_2 and f_1/f_2 among the signals taken at different locations from the same

tumor or from different tumors, will enable us to study intratumoral or intertumoral spatial heterogeneity of tumor vasculature. Since tumor vascular structure will be modified during therapies, the changes of γ_1/γ_2 and f_1/f_2 during a respiratory challenge (such as carbogen or pure oxygen inhalation) after treatments will show the effects of therapies. Therefore, multi-channel NIRS or imaging not only can detect vascular heterogeneity of tumor, but also can be a prognostic tool to monitor early effects of tumor treatments, such as radiotherapy, photodynamic therapy, or chemotherapy. The detection of early effects of cancer therapies will benefit patients to have a higher survival rate by treating the cancer with proper therapies and dosages.

In summary, I developed tumor vascular dynamic phantom models to support the previous hypothesis on tumor hemodynamics during hyperoxic gas inhalation. I believe that the bi-phasic feature of tumor blood oxygenation during carbogen/oxygen inhalation originates from tumors' distinct vascular structure, which is composed of both well-perfused and poorly perfused region. I have performed several tumor phantom experiments to find out what can cause NIR signals to have two time constants when the measured signals are fitted with the bi-exponential mathematical model. I have found that the two time constants obtained from the tumor hemodynamic phantoms can be caused by different blood flow velocities or anything that can cause changes in blood flow velocities, such as blood vessel diameters and the geometry of blood vessel network. In addition, I have also found that two different amplitudes in the tumor hemodynamic model (A_1 and A_2) result from two different absorptions in two

regions, which are possibly due to different blood oxygenation level (oxyhemoglobin concentration) or vascular density.

NIRS is a portable, low cost, and real time measurement system that can monitor changes of vascular oxygen levels in tissues by using minimum of two wavelengths. Previous reports from Dr. Liu's group used a single-channel NIRS system with one light source and one detector for global measurements of $\Delta[HbO_2]$ and $\Delta[Hb_{total}]$ in experimental tumors during respiratory challenges [21] [31] [33] [34]. Now, this dynamic phantom study demonstrates that a multi-channel NIRS can detect optical changes in region of interest (VMD-1 or 2) which are located inside of the phantom. Therefore, the NIRS multi-channel approach has a potential to detect and monitor the heterogeneity of tumor responses under therapeutic or adjuvant interventions in clinical cases such as breast cancer treatment. For the future work, I suggest 1) to further investigate and understand the meaning of vasculature coefficient, γ, and 2) to develop an NIR imaging system to be used as a monitoring tool for the efficacy of cancer therapy.

* Part of this chapter was presented at Biomedical Topical Meetings held by Optical Society of America in 2004. This chapter now is prepared for a manuscript and is going to be submitted to Applied Optics.

Jae G. Kim, and Hanli Liu, "Investigation of breast tumor hemodynamics using tumor vascular phantoms and FEM simulations", in Biomedical Topical Meetings on CD-ROM (The Optical Society of America, Washington, DC, 2004), WF16.

CHAPTER 4

INVESTIGATION OF BI-PHASIC TUMOR OXYGEN DYNAMICS INDUCED BY HYPEROXIC GAS INTERVENTION: A NUMERICAL STUDY

4.1 Introduction

It is well known that solid tumors develop regions of hypoxia during their growth due to an imbalance between the rate of tumor cell proliferation and branching of the blood vessels [79] [80] [81]. Tumor hypoxia can contribute to the failure of radiotherapy [72] [10], some forms of chemotherapy [12], and photodynamic therapy [11]. Therefore, increasing tumor oxygenation could be very helpful to improve cancer therapy efficacy. As one means to improve tumor oxygenation, breathing a hyperoxic gas has been used to enhance the cancer treatment [82] [83]. Previous *in vivo* animal studies in Dr. Liu's group have clearly demonstrated that either carbogen (95% CO_2 and 5% O_2) or 100% oxygen inhalation can improve the vascular oxygen level of breast and prostate tumors [31] [33] [34]. Specifically, the observed changes in oxygenated hemoglobin concentration ($\Delta[HbO_2]$) of tumor vasculature exhibited a bi-phasic feature: a rapid increase, followed by a gradual but significant increase, in response to oxygen intervention (Fig. 4.1).

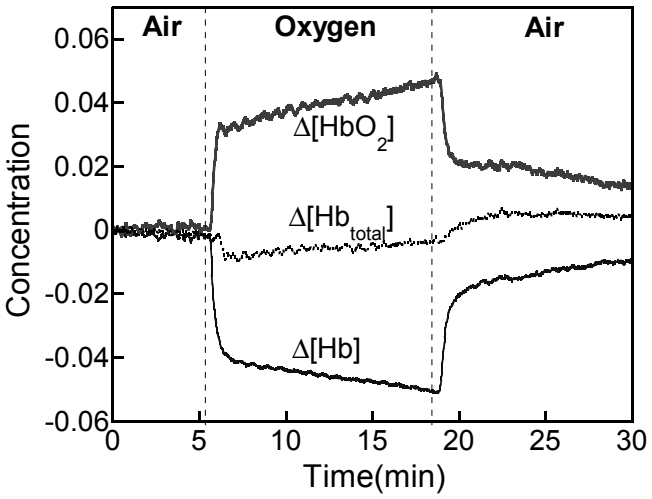

Fig. 4.1 A representative hemodynamic changes of rat breast tumor obtained with the NIRS measurement while the breathing gas was switched from air to oxygen and then back to air.

To explain this biphasic behavior of tumor hemodynamics, Liu *et al* have established a mathematical model based on Kety's approach [76] in their earlier publication [31]. They formed a hypothesis in Ref. 31 that tumor vasculature is comprised of a well-perfused and poorly perfused region that can be detected with the two time constants through $\Delta[HbO_2]$ readings derived from near infrared spectroscopy (NIRS). The mathematical model basically allowed one to associate the bi-phasic $\Delta[HbO_2]$ amplitudes and time constants to the ratio of vascular coefficients and vascular perfusion rates in the two different regions [31]. While the mathematical model seemed useful for interpretation of tumor hemodynamics and physiological factors, it was a suggested model without experimental or computational proof or confirmation at the time. To provide solid support and better understanding for this model and to further investigate heterogeneities of tumor vasculature, I have utilized a computational

approach to validate the dynamic NIRS measurements. The computational results given in this chapter strongly demonstrates that with the bi-phasic mathematical model, tumor vascular dynamics can be determined and monitored non-invasively using NIRS while a perturbation of hyperoxic gas intervention is given.

4.2 Review of previous mathematical model for tumor vascular oxygenation

In the previous report [31], Liu *et al* followed an approach used to quantify regional cerebral blood flow (*r*CBF) with diffusible radiotracers, as originally developed by Kety [76] in the 1950's. By applying Fick's principle and defining γ as the ratio of $\Delta[HbO_2]$ in the vascular bed to that in veins, $\Delta[HbO_2]$ induced by hyperoxic gas intervention in tumor vasculature could be mathematically modeled as Eq. (4.1):

$$\Delta[HbO_2]_{vasculature}(t) = \gamma H_o[1-\exp(-ft/\gamma)] = A[1-\exp(-t/\tau)], \quad (4.1)$$

where γ was defined as the vasculature coefficient of the tumor ($=\Delta[HbO_2]_{vasculature}/\Delta[HbO_2]_{vein}$), H_o was the arterial oxygenation input function, f represented the blood perfusion rate in cm^3/sec, τ is the time constant, $A=\gamma H_o$, and $\tau=\gamma/f$.

If a tumor has two distinct perfusion regions and the measured NIRS signals result from the both regions (Figure 4.2), it is reasonable to include two different blood perfusion rates, f_1 and f_2, and two different vasculature coefficients, γ_1 and γ_2, in the model.

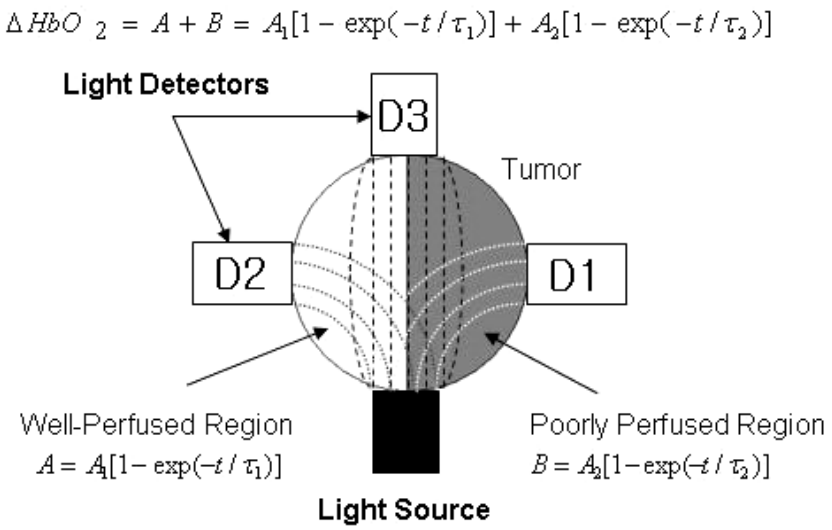

Fig. 4.2 A schematic diagram of light transmitting patterns in a tumor when the tumor has two distinct perfusion regions. The right side of tumor with gray color represents the poorly perfused region, whereas the left side of tumor corresponds to a well-perfused region. As shown, different detectors may interrogate different tumor volumes.

Eq. (4.1) becomes Eq. (4.2) to count for the double exponential feature observed in the NIRS experiments:

$$\Delta[HbO_2]_{vasculature}(t) = \gamma_1 H_o[1\text{-}\exp(-f_1 t/\gamma_1)] + \gamma_2 H_o[1\text{-}\exp(-f_2 t/\gamma_2)]$$

$$= A_1[1\text{-}\exp(-t/\tau_1)] + A_2[1\text{-}\exp(-t/\tau_2)] \qquad (4.2)$$

where f_1 and γ_1 are the blood perfusion rate and vasculature coefficient in the well perfused region, respectively; f_2 and γ_2 represent the same respective meanings for the poorly perfused region, and $A_1 = \gamma_1 H_o$, $A_2 = \gamma_2 H_o$, $\tau_1 = \gamma_1/f_1$, $\tau_2 = \gamma_2/f_2$. Since A_1, A_2, τ_1, and τ_2 can be determined by fitting Eq. (4.2) with $\Delta[HbO_2]$ readings taken from the

NIRS measurements, the ratios of two vasculature coefficients and the two blood perfusion rates can be obtained as:

$$\frac{\gamma_1}{\gamma_2} = \frac{A_1}{A_2}; \qquad \frac{f_1}{f_2} = \frac{A_1/A_2}{\tau_1/\tau_2}. \tag{4.3}$$

These two ratios enable one to understand more about tumor vascular structures and blood perfusion rates. In this chapter, computational evidence is shown to support the tumor hemodynamics model by simulating tumor dynamic phantoms described in Chapter 3.

4.3 Computer simulations using the finite element method

The Finite Element Method (FEM) was utilized to simulate the bi-phasic behavior of increases in $\Delta[HbO_2]$ with FEMLAB software (COMSOL Inc. Burlington, MA). It uses the numerical approach to solve partial differential equations (PDE) in modeling and simulating various engineering problems. The geometry of FEM simulations is given in Fig. 4.3, representing the simplified tumor vascular model shown in Fig. 4.2. E1 represents an overall tumor volume (diameter = 4 cm), and R5 shows the location of light source. Blood vessels in two different perfusion regions are represented by several rectangles (0.1 cm x 2.4 cm): R1 and R2 represent vessels with a fast flow rate, and R3 and R4 denote vessels with a slow flow rate.

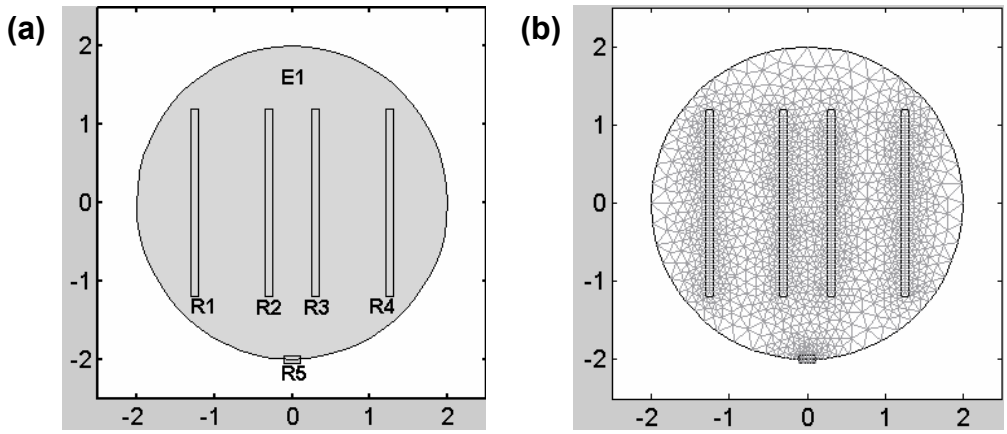

Fig. 4.3 (a) the geometry used in FEM simulations for a simplified tumor vascular model and (b) meshed FEM model. R1 and R2 rectangles are located in a fast flow region, while R3 and R4 are in a slow flow region within tumor. The units for both the X-axis and Y-axis are cm. The distances from R1 to R2 and from R2 to R3 are 1 cm and 0.5 cm, respectively.

To model the dynamic NIR signals, multiple FEM runs of the steady state photon diffusion model with Eqs. (4.4)–(4.6) were performed repeatedly with different lengths of R1, R2 and R3, R4, where the μ_a value of 1.5 cm^{-1} was used to simulate oxygenated blood within R1, R2, R3, and R4 regions. Each computed run/frame from the model was associated with the blood perfusion in the two vascular regions at a selected time. By assuming that both vascular regions in tumors are having a same vascular density, the perfusion rates of two regions is directly proportional to the blood flow rates. Therefore, the two different flow rates/perfusion rates passing through the two regions in tumors were mimicked by progressing the lengths of R1, R2 from 0 to 2.4 cm with an increment of 0.4 cm per frame to represent the fast flow process, and the lengths of R3, R4 with a smaller increment of 0.02 cm per frame were used to evolve the slow flow.

For each simulation with varying the length of R1, R2 and R3, R4, the steady state differential equation for light diffusion was applied as shown in Eq. (4.4):

$$-D\nabla^2\phi(\rho) + \mu_a\phi(\rho) = S(\rho)\,, \tag{4.4}$$

where $\phi(\rho)$ is the diffuse photon fluence rate at position ρ, $S(\rho)$ describes the photon source, $D = [3(\mu_a + \mu_s')]^{-1}$ is the photon diffusion coefficient, μ_a is the light absorption coefficient in tissue, and $\mu_s' = (1\text{-}g)\mu_s$ is the reduced light scattering coefficient in tissue. The anisotropy factor g is defined as the average cosine of the scattering angle. This diffusion equation assumes that light transport within a medium is scattering dominant rather than absorption, which is true for the light in NIR range in tissues. The solution to the diffusion equation gives the light distribution within the tissue as a function of spatial coordinates.

For the boundary conditions, a refractive index mismatch between the tissue and the external medium was considered [84]. In this case, the boundary condition must allow for internal reflection of the light back into the tissue. The condition should also account for the assumption that no photons travel inwardly at the boundary except for the source. Hence the photon fluence leaving the boundary of the tissue is the product of the photon fluence at the boundary and a factor A that accounts for the internal reflection at the surface. This condition is given by

$$\phi(r, z=0) - 2AD\vec{n}.\nabla\phi(r, z)\Big|_{z=0} = 0 \qquad (4.5)$$

where r is source detector separation, z is the depth from the surface, n is the unit vector normal to the surface and directed into the tissue, A=(1+r_d)/(1-r_d), and r_d is the internal reflectance caused by the refractive index mismatch between air and tissue. This can be estimated using the following empirically determined equation [85]:

$$r_d = -1.440\ n_{rel}^{-2} + 0.710\ n_{rel}^{-1} + 0.668 + 0.0636\ n_{rel} \qquad (4.6)$$

with $n_{rel} = n_{tissue}/n_{air}$.

In the simulation, 1.4 and 1.0 were used for n_{tissue} and n_{air}, respectively, to obtain A (=3.25). A value of D=0.033 cm was chosen for both the background and vasculature of phantom with μ_s'=10 cm^{-1}. The values of 0.03 cm^{-1} and 1.5 cm^{-1} were selected as absorption coefficients of the tissue background (E1) and oxygenated blood flowing through the simulated vessels (R1, R2, R3 and R4), respectively. In this simulation model, the absorption coefficients of perfused blood prior to carbogen intervention was assumed to be the same as tissue background since only changes of tumor blood oxygenation were measured from the baseline (air) to carbogen intervention. Therefore, the value of 1.5 cm^{-1} used in R1-R4 can be considered as a difference in absorption between preperfused blood and oxygenated blood after carbogen intervention. The simulation model was generated with FEMLAB having 1147 elements and 609 nodes (Fig. 4.3(b)). Finally, the model was solved using the stationary nonlinear solver type.

Figure 4.4 shows an example of a series of consecutive FEM outputs for the fast flow case, where each of the output frames corresponds to a time interval of 2 seconds. The frame rate in the calculation was kept the same for both fast and slow cases; thus, a series of discrete outputs of the FEM model can replicate the time-dependent NIR signals taken from the *in vivo* tumor model with a flow rate difference as large as 20 times between the two different perfusion regions.

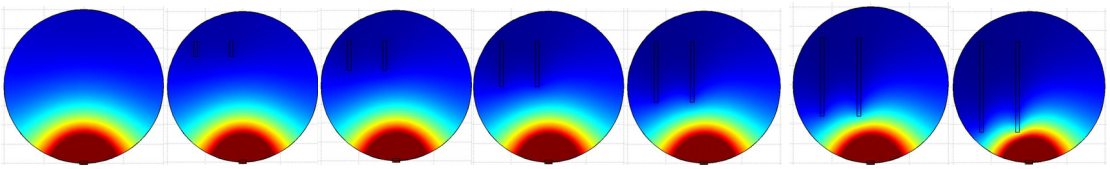

0^{th} Frame	1^{st} Frame	2^{nd} Frame	3^{rd} Frame	4^{th} Frame	5^{th} Frame	6^{th} Frame
Time=0 sec	2sec	4 sec	6 sec	8 sec	10 sec	12 sec

Fig. 4.4 Light distribution inside a simplified tumor vascular model simulated by FEM with the increase of R1 and R2 length to mimic the oxygenated blood flow in the well perfused region.

To investigate if the bi-phasic hemodynamic feature depends on the orientations of the vessels, I changed the position of source light to examine the effect of vessel geometry on NIR signals taken from the tumor hemodynamic measurements. Simulations were performed with the light source to be a) perpendicular to the vessels of the phantom and b) at the center of the phantom. In the former case, the light penetrates the slow-flow vessels first and then the fast-flow vessels. Such a simulation allowed one to investigate if in this geometry, the dynamic changes of NIR signals still have the bi-phasic behavior.

Changes in optical density (ΔO.D.) are used to calculate changes in photon fluence rates, ϕ, induced by the simulated flows along the boundary of phantom. Such ΔO.D. values are analogous to those observed in the previous animal experiments [31]; they are expressed as:

$$\Delta O.D. = log\left(\frac{\phi_{initial}}{\phi_{transient}}\right), \tag{4.7}$$

where $\phi_{initial}$ and $\phi_{transient}$ are the photon fluence rates at the initial and transient states.

4.4 Results

Figure 4.4 given above shows light distributions in a simplified tumor vascular model from seven simulation outputs to mimic a fast oxygenated blood flow in tumor by increasing the length of R1 and R2 with an increment of 0.4 cm per each frame, or 0.2 cm per second. The 0^{th} frame shows the light distribution in tumor vascular model when there is no blood flow, and all the other frames represent the light distributions with a fast oxygenated blood flow in R1 and R2. In a similar fashion, a slow flow rate of oxygenated blood in the poorly perfused region was simulated by increasing the length of R3 and R4 with a much slower rate of 0.02cm/frame (0.01 cm/sec).

Figure 4.5(a1) presents the light distribution of the simulated model when a fast oxygenated blood flow passed through R1 and R2 with a rate of 0.2 cm/sec; similarly, Fig. 4.5(b1) shows the light distribution when an oxygenated blood flow went into R3 and R4 with a slow flow rate of 0.01 cm/sec. Finally, Fig. 4.5(c1) shows the combined

light distribution in the phantom with both fast and slow flows in the two different regions. Figure 4.5(a1) is the result at the 6^{th} frame, while Fig. 4.5(b1) results from the 120^{th} frame. Figure 4.5(c1) is also the simulation output at the 120^{th} frame when the oxygenated blood flows passed through the entire lengths of all the simulated vessels.

In comparison with the results from the animal experiments [10-12], the light intensity values (proportional to the photon fluence rates,ϕ) were extracted at three positions of (2,0), (-2,0) and (0,2) from each frame of the simulations to calculate ΔO.D. values, which are plotted in the right column of Fig. 4.5. These three positions are corresponding to D1, D2 and D3 in Fig. 4.2. The time unit in these plots was obtained by associating each frame to 2 seconds. Thus, ΔO.D. shown in Fig. 4.5(a1) has 12 seconds to reach the maximum ΔO.D. since it has only 6 frames to simulate a fast flow rate, with a velocity of 0.2cm/sec. Similarly, ΔO.D. values in Fig. 4.5(b1) and 4.5(c1) will have 240 seconds to achieve their maximums because they have 120 frames to simulate a slow flow rate, with a velocity of 0.01 cm/sec.

Figure 4.5(a2) and 4.5(b2) show temporal ΔO.D. profiles taken from the three positions during a fast flow only and a slow flow only simulation, respectively. The former one shows that the ΔO.D. is the largest at (-2, 0) position and is the smallest at (2, 0) position when an oxygenated blood flow passes only into the vessels (R1 and R2) near D2 in the simulation.

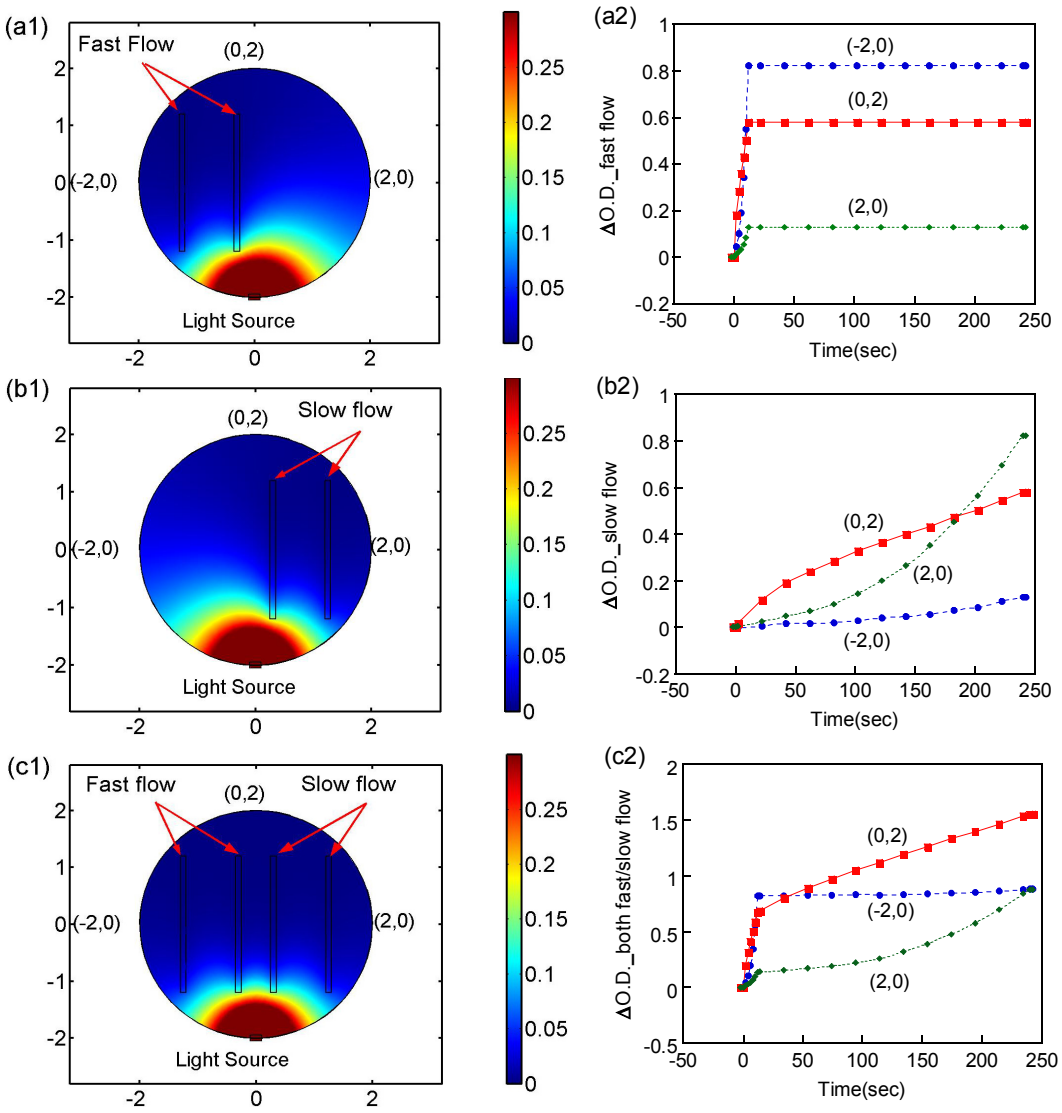

Fig. 4.5 Light distributions inside of a simplified tumor vascular model simulated by the FEM. Left column: (a1) is the output result with an only fast simulated flow rate (R1 and R2), (b1) is the result with an only slow flow rate (R3 and R4), and (c1) is the result with both fast and slow flow combined (R1, R2, R3 and R4). Right column: Optical density changes measured at three locations, (2,0), (-2,0), and (0,2), in the FEM simulations during fast flow only (a2), slow flow only (b2), and both fast and slow flow combined (c2).

Similar results are observed when the blood flowed only into the vessels in the slow perfusion region (R3 and R4), as seen in Fig. 4.5(b2). Namely, the ΔO.D. values are much larger at (2, 0) position than at (-2, 0). Moreover, Fig. 4.5(c2) shows that the temporal profiles of ΔO.D. taken at (2, 0) and (-2, 0) positions do not change significantly in comparison with those given in Figs. 4.5(a2) and 4.5(b2). However, in this case, the temporal ΔO.D. profile at (0, 2) position clearly shows a bi-phasic behavior, similar to that shown in Fig. 4.1, as often observed in the animal tumor studies [21] [31] [33] [34]. Notice that the portions in the ΔO.D. profile seem to be equally weighted by the fast and slow flows, implying that the fast and slow flows contribute to the measured NIR signals approximately equivalently. This indeed supports that it is necessary to contain two distinct flow or perfusion rates within tumors in order to exhibit the bi-phasic blood oxygenation dynamics during carbogen/oxygen inhalations.

The position of light source was also changed to be perpendicular to the vessels on the simulated phantom, as shown in Fig. 4.6(a1), or to be at the center of the phantom, shown in Fig. 4.6(b1). In this way, how blood vessel geometry within the tumor/phantom affects the bi-phasic feature of the tumor hemodynamics can be investigated.

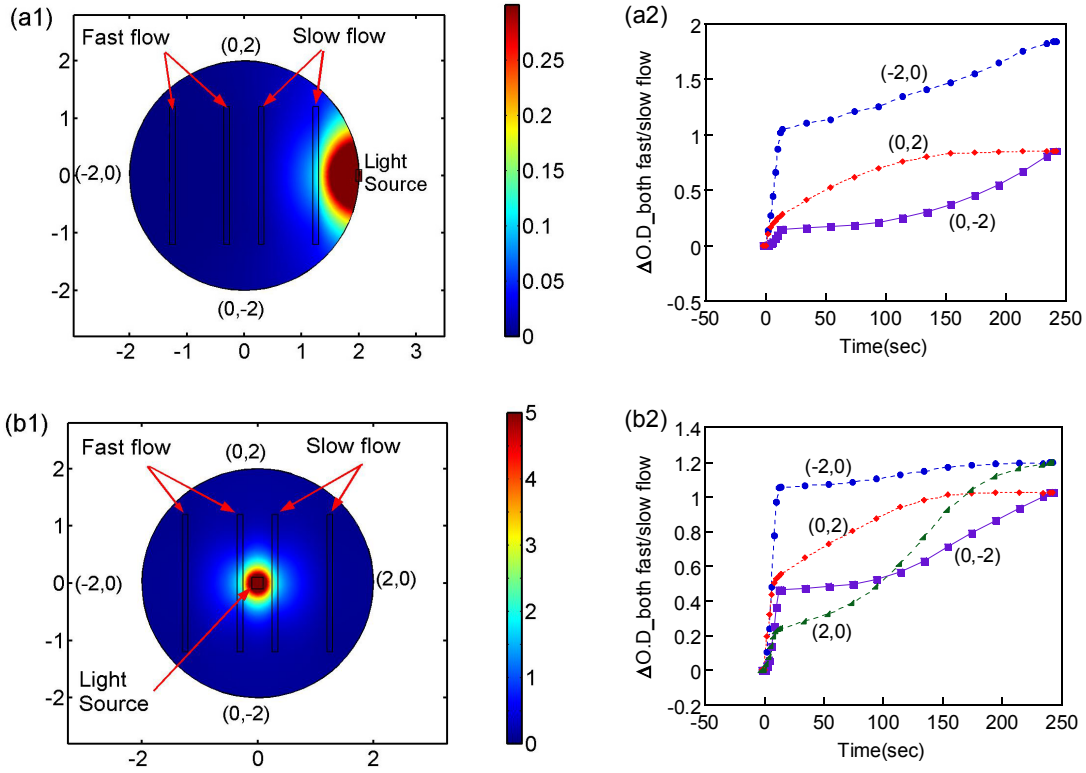

Fig. 4.6 FEM simulations of light distribution inside of a simplified tumor vascular model. Left column: (a1) shows the results when the light source is located perpendicular to the vessels, (b1) presents the results when the light source is located in the center of the model. Right column: Changes in O.D. measured at three locations, as labeled in Fig. 4.6(a1), with a fast and slow flow combined. (a2) plots three ΔO.D. profiles measured at the respective locations; (b2) reveals four ΔO.D. temporal profiles during the combined fast and slow flow.

Similar to Fig. 4.5(c1), Fig. 4.6(a1) shows light distribution within the simulated model when an oxygenated blood flow passed through R1 and R2 with a fast flow rate of 0.2 cm/sec and through R3 and R4 with a slow rate of 0.01 cm/sec. Temporal profiles of ΔO.D. at the three corresponding positions were quantified and plotted in Fig. 4.6(a2).

It shows that the detector at (0, 2) sees the change in optical density with a single-exponential shape, more dominated by the slow flow, while the detector at (0, -2) detects a small initial rise in ΔO.D. induced by the fast flow, followed by a gradual plateau and then a large increase by the slow flow. Such features can be expected based on their detection positions. Interestingly, the ΔO.D. profile taken at (-2, 0) exhibits an unambiguous bi-phasic exponential curve that results from both the fast and slow flow. This curve resembles very well the previously observed feature in animal studies done by Dr. Liu's group. (see Fig. 4.1 as an example).

Figures 4.6(b1) and 4.6(b2) simulate the light distribution and ΔO.D. profiles, respectively, obtained from the four positions of the tumor vascular dynamic phantom with the light source located at the center. The latter one displays that the detector at (-2, 0) is most sensitive to the signal from the fast flow only, while the readings of ΔO.D. at (2, 0) is affected by the fast flow at the initial onset and followed by a gradual increase. Furthermore, the ΔO.D. readings at (0, 2) and (0, -2) reveal somewhat bi-phasic behaviors with a fast increase in ΔO.D. initially, followed by an exponential and delayed exponential rise, respectively. These two bi-phasic profiles can be attributed to the fact that the detected NIR signals at (0, 2) and (0, -2) interrogated both fast and slow perfusion regions.

4.5 Discussion and conclusion

In this study, FEM method was employed to simulate the bi-phasic behavior that was frequently observed in blood oxygenation from animal tumors during

carbogen/oxygen inhalation. It is believed that the bi-phasic feature of tumor blood oxygenation during hyperoxic gas inhalation results from two distinct vascular structures of the tumor, namely, a well-perfused and poorly perfused region. These numerical simulations were performed to explore what can cause tumor hemodynamics to have two time constants, i.e., the bi-phasic feature. From the simulation results, it is confirmed that co-existence of two blood flow velocities can result in a bi-phasic change in optical density, thus leading further to a bi-phasic change in hemodynamics in tumor vasculature.

A comparison of Figs. 4.5(c2) and 4.6(a2) reveals that the bi-phasic or bi-exponential feature can be well present if both slow and fast perfusion regions exist within the interrogated area or volume of NIR source and detector, regardless of the orientation of vessels. Single exponential or non-exponential component of ΔO.D. exists if the NIR source and detector interrogates only the fast or slow perfusion area. Moreover, the contribution of each perfusion region to the NIR signal appears to be proportional to the vascular area or volume, i.e., the areas of R1, R2, R3, and R4 in this study. While it was shown that different flow velocities gave rise to bi-exponential profiles, such differences in flow velocity could arise from different blood vessel diameters with the same blood flow rate or from different blood flow rates with the same vessel diameter, both of which tumor vasculatures have. Detailed association between the measured NIR signals and vascular density and vessel sizes needs to be explored further in future studies.

In comparison, such a bi-phasic change in hemodynamics has been observed in MRI (Magnetic Resonance Imaging) studies during hypercapnic intervention or brain functional stimulation [86] [87]. Mandeville *et al*. have developed a modified Windkessel model to explain the bi-phasic increase of relative cerebral blood volume (rCBV) during 30 seconds of electrical stimulation on rat forepaw [86]. They explained the acute increase of rCBV by the fast elastic response from both capillary and vein and the slow increase of rCBV by a delayed venous compliance. Functional MRI can detect signals from large blood vessels such as artery and vein as well as those from small vessels including capillaries, while the NIRS measurement is most sensitive to microvessels [46] [88]. Therefore, the bi-phasic changes of $\Delta[HbO_2]$ observed by NIRS during carbogen intervention may not necessarily follow the same principle as explained by the modified Windkessel model.

In addition, the response of rCBV and relative cerebral blood flow (rCBF) in the brain due to stimulation is much faster than the blood oxygenation changes in tumor during carbogen intervention. The time constants of rapid and slow increases in rCBV were 1.9±0.7 second and 14±13 second [86], respectively, while the time constants of increases in $\Delta[HbO_2]$ in rat breast tumors during carbogen inhalation were much slower, varying from 3.9 sec to 150 sec (mostly 20-60 sec) for the rapid increase and 180 to 1500 sec during the gradual increase [31] [33] [34]. This suggests that the bi-phasic feature obtained in $\Delta[HbO_2]$ during tumor oxygenation may be a physiological and hemodynamic characteristic different from that observed in the brain. An investigation is currently undergoing to associate this experimental data with the modified

Windkessel model [89], following the approach that estimates the relative cerebral metabolic rate of oxygen ($rCMRO_2$) developed by Boas et al [90].

Padhani and Dzik-Jurasz have reviewed the heterogeneity in perfusion from extracranial tumors measured by dynamic contrast-enhanced MR imaging (DCE-MRI) [91]. They have shown that the kinetics of signal intensity changes obtained from T2*- or T1-weighted images are significantly varying within a tumor. Especially, Figs. 4 and 5 in their paper clearly support that the bi-phasic increase of $\Delta[HbO_2]$ from rat breast tumors during carbogen intervention could be from different perfusion rates in tumors, given that a single channel NIRS obtains global changes in tumor hemodynamics. In addition, other reports presented cerebral oxygenation during a relatively long period of hypercapnic challenge, e.g. 2 minutes [92] or 10 minutes [93], and did not show the bi-phasic feature in $\Delta[HbO_2]$.

Various mathematical models have been proposed to understand the cerebral hemodynamic parameters, including BOLD MRI signal, $rCMRO_2$, rCBV, rCBF during stimulation or hypercapnic intervention [86] [94] [95] [96] [97] [98] [99]. Since $\Delta[HbO_2]$ was showing large changes during carbogen inhalation in NIRS measurements, I have adopted $\Delta[HbO_2]$ as a sensitive parameter to obtain tumor hemodynamic features, just like changes in deoxyhemoglobin concentration used in BOLD MRI. Solid tumors are known to have both temporal and spatial heterogeneity in blood flow [100], and tumor blood vessels are much leakier and more porous than normal blood vessels [101]. Therefore, tumor hemodynamics may not follow the currently established mathematical models that estimate cerebral hemodynamics by considering autoregulation and vessel

reactivity. Based on the fact that solid tumors develop hypoxic regions which are poorly perfused in the center as they grow [102] [103], Liu *et al* hypothesized that the bi-phasic feature of $\Delta[HbO_2]$ stems from two different perfusion rates in tumors. This numerical approach is a simpler mathematical model in comparison with those presented for cerebral hemodynamic models. Currently, only the ratio of vascular coefficients and perfusion rates can be obtained by fitting the increase of $\Delta[HbO_2]$ since blood flow changes in tumor could not be measured [31]. To overcome this limitation, recently, Xia *et al* have followed an approach that estimates the $rCMRO_2$ developed by Boas et al. [90] to evaluate changes in tumor blood flow and metabolic rate of oxygen in tumor [89].

In this numerical study, the physiological complex of tumors in their hemodynamic structures was simplified by assuming the same absorption coefficients for the perfused blood prior to carbogen intervention and tissue background. While this simplified assumption is not realistic in actual tumors, the overall trend of mathematical simulations would remain the same. This is because the numerical simulations will always provide the changes in light intensity during tumor blood oxygenation, if an absorption difference exists in blood vasculature between the baseline (air) and carbogen intervention. With the current assumption and modeling setup, the bi-phasic feature could be enhanced for easy observation.

While the tumor vasculature and hemodynamics is very complex and chaotic, a simple numerical model, as demonstrated in this chapter, can support an initial mathematical hypothesis for tumor modeling. It is helpful to understand and to interpret

experimental data from animal studies, and lead to further development of more complex and realistic models for tumor investigations. The goal of this numerical study wa not to develop a comprehensive computational model for tumors, but rather focus on numerical support to better understand experimental observations during tumor oxygenation measured with NIRS.

In summary, a single-channel NIRS system have been previously used for global measurements of $\Delta[HbO_2]$ in tumors during respiratory challenges [21] [31] [33] [35], demonstrating that NIRS is a portable, low cost, and real time measurement system that can monitor changes of vascular oxygen levels in tumor tissues non-invasively. Now, the study shown in this chapter confirms that an NIRS multi-channel approach has great potential to detect and monitor tumor heterogeneity under therapeutic or adjuvant interventions. With an appropriate mathematical model, tumor vascular dynamics can be determined and monitored non-invasively while a perturbation of hyperoxic gas intervention is given. My suggestion for future work includes 1) to further investigate and understand the meaning of vasculature coefficient, γ and 2) to develop an NIR imaging system to be used as a monitoring tool for the efficacy of cancer therapy.

* Part of this chapter was presented at Biomedical Topical Meetings held by Optical Society of America in 2004. This chapter was later submitted to Optics Express and published in 2005.

J. G. Kim and H. Liu, “Investigation of bi-phasic tumor oxygen dynamics induced by hyperoxic gas intervention: A numerical study,” *Opt. Express*, **13**, 4465-75 (2005). http://www.opticsexpress.org/abstract.cfm?URI=OPEX-13-12-4465.

CHAPTER 5

INTERPLAY OF TUMOR VASCULAR OXYGENATION AND TUMOR pO_2 OBSERVED USING NIRS, OXYGEN NEEDLE ELECTRODE, AND ^{19}F MR PO_2 MAPPING

5.1 Introduction

It has long been known that hypoxic tumor cells are more resistant to radiation therapy than well-oxygenated tumor cells [9]. Breathing elevated oxygen (100%) or carbogen (95% O_2, 5% CO_2) has been used during therapy for an attempt to improve tumor oxygenation [13] [14]. To monitor tumor tissue oxygen tension [15] and its dynamic changes under respiratory interventions, various methods are available, including fiber optic sensors [16], oxygen electrodes [17], and electron spin resonance [17]. MRI has the further advantage of providing dynamic maps of pO_2, which can reveal tumor heterogeneity [18]. While NIRS does not quantify pO_2, it can indicate dynamic changes in vascular oxygenation and has the advantage of being entirely non-invasive, providing real-time measurements, and being cost effective and portable. Furthermore, it would be important to correlate the changes between tissue pO_2 and vascular oxygenation of the tumors since little is known about oxygen transfer from the tumor vasculature to tumor tissue.

The basic principle of NIRS rests on the fact that oxygenated and deoxygenated hemoglobin molecules are major chromophores in tissue in the near infrared region (700-900 nm), and they exhibit distinct absorption characteristics. In principle, the concentrations of oxygenated hemoglobin, [HbO_2], deoxygenated hemoglobin, [Hb], and oxygen saturation of hemoglobin, sO_2, can be determined by measuring light absorption and scattering in tissue based on diffusion theory. However, the theory works well only for large and homogeneous media [5] [7]. Therefore, accurate quantification of tumor oxygenation is currently limited to relative changes in [HbO_2] and [Hb_{total}] due to considerable heterogeneity and finite size of tumors.

The objective of this chapter is to investigate the correlation of tumor blood oxygenation and tumor pO_2 in response to carbogen intervention and to develop a suitable algorithm to estimate the hemoglobin oxygen saturation of the tumor under intervention. Specifically, in Section 2 of this chapter, an algorithm is derived to estimate absolute sO_2 values of the tumor during gas intervention. The algorithm will be validated through a tissue-simulating phantom and used to estimate tumor sO_2 in the animal measurement using both NIRS and mean pO_2 values, as mentioned in Sections 3 and 4. In Section 4, it will be shown that while NIRS results tend to be similar for several tumors, pO_2 electrode measurements show considerable variation even in the same tumor type, suggesting distinct tumor heterogeneity. In Section 5.5, the need to develop an NIR imaging technique will be discussed in order to study spatial heterogeneity of tumor vasculature under hyperoxic gas interventions. Finally, it is

concluded that the NIRS technology can provide an efficient, real-time, non-invasive approach to monitoring tumor physiology and is complementary to other techniques.

5.2 Algorithms development

5.2.1 Relationship among Normalized Δ[HbO_2], sO_2 and Blood pO_2

First, sO_2 values of the measured sample at the baseline, transient state, and maximal state are defined as $(sO_2)_{base}$, $(sO_2)_{t,}$ and $(sO_2)_{max}$, respectively:

$$(sO_2)_{base} = \frac{[HbO_2]_{base}}{[Hb_{total}]_{base}}, \tag{5.1}$$

$$(sO_2)_{t} = \frac{[HbO_2]_{t}}{[Hb_{total}]_{t}}, \tag{5.2}$$

$$(sO_2)_{\max} = \frac{[HbO_2]_{\max}}{[Hb_{total}]_{\max}}, \tag{5.3}$$

where $[HbO_2]_{base}$, $[HbO_2]_t$ and $[HbO_2]_{max}$ are corresponding oxygenated hemoglobin concentrations at the respective state. Mathematically, it follows that a reduced ΔsO_2 parameter can be defined as

$$\frac{\Delta sO_2}{\Delta sO_{2\max}} = \frac{(sO_2)_t - (sO_2)_{base}}{(sO_2)_{\max} - (sO_2)_{base}} \tag{5.4}$$

Such that

$$\frac{\Delta sO_2}{\Delta sO_{2\max}} = \left(\frac{[HbO_2]_t}{[Hb_{total}]_t} - \frac{[HbO_2]_{base}}{[Hb_{total}]_{base}} \right) \Bigg/ \left(\frac{[HbO_2]_{\max}}{[Hb_{total}]_{\max}} - \frac{[HbO_2]_{base}}{[Hb_{total}]_{base}} \right). \tag{5.5}$$

During a cycle of oxygenation and deoxygenation in a blood-perfused tissue, if the total concentration of hemoglobin remains constant and , the following condition will be valid: $[Hb_{total}]_{max} = [Hb_{total}]_t = [Hb_{total}]_{base}$. In the case of tumors under gas intervention, total hemoglobin concentration does not always remain constant, but the changes in $[Hb_{total}]$ appeared relatively small in comparison to the changes in $[HbO_2]$ [31] [104]. It is reasonable to assume that $\Delta[Hb_{total}] << [Hb_{total}]$, i.e., the condition of $[Hb_{total}]_{max} = [Hb_{total}]_t = [Hb_{total}]_{base}$ still holds approximately for the tumor under oxygen/carbogen interventions. Then, Eq. (5.5) becomes

$$\frac{\Delta sO_2}{\Delta sO_{2\max}} = \frac{(sO_2)_t - (sO_2)_{base}}{(sO_2)_{\max} - (sO_2)_{base}} = \frac{\Delta[HbO_2]}{\Delta[HbO_2]_{\max}}. \tag{5.6}$$

To make further correlation between the normalized $\Delta[HbO_2]$, i.e., $\Delta[HbO_2]/\Delta[HbO_2]_{max}$, and blood pO_2, Hill's equation [105] can be combined with Eq. (5.6) to characterize oxygen transport in the tissue vasculature:

$$\frac{\Delta[HbO_2]}{\Delta[HbO_2]_{\max}} = \frac{\dfrac{(pO_2^B)^n}{(P_{50}^B)^n + (pO_2^B)^n} - (sO_2)_{base}}{(sO_2)_{\max} - (sO_2)_{base}} = \frac{\dfrac{(pO_2^B)^n}{(P_{50}^B)^n + (pO_2^B)^n} - b}{a - b}, \quad (5.7)$$

where pO_2^B is the oxygen partial pressure in blood, P_{50}^B is the oxygen partial pressure in blood at sO_2=50%, n is the Hill coefficient, a = $(sO_2)_{max}$ and b = $(sO_2)_{base}$. This equation associates the normalized $\Delta[HbO_2]$ to blood pO_2 in tissues. Equation (5.6) indicates that normalized $\Delta[HbO_2]$ measured from tissues/tumors under gas interventions is associated with normalized sO_2 between $(sO_2)_{base}$ and $(sO_2)_{max}$ of the tissue/tumor, and Eq. (5.7) predicts the relationship between the normalized $\Delta[HbO_2]$ and blood pO_2 values in the tissue/tumor vasculature.

In tissue phantom studies using blood and Intralipid solution, the measured pO_2 values are considered as blood pO_2 in tissue vasculature since blood is well mixed in the solution (see details in Section 5.3.3). Therefore, values of P_{50}^B, n, a, and b in Eq. (5.7) can be fitted to the experimental data, which determines the initial, transient, and maximal values of sO_2 of the simulating tissue due to oxygen/nitrogen interventions.

5.2.2 Relationship between Normalized Δ[HbO_2] and Tissue/Tumor pO_2

In principle, blood pO_2 and tissue pO_2 are different, depending on the relative distance between a capillary vessel, oxygen consumption, and the location where pO_2 is measured [105]. It is shown that there exists a constant pressure drop between blood pO_2 and tissue pO_2 as the blood passes through a capillary vessel. Therefore, it is reasonable to assume

$$pO_2^B = \alpha \cdot pO_2^T, \tag{5.8}$$

where pO_2^B and pO_2^T are blood pO_2 and tissue pO_2 values, respectively, and α is a constant representing an oxygen partial pressure drop from blood pO_2 to a local tissue pO_2. Substituting Eq. (5.8) in Eq. (5.7) results in

$$\frac{\Delta[HbO_2]}{\Delta[HbO_2]_{\max}} = \frac{\dfrac{(pO_2^T)^n}{(P_{50}^T)^n + (pO_2^T)^n} - b}{a - b}, \tag{5.9}$$

where P_{50}^T is the oxygen partial pressure in tissue resulting from P_{50}^B, the meanings of n, a, and b remain the same as in Eq.(5.7). This equation shows how normalized Δ[HbO_2] measured from tissues under gas interventions is associated with both tissue pO_2 and normalized sO_2 between $(sO_2)_{base}$ and $(sO_2)_{max}$ in the tissue vasculature.

Ideally, when both $\Delta[HbO_2]$ and tissue pO_2 are measured at the same physical location, the maximal and initial oxygen saturations, i.e., a and b in Eq. (5.9), of the measured tissue vasculature can be obtained by fitting Eq. (5.9) to the measured data. In this tumor study, the maximal and initial hemoglobin oxygen saturations of the tumor can be still estimate by fitting the measured values of global $\Delta[HbO_2]$ and global tissue pO_2, which result from adding up all local pO_2 values obtained from ^{19}F MR pO_2 mapping.

5.3 Materials and Methods

5.3.1 Tumor Model

Dunning prostate rat tumors (eight R3327-HI and four R3327-AT1) [106] were implanted in pedicles on the foreback of adult male Copenhagen rats, as described in detail previously [107]. Once the tumors reached approximately 1 cm in diameter, the rats were anesthetized with 0.2 ml ketamine hydrochloride (100 mg/mL; Aveco, Fort Dodge, IA) and maintained under general gaseous anesthesia with isoflurane in air (1.3% isoflurane at 1 dm^3/min air) through a mask placed over the mouth and nose. Tumors were shaved to improve optical contact for transmitting light. Body temperature was maintained by a warm water blanket and was monitored by a rectally inserted thermal probe connected to a digital thermometer (Digi-Sense, model 91100-50, Cole-Parmer Instrument Company, Vernon Hills, IL). A pulse oximeter (model 8600, Nonin, Inc., Plymouth, MN) was placed on the hind foot to monitor arterial oxygenation (S_aO_2).

Tumor volume V (in cm^3) was estimated as $V = (4\pi/3)\ [(L+W+H)/6]$ [108], where L, W, and H are the three respective orthogonal dimensions.

In general, the source-detector fiber separation was about 1-1.5 cm in transmittance geometry, and thus the maximal tumor volume interrogated by NIR light can be estimated as follows. By diffusion approximation, the optical penetration depth from the central line between the source and detector is about one half of the separation (source-detector separation=d). The total tumor volume interrogated by NIR light can be estimated as a half of the spherical volume with a radius of one half of d, i.e., $\frac{\pi}{12}d^3$. In this way, the estimated tumor volume interrogated by NIR light is in the range of 0.25 – 1.0 cm^3, depending on the actual source-detector separation.

5.3.2 NIRS and pO_2 Needle Electrode Measurements

Figure 5.1 shows the schematic setup for animal experiments using both NIRS and a pO_2 needle electrode. The NIR system [31] [47] used in this study is a homodyne frequency-domain photon migration system (NIM, Inc., Philadelphia, PA) and uses commercially available in-phase and quadrature (IQ) demodulator chips to demodulate the detected, amplitude-modulated optical signal. The 5-mm diameter fiber bundles deliver the laser light at two wavelengths (758 and 785 nm) and detect the light transmitted through the implanted tumor. A needle type oxygen electrode was placed in the tumor, and the reference electrode was placed rectally.

The electrodes were connected to a picoammeter (Chemical Microsensor, Diamond Electro-Tech Inc., Ann Arbor, MI) and polarized at - 0.75 V. Linear two-point calibrations were performed with air (21% O_2) and pure nitrogen (0% O_2) saturated saline buffer solutions before the electrode was inserted into the tumor, and an instrumental precision was estimated as 2-3 mmHg. Measurement points of pO_2 were manually recorded, while the NIRS data were acquired automatically. Measurements of pO_2 and NIRS were initiated, while rats breathed air for ~10 minutes to demonstrate a stable baseline. The inhaled gas was then switched to carbogen for 15 minutes and switched back to air.

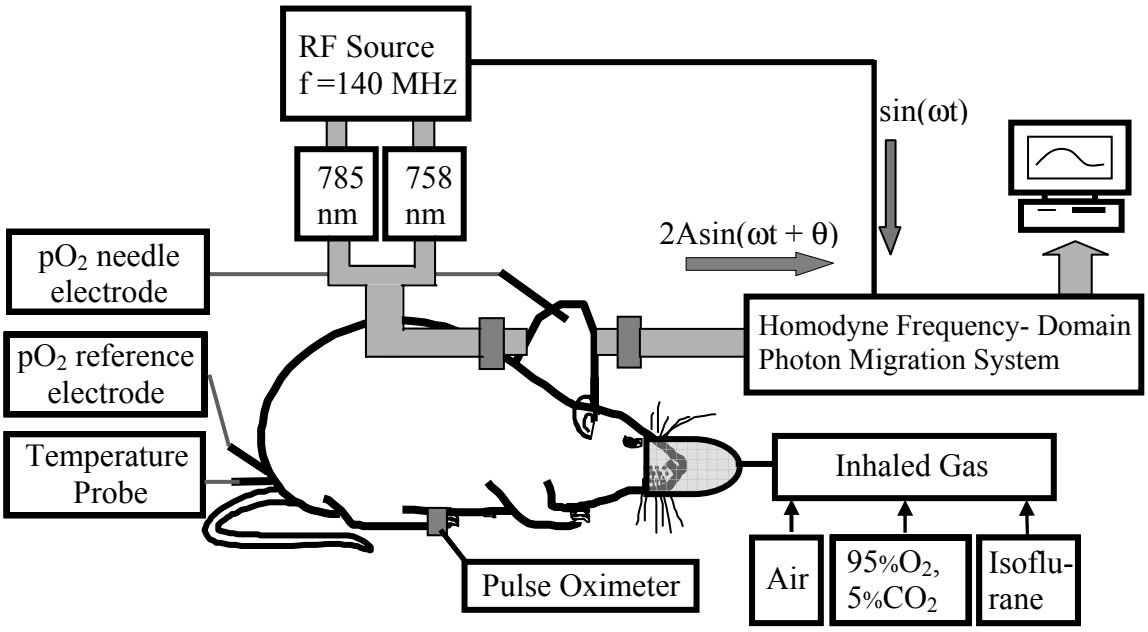

Fig. 5.1 Schematic experimental setup of one channel, near infrared, frequency domain IQ instrument for tumor investigation *in vivo*.

5.3.3 Tissue Phantom Solution Model

In order to study the relationship between pO_2 and $\Delta[HbO_2]$ in regular tissues, a tissue-simulating phantom study was conducted by using 200 mL of 0.01M phosphate buffered saline (P-3813, Sigma, St Louis, MO) and 1% Intralipid (Intralipid® 20%, Baxter Healthcare Corp., Deerfield, IL) with pH = 7.4 at ~37 ^{o}C. In normal tissues, there are several steps of oxygen transport from the blood to tissue cells [109]. In the tissue-simulating phantom, blowing oxygen gas represents oxygenation process of blood in the lungs, and blowing nitrogen gas simulates deoxygenation process of blood in the tissues. The differences between the tissue-simulating phantom and real tissues are that there is no capillary membrane in the phantom, and that the phantom is more homogeneous than real tissues. Capillary membranes have high permeability of oxygen, so oxygen transport from blood to tissues crossing the capillary membranes occurs straightforwardly. Furthermore, normal tissues are well vascularized, and NIR techniques are more sensitive toward measuring small vessels and vascular bed of the tissue [46]. Therefore, vasculature of normal tissues has been simulated by a turbid solution mixed with blood as a simplified laboratory model in NIRS measurements for oxygen transport from blood to normal tissues [7] [47] [104].

The experimental setup shown in Fig. 5.2 was made to simulate tumor oxygenation/deoxygenation. Oxygen needle electrodes, a pH electrode and a thermocouple probe (model 2001, Sentron, Inc., Gig Harbor, WA) were placed in the solution, and the gas tube for delivery of N_2 or air was placed opposite to the NIRS probes to minimize any liquid movement effects. Source and detector probes for the

NIRS were placed in reflection geometry with a direct separation of 3 cm. The solution was stirred constantly to maintain homogeneity by a magnetic stirrer at ~ 37 ^{o}C. Fresh whole rabbit blood (2 mL) was added to the 200 mL solution before baseline measurement. Nitrogen gas and air were used to deoxygenate and oxygenate the solution, respectively.

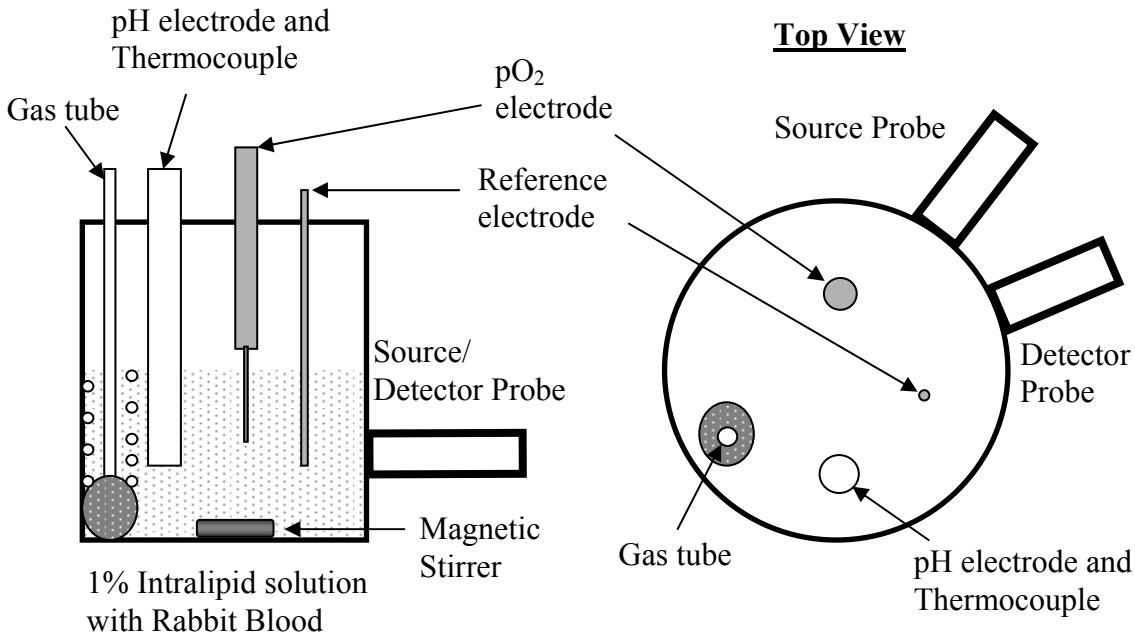

Fig. 5.2 Experimental setup for phantom study using 1% Intralipid in saline buffer.

5.3.4 MRI Instrumentation and Procedure

To support the findings obtained from the pO_2 electrode measurements and NIRS, MRI experiments were conducted using an Omega CSI 4.7 T 40 cm system with actively shielded gradients. A homebuilt tunable $^{1}H/^{19}F$ single turn solenoid coil was

placed around the tumor. 45 μL hexafluorobenzene (HFB; Lancaster, Gainesville, FL) was administered directly into the tumor using a Hamilton syringe (Reno, NV) with a custom-made fine sharp (32 gauge) needle and HFB was deliberated dispersal along several tracks to interrogate both central and peripheral tumor regions, as described in detail previously [16]. HFB is ideal for imaging pO_2, because it has a single resonance, and its relaxation rate varies linearly with oxygen concentration. ^{1}H images were acquired for anatomical reference using a traditional 3D spin-echo pulse sequence. Conventional ^{19}F MR images were taken to show the 3D distribution of the HFB in the tumor. ^{19}F MR images were directly overlaid over ^{1}H images to show the position of the HFB in that slice.

Tumor oxygenation was assessed using FREDOM (Fluorocarbon Relaxometry using Echo planar imaging for Dynamic Oxygen Mapping) based on ^{19}F pulse burst saturation recovery (PBSR) echo planar imaging (EPI) of HFB [63]. The PBSR preparation pulse sequence consists of a series of 20 non-spatially selective saturating 90° pulses with 20 ms spacing to saturate the ^{19}F nuclei. Following a variable delay time τ, a single spin-echo EPI sequence with blipped phase encoding was applied [110]. Fourteen 32×32 PBSR-EPI images, with τ ranging from 200 ms to 90 sec and a field of view (FOV) of 40×40 mm, were acquired in eight minutes using the ARDVARC (Alternated Relaxation Delays with Variable Acquisitions to Reduce Clearance effects) acquisition protocol [63]. An $R1$(=1/T1) map was obtained by fitting signal intensity of each voxel of the fourteen images to a three parameter relaxation model by Levenberg-Marquardt least squares algorithm:

$$y_n(i,j) = A(i,j) \cdot [1 - (1+W) \cdot \exp(-R1(i,j) \cdot \tau_n)] \quad (5.10)$$

(n = 1, 2, ……,14)

(i,j = 1,2,……..32)

where $y_n(i,j)$ is the measured signal intensity corresponding to delay time τ_n (the nth images) for voxel (i,j), $A(i,j)$ is the fully relaxed signal intensity amplitude of voxel (i, j), W is a dimensionless scaling factor allowing for imperfect signal conversion, and $R1(i,j)$ is the relaxation rate of voxel (i,j) in unit of sec^{-1}. A, W and $R1$ are the three fit parameters for each of the 32 x 32 voxels. Finally, the pO_2 maps were generated by applying the calibration curve, $pO_2(mmHg) = [R1(s^{-1}) - 0.0835]/0.001876$ at 37 ^oC, to the $R1$ maps [63].

5.4 Results

5.4.1 Tumor Study

Relative changes of $[HbO_2]$, [Hb], $[Hb_{total}]$ and tumor tissue pO_2 (electrode) were measured from eight Dunning prostate R3327-HI tumors, and Fig.5.3 shows three representative data sets. The unit of $\Delta[HbO_2]$ is mM/DPF, where DPF is equal to the optical path length divided by the source-detector separation. Dotted vertical line marks the time when the gas was changed.

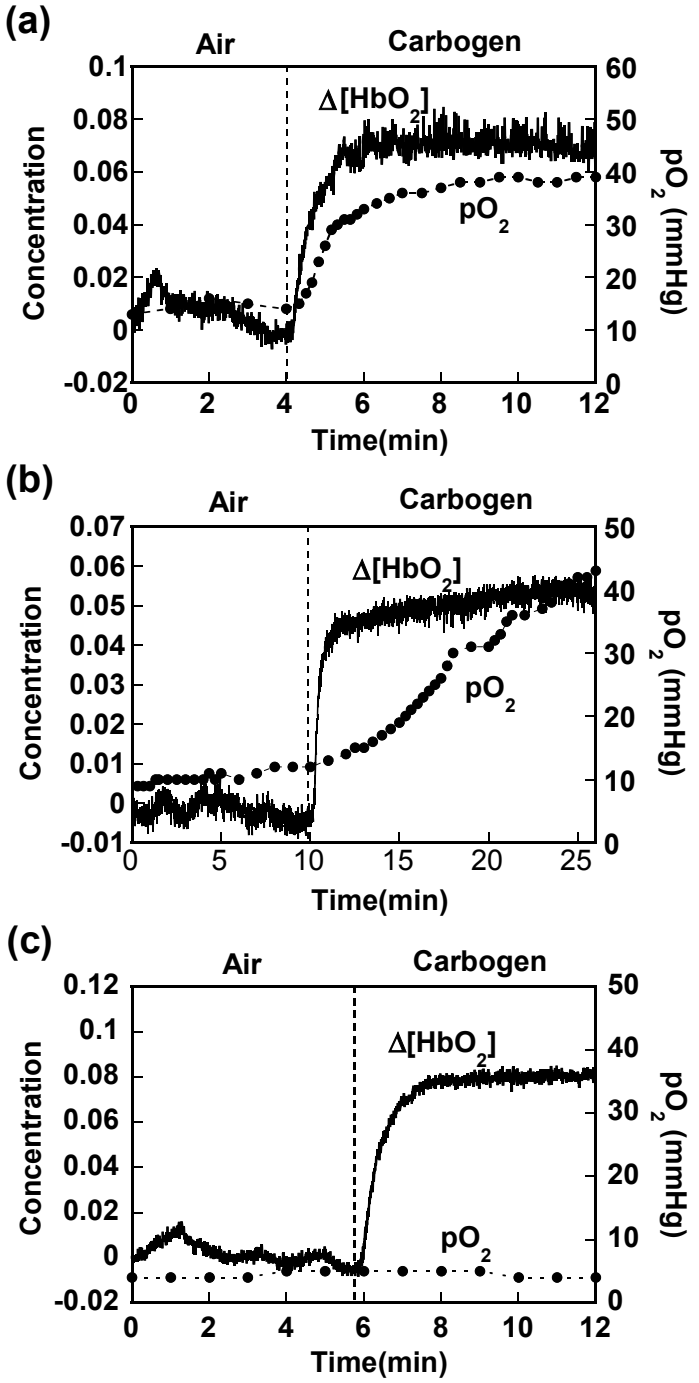

Fig. 5.3 Simultaneous dynamic changes of $\Delta[HbO_2]$ and pO_2 in R3327-HI rat prostate tumors using NIRS and pO_2 needle electrode.

Figure 5.3(a) shows the temporal profiles of $\Delta[HbO_2]$ and pO_2 in a small Dunning prostate R3327-HI tumor (1.5 cm^3) measured simultaneously with NIRS and the pO_2 needle electrode during respiratory challenge. After a switch from air to carbogen, $\Delta[HbO_2]$ increased rapidly, along with tumor tissue pO_2. Figure 5.3(b) was obtained from a large tumor (3.1 cm^3): the electrode readings showed a slower pO_2 response, whereas the NIRS response was biphasic, which has been a commonly observed dynamic feature [31]. In a third tumor (1.6 cm^3), NIRS behaved as before, but pO_2 did not change (Fig. 5.3(c)).

In four tumors from a separate subline (Dunning prostate R3327-AT1), NIRS and ^{19}F MRI were taken sequentially with carbogen challenge, and two representative data sets are shown in Fig. 5.4. The solid curves represent $\Delta[HbO_2]$, and the solid lines with solid circles represent mean $pO_2 \pm$ SE (Standard Error) of 21 (Fig. 5.4(a)) and 45 (Fig. 5.4(b)) voxels of the respective tumor. Dashed lines with open symbols are 4 representative voxels for each case. After a gas switch from air to carbogen, the mean pO_2 values of both tumors increased, but individual voxels showed quite different responses, indicating oxygen heterogeneity in the tumors. The tumor sizes were 3.2 cm^3 and 2.7 cm^3 for (a) and (b), respectively. NIRS response showed vascular oxygenation changes as before, and FREDOM revealed the distinct heterogeneity of the tumor tissue response. Initial pO_2 was in the range of 1 to 75 mmHg, and carbogen challenge produced pO_2 values in the range of 6 to 350 mmHg.

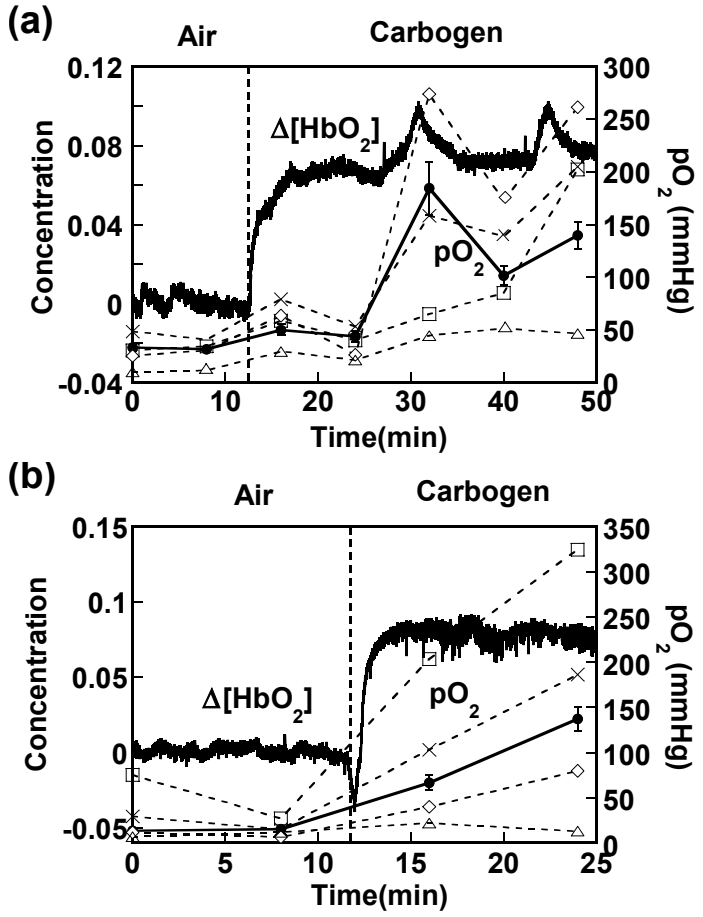

Fig. 5.4 Dynamic changes of $\Delta[HbO_2]$ and pO_2 in two R3327-AT1 rat prostate tumors measured sequentially using NIRS and ^{19}F MR pO_2 mapping.

In addition, mean pO_2 values were calculated by averaging all available pO_2 readings over 21 and 45 voxels for the two respective tumors. Usually pO_2 temporal profiles from individual voxels were obtained among 200 to 400 voxels in a tumor during the entire intervention period. The pO_2 readings presented here were picked up to show heterogeneity of the tumor. In Fig. 5.4(a), the closest distance between the two voxels is 1.25 mm (between ◇ and □), and the furthest distance is 7.6 mm (between ×

and △). In Fig. 5.4(b), the closest distance is 3.6 mm (between × and △) and the furthest distance is 16 mm (between × and □). These indeed showed that tumor pO_2 responses to carbogen intervention could be quite different at different locations.

Notice that Fig. 5.4(a) showed spikes of $\Delta[HbO_2]$ during the measurement. This is expected to be caused by sudden changes in rat respiratory circulation or motion, rather than resulting from simple instrumental noise. It is also seen that mean pO_2 values have displayed a consistent increase when $\Delta[HbO_2]$ showed spikes, suggesting that such spikes may result from changes in rat physiological conditions.

5.4.2 Tissue Phantom Study

Figure 5.5 shows a temporal profile for $\Delta[HbO_2]$ and pO_2 measured from the tissue phantom during a cycle of gas change from air to nitrogen and back. The first three minutes were measured as a baseline after adding 2 ml blood. Bubbling nitrogen deoxygenated the solution and caused the pO_2 values to fall; $\Delta[HbO_2]$ declined accordingly with a small time lag. After the bubbling gas was switched from nitrogen to air, both $\Delta[HbO_2]$ and pO_2 started to increase simultaneously, but the recovery time of $\Delta[HbO_2]$ to the baseline was faster than that of pO_2. The small time lag between the changes of $\Delta[HbO_2]$ and pO_2 is probably due to the allosteric interactions between hemoglobin and oxygen molecules. According to the hemoglobin oxygen-dissociation curve [105] [111], oxy- hemoglobin starts to lose oxygen significantly when pO_2 falls below 70 mmHg at standard conditions (pH = 7.4, pCO_2 = 40 mmHg and temperature =

37 ^{o}C). The same principle can explain why $\Delta[HbO_2]$ has a faster recovery than that of pO_2.

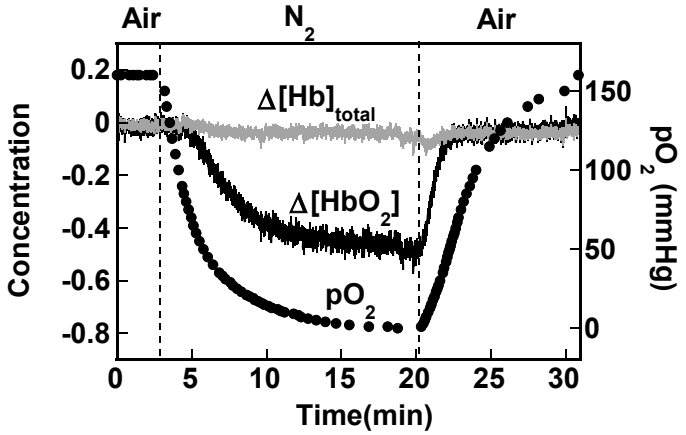

Fig. 5.5 Simultaneous dynamic changes of $\Delta[HbO_2]$, $\Delta[Hb]_{total}$ and pO_2 in the phantom solution measured using NIRS and pO_2 needle electrode. The unit of $\Delta[HbO_2]$ is mM/DPF.

Figure 5.5 shows that $\Delta[HbO_2]$ is already saturated when pO_2 is at 50 mmHg, while the solution was still being oxygenated. This may be due to low pCO_2 in the solution where this can shift the oxyhemoglobin dissociation curve to the left, causing oxyhemoglobin to be saturated at lower pO_2. Importantly, $\Delta[Hb_{total}]$ remained unchanged, as expected, during a cycle of deoxygenation and oxygenation.

5.4.3 Correlation between pO_2 and Normalized $\Delta[HbO_2]$

5.4.3.1 Tissue Phantoms Study

Figure 5.6(a) replots the data given in Fig. 5.5, showing the relationship between normalized $\Delta[HbO_2]$ and pO_2 measured from the tissue phantom during the

oxygenation (air blowing) period after the nitrogen blowing. Open circles are the measured data, and the solid line is the fitted curve using Eq. (5.9). The error bars for the data were not shown here since they are smaller than the symbols of the data points. For the curve fitting procedure, a non-linear curve-fitting routine provided through KaleidaGraph (Synergy software, Reading, PA) was used. The fitted parameters are n = 1.9, P_{50} = 15.2 mmHg, $[sO_2]_{base}$=0%, and $[sO_2]_{max}$=99% with R = 0.997 and minimized chi-square.

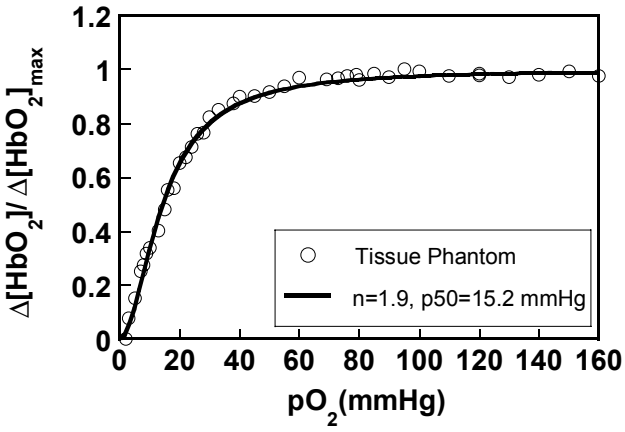

Fig. 5.6 Changes of tissue pO_2 with normalized changes of oxygenated hemoglobin in the phantom solution using the NIRS and pO_2 needle electrode.

The fitted values of $[sO_2]_{base}$ and $[sO_2]_{max}$ are in good agreement with the expected values, since the corresponding pO_2 values are 0 and 160 mmHg, respectively. This agreement validates Eq. (5.9) and further indicates that approximate sO_2 values during the gas interventions in a homogeneous system can be measured by fitting Eq. (5.9) to the experimental data even though absolute $[HbO_2]$ is not measured. The Hill

coefficient (n) and pO_2 value at 50% of sO_2 (P_{50}) are smaller than the values from a standard oxyhemoglobin saturation curve, probably due to the shift of the oxyhemoglobin dissociation curve.

5.4.3.2 Tumor Study

Figure 5.7 replots the data given in Figs. 5.3 and 5.4, showing a direct relationship between the normalized $\Delta[HbO_2]$ and tissue pO_2 in the tumors. NIRS results tended to be similar for several tumors, while pO_2 electrode measurements (open symbols in Fig. 5.7) showed considerable variation even in the same tumor type, suggesting distinct tumor heterogeneity. This was substantiated by the ^{19}F MR pO_2 mappings (Fig. 5.4): indeed, in some cases, pO_2 values did not change with respiratory challenge, especially when baseline pO_2 values were lower than 10 mmHg.

Equation (5.9) can be used to estimate values of $[sO_2]_{base}$ and $[sO_2]_{max}$ for the tissue-simulating phantom (a homogeneous system). However, the relationship fails for heterogeneous systems such as tumors. The NIRS measurements interrogate a large volume of tumor tissue, giving a global value of normalized $\Delta[HbO_2]$, whereas the pO_2 readings are local near the tip of the needle electrode. However, to estimate mean values of $[sO_2]_{base}$ and $[sO_2]_{max}$, it is reasonable to compare the global normalized $\Delta[HbO_2]$ with global tissue pO_2, which can be obtained by summing up all local pO_2 readings at different pixels measured from the ^{19}F MRI mapping, as done in Section 5.4.1 and shown by solid lines in Fig. 5.4.

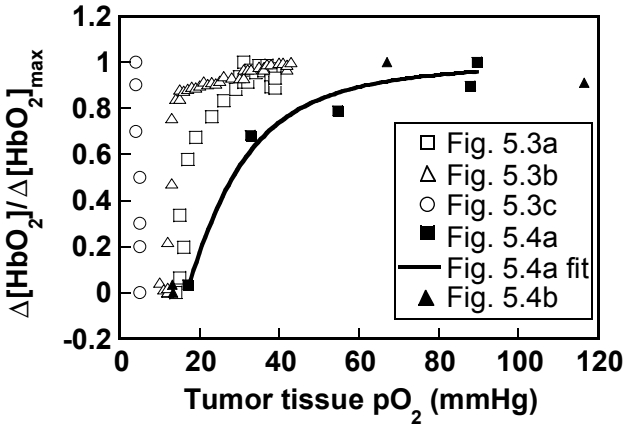

Fig. 5.7 Changes of tissue pO_2 with normalized changes of oxygenated hemoglobin in tumors measured with NIRS, pO_2 needle electrode, and ^{19}F MR pO_2 mapping.

The data shown in Fig. 5.7 with solid symbols are the global mean pO_2 values calculated from the corresponding MRI data. In this case, the fitting parameters are P_{50}, $[sO_2]_{base}$, and $[sO_2]_{max}$ with a fixed Hill coefficient, n, to be the same as that under standard conditions. The best fitting curve of Eq. (5.9) is shown in Fig. 5.7, having P_{50} = 20.6 ± 4.1 mmHg, $[sO_2]_{base}$=37 ± 13%, and $[sO_2]_{max}$ = 100% with R = 0.985 and goodness-of-fit, χ^2 = 0.031. Standard deviations for P_{50} and $[sO_2]_{base}$ are not insignificant, and a better fit could be found by measuring pO_2 with better temporal resolution.

5.5 Discussion and Conclusion

Tumor oxygenation involves a complex interplay of multiple compartments and parameters: blood flow, blood volume, blood vessel structure, and oxygen consumption. NIRS provides a global non-invasive estimate of average vascular oxygenation

encompassing arterial, venous and capillary compartments. In agreement with the previous observations from Dr. Liu's lab [31], the $\Delta[HbO_2]$ response is often biphasic, which is believed to represent rapid elevation of oxygenation in well perfused/periphery region, followed by more sluggish oxygenation in poorly perfused/central region of tumors.

Comparison with simultaneous electrode measurements indeed revealed that tumors are heterogeneous. Like NIRS measurements, pO_2 electrodes provide rapid assessment of pO_2 facilitating real time observation of dynamic changes. In Fig. 5.3(a), pO_2 starts at a baseline value ~ 15 mmHg and increases rapidly in response to respiratory challenge with carbogen. Indeed, the rate approaches that of the vascular compartments. In a second tumor (Fig. 5.3(b)), where the interrogated location showed a slightly lower pO_2, the tissue response was more sluggish. For a third HI tumor, local baseline pO_2 was found to be < 5 mmHg, and this did not change with carbogen inhalation despite the response observed by NIRS. This suggests a danger of comparing a global vascular measurement with regional tumor pO_2, since tumors are known to be highly heterogeneous. This also demonstrates an essential need for NIR imaging of tumors to provide regional tumor vascular oxygenation details.

FREDOM measurements in Fig. 5.4 revealed the heterogeneity in baseline oxygenation within individual tumors of this second tumor subline as also reported previously [63]. Baseline pO_2 ranged from 1 – 75 mmHg, and response to carbogen was variable in terms of rate and extent, as also seen for the HI subline using electrodes (Fig. 5.3). As with the electrodes, the better oxygenated tumor regions showed a faster

and greater response to carbogen inhalation. The oxygen electrode measurements in Fig. 5.3 showed a maximum pO_2 of around 45 mmHg, though values as high as 95 mmHg were observed in other experiments by using oxygen needle electrode. Observations using the fluorescence-based OxyLite™ fiber-optic devices for measuring HI tumor reached the maximum detectable pO_2 of 100 mmHg during carbogen inhalation [16]. FREDOM has shown values of less than 5 mmHg and greater than 160 mmHg under air breathing condition, and reaching 350 mmHg in HI tumors while breathing carbogen [16]. Each method indicates that tumors are highly heterogeneous, but it has been shown that there can be a positive linear relationship between baseline pO_2 and maximum pO_2 during carbogen inhalation in the Dunning prostate AT1 tumor line [20].

The phantom measurements indicate and validate the reliability of the NIRS technique and also prove that normalized $\Delta[HbO_2]$ is closely related to the normalized hemoglobin-oxygen dissociation curve. The phantom data confirmed that it is possible to obtain absolute sO_2 values in a homogeneous system by measuring both $\Delta[HbO_2]$ and pO_2. Mean sO_2 values of the tumor under intervention were estimated by using global $\Delta[HbO_2]$ and averaged pO_2 readings, and the fitting errors are expected to be improved by having more pO_2 data points. Correlation between local $\Delta[HbO_2]$ and pO_2 could be obtained by measuring regional tumor vascular oxygenation from NIR imaging of tumors and by obtaining local values of tissue pO_2 from ^{19}F MR pO_2 mapping which should be helpful to understand the oxygen transport process from tumor vasculature to tumor tissue.

Both NIRS and electrodes offer essentially real time measurement of changes in oxygenation, which can be rapid (Fig. 5.3). Indeed, the inflow kinetics of vascular O_2 detected by NIRS is similar to those previously reported in the HI tumor line following a bolus of the paramagnetic contrast agents Gd-DTPA [112]. FREDOM has lower temporal resolution, but reveals the tumor heterogeneity and differential response of regions exhibiting diverse baseline pO_2. The results here correspond closely with more extensive observation [16] [20] [63]. While FREDOM currently requires 6½ minutes per pO_2 map, Mason *et al* have previously demonstrated an alternative data acquisition protocol achieving 1 s time resolution in a perfused heart, albeit providing less precision in measurements and only a global determination [113]. Such an approach could allow one to measure global $\Delta[HbO_2]$ and global pO_2 simultaneously with a high temporal resolution, to understand the relationship between global $\Delta[HbO_2]$ and global pO_2, and to obtain absolute values of sO_2 of the tumors as tumors grow.

In conclusion, relative $[HbO_2]$ changes in tumor vasculature and tumor tissue pO_2 under carbogen intervention were measured using NIRS and needle type pO_2 electrode, and the pO_2 data were also supported by the ^{19}F MR pO_2 mapping. An algorithm was also developed to estimate sO_2 values in the tumor during respiratory interventions. The NIRS data showed significant changes in vascular oxygenation accompanying respiratory interventions, and changes in tumor vascular oxygenation preceded tumor tissue pO_2. Oxygen electrode measurements and ^{19}F MR pO_2 mapping results proved that tumors are highly heterogeneous. The phantom data confirmed that normalized $\Delta[HbO_2]$ data together with pO_2 measurements can be used to estimate

absolute sO_2 values in a homogeneous system. For a highly heterogeneous medium, such as tumors, local comparison between the $\Delta[HbO_2]$ and pO_2 value is desired and required in order to reveal the process of oxygen delivery from the tumor vascular bed to the tumor tissues. Therefore, this study not only demonstrates that the NIRS technology can provide an efficient, real-time, non-invasive approach to monitoring tumor physiology and is complementary to other techniques, but also emphasizes the need to develop an imaging technique to study spatial heterogeneity of tumor vasculature under oxygen or other therapeutic interventions.

* Part of this chapter was presented at the Photonics West Meeting held by SPIE in 2001. This chapter was later submitted to the Journal of Biomedical Optics and published in 2003.

Jae Gwan Kim, Yulin Song, Dawen Zhao, Anca Constantinescu, Ralph P. Mason, and Hanli Liu, "Interplay of Tumor Vascular Oxygenation and pO_2 in Tumors Using NIRS and Needle Electrode", *Proc. SPIE-Int. Soc. Opt. Eng.*, **4250**, 429-436 (2001)

J. G. Kim, D. Zhao, Y. Song, A. Constantinescu, R. P. Mason, and H. Liu, "Interplay of Tumor Vascular Oxygenation and Tumor pO_2 Observed Using NIRS, pO_2 Needle Electrode and ^{19}F MR pO_2 Mapping," *J. Biomed. Opt.*, **8**, 53-62 (2003).

CHAPTER 6

ACUTE EFFECTS OF COMBRETASTATIN A4 PHOSPHATE ON BREAST TUMOR HEMODYNAMICS MONITORED BY NEAR INFRARED SPECTROSCOPY

6.1 Introduction

It has been well accepted that angiogenesis is essential for tumors to keep growing since it was first proposed by Judah Folkman in 1971 [114]. Therefore, it is rational to approach tumor treatment by targeting tumor blood vessels as well as the tumor itself. Recently, many vascular disrupting agents (VDA's), including combretastatin A4 phosphate (CA4P), have been intensively studied either for their own therapeutic effects [115] or for their therapeutic enhancement by combining with other cancer therapies, such as conventional chemotherapy [116], radiotherapy [117], and radioimmunotherapy [118]. Combretastatin A4 phosphate is a soluble form of combretastatin and cause depolymerization of microtubules in endothelial cells which changes the shape of endothelial cells from flat to round. Besides this change in endothelial cell shape, CA4P increases plasma protein permeability. These two functions of CA4P eventually stop the blood flow in tumor capillaries by increasing the resistance to blood flow so that tumor cells starve to death. For more details on CA4P, many review articles are available [115] [119] [120] [121] [122].

Since these VDA's will disrupt the blood vessels in the tumor, thus results in changes in vascular function in the tumor. To understand the mechanism and also to assess the effects of CA4P, many imaging tools have been adopted such as fluorescence immunohistochemistry and imaging [123] [124], intravital microscopy [125] [126] [127], scintigraphic imaging [128], magnetic resonance imaging (MRI) [129] [130] [131], and positron emission tomography (PET) [132] [133]. A review of clinical monitoring of tumor responses to antiangiogenic and antivascular drugs is also available [134].

Near-infrared spectroscopy (NIRS), which utilizes the light in the near infrared region (700~900nm), can detect the changes of hemoglobin derivative concentrations in tissue non-invasively and has been applied to study various types of tissue, such as muscles [65] [66] [67], cancers [31] [71] [135], and the brain [68] [70] [136]. Because of high sensitivity to blood absorption, NIRS can be a tool to monitor tumor responses to VDA's, since they will alter the hemodynamic parameters, such as blood volume, blood oxygenation, and blood flow. Kragh *et al.* have reported the effects of 5 vascular modifying agents (VMA's) including CA4P on tumor perfusion and tumor blood volume changes by utilizing the laser Doppler flowmetry and a single wavelength NIRS [137]. However, they did not show dynamic changes in oxyhemoglobin, $\Delta[HbO_2]$, deoxyhemoglobin, $\Delta[Hb]$, and total hemoglobin, $\Delta[Hb_{total}]$, modulated by VMA's throughout the whole experimental time.

Since NIRS can monitor changes of $[HbO_2]$, $[Hb]$, and $[Hb_{total}]$ in tissues, NIRS has been applied to study the effects of hyperoxic gases (carbogen, oxygen) on tumor

oxygenation changes [21] [31] [33] [34]. A biphasic increase in $\Delta[HbO_2]$, which has a rapid increase and is followed by a gradual increase, during hyperoxic gas intervention has been frequently observed, and Liu *et al.* have developed a mathematical model to understand this bi-phasic hemodynamics during a hyperoxic gas intervention [31]. The mathematical model was based on Liu *et al*'s hypothesis that tumor vasculature is comprised of a well-perfused and poorly perfused region that could be detected with the two time constants through $\Delta[HbO_2]$ readings derived from the NIRS. This mathematical model has been supported and validated by my recent studies using both dynamic vascular phantoms [138] and computational simulations [139], as shown in Chapters 3 and 4. Thus, this mathematical model is a basis to associate the NIRS measurements, i.e., bi-phasic $\Delta[HbO_2]$ amplitudes and time constants, with the tumor physiology, i.e., the ratio of vascular coefficients and vascular perfusion rates in the two distinct regions.

In this chapter, I will report my studies where the changes of $[HbO_2]$, [Hb], and $[Hb_{total}]$ have been continuously monitored by using an NIRS system in rat tumors after CA4P administration. The oxygen interventions were given to the rats before, 2 hrs, 24 hrs, and 48 hrs after CA4P administration to compare the changes in tumor hemodynamics. I expect that such changes in $[HbO_2]$ can provide one with information on alterations in tumor physiology induced by the CA4P treatment. This study plans to show the possibility of NIRS to serve as a tool for assessing the effects of VDA treatments so as to find an optimal treatment plan.

6.2 Materials and Methods

6.2.1 Animal and Tumor Model

Rat mammary 13762NF adenocarcinomas (original obtained from the Division of Cancer Therapeutics, NIH, Bethesda, Maryland) were implanted on the hind limb of Fisher 344 female rats (n= 10, ~160g, Halan). The tumor diameter was measured in three orthogonal axes (a, b, c), and the tumor volume was estimated using the formula of $V= \pi/6*(abc)$. Among 10 rats, 5 were used as a control group and the other 5 rats were treated with a single dose of CA4P. All animal protocols were approved by the Institutional Animal Care and Use Committee at the University of Texas Southwestern Medical Center at Dallas for investigation.

6.2.2 Drug Preparation and Dose

CA4P was kindly provided by OXiGENE (Waltham, MA). It was dissolved in phosphate buffered saline solution with a concentration of 30 mg/mL, and a single dose of CA4P (30mg/kg rat body weight) was administered intraperitoneally for each experiment since it was considered as a clinically relevant dose [126].

6.2.3 Near-Infrared Spectroscopy

A tungsten-halogen broadband light (20W, 360 – 2000 nm) was used as a light source (HL-2000-HP, Ocean Optics Inc., Dunedin, FL), and a visible-NIR spectrometer (USB2000, Ocean Optics Inc., Dunedin, FL) having 350 – 1100 nm as an effective range was used as a light detector. A fiber bundle that has 3 mm core diameter was used

to deliver light from the source to the tumor, while another 0.6 mm diameter fiber was set up in a transmittance mode to deliver the collected light from the tumor to the spectrometer. The schematic setup for the experiments is shown in Fig. 6.1. The detected spectral responses over time were recorded by the software provided by the company (OoiBase32, Ocean Optics Inc., Dunedin, FL) with a sampling rate of 0.2-0.5 Hz depending on tumor size.

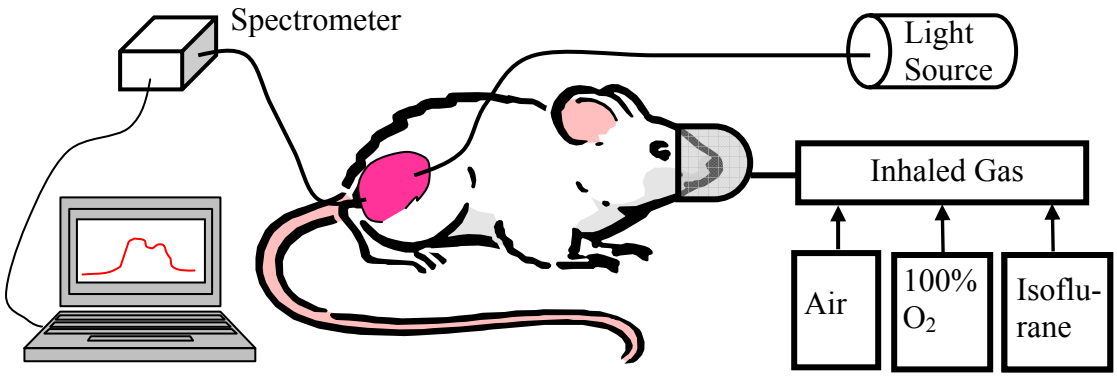

Fig. 6.1 A schematic diagram of experimental setup.

The OOiBase32 software can trace a maximum of 6 wavelengths that the operator selects, which should result in better accuracy of $\Delta[HbO_2]$, $\Delta[Hb]$ and $\Delta[Hb_{total}]$ calculations. However, as shown in Section 2.6, a proper selection of two wavelengths (750 nm and 830 nm) gave accuracy in $\Delta[HbO_2]$, $\Delta[Hb]$ and $\Delta[Hb_{total}]$ similar to the values obtained by using 6 wavelengths. Therefore, in this study, the light intensity values at 750 and 830 nm were used to obtain the calculations of $\Delta[HbO_2]$, $\Delta[Hb]$ and $\Delta[Hb_{total}]$ during the experiments. Based on the development and

modification on the algorithms for quantification of hemoglobin derivative concentrations, as given in Chapter 2, modified Beer-Lambert's law is utilized to give rise to the following equations:

$$\Delta[HbO_2] = [-0.653*\log (A_B/A_T)^{750} + 1.293*\log (A_B/A_T)^{830}] / L, \quad (6.1)$$

$$\Delta[Hb] = [0.879*\log (A_B/A_T)^{750} - 0.460*\log (A_B/A_T)^{830}] / L, \quad (6.2)$$

$$\Delta[Hb_{total}] = \Delta[Hb] + \Delta[HbO_2]$$
$$= [0.226*\log (A_B/A_T)^{750} + 0.833*\log (A_B/A_T)^{830}] / L, \quad (6.3)$$

where A_B = baseline amplitude; A_T = transition amplitude; L = optical pathlength between source/detector. The constants contained in these equations were computed with the extinction coefficients for oxygenated and deoxygenated hemoglobin at the two wavelengths used [30], i.e., at 750 nm and 830 nm. In principle, L should be equal to the source–detector separation, d, multiplied by a differential pathlength factor (DPF), i.e., L=d*DPF. Little is known about DPF for tumors, although a DPF value of 2.5 has been used on tumors by others [71]. Since the focus of this study is on dynamic changes and relative values of tumor $[HbO_2]$ in response to oxygen intervention, the DPF is included in the unit, and Eqs. (6.1)-(6.3) become as follows:

$$\Delta[HbO_2] = [-0.653*\log (A_B/A_T)^{750} + 1.293*\log (A_B/A_T)^{830}] / d, \quad (6.4)$$

$$\Delta[Hb] = [0.879*\log (A_B/A_T)^{750} - 0.460*\log (A_B/A_T)^{830}] / d, \quad (6.5)$$

$$\Delta[Hb_{total}] = \Delta[Hb] + \Delta[HbO_2]$$

$$= [0.226*\log (A_B/A_T)^{750} + 0.833*\log (A_B/A_T)^{830}] / d, \quad (6.6)$$

where the unit of $\Delta[HbO_2]$, $\Delta[Hb]$ and $\Delta[Hb_{total}]$ in Eqs. (6.4) – (6.6) is mM/DPF.

6.2.4 Experimental Design

Once the tumors grew to around 1 cm in diameter, the animals were sedated with a 120 µl injection of Ketamine Hydrochloride intraperitoneally (100 mg/kg, Aveco, Fort Dodge, IA) and were placed under general gaseous anesthesia during the period of experiments with 1.0% isoflurane (Baxter International Inc., Deerfield, IL) and air. The dynamic changes of tumor oxygenation and blood volume in response to CA4P were continuously monitored by the broadband NIRS system. Pure oxygen gas was given to the animals to generate tumor hemodynamic changes, and such intervention was used as an intrinsic contrast to enhance the NIR signals from the tumors. Fitting the mathematical model [31], as reviewed in Sections 3.2.1 and 4.2, with the hemodynamic data during oxygen intervention provides one with direct observation and comparison for the effects of CA4P on tumor vasculatures.

For the experiments, the rats were divided into two groups: one group (n=5) received a saline administration as a control group, and the other group (n=5) had a CA4P injection with a dose of 30 mg/kg via i.p. as a treatment group. During the NIRS measurements, the following respiratory challenge paradigm was employed:

Air (15 min) –> O_2 (20 min) –> Air (15 min) –> Saline or CA4P administration –> Air (2 hours) –> O_2 (20 min) –> Air (5 min)

To investigate the long term effect of CA4P on breast tumors, the NIRS measurements were repeated when the oxygen intervention to the experimental rats was given again at 24 hrs and 48 hrs after CA4P treatment. In this case, air was breathed for 15 min, and then oxygen intervention was given for 20 min to cause hemodynamic changes in the tumors.

6.2.5 Estimation of percent changes in tumor blood volume

I have also traced the detected signal changes at 803 nm, which is close to the isobestic point of HbO_2 and Hb. Optical density (*O.D.*) at 803 nm can be expressed with the following equation, assuming that HbO_2 and Hb are the main chromophores in tissue at this wavelength and others, such as water and fat, are negligible.

$$O.D.^{803} = Log\left(I_o / I\right)^{803} = \left\{\varepsilon_{Hb}^{803}[Hb] + \varepsilon_{HbO_2}^{803}[HbO_2]\right\} L, \qquad (6.7)$$

where I_o and I are the incident and detected optical intensities in the measurement of a non-scattering medium, ε_{Hb}^{803} and $\varepsilon_{HbO_2}^{803}$ are the extinction coefficients of Hb and HbO_2 at 803 nm, and L is the optical path length between the source and detector. Since $\varepsilon_{Hb}^{803} \cong \varepsilon_{HbO_2}^{803}$ [30] and $[Hb_{total}] = [Hb] + [HbO_2]$, the optical density at 800 nm during the baseline and transient condition can be further expressed, respectively, as follows:

$$Log\left(I_o / I_B\right)^{803} = \left\{2\varepsilon_{Hb}^{803}[Hb_{total}]_B\right\}L\,, \tag{6.8}$$

$$Log\left(I_o / I_T\right)^{803} = \left\{2\varepsilon_{Hb}^{803}[Hb_{total}]_T\right\}L\,, \tag{6.9}$$

where I_B and I_T are the detected optical intensities during the baseline and transient condition, respectively, and $[Hb_{total}]_B$ and $[Hb_{total}]_T$ are the total hemoglobin concentration at the baseline and transient stage. The difference of total hemoglobin concentration between the respective conditions can be obtained by subtracting $[Hb_{total}]_T$ from $[Hb_{total}]_B$, as shown below:

$$[Hb_{total}]_B - [Hb_{total}]_T = \frac{Log\left(I_T / I_B\right)^{803}}{2 \cdot \varepsilon_{Hb}^{803} \cdot L}\,. \tag{6.10}$$

By dividing both sides of Eq. (6.10) by $[Hb_{total}]_B$, the percent change of total hemoglobin concentration in the tumor after CA4P administration can be estimated:

$$1-\frac{[Hb_{total}]_T}{[Hb_{total}]_B}=\frac{Log\left(I_T/I_B\right)^{803}}{2\cdot\varepsilon_{Hb}^{803}\cdot[Hb_{total}]_B\cdot L}. \tag{6.11}$$

In the case of a scattering medium, L is not exactly equal to the source-detector separation, d, but rather approximated as L=d · DPF, where DPF is a Differential Pathlength Factor. The DPF was introduced to take into account light scattering effects in Beer-Lambert's law [140]. Substituting L=d·DPF into Eq. (6.11) leads to

$$\frac{[Hb_{total}]_T}{[Hb_{total}]_B}=1-\frac{Log\left(I_T/I_B\right)^{803}}{2\cdot\varepsilon_{Hb}^{803}\cdot[Hb_{total}]_B\cdot d\cdot DPF} \tag{6.12}$$

As can be seen from Eq. (6.12), it is necessary to know the values of $[Hb_{total}]_B$ and DPF to obtain the percent changes in tumor blood volume. It has been found that the blood volume measured by NIRS is around 15 to 30% of total blood volume in the tumors depending on DPF values [141]. By using ^{19}F MRS with an emulsion of perflubron (OxygentTM, Alliance Pharmaceutical Corp., San Diego, CA), values of total blood volume of the tumors with sizes from 2 to 7 cm^3 were measured, and it was found that there is a linear correlation between the total blood volume in the tumors and physical tumor volume [142], as expressed: Total tumor blood volume=0.1073*Tumor physical volume + 0.1979.

By applying this correlation, the total blood volume in the tumors used in this study was estimated, using the known physical tumor sizes. Then, further estimation for $[Hb_{total}]_B$ in the tumor was taken by multiplying γ to the value of total tumor blood volume estimated by ^{19}F MRS (Eq. 6.13) [141].

$$[Hb_{total}]_{B\_NIRS} = \gamma * [Hb_{total}]_{B\_MRS} \tag{6.13}$$

where γ is the the fraction of tumor blood volume sampled by NIRS and MRS in tumors (γ = 30% when DPF = 2), $[Hb_{total}]_{NIRS}$ and $[Hb_{total}]_{MRS}$ are the tumor blood volumes estimated by NIRS and by MRS during the baseline, respectively.

By assuming γ = 30%, The estimated $[Hb_{total}]_B$ with in the tumor was in the range of 84 to 158 μM depending on the tumor size. These values are consistent with the total hemoglobin concentrations found from human breast cancer (12 to 174 μM) [143] and arm vasculature (90 μM) [144], and these values are much higher than those in healthy breast tissue (20-35 μM) [145] [146]. It is noteworthy that the concentration unit here is hemoglobin molecules per unit volume of tissue rather than hemoglobin molecules per unit volume of blood.

By replacing $[Hb_{total}]_B$ in Eq. (6.12) by $[Hb_{total}]_{B\_NIRS}$ in Eq. (6.13), it becomes Eq. (6.14).

$$\frac{[Hb_{total}]_T}{[Hb_{total}]_B} = 1 - \frac{Log\left(I_T / I_B\right)^{803}}{2 \cdot \varepsilon_{Hb}^{803} \cdot \gamma \cdot [Hb_{total}]_{B\_MRS} \cdot d \cdot DPF} \tag{6.14}$$

Even though the γ depends on the DPF value (γ = 0.3 with DPF = 2 and γ = 0.15 with DPF = 4) [141], the multiplication of γ and DPF becomes constant (γ *DPF = 0.6).

$$\frac{[Hb_{total}]_T}{[Hb_{total}]_B} = 1 - \frac{Log\left(I_T / I_B\right)^{803}}{1.2 \cdot \varepsilon_{Hb}^{803} \cdot [Hb_{total}]_{B\_MRS} \cdot d} \tag{6.15}$$

Therefore, by estimating both $[Hb_{total}]_B$ and the DPF value of the tumors along with the NIRS readings at 803 nm, I could quantify the percent changes in tumor blood volume after CA4P treatment, using Eq. (6.15).

6.2.6 Statistical Analysis

Statistical significance of $\Delta[HbO_2]$ and $\Delta[Hb_{total}]$ changes over the 2 hours after saline injection (control group) and CA4P treated group was assessed by using Student's t tests. Single factor ANOVA tests were first performed to reveal significant differences of fitted parameters (A1, A2, τ_1, τ_2) among different time courses, such as Pre-CA4P, 2h post, 24 h post, and 48 h post CA4P. Once the single factor ANOVA tests resulted in significant differences of the fitted parameters among different time courses, a Tukey test was further performed for each of the individual fitted parameters.

6.3 Results

6.3.1 Control group

A representative result from the control group measured by NIRS is shown in Fig.6.2. After 15 minutes of air breathing measurement as the baseline, the inhaled gas was switched from air to oxygen, causing a sharp increase in $\Delta[HbO_2]$ ($p < 0.0001$, 1~2 min. after gas switch) followed by a further gradual, but significant increase over the next 20 min ($P < 0.0001$). The readings in $\Delta[Hb_{total}]$ first dropped after switching gas from air to oxygen and then slowly recovered during the next 15 minutes of oxygen inhalation. After returning to air inhalation, $\Delta[HbO_2]$ decreased and $\Delta[Hb]$ increased, both reaching approximately their respective baseline levels.

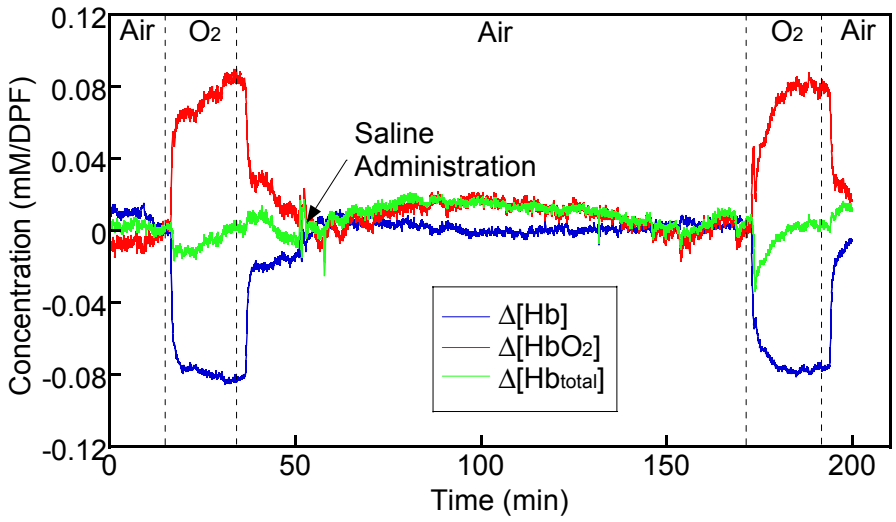

Fig. 6.2 Time course of tumor vascular $\Delta[HbO_2]$, $\Delta[Hb]$, and $\Delta[Hb_{total}]$ taken from a 13762NF breast tumor with the inhaled gas under the sequence of air-oxygen-air-oxygen-air. After the first oxygen intervention, saline was administered in the rat via i.p. injection. (Tumor volume: 4.08 cm^3)

Fifteen minutes after the air breathing, a saline solution was given by i.p. injection, and the tumor hemodynamics was continuously monitored for the next 2 hours.

The second oxygen intervention was given in order to compare tumor responses before and after saline injection, followed again by air inhalation, using the same procedure during the pre-saline period. As seen in Fig. 6.2, the tumor response to oxygen during the second oxygen intervention shows a trend of $\Delta[HbO_2]$ similar to that observed during the first oxygen intervention.

6.3.2 CA4P treated group

The same experimental procedure was applied to the CA4P treated group except that CA4P was administered in place of the saline. Fig. 6.3 shows a representative result from a CA4P treated rat. It is seen that the tumor response to the first oxygen intervention before CA4P treatment was very similar to that seen in the control group. After CA4P administration, unlike the data shown in the control group (Fig. 6.2), $\Delta[HbO_2]$ and $\Delta[Hb_{total}]$ both dropped significantly at about 40 seconds, while $\Delta[Hb]$ decreased slightly then slowly reached the baseline level. Both $\Delta[HbO_2]$ and $\Delta[Hb_{total}]$ became stabilized 20 minutes after CA4P injection and remained constant until the second oxygen intervention was given. The second oxygen intervention was applied 2 hours after CA4P administration, but both $\Delta[HbO_2]$ and $\Delta[Hb_{total}]$ showed little change compared to those during the first oxygen intervention. These results clearly show the effect of CA4P on tumor vasculature and also prove that NIRS has a great potential to

serve as a monitoring tool to detect the effectiveness of VDA's, including CA4P in cancer treatments.

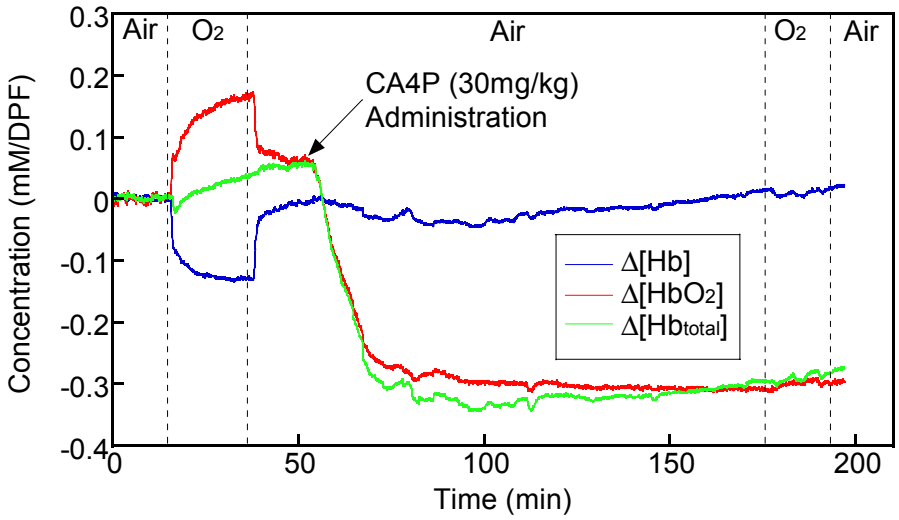

Fig. 6.3 Time course of tumor vascular $\Delta[HbO_2]$, $\Delta[Hb]$, and $\Delta[Hb_{total}]$ taken from another 13762NF breast tumor with the inhaled gas under the sequence of air-oxygen-air-oxygen-air. After the first oxygen intervention, CA4P was administered in the rat. (tumor volume: 0.9 cm^3)

As I have shown in Section 2.6 that selecting two appropriate wavelengths can give accuracy in $\Delta[HbO_2]$, $\Delta[Hb]$ and $\Delta[Hb_{total}]$ similar to the values obtained by using 6 wavelengths. Nonetheless, I have reprocessed Fig. 6.3 with the algorithm that uses 6 wavelengths, and shown the absolute differences of $\Delta[HbO_2]$, $\Delta[Hb]$ and $\Delta[Hb_{total}]$ in Fig. 6.4. It clearly shows that the differences are negligible (less than 5% of $\Delta[HbO_2]$, $\Delta[Hb]$, and $\Delta[Hb_{total}]$ values shown in Fig. 6.3) and thus two wavelengths algorithm was used throughout the rest of the study.

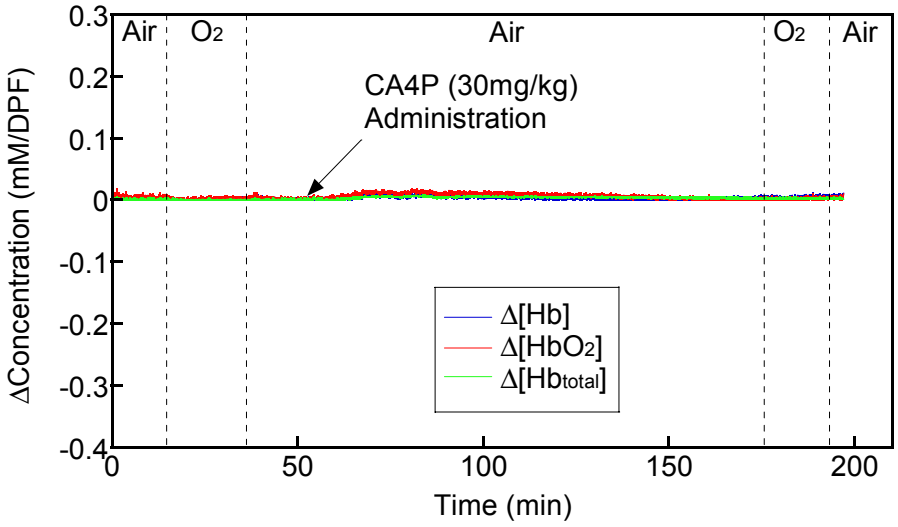

Fig. 6.4 The absolute differences in $\Delta[HbO_2]$, $\Delta[Hb]$, and $\Delta[Hb_{total}]$ between Fig. 6.3 (calculated by using 2 wavelengths algorithm) and the results from 6 wavelengths algorithm (not shown here).

6.3.3 Comparison of tumor responses between control and CA4P treated groups

Oxygen intervention was given again 1 day after either saline or CA4P administration to compare the tumor response with the responses observed before and 2 hours after CA4P injection. Figures 6.5(a) and 6.5(b) show the hemodynamic results of oxygen intervention 1 day after saline and CA4P administration, respectively, from the same tumors used to obtain the data in Figs. 6.2 and 6.3. Figure 6.5(a) demonstrates that the tumor responses to oxygen inhalation before and 1 day after saline injection are very similar, with a similar level of $\Delta[HbO_2]$ increase induced by the intervention. However, the increase in $\Delta[HbO_2]$ observed from the CA4P treated tumor shown in Fig. 6.5(b) is only about 15 percent of the maximum of $\Delta[HbO_2]$ during the first oxygen intervention. It is higher than the response monitored 2 hrs after the injection (see Fig. 6.3), but still much lower than the response before the CA4P administration. This implies that the

effect of CA4P in tumor vasculature is not completely vanished and still affecting the tumor blood vessels.

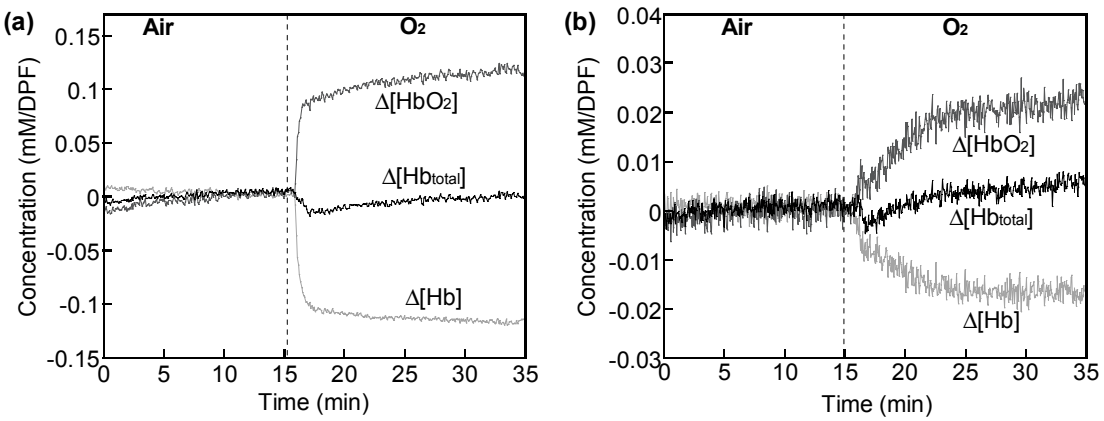

Fig. 6.5 Changes in $\Delta[HbO_2]$, $\Delta[Hb]$, and $\Delta[Hb_{total}]$ from breast tumors shown in Fig. 6.2 and 6.3 during respiratory challenges from air to oxygen at 1 day after saline (a) and CA4P (b) administration.

6.3.4 Changes in hemodynamics after CA4P treatment

To examine temporal changes of CA4P effects on tumor vasculature, I collected the tumor responses to oxygen intervention before and 2 hours, 24 hours, and 48 hours after CA4P administration. The data are plotted in Fig. 6.6. Figure 6.6(a) summarizes the results taken from the same tumor that was used for Figs. 6.3 and 6.5(b), and a set of repeated trends is observed from another tumor, as plotted in Fig. 6.6(b). These figures clearly show evolving changes of tumor vascular responses to oxygen intervention before and after CA4P administration. The bi-phasic feature of $\Delta[HbO_2]$ increase during oxygen intervention is very evidently shown at the pre-treatment stage in each of the two cases (Figs. 6.6(a) and 6.6(b)). However, it is hard to find the fast

component from the tumor response during oxygen inhalation 2 hours after CA4P administration. Interestingly, the initial fast increase of $\Delta[HbO_2]$ returns gradually through Day 1 and 2 after CA4P administration.

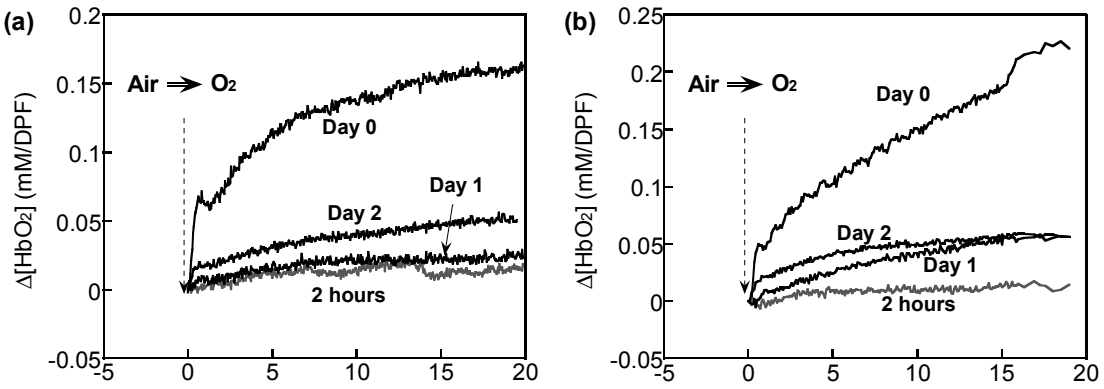

Fig. 6.6 Dynamic changes of $\Delta[HbO_2]$ from rat breast tumors during oxygen intervention before and after administration of CA4P.

To get more information about tumor physiology, I applied the bi-exponential model, as given in Eq. (3.2) or (4. 2), to the increase of $\Delta[HbO_2]$ during oxygen inhalation (Fig. 6.7). This set of figures shows the raw data (open circles) with the fitted curves (solid lines) for the increases of $\Delta[HbO_2]$ during oxygen intervention before, 2 hrs post, 24 hrs post and 48 hrs post CA4P administration. The bi-phasic behavior is clearly shown in Fig. 6.7(a), while it is greatly diminished in Figs. 6.7(b) and 6.7(c).

However, Fig. 6.7(d) taken 48 hours after CA4P administration shows a clear return of bi-phasic increase of $\Delta[HbO_2]$ during oxygen inhalation. This result again indicates that tumor vasculature (possibly in the well perfused region) initially lost its

function by CA4P treatment, but it recovers its function gradually 24 hrs and 48 hrs after CA4P administration.

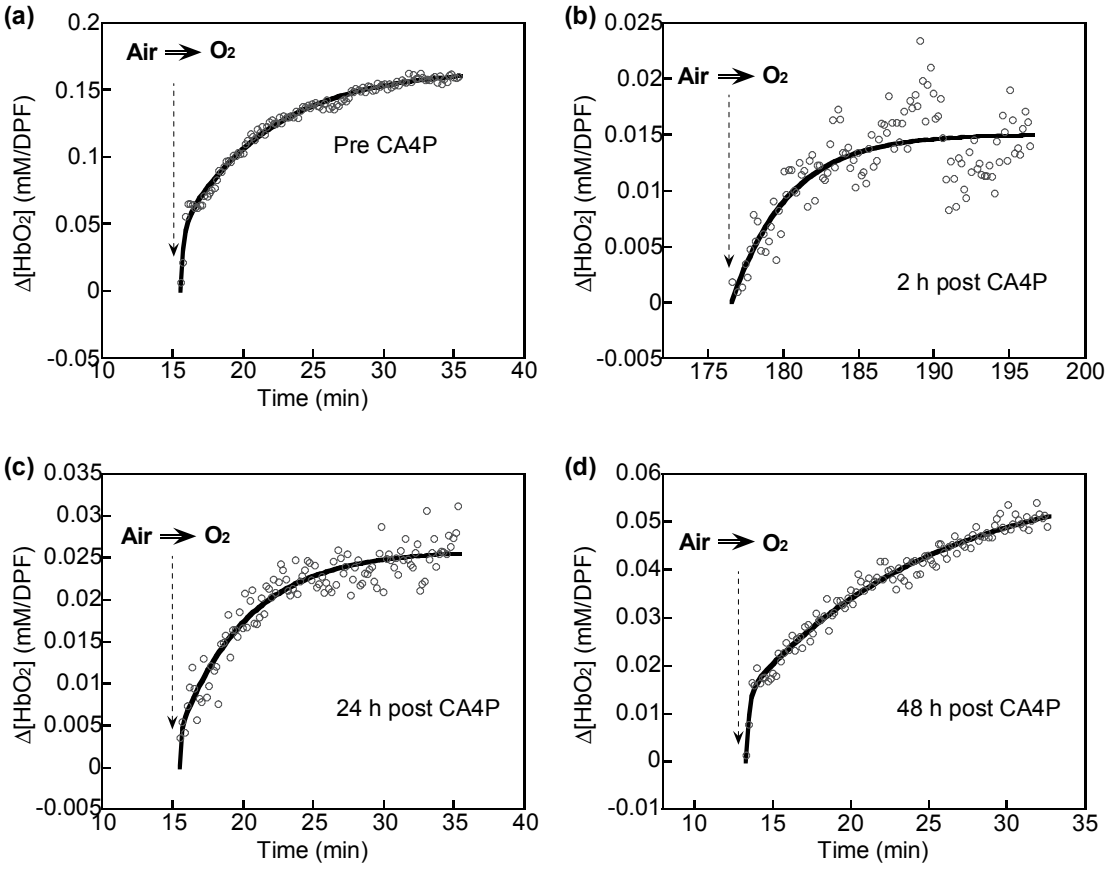

Fig. 6.7 Changes of $\Delta[HbO_2]$ during oxygen intervention before (a) and after (b, c, d) CA4P administration. Raw data were plotted with open circles, and fitted curves were shown as solid lines.

According to the bi-phasic model, namely, Eq. (3.2) or (4.2), four parameters, i.e., A_1, A_2, τ_1, and τ_2, can be fitted using the tumor hemodynamic measurements. These fitted parameters are utilized to interpret and reveal tumor vascular changes and physiological alternations induced by CA4P, as to be presented in the next four sub-

sections. Four summarized sets of the fitted parameters are to be graphically shown in Figs. 6.8, 6.11, 6.13, and 6.15, and I will compare them with published records for better understanding of my measurements. All the mean values were taken from 5 tumors and are shown as solid circles, and the error bars represent standard errors.

6.3.4.1 Changes in bi-phasic amplitudes of [HbO_2] after CA4P treatment

As the first set, Figs. 6.8(a) and 6.8(b) plot both fitted A_1 and A_2 values, which are dropped significantly 2 hrs post CA4P and show a slow recovery 24 and 48 hrs after CA4P treatment. Since A_1 and A_2 values represent the increased amount of [HbO_2] due to oxygen intervention in well perfused/periphery and poorly perfused/central regions of tumor, respectively, the decrease of A_1 and A_2 values represents the reduction of [HbO_2] increase in the two respective regions of the tumor during oxygen intervention. In other words, a drop in A_1 implies that the amount of [HbO_2] increase during oxygen intervention has been decreased in the well perfused region after CA4P treatment, while a decrease in [HbO_2] increase in the poorly perfused region during oxygen intervention is reflected by a drop of A_2 after CA4P treatment.

Even though both A_1 and A_2 values recovered by 24 hours post CA4P towards their original states prior to CA4P treatment, A_1 shows continuous recovery at 48 hours, while A_2 seems to reach a steady state. This result is consistent with a recent report by Zhao *et al.* using a dynamic contrast enhanced (DCE) MRI [131]. Figure 6.9 is a replot of Fig. 1(A) in their report, showing changes in Gd-DTPA signal enhancement before and after CA4P administration.

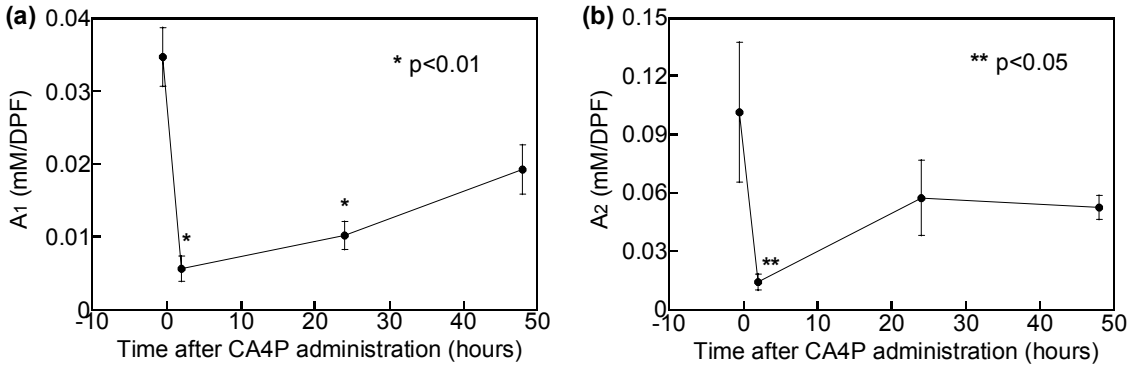

Fig. 6.8 Summary of two fitted parameters, A_1 (a) and A_2 (b), by using the bi-exponential model. Mean values from 5 tumors are shown by solid circles with standard errors. * represents significant difference with $P < 0.01$; ** represents significant difference with $P < 0.05$ in comparison with the corresponding parameters obtained before CA4P treatment.

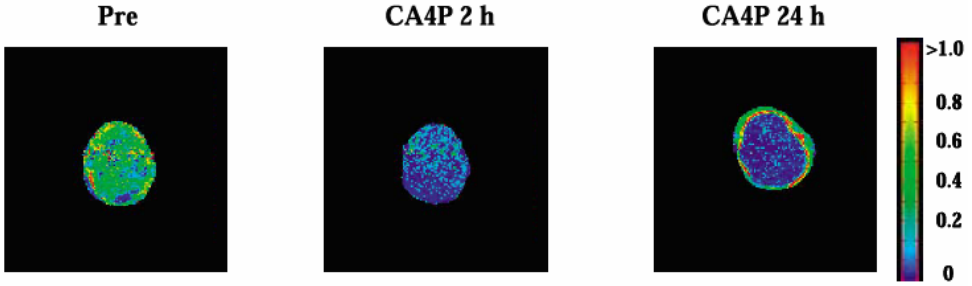

Fig. 6.9 Dynamic contrast-enhanced magnetic resonance imaging (DCE-MRI) performed before, 2 h, and 24 h after treatment with CA4P (30 mg/kg). (Reprinted from ref. [131]).

In that report, Zhao *et al.* showed changes in permeability/diffusivity in tumors before and after CA4P treatment by monitoring the signal enhancement after GD-DTPA administration. Figure 6.9 shows that the area of high signal enhancement (>0.5) at 24 hrs post CA4P is smaller than that at pre CA4P even though the amount of signal enhancement itself has fully recovered to its baseline level in the periphery. In contrast, the central region of the tumor did not show much recovery to the baseline level even

24 hrs after CA4P administration. Therefore, only small parts of the tumor periphery region (tumor rims) showed full recovery, while most of other parts of tumor, including the central region, did not show any noticeable improvement in signal enhancement. This finding is consistent with and supportive to my interpretation for Fig. 6.8: A_1 value basically represents a well-perfused region or the peripheral region of the tumor which shows high signal enhancement in Fig. 6.9. Therefore, small recovery of A_1 values at day 1 in Fig. 6.8(a) represents a partial recovery of high signal enhancement area in tumor periphery at CA4P 24 hours in Fig. 6.9.

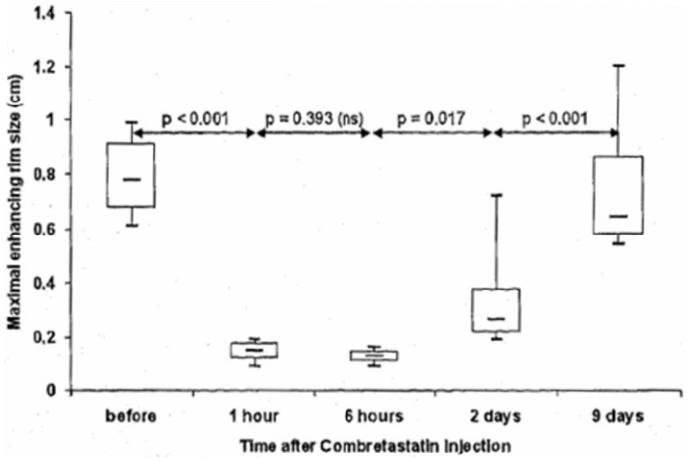

Fig. 6.10 The maximal enhancing rim sizes versus time after CA4P, measured using T1-weighted MR images. (Reprinted from ref. [147])

Figure 6.10 is taken from Fig. 5 in Theony *et al*'s report [147] and shows the maximal signal enhancing tumor rim sizes with a large dose of gadodiamide administration before and after CA4P administration. This figure also strongly supports the findings in A1 changes (Fig. 6.8(a)) since A1 represents the well perfused/periphery

region of tumors and should correspond directly with the tumor rim. It is unambiguous to observe the close similarity of the profiles between Figs. 6.8(a) and 6.10. Overall, Figs. 6.9 and 6.10 strongly strengthen my interpretation that A_1 component fitted from the bi-phasic increase of tumor hemodynamics during oxygen inhalation is highly associated with the volume of well perfused/periphery region of tumors.

6.3.4.2 Changes in bi-phasic time constants of $\Delta[HbO_2]$ after CA4P treatment

Besides A_1 and A_2, both τ_1 and τ_2 are also fitted so as to study the dynamic features of bi-phasic changes in $[HbO_2]$ induced by CA4P injection. Both $1/\tau_1$ and $1/\tau_2$ are plotted in Figs. 6.11(a) and 6.11(b), showing a decrease at 2 hrs after CA4P administration and then return to the same level as that at pre-CA4P administration. Since the relationship between $1/\tau$ and blood flow velocity is nearly linear [138], a decrease of $1/\tau$ implies a decrease in tumor blood flow velocity. Fig. 6.11(a) shows a significant decrease of tumor blood flow velocity in the well perfused region within the tumors 2 hours post CA4P administration, while the decrease of tumor blood flow velocity in the poorly perfused region 2 hours post CA4P does not show a statistically significant difference from that pre CA4P treatment. This observation is understood since the central region of the tumors has a low blood flow velocity even before CA4P treatment, and thus it may not show a significant effect of CA4P on the blood flow velocity in the central region of the tumors.

On inspection of both Figs. 6.8(a) and 6.11(a), A_1 value at 24 hrs post CA4P is much smaller than that before CA4P injection, but at the same time $1/\tau_1$ value already

returns to its baseline level. Since $1/\tau_1$ values are related to the blood flow velocity in the well perfused/periphery region, Fig. 6.10(a) implies that within 24 hours, tumor blood flow velocity at the periphery region of the tumors has been already recovered from CA4P treatment. The recovered periphery volume, however, is still limited to a small fraction of the original periphery volume prior to the treatment.

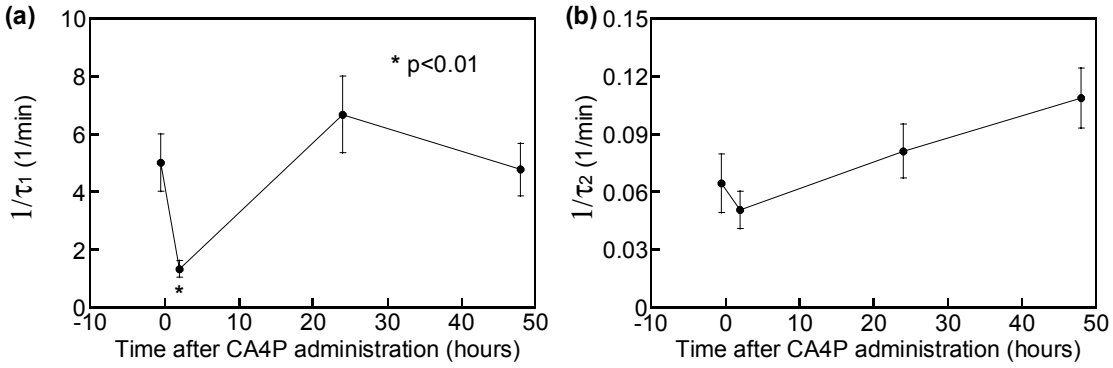

Fig. 6.11 Summary of two fitted parameters, $1/\tau_1$ (a) and $1/\tau_2$ (b), by using the bi-exponential model. Mean values are shown as a solid circles and the error bars represent the standard error. * represents a significant difference with $P < 0.01$ in comparison with $1/\tau_1$ and $1/\tau_2$ before CA4P treatment.

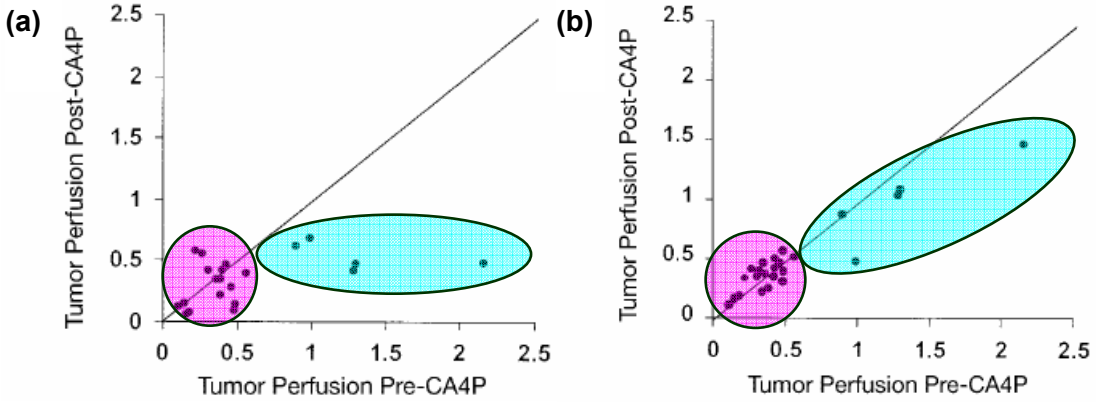

Fig. 6.12 The relationship between pre- and post- combretastatin A4 phosphate (CA4P) administration measurements of tumor perfusion in 13 patients with advanced solid tumors. (a) 30 minutes after drug administration; (b) 24 hours after drug administration. (Reprinted from ref. [133])

Figure 6.12 is reprinted from Figure 3 of Anderson *et al.* [133], supporting the interpretation given above. From Fig. 6.12, the tumor site that already has a low perfusion (pink shadow) is hardly affected by CA4P administration, while the site that has a high perfusion (blue shadow) shows significant decrease in perfusion 30 min after CA4P treatment (Fig. 6.12(a)), but shows great recovery 24 hours after CA4P administration (Fig. 6.12(b)). These results are in excellent agreement with the data shown in Fig. 6.11.

6.3.4.3 Changes in bi-phasic perfusion rates of tumors after CA4P treatment

According to Liu *et al*'s mathematical model [31], the perfusion rates in two different regions within the tumors are represented by f_1 and f_2 values. ($f = A/\tau$) Both f_1 and f_2 values show significant decreases 2 hours after CA4P administration with respect to the baseline (Figs. 6.13), followed by slow recovery to return to the baseline 24 hours and 48 hours after drug injection.

Maxwell *et al.* showed that the therapeutic effect of CA4P on tumor blood perfusion is dependent of dosage of CA4P [148]. When tumor blood perfusion was 0.35 ml/g/min prior to CA4P treatment, the perfusion was reduced to 0.04 ml/g/min (11% of its baseline) 6 hours after 10mg/kg CA4P injection, and for 100 mg/kg dose of CA4P to less than 0.01 ml/g/min (3% of its baseline) [148]. The percent decrease in perfusion rate in their report is close to the relative decreases in f_1 and f_2 values, as shown in Fig. 6.13(a) and 6.13(b), respectively. It can be also seen that f_1 is nearly 20 times higher

than the value of f_2, representing the significant difference in tumor perfusion between periphery and central region of the tumor.

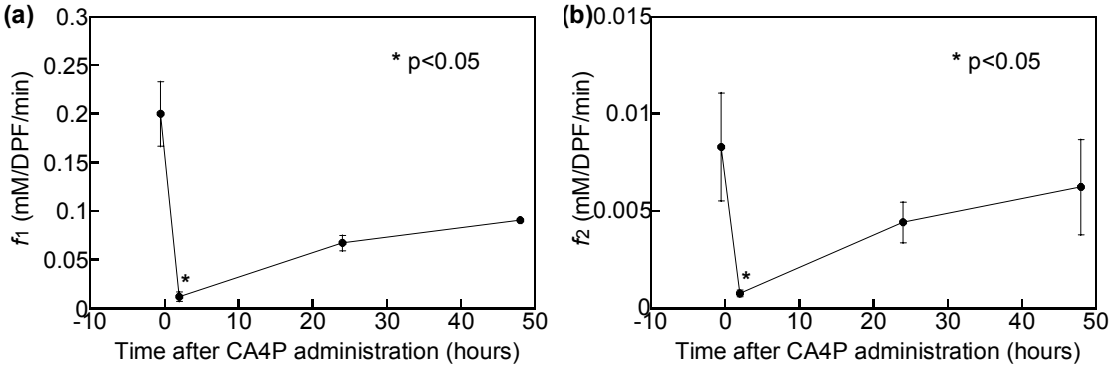

Fig. 6.13 Summary of two fitted parameters, f_1 (a) and f_2 (b), by using the bi-exponential model. Mean values from 5 rat tumors are shown as solid circles and the error bars represent the standard error. * represents a significant difference with $P < 0.05$ in comparison with the initial values of f_1 and f_2 before CA4P treatment.

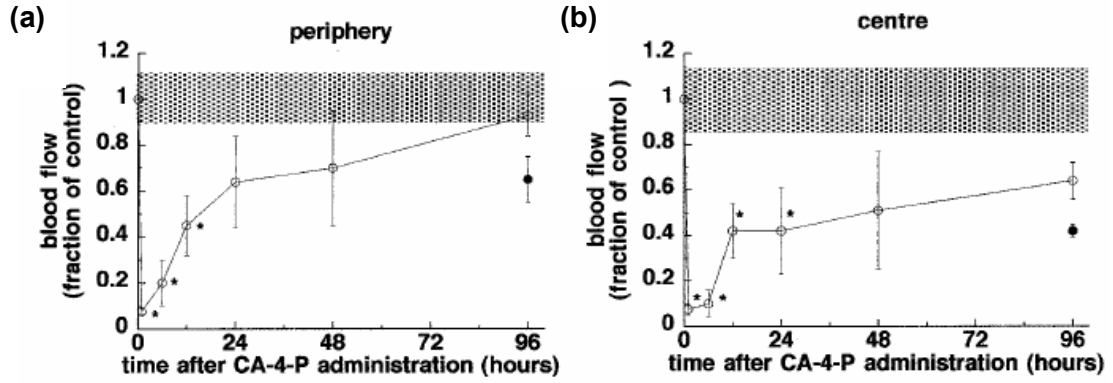

Fig. 6.14 The effect of 10 mg/kg CA4P on blood flow to peripheral (a) and central (b) regions of the tumor. (Reprinted from ref. [126])

Figure 6.14 is a replot from Fig. 5 published by Prise *et al.* [126], and it shows the blood flow/perfusion changes in periphery and central regions of the tumors after

CA4P administration. Both the periphery and central regions are showing recovery of blood flow 24 hours after CA4P administration, but the central tumor region tends to have a slower recovery rate than that in the periphery region of the tumors. As compared to this, Figs. 6.12(a) and 6.12(b) do not show clear differences in perfusion recovery rate after CA4P administration. However, Fig. 6.12(b) shows a possible delayed recovery at 48 hours after drug treatment since it has a higher standard error. In addition, the dosage of CA4P used in Fig. 6.13 was 10 mg/kg, much lower than the dosage used in my study (30 mg/kg). Prise *et al.* did show in their report that the perfusion recovery after CA4P administration can be delayed with a high dose of CA4P administration. (Fig. 3 in ref [126]).

Moreover, Prise *et al.* [126] proposed that the central region of tumor already has a very poor perfusion, and thus same percent decrease in perfusion in the central region as that in the periphery region of tumor (see Fig. 6.13(a) and 6.13(b)) will have a more damaging effect on the central region of tumor, leading to necrosis development in the central tumor region. The data shown in Fig. 6.13 are consistent with this proposed tumor-killing mechanism and can be used to predict or reveal changes/decreases in tumor perfusion within both the central and periphery regions of tumor.

6.3.4.4 Changes in A_1/A_2, τ_1/τ_2, and f_1/f_2 after CA4P treatment

Changes in ratios of A_1/A_2, τ_1/τ_2, and f_1/f_2 after CA4P injection are shown in Fig. 6.15. The ratio of A_1/A_2, as plotted in Fig. 6.15(a), represents how much of $\Delta[HbO_2]$

increase during oxygen intervention is from the well perfused region compared to that from the poorly perfused region within the tumors. Since the ratios of A_1/A_2 at different times after CA4P injection do not have significant difference in comparison with the baseline reading, I do not draw much conclusion from this plot.

Changes in ratio of τ_1 and τ_2 are plotted in Fig. 6.15(b), and a significant increase of τ_1/τ_2 was observed at 2 hrs post CA4P treatment. Since both τ_1 and τ_2 values were increased at 2 hrs post treatment, the increase of τ_1/τ_2 must be from a significant increase of τ_1, or a decrease of $1/\tau_1$, as shown in Fig. 6.11(a). Again, τ values are inversely proportional to blood flow velocity, this increase of τ_1/τ_2 represents that the decrease of blood flow velocity in periphery region is significantly greater than that in central region of the tumors. The ratio of τ_1/τ_2 returned to its baseline level 24 hours after CA4P treatment, representing the recovery of tumor blood flow velocity in both periphery and central region of the tumors.

Figure 6.15(c) shows the changes of f_1/f_2 after CA4P treatment. Since this f_1/f_2 ratio is obtained by dividing A_1/A_2 by τ_1/τ_2 [31], the decrease in f_1/f_2 2 hours after drug treatment comes from more significant increase in τ_1/τ_2 than the decrease of A_1/A_2 as shown in Fig. 6.15(a) and 6.15(b). Both Figs. 6.13(a) and 6.13(b) show the decrease of f_1 and f_2 at 2 hours post CA4P treatment, indicating that the decrease of f_1/f_2 results more from a faster decrease rate in f_1 than the decrease rate in f_2.

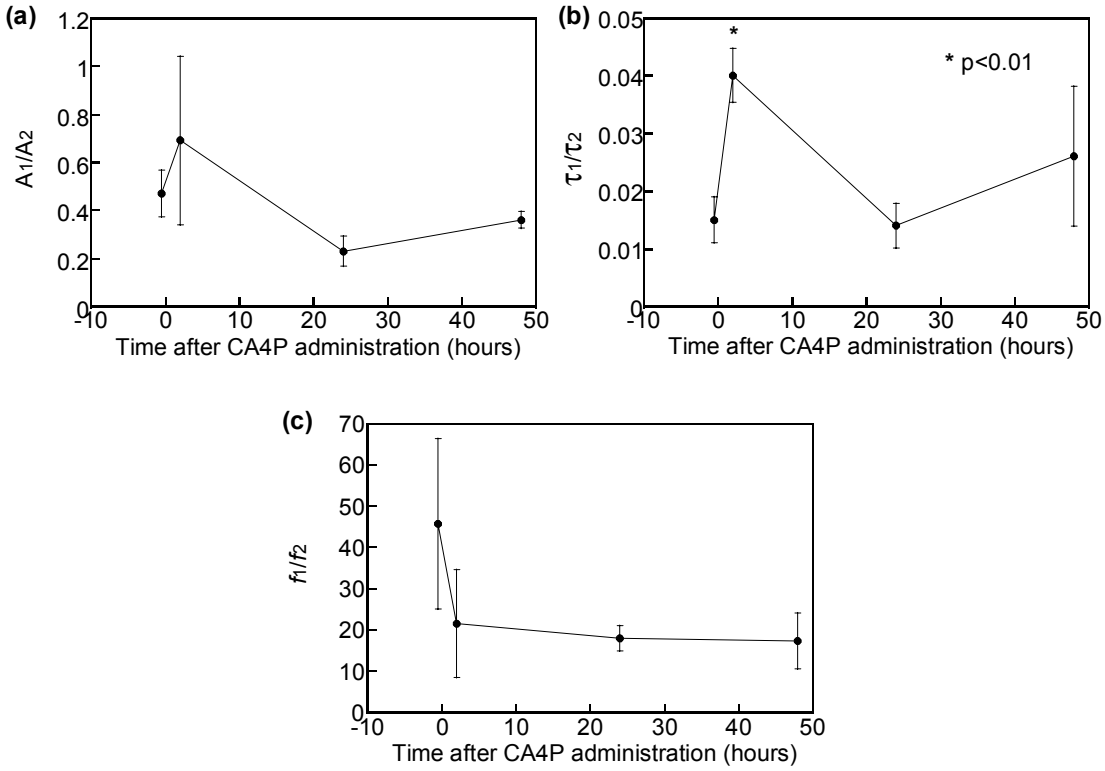

Fig. 6.15 Summary of the fitted parameters: A_1/A_2 (a), τ_1/τ_2 (b), and f_1/f_2 (c), by using a bi-exponential model. Mean values are shown as solid circles and the error bars represent the standard error. *: Significant difference ($P < 0.01$) in comparison with the baseline readings before CA4P treatment.

In other words, CA4P treatment affected the perfusion in the well perfused/periphery region more significantly than that in the central region of the tumors. Both f_1 and f_2 show recoveries at 2 hours post CA4P treatment, making the f_1/f_2 ratio maintained constant with respect to the ratio 2 hours after CA4P administration.

6.3.5 Changes in blood volume and [HbO_2] 2 hours after CA4P administration

Percent changes in tumor blood volume after CA4P treatment were also estimated by using Eq. (6.15). Values of tumor blood volume decreased immediately

within a minute after CA4P administration and showed 45 ± 15% reduction from the baseline blood volume 2 hrs after CA4P administration. Anderson *et al.* have applied ^{15}O-labeled carbon monoxide ($C^{15}O$) positron emission tomography to monitor the changes in tumor blood volume after CA4P treatment from the patients with advanced solid tumors and reported a maximum of 50% reduction of blood volume from the baseline level (mean=15%), depending on the CA4P dose 30 min after CA4P administration [133].

Mean values of decreased blood volume and decreased $\Delta[HbO_2]$ after CA4P administration are plotted in Figs. 6.16(a) and 6.16(b), respectively. To have a quantitative estimation of how fast both blood volume and $\Delta[HbO_2]$ decrease, both Fig. 6.16(a) and 6.16(b) were fitted with exponential decay functions. It turns out that there is no significant difference in time constant between blood volume decrease (12.5 ± 3.3 min) and $\Delta[HbO_2]$ decrease (11.0 ± 4.0 min) ($P > 0.5$).

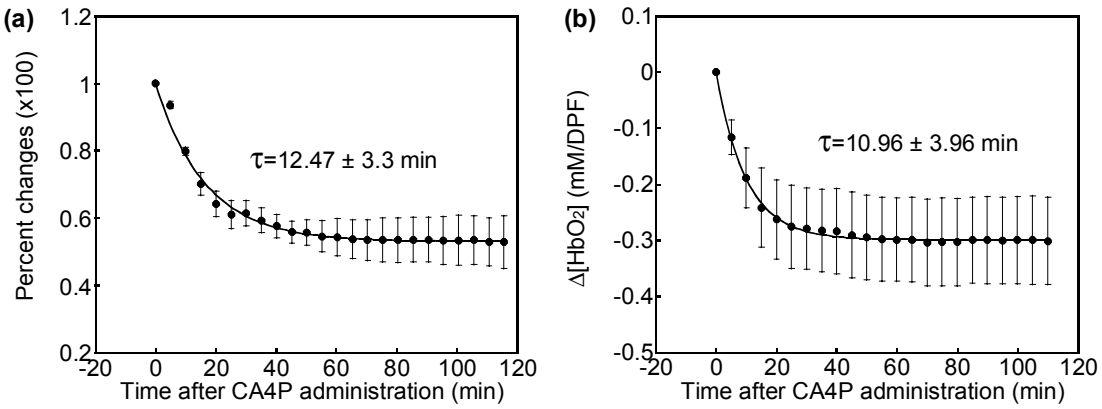

Fig. 6.16 The averaged value of percent changes in blood volume (a) and $\Delta[HbO_2]$ (b) after CA4P administrations. Mean values are shown as solid circles, and the error bars represent the standard error.

Tozer *et al.* [125] have measured the changes in red blood cell velocity in tumor venules by monitoring red blood cells under fluorescence microscopy. They showed that at 1 hour post CA4P, the red blood cell velocity decreased to nearly 10% of the original values prior to CA4P administration. I have fitted the same exponential decay function with their data so as to obtain the time constants for comparison (Fig. 6.17(a)). The percent changes of nonfunctioning vessel number with respect to the number before CA4P treatment [125] are also replotted in Fig. 6.17(b) with a fitted exponential curve. The time constants for the decrease in red blood cell velocity and the increase in nonfunctioning vessel numbers were 13.7 ± 1.2 min and 13.8 ± 3.4 min, respectively. These two time constants are surprisingly close to each other and to those values I obtained from the decrease in blood volume and $\Delta[HbO_2]$ after CA4P administration.

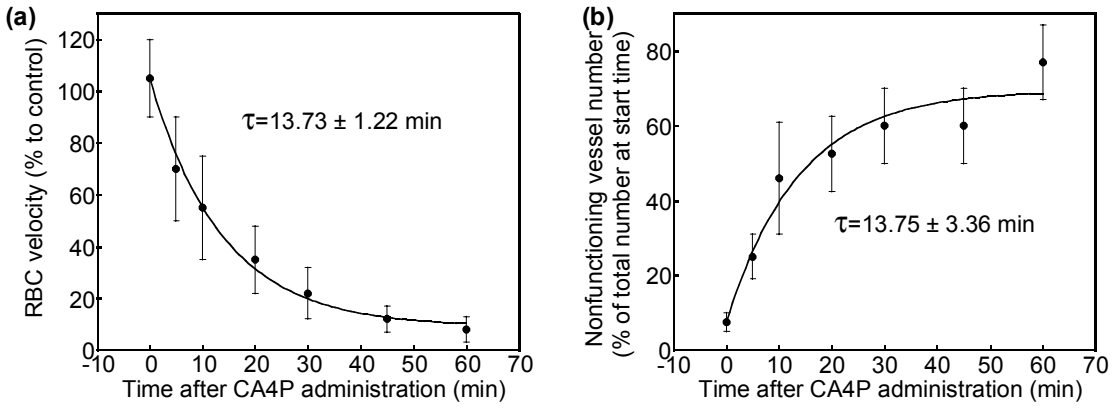

Fig. 6.17 Relative changes of red blood cell velocity (a) and nonfunctioning vessel number (b) after CA4P administration. Solid circles are the mean values, and standard error is shown as error bars. (Replotted from ref. [125]) The solid curves are obtained by fitting an exponential function to the respective data.

This excellent agreement between my data and Tozer *et al*'s implies that a decrease of blood volume after CA4P administration is mainly due to a decrease in blood flow velocity and an increase in nonfunctioning blood vessels.

To statistically compare the tumor response to oxygen intervention between saline (as control) and CA4P administration, I normalized the changes of maximum $\Delta[HbO_2]$ increase ($\Delta[HbO_2]_{max}$) during oxygen intervention after saline/CA4P administration to the changes before injections. The mean and standard deviation of the normalized $\Delta[HbO_2]_{max}$ from the tumors (n=5) are plotted in Fig. 6.18(a). It is clear that there is no significant change observed among the control group ($p>0.5$) at Day 0 and Day 1, while the treated group with CA4P shows significant changes from pre-CA4P condition to 2 hrs and to 1 day after CA4P injection ($p<0.05$). This may be caused by the reduction of functioning blood vessels in tumors after CA4P treatment since an increase in non functioning vessels (disappeared or no blood flow) will give rise to a decrease in $\Delta[HbO_2]$ increase in the tumors when hyperoxic gas is introduced. Tozer *et al.* [125] showed that the number of non-functioning vessels 1 hour after CA4P treatment has increased to nearly 80% of that prior to CA4P administration (Fig. 6.17(b)). This 80% increase in the number of non-functioning vessels is very close to the percentage of decrease in $\Delta[HbO_2]_{max}$, i.e., 2 hrs after drug injection $\Delta[HbO_2]_{max}$ decreases to ~14% of the control value, as viewed by the two cases labeled with "d" and "e" in Fig. 6.18(a).

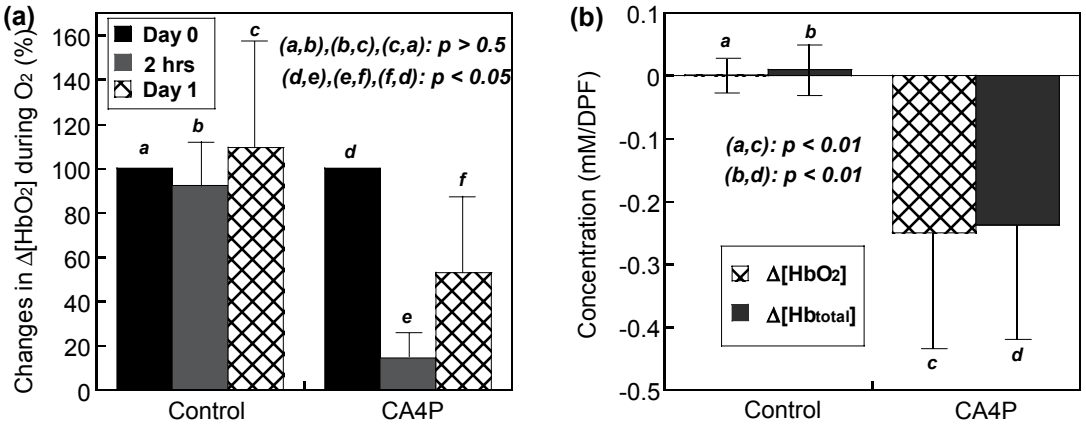

Fig. 6.18. (a) Percentage of changes in $\Delta[HbO_2]$ from rat breast tumors during oxygen intervention before and after administration of saline and CA4P. (b) Changes in $\Delta[HbO_2]$ and $\Delta[Hb_{total}]$ from rat breast tumors during 2 hours after administration of saline and CA4P.

I also plotted the mean and standard deviation of $\Delta[HbO_2]$ and $\Delta[Hb_{total}]$ from the values at 2 hours after saline and CA4P administration, as given in Fig. 6.18(b). This figure shows that saline administration did not cause any significant change in $\Delta[HbO_2]$ or $\Delta[Hb_{total}]$ during 2 hours after its administration, while $\Delta[HbO_2]$ and $\Delta[Hb_{total}]$ from CA4P group showed significant decrease during 2 hours after CA4P administration.

6.4 Discussion and conclusion

The effects of CA4P on tumor hemodynamics have been studied intensively in this chapter by using non-invasive NIRS. It was observed that both tumor blood oxygenation and blood volume were significantly reduced from baseline values right after CA4P administration, while the control group did not show any significant change

in either [HbO_2] or [Hb_{total}]. Another oxygen intervention was given 2 hours after CA4P administration, but little response of tumor Δ[HbO_2] was observed, indicating that tumor vasculature lost its function. The respiratory challenge was applied again 24 hours after CA4P administration, and the results showed that tumor vasculature slowly recovered function. The recovery process became clearer 48 hours after CA4P administration. The results from this study strongly support that NIRS can be a great tool to non-invasively monitor the effects of vascular disrupting/modifying agents on tumors.

NIRS has served as a non-invasive monitoring tool in various areas of study as mentioned in the introduction. However, only a few studies have reported applications of the optical method to monitor cancer therapeutic effects. Jakubowski *et al.* [149] reported that significant reductions in water and [Hb_{total}] were observed 5 days after neoadjuvant chemotherapy by using diffuse optical spectroscopy. Zhu *et al.* [143] showed that [Hb_{total}] dropped significantly after neoadjuvant chemotherapy by utilizing an optical tomography with ultrasound localization. However, all of their results came from the measurements during a static state. In my study, the dynamic change of [HbO_2] during oxygen intervention was used as a signature to monitor therapeutic effects from cancer treatments without measuring absolute values of [HbO_2], [Hb], and [Hb_{total}]. The methodology in data processing and analysis on hemodynamic changes in [HbO_2] and [Hb_{total}], developed in this chapter, is novel and provides non-invasive observation on evolution and alternation of tumor vasculature as well as tumor perfusion under therapeutic treatment. Combination of this newly developed

methodology with NIR imaging will enhance greatly the power of NIRS imaging as a useful and possibly clinical means to diagnose cancer and to monitor cancer therapeutic treatements. As one type of VDA, CA4P depolymerizes the microtubules in the endothelial cells, resulting in changes of their shapes from flat to round and eventually causing the blood flow to stop within the tumor vasculature. CA4P also increases the permeability of plasma proteins, which causes increases in blood viscosity and interstitial fluid pressure. While blood flow was not measured directly from the NIRS measurement, diffuse correlation spectroscopy/imaging has been developed and used to measure relative changes in blood flow from various tissues by Yodh's group [150] [151] [152]. Instead, I have applied oxygen interventions to the tumor-bearing rats and utilized previously developed bi-exponential mathematical model to investigate the changes in tumor physiology after CA4P treatment. Such a dynamic approach is novel and unique, particularly it permits investigation and quantification of tumor blood perfusion and vascular evolution induced by drug treatments.

Kragh *et al.* have reported the effects of a few VMA's on changes in tumor blood flow and tumor blood volume measured by a laser Doppler flowmeter and a single wavelength reflectance NIRS [135]. The blood volume reduction in tumors 1 hr after CA4P treatment was shown to be minimal (mean=2%) compared to other vascular targeting agents such as flavone acetic acid (FAA), 5,6-dimethylxanthenone-4- acetic acid (DMXAA) and hydralazine (HDZ). Meanwhile, Anderson *et al.* have documented that blood volume changes in tumors 30 min after CA4P administration decreased by a mean of 11% (with doses ranging from 5 to 114 mg/m^2) to 15% (with doses from 52 to

114 mg/m^2) [133]. It has been shown that different tumor lines have various responses to CA4P. The tumor line that Kragh *et al.* used was C3H mouse mammary carcinoma, and the data shown by Anderson *et al.* were from 34 patients who had various types of cancer. Parkins *et al.* [153] have shown that there is a significant difference of tumor response to CA4P treatment depending on tumor type. A syngeneic breast adenocarcinoma CaNT tumor showed more than 50% reduction in vascular volume from the baseline with the dose of 50 mg/kg of CA4P, while the vascular volume of a sarcoma SaS tumor after CA4P treatment (500 mg/kg) showed a 66% decrease from its baseline. Comparison between the dosages used in these two cases suggests that CaNT tumor is approximately ten fold more sensitive to CA4P than SaS tumor. SW1222 is another tumor type and was studied by Pedley *et al.* [118], the results showed a 75% decrease of its vascular volume 3 hours after CA4P treatment (200 mg/kg) in comparison to the control vascular volume. There is no report on changes in blood volume after CA4P treatment from rat mammary carcinoma 13762NF, which has been used in my study. However, it is expected to see significant changes in blood volume from this tumor line after CA4P treatment since this kind of tumor showed a significant decrease in pO_2 after CA4P treatment [131]. Moreover, it has been found that the effect of different types of VDA's varies among tumor lines. HT29 tumor cells did show poor response to CA4P [154] [155], but great response to DMXAA. Given a great need or demand to test responses of various types of VDA's, NIRS can be a great monitoring tool to determine non-invasively the type of VDA's to be used for particular tumors, leading to optimal treatments and better treatment efficacy.

It is not well known why the peripheral region of tumor shows faster recovery from CA4P than the central region of tumor, which is normally poorly perfused. However, it was proposed that the periphery region of tumor can get supply of blood by recruiting the blood vessels in normal tissues surrounding the tumor, and also the blood flow at the periphery region is less affected than at the central region of tumor [120]. Then why is A_1 value at 24 hrs post CA4P treatment still much smaller than the control value at pre-CA4P? The answer to this question can be found from a recent study by Zhao *et al.* using the same type of tumors [131]. Their data showed a significant decrease of signal enhancement at 2 hrs post CA4P treatment and a full recovery of signal enhancement from the periphery region at 24 hours post CA4P treatment, while the signal enhancement from the central region remained constant from 2 hrs to 24 hrs after CA4P administration (Fig. 6.9). However, it can be seen from their data that the recovery of signal enhancement at the tumor periphery region is limited to a small fraction even though the amount of signal enhancement is nearly as high as that from the pretreatment. Therefore, the amplitude of A_1, detected by NIRS, does not show fully recovery to its baseline at day 1 since it represents the tumor volume from the well-perfused (i.e. periphery) region. But τ_1 value, representing the tumor blood flow velocity, clearly shows its recovery to the baseline, which is in good agreement with the signal enhancement data given by Zhao *et al.* [131].

As a conclusion for this chapter, a non-invasive, broadband, CCD-based NIRS system was utilized to monitor the effect of CA4P on tumor vasculature. I have developed and performed novel data analysis on dynamic signals of $\Delta[HbO_2]$ and

$\Delta[Hb_{total}]$ after CA4P administration. The new methodology for data analysis is a key development of my study in this chapter and allows me to prove that CA4P has significant effects on tumor vasculature and perfusion, based on the non-invasive NIRS results taken. Specifically, tumor vasculature showed poor response to oxygen intervention 2 hrs post CA4P administration, but a slow recovery of its function appeared 1 day after CA4P administration by showing a returned response to oxygen intervention. Two days after CA4P treatment, tumor vasculature showed even more response to oxygen intervention. By fitting the bi-phasic mathematical model with the increase of $\Delta[HbO_2]$ during oxygen intervention, the effects of CA4P on tumor physiology could be investigated, including volumes of periphery/central region of the tumor, tumor blood flow velocities, and tumor perfusion rates. My interpretations to associate the fitted hemodynamic parameters to tumor vasculature and perfusion are strongly supported by a variety of published literatures. This chapter indeed provides solid evidence that NIRS can be used as an effective and useful tool to monitor tumor hemodynamic responses to vascular disrupting agents including CA4P. Furthermore, NIRS can be used to monitor the effects of other cancer therapies, such as radiotherapy, photodynamic therapy, and conventional chemotherapy. Since tumor vasculature will change in its function and structure during and after cancer therapies, NIRS is surely able to detect and monitor those changes non-invasively, continuously, and in real-time if needed.

For future studies, NIRS imaging will be applied to assess the effects from VDT's since it will permit to obtain spatially distributed effects of VDT's on tumor

vasculature. Combination of NIRS imaging with oxygen intervention in animal studies could be beneficial to drug-developing companies to test their newly developed drugs and to clinicians to design optimal treatment plans for cancer patients as well as to determine the effectiveness of therapies so that over- or under- treatment could be avoided.

*This chapter is being prepared for a manuscript and will be submitted to Proceedings of the National Academy of Sciences of the United States of America.

Jae G. Kim, Dawen Zhao, Ralph P. Mason, and Hanli Liu, "Acute Effects of Combretastatin on Breast Tumor Hemodyamics Monitored by Near-Infrared Spectroscopy," *Proc. Natl. Acad. Sci. USA*, ready to submit.

CHAPTER 7

NON-UNIFORM TUMOR VASCULAR OXYGEN DYNAMICS MONITORED BY MULTI-CHANNEL NEAR INFRARED SPECTROSCOPY

7.1 Introduction

Solid tumors develop regions of hypoxia during their growth due to an imbalance between the rate of tumor cell proliferation and the proliferation and branching of the blood vessels [79] [80] [81]. Tumor hypoxia is responsible for the failure of radiotherapy [72], some forms of chemotherapy [12], and photodynamic therapy [11]. In addition, a number of clinical trials have found that patient survival measured either as tumor regression or as local control depends largely on tumor oxygenation [73]. Tumor hypoxia can occur through diffusion-limited or chronic hypoxia and perfusion-limited or acute hypoxia [156]. Therefore, measurement of distribution of tumor perfusion rate could be important for tumor treatment planning and assessing methods designed to modulate tumor oxygenation.

Solid tumors are known to exhibit heterogeneous blood flow distribution [57] [58]. There are many methods used to measure tumor perfusion heterogeneity, such as Doppler ultrasound [59], dynamic contrast MRI [157], and the use of tumors grown in windowed chambers [62]. Intensive studies from Mason's group using ^{19}F MR pO_2 mapping have revealed intratumoral heterogeneity of pO_2 distribution and also

heterogeneous response to hyperoxic gas breathing [16] [20] [63]. Their findings of severe pO_2 heterogeneity in tumors can indirectly indicate the heterogeneous distribution of blood flow, since tissue pO_2 level is decided by a balance between the supply of oxygen from blood vessels and oxygen consumption by tissue cells [64]. Unlike the ^{19}F MR pO_2 mapping technique, near-infrared spectroscopy (NIRS) techniques cannot measure pO_2 in tissue but can measure *in vivo* hemoglobin oxygenation and also concentration.

In a previous study by Liu *et al*, they have established a mathematical model of tumor oxygen dynamics during hyperoxic gas, such as carbogen (95% CO_2 and 5% O_2) or oxygen inhalation [31]. For their model, they formed a hypothesis that changes in oxygenated hemoglobin concentration ($\Delta[HbO_2]$) are composed of signals from a well-perfused and poorly perfused region to explain why there is a bi-phasic feature shown in $\Delta[HbO_2]$ data. This model has been supported by my laboratory and computational studies, as given in Chapters 3 and 4. It is also extensively utilized to analyze the NIRS hemodynamic measurements of rat breast tumors in response to hyperoxic gas intervention and to a vascular disrupting agent (i.e., CA4P), as given in Chapters 5 and 6. In this chapter, I will demonstrate that a multi-channel NIRS system is able to detect inter and intratumoral vascular heterogeneity. Each detector's signal will come from a different region of the tumor, and thus it will reveal differences of the fitting parameters among multi-detectors.

The goals of the study in this chapter are 1) to measure $\Delta[HbO_2]$ in tumor vasculature during carbogen/oxygen inhalation using a multi channel NIRS system, and

2) to reveal inter- and intra- tumoral vascular heterogeneity by fitting the proved mathematical model with the measured $\Delta[HbO_2]$ data.

7.2 Materials and Methods

7.2.1 Tumor Model and Measurement

For this study, rat mammary adenocarcinomas 13762NF grown in the hind limb of adult female Fisher 344 rats (~200 g) were used. Once these tumors reached approximately 2-3 cm in diameter, the rats were anesthetized with 0.2 ml ketamine hydrochloride (100 mg/ml; Aveco, Fort Dodge, IA) and maintained under general gaseous anesthesia using a small animal anesthesia unit with air (1 dm^3/min) and 1.3% isoflurane (Ohmeda PPD Inc., Fort Dodge, IA) through a mask placed over the mouth and nose. After anesthesia, the rat was placed on a warm blanket to maintain body temperature, which was monitored with a rectally-inserted thermal probe connected to a digital thermometer (Digi-Sense, model 91100-50, Cole-Parmer Instrument Company, Vernon Hills, IL). Tumors were shaved to improve optical contact for transmitting light, and a light source and three or four detectors were attached to the tumor using posts and swivel post clamps.

For three channel NIRS measurements, one of the three detectors (detector #3) was placed opposite the light source in order to detect light in a transmission mode, and the other two detectors (detectors #1 and #2) were set in the semi-reflectance mode, as shown in Fig. 7.1(b). I expected that the detector placed in the transmittance mode (detector #3) would collect signals from both the central and peripheral regions of

tumors, while the detector placed closest to the light source (detector #1) would collect most signals from the tumor periphery. Figure 7.1(c) shows the top view of displacement of four-channel NIRS detectors. In this setup, all detectors would collect similar amount of signals from the tumor, and the collected light would interrogate both the central and peripheral region of tumors. Figure 7.1 shows a schematic diagram for the animal experiments using the multi-channel NIRS system.

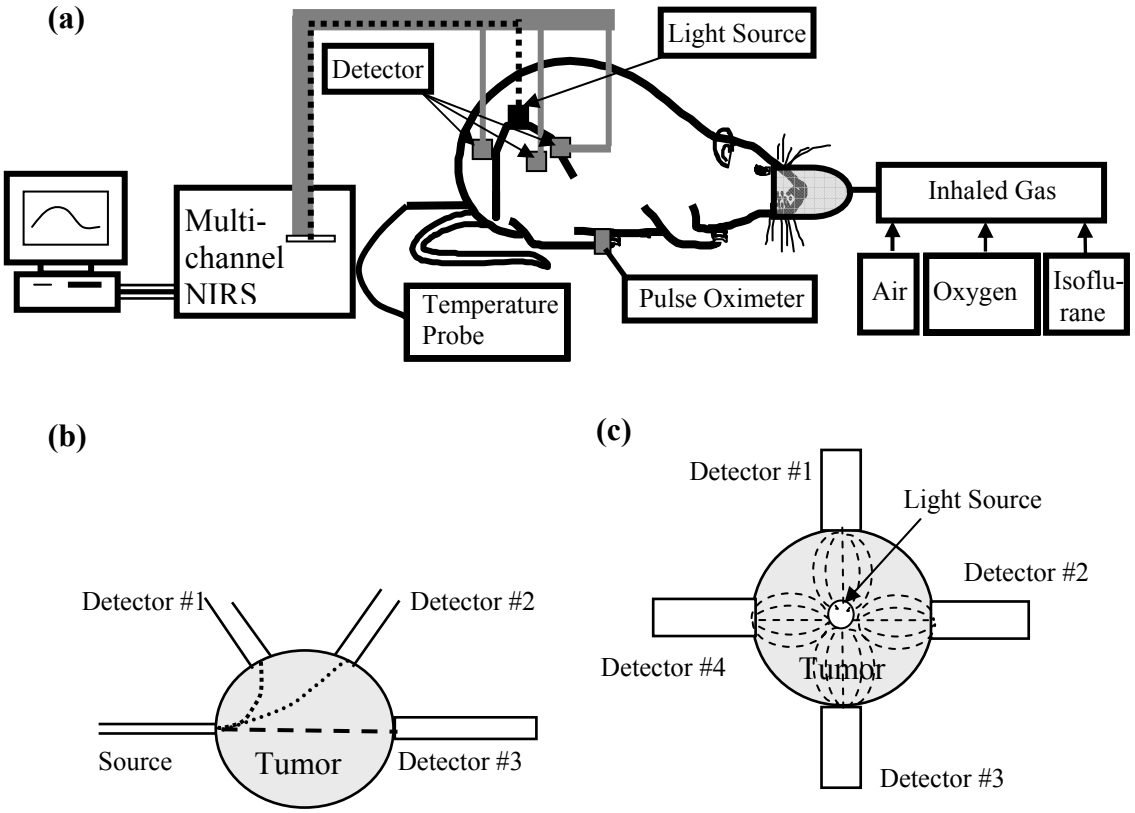

Fig. 7.1 (a) A schematic experimental setup for the animal experiments. A top view of placement of light source and three (b) or four (c) NIRS detectors is also shown; the dotted lines are the light paths transmitted through the tumor.

All measurements were performed in a dark room, and the measurements were initiated while the rats breathed air for 10 minutes to get a stable baseline. After 10 min of baseline measurement, the inhaled gas was switched to carbogen or oxygen for 15 minutes, and then back to air for 15 minutes. Tumor volume V (in cm^3) was estimated as $V = (4\pi/3)\ [(L+W+H)/6]$ [108], where L, W, and H were the three respective orthogonal dimensions. Raw amplitude data from three or four detectors were recorded simultaneously during the experiments and processed after the experiments to obtain the changes in oxygenated hemoglobin concentration, $\Delta[HbO_2]$, and total hemoglobin concentration, $\Delta[Hb_{total}]$. In common with my previous data analysis reported in Chapter 6, time constants, τ_1 and τ_2, signal amplitudes, A_1 and A_2, γ_1/γ_2, and f_1/f_2 were calculated by fitting the $\Delta[HbO_2]$ data using Kaleidagraph software (Synergy Software, Reading, PA).

7.2.2 Multi-Channel NIR Spectroscopy

The multi-channel NIR spectroscopy system has one light source and eight detectors to measure light signals from eight different locations, but due to the finite size of tumor and detector, I used only three or four detectors to monitor tumor vascular oxygen dynamics during respiratory challenges. In common with previous work [31] [33], I assume that oxyhemoglobin and deoxyhemoglobin are the only significant absorbing materials in the blood-perfused tissue. The absorption coefficients comprise the extinction coefficients for deoxyhemoglobin and oxyhemoglobin multiplied by their respective concentrations (Eqs. 7.1 and 7.2).

$$O.D.^{730} = \{\varepsilon_{Hb}{}^{730}[Hb] + \varepsilon_{HbO2}{}^{730}[HbO_2]\}L, \quad (7.1)$$

$$O.D.^{850} = \{\varepsilon_{Hb}{}^{850}[Hb] + \varepsilon_{HbO2}{}^{850}[HbO_2]\}L. \quad (7.2)$$

where $O.D.^{\lambda}$ is the optical density or absorbance at wavelength λ, $\varepsilon_{Hb}{}^{\lambda}$ and $\varepsilon_{HbO2}{}^{\lambda}$ are the extinction coefficients at wavelength λ for molar concentrations of deoxygenated hemoglobin ([Hb]) and oxygenated hemoglobin ($[HbO_2]$), respectively, and L is optical path length between the source and detector. Wavelengths are limited to 730 and 850 nm for this multi-channel NIRS.

The data presented in this chapter are analyzed using modified Beer-Lambert's law (Eq. 7.3), and the amplitudes measured from the multi-channel NIRS are used to find the changes in absorption. By manipulating Eqs. (7.1)-(7.3), changes in oxygenated hemoglobin, deoxygenated hemoglobin and total hemoglobin concentrations ($[Hb_{total}]$) are calculated from the amplitudes of light transmitted through the tumor (Eqs. 7.4, 7.5 and 7.6).

$$\Delta O.D. = O.D._B - O.D._T = \log (A_B/A_T) / L, \quad (7.3)$$

$$\Delta[HbO_2] = [-0.6740*\log (A_B/A_T)^{730} + 1.1171*\log (A_B/A_T)^{850}] / L, \quad (7.4)$$

$$\Delta[Hb] = [0.9943*\log (A_B/A_T)^{730} - 0.3758*\log (A_B/A_T)^{850}] / L, \quad (7.5)$$

$$\Delta[Hb]_{total} = \Delta[Hb] + \Delta[HbO_2]$$

$$= [0.3203*\log (A_B/A_T)^{730} + 0.7413*\log (A_B/A_T)^{850}] / L, \quad (7.6)$$

where A_B = baseline amplitude; A_T = transition amplitude; L = optical pathlength between source/detector. The constants were computed with the extinction coefficients for oxy and deoxyhemoglobin at the two wavelengths used [30].

In principle, L should be equal to the source–detector separation, d, multiplied by a differential pathlength factor (DPF), i.e., L=d*DPF. Little is known about DPF for tumors, although a DPF value of 2.5 has been used by others [158]. Since my focus is on dynamic changes and relative values of tumor [HbO_2] with respect to carbogen/oxygen intervention, I have taken the approach of including the DPF in the unit, i.e., modifying Eq. (7.4) as follows:

$$\Delta[HbO_2] = [-0.6740*\log (A_B/A_T)^{730} + 1.1171*\log (A_B/A_T)^{850}] / d, \quad (7.7)$$

where d is the direct source-detector separation in cm, and the unit of $\Delta[HbO_2]$ in Eq. (7.7) is mM/DPF. The same process can be applied to Eqs. (7.5) and (7.6) so that the units of $\Delta[Hb]$ and $\Delta[Hb_{total}]$ are consistent with that of $\Delta[HbO_2]$.

7.3 Results

7.3.1 Three channel NIRS experiments

Figure 7.2(a) shows a set of $\Delta[HbO_2]$ profiles obtained from three detectors attached on a breast tumor (Tumor A with V=16.6 cm^3), with a source-detector separation of 1.5 cm for detector #1, 2.5 cm for detector #2, and 2.8 cm for detector #3, respectively. After 10 minutes of air breathing measurement as the baseline, the inhaled gas was switched from air to carbogen, causing a sharp increase in $\Delta[HbO_2]$ ($p < 0.0001$ 1 min after gas switch) followed by a further gradual, but significant, increase over the next 15 min ($P < 0.0001$).

The rising parts of $\Delta[HbO_2]$ from detector #1, #2, and #3 after gas switch are shown in Fig. 7.2(b) – 7.2(d), respectively, along with the fitted curves. I used both single-exponential (Eq. 3.1 or 4.1) and double-exponential expressions (Eq. 3.2 or 4.2) to fit the data of the rising portion of $\Delta[HbO_2]$, and it appears that the double-exponential expression gives a much better fit, as confirmed by the respective R^2 values [0.95 ~ 0.96 for the double-exponential versus 0.79 ~ 0.84 for the single-exponential (not shown in Table 7.1)].

From Fig. 7.2, increase of $\Delta[HbO_2]$ during carbogen intervention is much larger at detector #1 than those taken at detectors #2 and #3. Detector #1 was located closest to the light source and thus would most likely detect the light through peripheral region of the tumor. I did not have a histological section of the tumor made in this study, but a previous histology section (Fig. 7.3) taken from the same tumor line showed significant

development of necrosis at the center of the tumors, while tumor periphery exhibited a large portion of viable tumor cells [142].

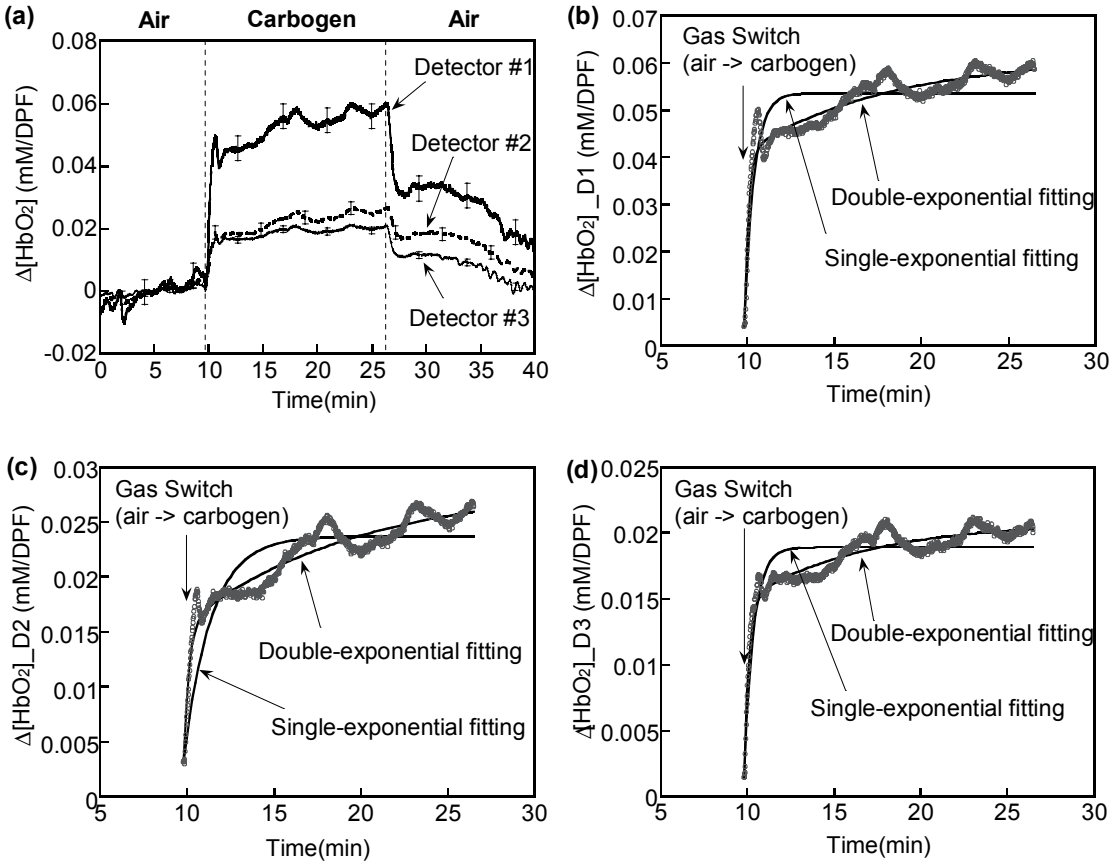

Fig. 7.2 Dynamic changes of [HbO_2] from three detectors in a rat breast tumor (Tumor A with a volume of 16.6 cm^3). Dotted vertical lines mark the temporal points when the gas was changed (a). Figsures 7.2(b)-7.2(d) are taken from detectors #1-#3, respectively. The rising part of Δ[HbO_2] from the three detectors was fitted using both single-exponential and double-exponential expressions.

Even though the histological section showed a substantial spatial heterogeneity in the distribution of tumor cells, two distinct regions in terms of viability could be found in the tumor (See Fig. 7.3). The well perfused peripheral region of the tumor

shows viable tumor cells, while the poorly perfused central region of the tumor exhibits extensive necrosis. Therefore, detector #1 is expected to collect most signal from the peripheral region of the tumor and to show a large increase in $\Delta[HbO_2]$ during carbogen inhalation. This is because the peripheral region of the tumor is well vascularized and thus will have a greater supply of oxyhemoglobin during carbogen inhalation (Fig. 7.2(a)).

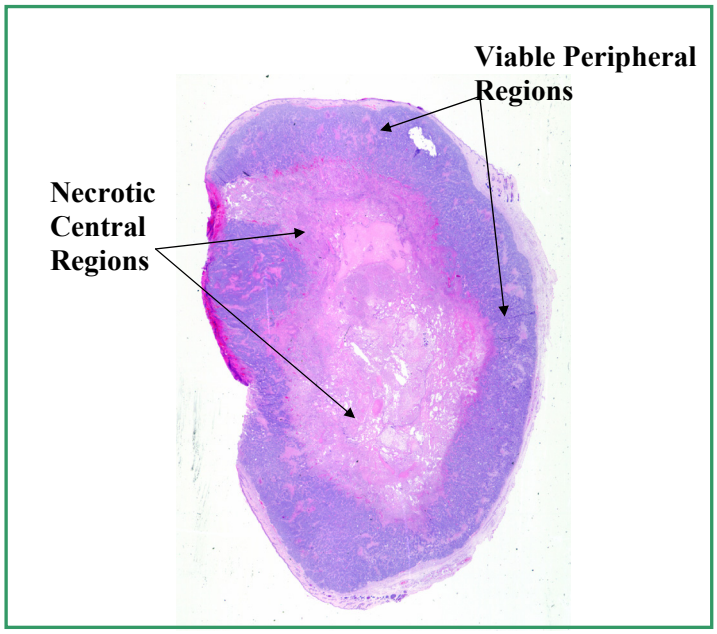

Fig. 7.3 Gross view of a histological section of a tumor (5.7 cm^3), exhibiting marked spatial heterogeneity in tumor cell distribution. (Reprinted from Song [142].)

Compared to detector #1, the amount of $\Delta[HbO_2]$ increase during carbogen intervention observed at detectors #2 and #3 is shown to be less than 50% of that from detector #1. This may imply that the tumor volumes interrogated by the light between the source and detectors #2 and #3, respectively, include a certain portion of poorly

vascularized regions so that the detected signals show much less response in $\Delta[HbO_2]$ increase during carbogen intervention.

Table 7.1 Summary of vascular oxygen dynamics determined at the three detectors as shown in Figure 7.2 (Tumor A).

Double-Exponential fitting $\Delta HbO_2 = A_1[1-\exp(-t/\tau_1)] + A_2[1-\exp(-t/\tau_2)]$			
Parameters	Detector #1 (Fig. 7.2(b))	Detector #2 (Fig. 7.2(c))	Detector #3 (Fig. 7.2(d))
Separation: d (cm)	1.5	2.5	2.8
A_1 (mM/DPF)	0.0370 ± 0.0004	0.0125 ± 0.0002	0.0134 ± 0.0002
τ_1 (min)	0.24 ± 0.01	0.30 ± 0.02	0.27 ± 0.01
A_2 (mM/DPF)	0.020 ± 0.001	0.0130 ± 0.0004	0.0060 ± 0.0001
τ_2 (min)	8.3 ± 0.7	9.9 ± 0.8	7.0 ± 0.6
f_1 (mM/DPF/min)	0.154 ± 0.007	0.042 ± 0.003	0.050 ± 0.002
f_2 (mM/DPF/min)	0.0024 ± 0.0002	0.0013 ± 0.0001	0.0009 ± 0.0001
$\gamma_1/\gamma_2 = A_1/A_2$	1.85 ± 0.07	0.96 ± 0.05	2.23 ± 0.08
τ_1/τ_2	0.029 ± 0.004	0.030 ± 0.004	0.039 ± 0.005
f_1/f_2	64 ± 9	32 ± 5	56 ± 9

The time constants and amplitudes from the three fitted curves at Figs. 7.2(b), 7.2(c), and 7.2(d) are summarized in Table 1, and the corresponding ratios of γ_1/γ_2 and f_1/f_2 given in Eq. 3.3 or 4.3 to describe tumor vascular structure and blood perfusion are also listed in the table. When A_1/A_2 is close to 1, it implies that the measured optical

signal results equally from both region 1 and 2 (Fig. 7.2(c)); if $A_1/A_2 > 1$, the measured signal results more from region 1 than from region 2 (Figs. 7.2(b) and 7.2(d)). As Table 7.1 demonstrates, only detector #2 has a ratio of A_1/A_2 near 1, and the readings from detectors #1 and #3 have a ratio of A_1/A_2 greater than 1. This may suggest that the tumor volume optically interrogated by detector #2 consists of equal volumes from region 1 (i.e., well perfused/periphery region) and region 2 (poorly perfused/central region). The optical signals detected by detectors #1 and #3 result more from region 1 than from region 2 within the tumor. In other words, there is a more well-perfused tumor volume than the poorly perfused tumor volume along the optical interrogation path between the light source and detectors #1 and #3. Furthermore, all the ratios of f_1/f_2 from Tumor A at the three locations are much greater than 1, indicating that the blood perfusion rate in region 1 is much higher than that in region 2.

Figure 7.4 depicts $\Delta[HbO_2]$ obtained from a second breast tumor, Tumor B, with a tumor volume of 20.6 cm^3. The fast and significant increases of $\Delta[HbO_2]$ after switching gas from air to carbogen are similar to those shown in Figure 7.2, and the double-exponential fitting also shows better fits compared to the single-exponential expression. However, as shown in Table 7.2, Tumor B has several different characteristics compared to those displayed in Tumor A. Firstly, Tumor B has quite different time constants at the three different detectors, while Tumor A had a relatively similar range of time constants, for both τ_1 and τ_2, among the three channels. Secondly, it is noticed that for the same tumor (Tumor B), τ_1 obtained at detector #2 is about 3

times greater than that measured at detector #3, and also τ_2 at detector #2 is nearly 4 times greater than that measured at detector #3.

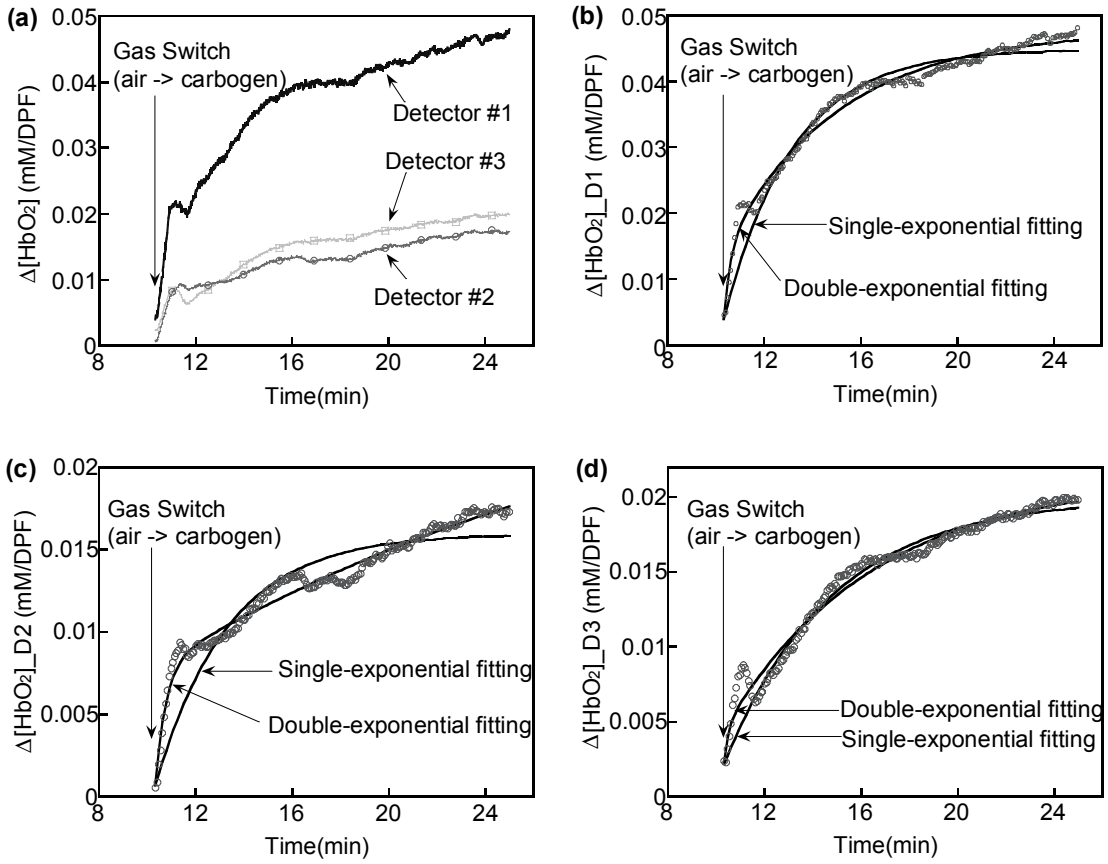

Fig. 7.4 Dynamic changes of [HbO_2] measured from the three detectors from a second rat breast tumor (Tumor B with a volume of 20.6 cm^3). Dotted vertical lines mark the temporal points when the gas was changed (a). Figures 7.4(b)-7.4(d) show the rising part of Δ[HbO_2] taken at detectors #1-#3, respectively, after gas was switched from air to carbogen along with the fitted curves.

Since time constant is inversely related to blood flow velocity in the tumor [138] [139], as also shown in Chapter 3, this implies that the blood flow velocity at the interrogated tumor volume between the light source and detector #3 could be 3 times

and 4 times higher than that at the interrogated tumor volume between the source and detector #2. Moreover, it is clearly seen that the ratios of γ_1/γ_2 and f_1/f_2 are quite different when comparing the two tumors (Tumor A versus Tumor B). Tumor B has all the γ_1/γ_2 values less than 0.35, whereas γ_1/γ_2 values for Tumor A are near or larger than 1, implying that the signals obtained at all three detectors from Tumor B result mainly from region 2, the poorly perfused region. The ratios of perfusion rate, f_1/f_2, determined from Tumor B at the three locations are also much smaller than those obtained from Tumor A, which implies that the difference in perfusion rate between the well perfused and poorly perfused region is smaller in Tumor B than in Tumor A..

Table 7.2 Summary of vascular oxygen dynamics taken at the three detectors as shown in Figure 7.4 (Tumor B)

Double-Exponential fitting $\Delta HbO_2 = A_1[1-\exp(-t/\tau_1)] + A_2[1-\exp(-t/\tau_2)]$			
Parameters	Detector #1 (Fig. 7.4(b))	Detector #2 (Fig. 7.4(c))	Detector #3 (Fig. 7.4(d))
Separation: d (cm)	2	2.5	3
A_1 (mM/DPF)	0.0100 ± 0.0003	0.0072 ± 0.0001	0.0023 ± 0.0001
τ_1 (min)	0.27 ± 0.03	0.43 ± 0.02	0.16 ± 0.04
A_2 (mM/DPF)	0.0330 ± 0.0003	0.0210 ± 0.002	0.0170 ± 0.0001
τ_2 (min)	4.7 ± 0.1	23 ± 3	6.1 ± 0.2
f_1 (mM/DPF/min)	0.037 ± 0.004	0.0167 ± 0.0008	0.014 ± 0.004
f_2 (mM/DPF/min)	0.0070 ± 0.0002	0.0009 ± 0.0002	0.0028 ± 0.0001
$\gamma_1/\gamma_2 = A_1/A_2$	0.30 ± 0.01	0.34 ± 0.03	0.135 ± 0.009
τ_1/τ_2	0.058 ± 0.007	0.019 ± 0.003	0.026 ± 0.007
f_1/f_2	5.2 ± 0.7	18 ± 4	5 ± 1

7.3.2 Four channel NIRS experiments

In this study, I utilized either three detectors (Fig. 7.2 and 7.4) or four detectors for the measurement. By placing 4 detectors with nearly equal distances from the light source, which was located at the top center of the tumor (Fig. 7.1(c)), I was able to investigate the spatial heterogeneity of tumor vasculature. A representative set of data taken from four-channel NIRS experiments is shown in Fig. 7.5. After about 10 minutes of baseline measurement with air breathing, gas was switched to pure oxygen, causing a rapid increase in tumor [HbO_2]. These changes were measured simultaneously from four locations of the tumor. Distances between detectors #1, #2, #3, #4 and the light source are 1.9 cm, 1.6 cm, 1.7 cm, and 1.8 cm, respectively.

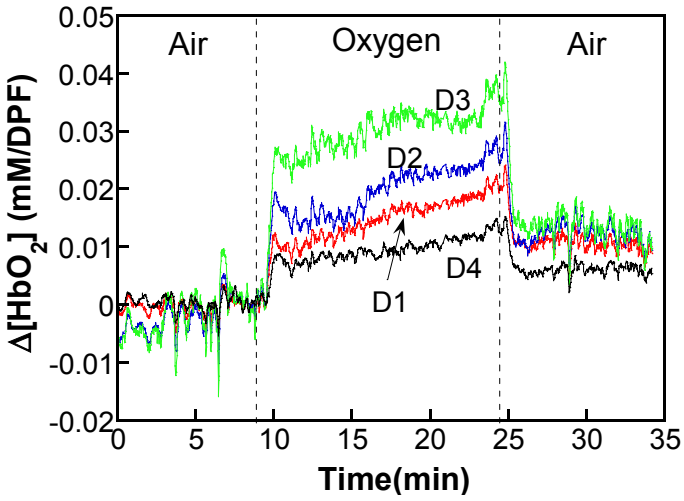

Fig. 7.5 Dynamic changes of [HbO_2] from the four detectors taken from another rat breast tumor (Tumor C with a volume of 11.4 cm^3). Dotted vertical lines mark the temporal points when the gas was changed.

Even though 4 detectors were located nearly equally distant from the light source, implying that the optically interrogated tumor volumes between the light source

and 4 detectors are approximately equal, I still observed great differences in maximum values of $\Delta[HbO_2]$ measured from different detectors. It is seen from Fig. 7.5 that while the overall trends detected at the four locations are similar, the amplitudes of $\Delta[HbO_2]$ are different at different detectors. The differences in maximum values of $\Delta[HbO_2]$ are mostly due to the differences in amplitude of fast component (A_1 value in Table 7.3) among 4 detectors.

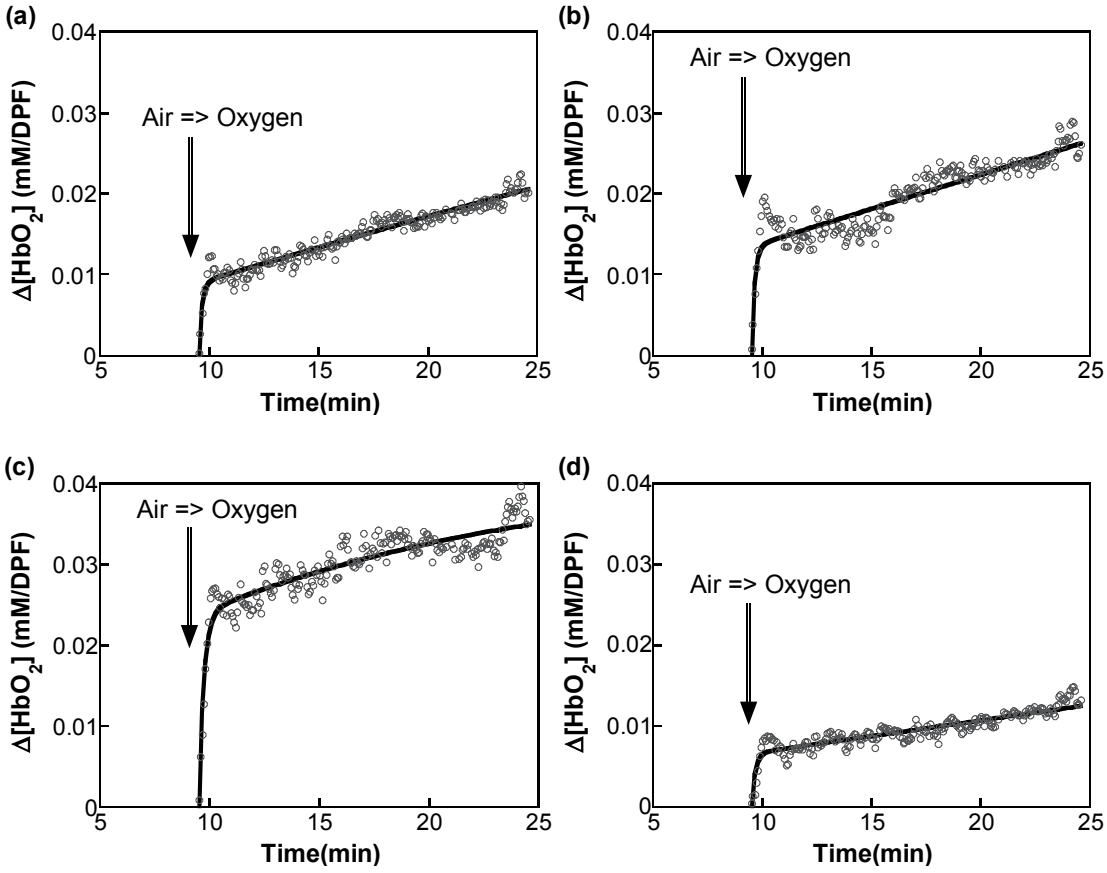

Fig. 7.6 Dynamic changes of tumor $[HbO_2]$ from four locations in Tumor C. The rising parts of $\Delta[HbO_2]$ from the four locations were fitted using a double-exponential expression. Figures 7.6(a)-6(d) were taken from locations #1-#4, respectively. (Tumor C with a tumor volume of 11.4 cm^3)

To understand better tumor vasculatures, $\Delta[HbO_2]$ increases from 4 detectors during oxygen intervention shown in Fig. 7.5 were fitted by the bi-exponential model (Eq. 3.2 or 4.2) and are plotted in Fig. 7.6. Open circles show the raw data measured by multi-channel NIRS, and the solid black lines represent the fitted curves using the bi-exponential model during oxygen intervention [31]. All the figures are plotted with the same scale in $\Delta[HbO_2]$ to show significant differences in amplitude. The fitted parameters from Fig. 7.6 are summarized in Table 7.3. It confirms that the differences in maximum $\Delta[HbO_2]$ observed among 4 detectors came mainly from the differences in A_1 values, which represent $\Delta[HbO_2]$ increases in the well perfused region of the tumor. A2 values are relatively similar to one another among the four detectors.

The ratios of A_1/A_2 and f_1/f_2 characterize tumor vascular structure and blood perfusion within the tumor volume interrogated by light [31]. In principle, when $A_1/A_2=\gamma_1/\gamma_2$ is larger than 1 (Fig. 7.6(c)), it implies that the measured optical signal results more from regions 1 (*i.e.*, well perfused region) than from region 2 (i.e., poorly perfused region); if A_1/A_2 less than 1, the measured signal results more from region 2 than from region 1 [Figs. 7.6(a), 7.6(b) and 7.6(d)]. As Table 7.3 demonstrates, only location #3 has a ratio of A_1/A_2 higher than 1, and the readings from locations #1, #2 and #4 have the ratios of A_1/A_2 less than 1. This may suggest that the optically interrogated tumor volume at location #3 was dominated by the well perfused region, while most of other tumor volumes detected at locations #1, #2 and #4 are composed of more poorly perfused regions. Furthermore, all the ratios of f_1/f_2 from four detectors of the tumor shown in Fig. 7.6 are much greater than 1, indicating that the blood perfusion

rate in the well perfused region is much greater than that in the poorly perfused region. In addition, f_1/f_2 values from all 4 detectors are varying widely, indicating a high level of intratumoral heterogeneity in dynamic vascular structure.

Table 7.3 Summary of vascular oxygen dynamics determined at four detectors as shown in Fig. 7.5. (Tumor C)

Double-Exponential fitting $\Delta HbO_2 = A_1[1-\exp(-t/\tau_1)] + A_2[1-\exp(-t/\tau_2)]$				
Parameters	Detector #1 (Fig. 7.6(a))	Detector #2 (Fig. 7.6(b))	Detector #3 (Fig. 7.6(c))	Detector #4 (Fig. 7.6(d))
Separation: d (cm)	1.9	1.6	1.7	1.8
A_1 (mM/DPF)	0.0080±0.0001	0.0120±0.0002	0.0240±0.0003	0.0070±0.0001
τ_1 (min)	0.14 ± 0.01	0.14 ± 0.02	0.23 ± 0.01	0.17 ± 0.02
A_2 (mM/DPF)	0.015 ± 0.006	0.018 ± 0.003	0.018 ± 0.002	0.013 ± 0.004
τ_2 (min)	11.4 ± 7.6	12.7 ± 3.5	16.2 ± 3.6	25.4 ± 1.2
f_1(mM/DPF/min)	0.058 ± 0.001	0.086 ± 0.002	0.105 ± 0.001	0.038 ± 0.001
f_2(mM/DPF/min)	0.001±0.001	0.0014±0.0004	0.0011±0.0003	0.0005±0.0003
$\gamma_1/\gamma_2 = A_1/A_2$	0.5 ± 0.2	0.70 ± 0.12	1.30 ± 0.16	0.53 ± 0.19
τ_1/τ_2	0.012 ± 0.008	0.011 ± 0.003	0.014 ± 0.003	0.007 ± 0.003
f_1/f_2	44.1 ± 33.9	61.5 ± 19.6	93.4 ± 23.6	76.9 ± 44.3

7.4 Discussions and conclusions

Tumor heterogeneity in terms of tissue pO_2 using ^{19}F MR pO_2 mapping is reported from Mason's research group [16] [20] [63]. ^{19}F MR pO_2 mapping clearly showed that tumor tissue has a wide distribution of pO_2, and also different responses to respiratory challenges even within a tumor. It is known that tissue pO_2 is mainly

decided by the balance between the supply of oxygen from blood vessels and the oxygen consumption by tissue cells. With the assumption of constant oxygen consumption during a gas switch from air to carbogen, tumor tissue pO_2 will be mainly dependent of blood oxygen level changes.

The setup for three-channel NIRS measurements intended to collect hemodynamic readings from different regions of the tumors by placing three detectors with three different separations from the light source. Detector #1 was located closest to the light source so that it would detect the signals most likely from the well perfused/peripheral region of tumors, and detectors #2 and #3 had enough separations so that they would collect the signals from both peripheral and central region of the tumors. However, there was a limit for the closest distance between the light source and detector #1 due to the physical sizes of the light source and detectors. In addition, when detector #1 was placed too close to the light source, the collected signal was too high and became saturated. Therefore, there was a certain distance between the light source and detector #1 (1.5 and 2 cm for Figs. 7.2(b) and 7.4(a).)

With these separations and the geometry between the light source and detector #1, the light would penetrate through the tumors at least deeper than 0.5 cm from the surface of the tumors, which should contain both well perfused and poorly perfused regions in the tumors, as quantified in Table 7.1 and 7.2. Although detector #1 should collect the light from both periphery and central region of the tumor, it can be seen from Table 7.1 that the majority of signals collected at detector #1 came from the well perfused/peripheral region of the tumors (high A_1/A_2 value), matching with my

expectation. However, Fig. 7.4(b) did not show that the well perfused signal is dominant in the collected signals at detector #1, possibly due to a large separation between the light source and detector #1 (2 cm) or due to its own vascular structure of Tumor B (e.g., a thin periphery region in Tumor B). The histological data could provide a strong support for this speculation and could be a possible future study for correlating the tumor vascular structure with the bi-phasic hemodynamic observations from multi-detectors.

For four-channel NIRS experiments, each detector was placed on the side of the tumors to have an equal distance from the light source on the top center of the tumors. However, many of tumors had an oval shape rather than a circular shape, so there were two sets of equal-distance, source-detector separations: two detectors facing each other were nearly equal distanced from the light source. The main objective of 4-channel NIRS experiments was to observe spatial heterogeneity of tumor vasculature. Figure 7.6 indeed confirms the observation of intratumor heterogeneity by showing different values of the fitted parameters, which are highly associated with tumor vascular structure and perfusion.

Specifically, the ratio of A_1/A_2 is similar between detector #1 and #4 (~ 0.5), which means the signals from peripheral region of the tumor are about 50% of the signals from central region of the tumor within the optically interrogated tumor volume between the light source and detectors #1 and #4. Meanwhile, detector #2 shows that the signals from peripheral region of the tumor are about 70% of the signals from central region of the tumor, and the detector #3 shows that the periphery signal is 1.3

times higher than that from central region of the tumor. In this way, one can non-invasively reveal intratumor heterogeneity.

In summary, I applied a three- or four- channel NIRS system to show intra- and inter- tumor heterogeneity in terms of blood perfusion rate and vascular coefficients. All detector readings taken from the tumors showed a sharp rise of $\Delta[HbO_2]$, which was followed further by a slow and gradual increase. In addition, the differences among the signals taken from each detector could be found by applying the bi-exponential mathematical model to fit the $\Delta[HbO_2]$ data during carbogen or oxygen inhalation. Although all signals detected at different locations showed bi-phasic behavior in $\Delta[HbO_2]$, as already demonstrated in Figs 7.2, 7.4, and 7.6, their time constants and ratio of γ_1/γ_2 and f_1/f_2 are different, revealing that tumor vasculature is heterogeneous with respect to blood perfusion rate and percentage of the well-perfused region within the tumors. This study shows the possibility of using a multi-channel NIRS system to monitor tumor heterogeneities, within a tumor or among tumors, in response to the cancer therapy. Such a multi-channel NIRS system could be used as a prognostic tool to predict the therapeutic responses.

* This chapter was presented at Photonics West held by SPIE in 2003. This chapter is going to be prepared for a manuscript and is going to be submitted to the Journal of Biomedical Optics.

J. G. Kim, Y. Gu, A. Constantinescu, R. P. Mason, and H. Liu, “Non-Uniform Tumor Vascular Oxygen Dynamics Monitored By Three-Channel Near-Infrared Spectroscopy”, *Proc. SPIE-Int. Soc. Opt. Eng*., 4955, pp. 388-396 (2003)

CHAPTER 8

CHEMOTHERAPEUTIC (CYCLOPHOSPHAMIDE) EFFECTS ON RAT BREAST TUMOR HEMODYNAMICS MONITORED BY MULTI-CHANNEL NIRS

8.1 Introduction

Many types of cancer therapy are available for cancer patients including radiotherapy, photodynamic therapy and chemotherapy. Chemotherapy plays an important role to treat cancers even though it has some side effects. Currently, the effect of chemotherapy is monitored by MRI or CT that can measure tumor volume changes during cancer treatment. However, it can take up to 3 weeks to detect such changes, and this results in an undesired delay for clinicians to decide whether initial therapeutic strategy should be continued or modified. This delay in detection of chemotherapy effect can reduce a patient's quality of life, and an ineffective therapy is costly. Therefore, many researchers are trying to develop tools that can detect the early response to cancer treatment. For example, Li *et al.* [159] have used ^{31}P nuclear magnetic resonance spectroscopy (NMRS) to measure the effectiveness of cyclophosphamide (CTX) treatment in radiation-induced fibrosarcoma (RIF). They found that the ratio of inorganic phosphate to other phosphate metabolites in the CTX treated group was significantly decreased during the tumor growth delay period

compared to the age-matched controls. Poptani *et al.* studied the effects of CTX treatment in RIF-1 tumors in tumor oxygenation and glycolytic rate changes by utilizing ^{13}C MRS, Eppendorf electrode, and Redox scanning [160]. They observed that CTX treatment caused reduction in glycolytic rate, a significant decrease in tumor tissue pO_2, and also an increase of NADH levels 24 hours after the treatment while tumor volume did not show any significant difference between the CTX-treated and control groups. Zhao *et al*. have reported significant changes in rat breast tumor perfusion following either single dose CTX or continuous low dose "metronomic" therapy [161].

I have reviewed a mathematical model of tumor oxygen dynamics during hyperoxic gas intervention established by Liu *et al* [31] in Chapters 3 and 4. For that model, they formed a hypothesis that changes in oxygenated hemoglobin concentration ($\Delta[HbO_2]$) are composed of signals from a well-perfused and poorly perfused region to explain why there is a bi-phasic feature shown in $\Delta[HbO_2]$ data. This model has been supported by my laboratory and computational studies, as given in Chapters 3 and 4. It is also extensively utilized to analyze the NIRS hemodynamic measurements of rat breast tumors in response to hyperoxic gas intervention and to a vascular disrupting agent (i.e., CA4P), as given in Chapters 5 and 6. In Chapter 7, I demonstrated that a multi-channel NIRS system is able to detect inter- and intra- tumoral vascular heterogeneity in response to hyperoxic gas intervention. Each detector's signal came from a different region of the tumor, and thus the study given in Chapter 7 revealed differences of the fitted parameters among the multi-detectors.

In this chapter, I apply a multi-channel NIRS system to monitor heterogeneous responses of tumor oxygenation during oxygen intervention before and after CTX administration. The purpose for this study is to explore multi-channel NIRS as a possible tool for monitoring heterogeneous tumor responses to chemotherapy. This work is based on the following hypothesis: when the tumor is treated with chemotherapy, changes in blood perfusion and vascular density in the tumor will occur heterogeneously due to its non-uniform vascular structures and will be seen by heterogeneous changes in the fitted parameters from different locations on the tumor by NIRS measurements. In addition, NIRS can be used, to be complimentary with monitoring of the reduction in tumor size, to detect the changes of tumor physiological conditions, which are essential for tumor treatment planning and tumor prognosis.

8.2 Materials and methods

8.2.1 Tumor Model and Experimental Procedure

The experimental rats were divided into three groups for this study. Two groups were treated with CTX at two different doses: one with 200 mg/kg for a single high dose group (n=5) and another dose with 20 mg/kg per day for consecutive 10 days for a metronomic low dose group (n=3). The other group was administered with saline instead of CTX as a control group (n=3). The tumor line was rat mammary adenocarcinomas 13762NF (cells were originally provided by the Division of Cancer Therapeutics, NCI), and the tumors were implanted in the hind limb of adult female Fisher 344 rats (~200 g).

Cyclophosphamide was chosen as a chemotherapeutic agent for this study since this tumor line is highly responsive to alkylating agents and platinum chemotherapeutic agents [162]. CTX is an antineoplastic alkylating agent, and it has been used to treat lymphomas, cancers of the ovary, breast and bladder, and chronic lymphocytic leukaemia [163] [164]. The rats were anesthetized with 0.2 ml ketamine HCl (100 mg/ml; Aveco, Fort Dodge, IA) when the tumors reached approximately 1 cm in diameter and maintained under general gaseous anesthesia using a small animal anesthesia unit with air (1 dm^3/min) and 1% isoflurane through a mask placed over the rat mouth and nose.

During the experiments, the rat was placed on a warm blanket to maintain body temperature, which was monitored with a rectally inserted thermal probe connected to a digital thermometer (Digi-Sense, model 91100-50, Cole-Parmer Instrument Company, Vernon Hills, IL). The tumors were shaved before measurements to improve optical contact for transmitting light. A pulse oximeter (model: 8600V, Nonin, Inc.) was placed on the hind foot to monitor arterial oxygenation (S_aO_2) and heart rate. For the single high dose group (n=5), a light source and four detectors from a multi-channel, CW (continuous wave) NIRS (NIM, Inc, Philadelphia, PA) system were attached to the tumor using posts and swivel post clamps (see Fig. 8.1).

For the multi low dose (n=3) and control (n=3) groups, I have used a four-channel, frequency domain (FD), NIRS (ISS, Champaign, IL) system. In this case, the four sets of light sources at two wavelengths replaced the four detectors shown in Fig.

8.1(b), and one detector fiber was placed on top of the tumor to obtain signals from four different regions of the tumor.

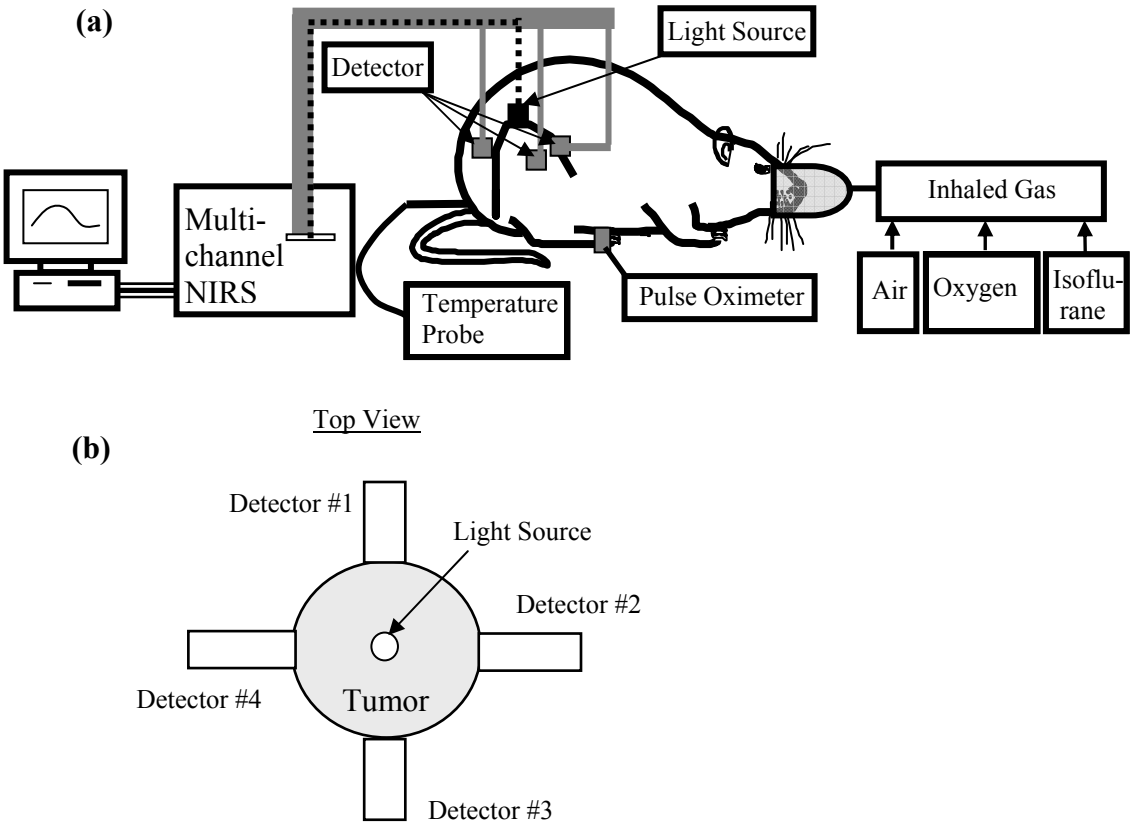

Fig. 8.1 (a) A schematic diagram of experimental setup for the multi-channel NIRS measurement on rat tumors. (b) A top view of light source and detector arrangement of the multi-channel CW NIRS system. In the setup of 4-channel FD NIRS system, the four sets of light sources replaced the four detectors, and one detector fiber was placed on the top center of the tumor.

All the measurements were performed in a dark room, and the measurements were initiated while the rats breathed air for 10 minutes to get a stable baseline. After the baseline measurement, the inhaled gas was switched to oxygen for 15 minutes, and

then back to air for 15 minutes. This experimental procedure was repeated before and after the CTX treatment, and the four detectors were intended to be located at the same positions for each measurement on different days.

Using an ellipsoidal approximation, tumor volume V (cm^3) was estimated as $V = (\pi/6)\cdot L\cdot W\cdot H$, where L, W, and H are the three respective orthogonal dimensions. The raw amplitude data from four locations were recorded simultaneously during the experiments and processed after the experiments to obtain values of $\Delta[HbO_2]$ and $\Delta[Hb_{total}]$. The amplitude and time constant of $\Delta[HbO_2]$ were calculated by fitting the two-exponential model to the data using Kaleidagraph (Synergy Software, Reading, PA). The corresponding vasculature coefficients and perfusion rates, i.e., A_1, A_2, τ_1, τ_2, f_1, and f_2, were also calculated to show static and dynamic heterogeneities of the tumors at different locations.

8.2.2 Measurement System

As mentioned above, two different multi-channel NIRS systems were used for this study: a multi-channel, CW, NIRS system was used in the single high dose study, while an ISS, 4-channel, frequency-domain, NIRS system was applied in the continuous low dose study. Since the same multi-channel CW NIRS system was utilized in Chapter 7, the detailed information on the system hardware and the algorithm to obtain $\Delta[HbO_2]$, $\Delta[Hb]$, and $\Delta[Hb_{total}]$ using two wavelengths were already described in Section 7.2.2 previously.

Since the wavelengths of light sources from the ISS, frequency-domain, NIRS system were 750 nm and 830 nm, different from 730 nm and 850 nm being used in the multi-channel CW NIRS system, the corresponding equations for $\Delta[HbO_2]$, $\Delta[Hb]$, and $\Delta[Hb_{total}]$ are modified from Eqs. (7.4)-(7.6), as given in the following:

$$\Delta[HbO_2] = [-0.653*\log (A_B/A_T)^{750} + 1.293*\log (A_B/A_T)^{830}] / d, \quad (8.1)$$

$$\Delta[Hb] = [0.879*\log (A_B/A_T)^{750} - 0.460*\log (A_B/A_T)^{830}] / d, \quad (8.2)$$

$$\Delta[Hb_{total}] = \Delta[Hb] + \Delta[HbO_2]$$

$$=[0.226*\log (A_B/A_T)^{750} + 0.833*\log (A_B/A_T)^{830}] / d. \quad (8.3)$$

where A_B = baseline amplitude; A_T = transient amplitude; d is the direct source-detector separation in cm, and the units of $\Delta[HbO_2]$, $\Delta[Hb]$, and $\Delta[Hb_{total}]$ in Eqs. (8.1)-(8.3) are mM/DPF.

8.3 Results

8.3.1 Body weight and tumor volume changes during chemotherapy

Body weight and tumor volume of control and the treated rats were monitored before and after the CTX treatments to examine the tumor responses and side effects due to chemotherapy. Changes in rat body weight and tumor volume were normalized

to day 0 (before CTX or saline administration). In Figs. 8.2(a) and 8.2(b), solid circles represent the data taken from the control group, and open squares and open diamonds represent the continuous low dose group and single high dose group, respectively.

In the single high dose treatment group, the body weight of rats was in the range of 170g to 225g, and the tumor volume was between 2.5 cm^3 and 11.5 cm^3 at day 0. The body weights decreased until 6 days after the treatment, but later increased for the rest of days of observation. Two rats among five in this group died by day 6 due to the toxicity from the high dose CTX treatment. Therefore, the data shown at days 8 and 10 represent a smaller group of rats, which survived during the high dose treatment. The tumor volume decreased initially after a single high dose of CTX treatment, but did not further decrease after day 4 (Fig. 8.2(b)).

In comparison, the rats in the continuous low dose treatment group had the body weight in the range between 170g and 190g, and the tumor volume was in the range from 0.5 cm^3 to 0.6 cm^3 before CTX treatments. This group initially lost their weight after a low dose of CTX administration, but gradually gained their weight back during the treatment, presenting low toxicity from the treatment. This group also showed a significant decrease in tumor volume during the treatment for 10 days.

For the control group, the initial body weight was in the range between 170g and 190g, and the tumor volume ranged from 0.57 cm^3 to 1 cm^3. For this group, a saline solution was injected into the rats instead of CTX. A gradual decrease of rat body weight was observed, while their tumor volumes increased exponentially.

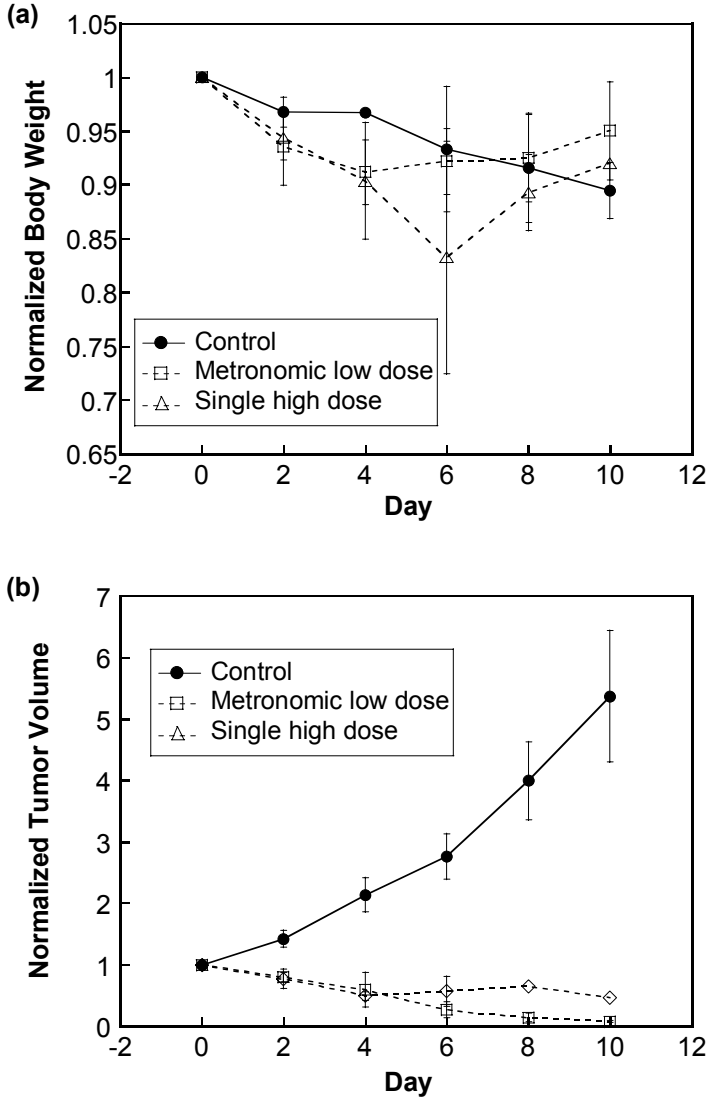

Fig. 8.2 Normalized changes in rat body weight (a) and tumor volume (b) during the saline and CTX treatments. (n=3 for both the control and metronomic low dose group, and n=5 for the single high dose group.)

8.3.2 Vascular hemodynamic changes from the control group

For the control group, the tumor hemodynamics during oxygen intervention were measured before and after administration of saline. The representative data from

the control group is shown in Fig. 8.3. Open symbols are the raw data taken from the measurements, and solid lines are the fitted curves using the double exponential model. As mentioned before, there were 4 sets of light sources placed on the surface of tumor.

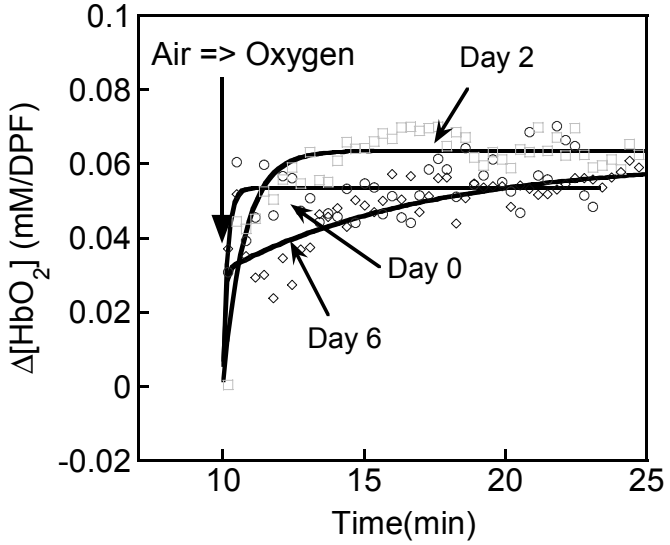

Fig. 8.3 Dynamic profiles of $\Delta[HbO_2]$ taken at location #1 from a rat breast tumor (Control group, Tumor A) before and after administration of saline. The rising part of $\Delta[HbO_2]$ from location #1 was fitted using either a single or a double-exponential expression.

Figure 8.3 shows the acute and then gradual changes of $[HbO_2]$ after switching the breathing gas from air to oxygen, and the data were observed at the same (or nearly the same) location of the same rat tumor from day 0 to day 6. The first thing that can be noticed is a decrease in fast component and an increase in slow component of $\Delta[HbO_2]$ during oxygen intervention at day 6. This respectively represents a decrease of well perfused region and also an increase of necrotic area in tumor as the tumor grows. The trend of $\Delta[HbO_2]$ at day 2 also differs from that at day 0 by showing a slower increase

of $\Delta[HbO_2]$ during oxygen intervention than the increase at day 0. Therefore, this figure indicates that the internal changes of tumor vasculature as the tumor grows can be monitored by NIRS with oxygen interventions.

The amplitudes and time constants obtained from $\Delta[HbO_2]$ increase (Fig. 8.3) are summarized in Table 8.1. The data at days 0 and 2 in Fig. 8.3 were fitted well with a mono exponential model rather than a bi-exponential model, implying that the tumor vasculature is relatively pretty much homogeneous. However, the $\Delta[HbO_2]$ increase at day 6 (Fig. 8.3) was better fitted with the bi-exponential model, implying that tumor vasculature became heterogeneous, and possibly a hypoxic/necrotic region was developed in the central region of the tumor.

Table 8.1 Summary of vascular oxygen dynamics determined at location #1 from the rat tumor shown in Fig. 8.3 as a control (control group, Tumor A).

Day	A_1	A_2	τ_1	τ_2	$f_1 = A_1/\tau_1$	A_1/A_2	τ_1/τ_2	f_1/f_2
0	0.053		0.16		3.3			
2	0.063		0.77		0.08			
6	0.031	0.030	0.07	7.21		0.44	0.004	110

The tumor sizes at day 0 and 2 were 0.55 and 0.74 cm^3, which can be considered as small tumors, whereas the tumor size at day 6 was 1.67 cm^3, which represents a large tumor and could possibly have developed hypoxic/necrotic regions within the tumor. Since the time constants are inversely related to the blood flow velocity in tumor [138] [139], the increase in time constant represents the decrease in blood flow velocity. The

time constant at day 2 was increased compared to the value at day 0 (Table 8.1), indicating a decrease in average blood flow velocity/perfusion rate in tumor as the tumor grows bigger.

8.3.3 Vascular hemodynamic changes from the metronomic low dose CTX treated group

Figure 8.4 shows representative data from the metronomic low dose group. Although some changes in hemodynamics were observed from the control group with saline administration, they were not as significant as those found in the CTX treated group (Figs. 8.4 and 8.5). Figure 8.4 shows the changes in tumor hemodynamics during a metronomic low dose treatment of CTX. It needs to be noticed that the fast component of $\Delta[HbO_2]$ increase during oxygen intervention became much smaller at Days 2 and 6 compared to Day 0 while the slow component of $\Delta[HbO_2]$ increase maintained relatively unchanged (See Table 8.2). This observation implies a significant decrease in signal from the well perfused region, but not from the poorly perfused region. In other words, the therapeutic effects occur at the well perfused/periphery region faster than in the poorly perfused/central region within the treated tumors. This interpretation can be understood since CTX molecules have an access to the tumor cells easier in the well perfused region than in the poorly perfused region.

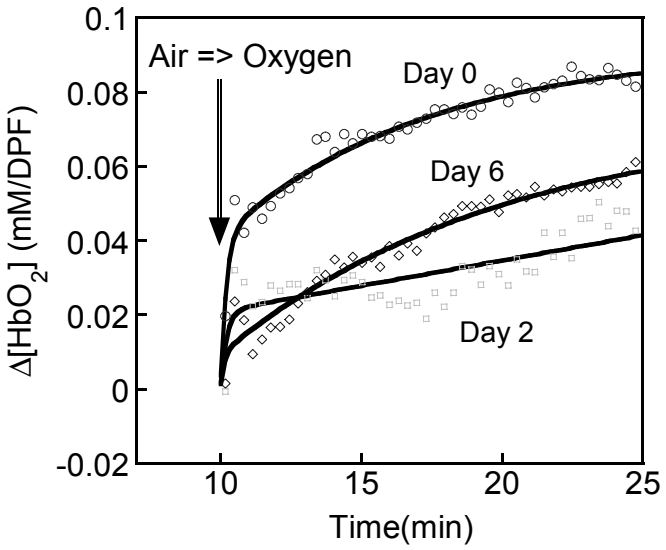

Fig. 8.4 Dynamic trends of $\Delta[HbO_2]$ taken at location #1 from a rat breast tumor (Metronomic low dose group, Tumor A) before and after administration of metronomic low dose of CTX (20 mg/kg for 10 days). The rising part of $\Delta[HbO_2]$ from location #1 was fitted using the double-exponential expression.

Table 8.2 Summary of vascular oxygen dynamics determined at location #1 from the tumor shown in Fig. 8.4 before and after a metronomic low dose of CTX treatment.

Day	A_1	A_2	τ_1	τ_2	A_1/A_2 $(=\gamma_1/\gamma_2)$	τ_1/τ_2	f_1/f_2
0	0.041	0.05	0.20	7.19	0.82	0.028	29.3
2	0.021	0.02	0.21	12.7	1.05	0.017	61.8
6	0.009	0.06	0.12	9.96	0.15	0.006	25

The fitted parameters from Fig. 8.4 are summarized in Table 8.2. It shows that time constant values of the well perfused/periphery region of tumor (τ_1) were decreased as the CTX treatments were undergoing. While a control rat tumor with saline administration showed a decrease in τ_1 from day 0 to day 6, it was not as significant as one seen in Fig. 8.4. Table 8.2 clearly shows a decrease in A_1 values but a relative

constant in A_2 values from Day 0 to Day 6. This implies that the major decrease in maximum $\Delta[HbO_2]$ during oxygen interventions came mostly from the well perfused region rather than from the poorly perfused region.

8.3.4 Vascular hemodynamic changes from the high single dose CTX treated group

Figure 8.5 shows the changes of tumor hemodynamics during oxygen intervention, before and after a single high dose of CTX treatment, measured by the multi-channel CW NIRS. This clearly demonstrates that significant changes in tumor hemodynamics occur after chemotherapy and can be detected by using NIRS with respiratory challenge as a mediator. Similar to the case with a metronomic low dose of CTX treatment (Fig. 8.4), a single high dose also caused a significant decrease in fast component of $\Delta[HbO_2]$ increase during an oxygen intervention. At day 5 after the high dose treatment, it is hard to see any fast component in $\Delta[HbO_2]$ increase during the oxygen intervention. Figure 8.5 also illustrates that the therapeutic effect of CTX on the poorly perfused/central region of the tumor is finally shown by a decrease in slow component of $\Delta[HbO_2]$ increase at days 3 and 5.

The fitted amplitudes and time constants obtained from $\Delta[HbO_2]$ increase (Fig. 8.5) are summarized in Table 8.3. Both A_1 and τ_1 values are significantly decreased after CTX administration, implying that the volume of well perfused or periphery region of the tumor is significantly reduced while the blood flow velocity in the same region has been increased. At day 5, the double exponential model does not give a better fitting than the single exponential model, again representing that the vascular

structure of tumor becomes more homogeneous between the well perfused and poorly perfused regions than that before the CTX treatment.

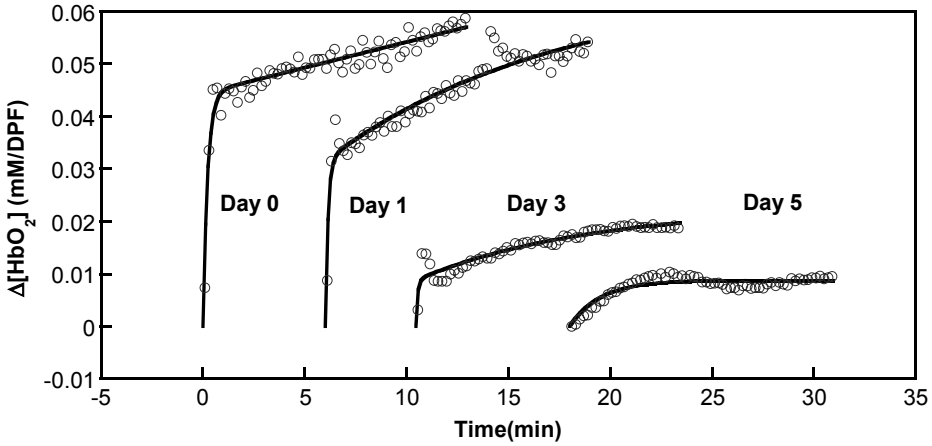

Fig. 8.5 Dynamic changes of [HbO_2] taken at location #1 from a rat breast tumor (Single high dose group, Tumor A) before and after a single high dose of CTX treatment (200mg/kg). The rising parts of Δ[HbO_2] traces from location #1 were fitted (solid curves) using either a single- or double- exponential expression.

Table 8.3 Summary of vascular oxygen dynamics determined at location #1 from the tumor shown in Fig. 8.5 before and after a single high dose of CTX treatment.

Day	A_1	A_2	τ_1	τ_2	A_1/A_2 ($=\gamma_1/\gamma_2$)	τ_1/τ_2	f_1/f_2
0	0.044	0.031	0.23	25.21	1.42	0.0091	156
1	0.032	0.033	0.13	11.36	0.97	0.0114	85
3	0.0087	0.014	0.089	8.36	0.62	0.0106	58
5	0.0087		1.27				

8.3.5 Intratumoral heterogeneity in tumor response to CTX treatment

One purpose of using multi-channel NIRS was to find a heterogeneous response of tumor to the chemotherapy. Figure 8.6 shows hemodynamic changes taken from 4

locations of a tumor (i.e., high-dose group, Tumor A) before and after the single high dose of CTX treatment, measured with the multi-channel CW NIRS system.

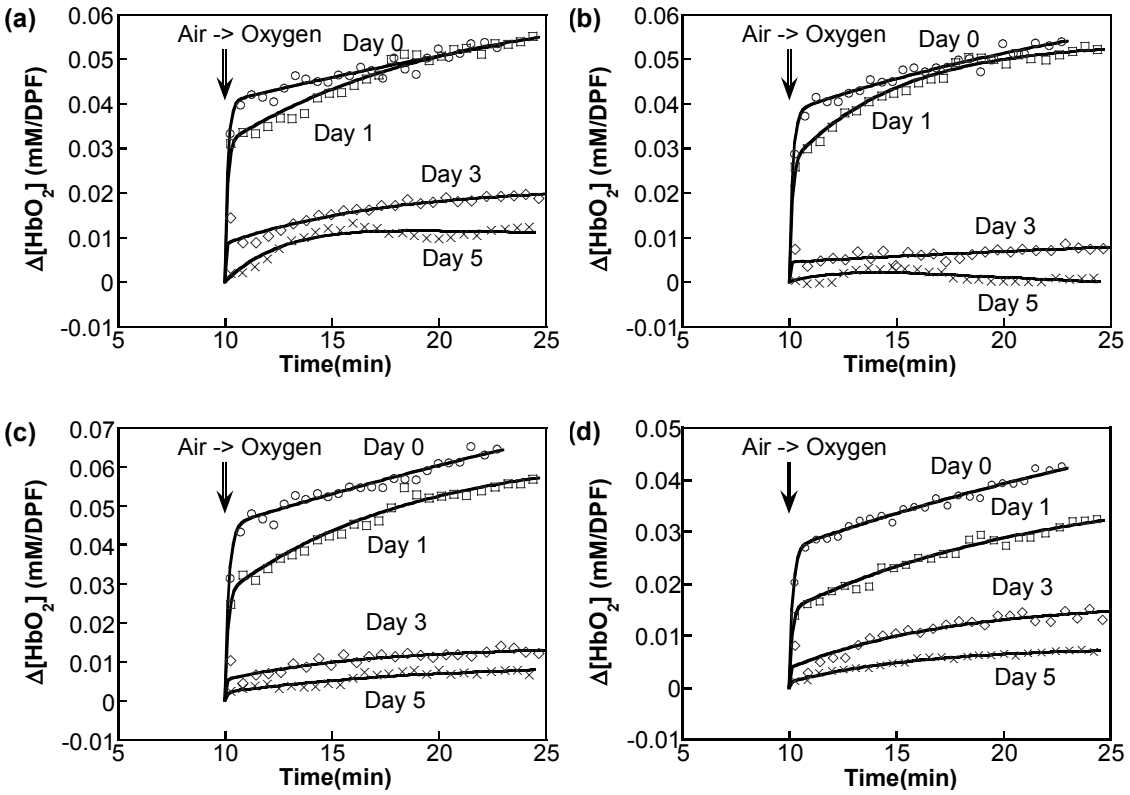

Fig. 8.6 Dynamic changes of [HbO_2] taken at 4 locations from a rat breast tumor (Single high dose group, Tumor A) before and after a single high dose of CTX treatment (200mg/kg). The Δ[HbO_2] increases during oxygen intervention were fitted using the double-exponential expression.

They all share several common responses to CTX while they also show variances in response to CTX administration. Three among the four sections exhibit a little response to the treatment at day 1 by displaying a little alteration of Δ[HbO_2] hemodynamics from those observed at day 0 (Figs. 8.6(a), 8.6(b), and 8.6(c)). However, one section of the tumor reveals a notable response to CTX treatment even at Day 1

(Fig. 8.6(d)). All four sections of the tumor show decreases in fast component of $\Delta[HbO_2]$ after CTX administration, as seen previously in other tumors, such as those shown in Figs. 8.4 and 8.5.

The individual figures given in Fig. 8.6 also illustrate great responses in all 4 sections at day 3: the bi-phasic feature of $\Delta[HbO_2]$ increase during oxygen intervention is hardly seen at three sections (see Figs. 8.6(b) to 8.6(d)) even though it still is observed better in the section (Figs. 8.6(a)). This set of data tells one that the tumor vasculature in three sections became relatively homogeneous, with the poorly perfused regions disappeared.

In other words, one of the four sections of the tumor still has two distinct perfusion rates within the optically interrogated volume. Furthermore, at day 5, it is obvious that the bi-phasic feature is completely gone in all of the sections. All of these results indeed prove that multi-channel NIRS in conjunction with hyperoxic gas intervention can be a very useful tool to detect intratumoral heterogeneity in tumor response to cancer treatments.

8.3.6 Intertumoral heterogeneity in tumor response to CTX treatment

In Section 8.3.5, I have discussed heterogeneity in therapeutic response within a tumor, and I will show in this section heterogeneity of therapeutic response among different tumors. Figure 8.7 represents respective tumor hemodynamic responses to the single high dose of CTX treatment from 4 different rat breast tumors (Single high dose

group, Tumors B to E), showing profiles in $\Delta[HbO_2]$ increase during oxygen intervention from one of the four channels in CW NIRS.

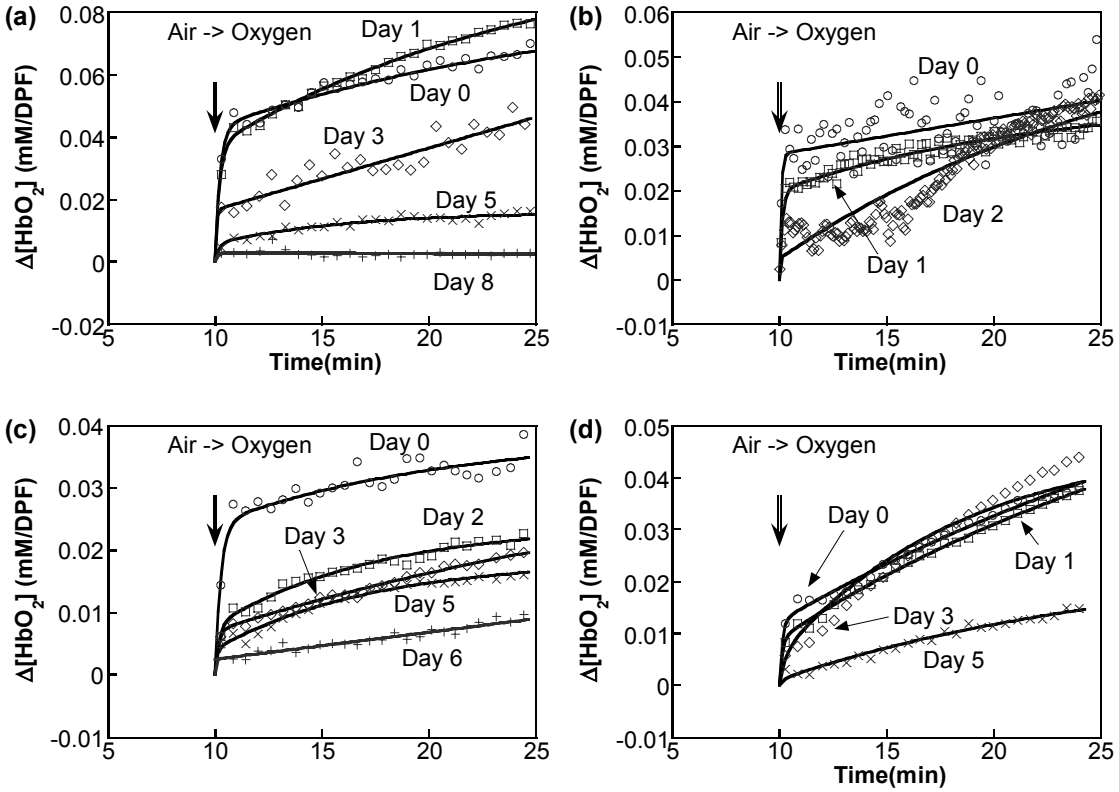

Fig. 8.7 Dynamic changes of $[HbO_2]$ taken from 4 different rat breast tumors (Single high dose group, Tumors B, C, D, and E), respectively, before and after a single high dose of CTX treatment (200mg/kg). The $\Delta[HbO_2]$ increases during oxygen intervention were fitted using the double-exponential expression. Tumor volumes are (a) 6.5 cm^3 for Tumor B, (b) 8.2 cm^3 for Tumor C, (c) 11.5 cm^3 for Tumor D, and (d) 2.6 cm^3 for Tumor E, respectively.

Figure 8.7 clearly shows variation of therapeutic responses among the four tumors even though the tumors shown in Figs. 8.7(a) and 8.7(c) exhibit very similar responses to the CTX treatment. The rat being used for Fig. 8.7(b) died at day 3 after CTX administration, while the rat for Fig. 8.7(a) was still healthy at day 10. The tumor

for Fig. 8.7(d) did not show much response to the CTX treatment until day 3 after the drug administration, but followed by a sudden and significant response at day 5.

8.3.7 Changes in fitted parameters before and after chemotherapy

The data analysis in this subsection is based on the multi-channel CW NIRS readings from Tumor A in the high-dose treatment group. Several sets of the fitted parameters from Fig. 8.6 are graphically summarized in Figs. 8.8-8.11. Each symbol represents a fitted value, and each error bar represents the standard error of fitting. Figure 8.8 shows changes of A_1 and A_2 values from all four channels after the high-dose CTX treatment. Even though both A_1 and A_2 show large decreases at all channels after the treatment, it seems that the relative decrease in A_1 between days 0 and 3 after CTX treatment is greater than that in A_2 values.

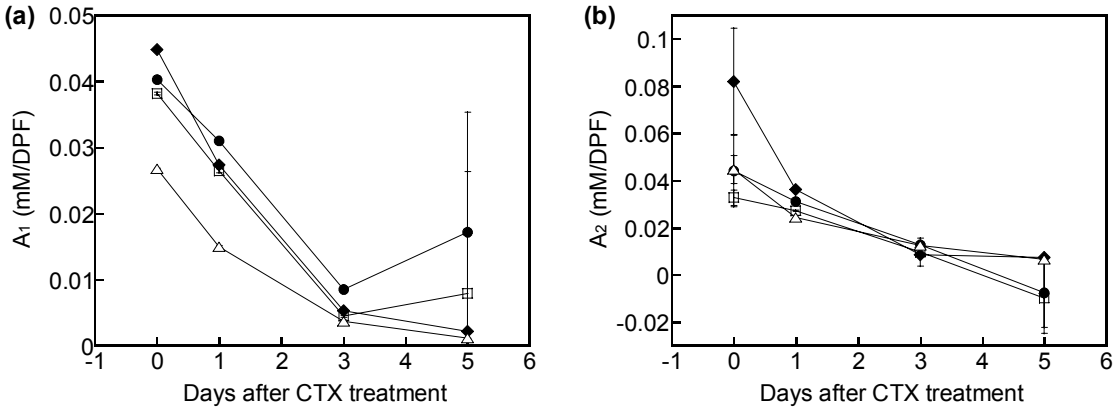

Fig. 8.8 Summary of the fitted parameters, A_1 (a) and A_2 (b), by using the bi-exponential model. The four traces represent the four readings taken from all four detectors.

This observation implies that tumor cells in the well perfused/periphery region were more treated by CTX than those in the poorly perfused/central region of tumor in the beginning of treatment. Two sections of the tumor show negative values of A_2 at day 5 (Fig. 8.8(b)) due to the gradual decrease of $\Delta[HbO_2]$ after an initial increase during oxygen intervention which could be due to the changes in vascular permeability after CTX treatment.

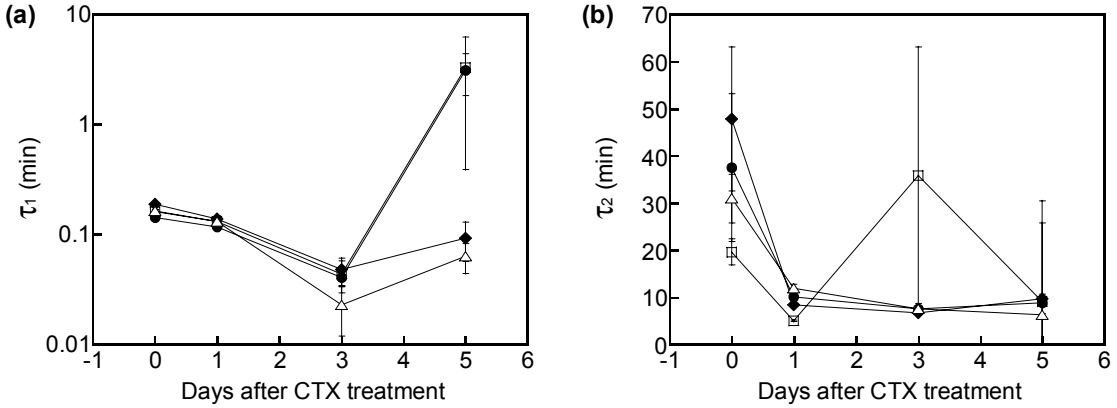

Fig. 8.9 Summary of the fitted parameters, τ_1 (a) and τ_2 (b), by using the bi-exponential model. The four traces represent the four readings taken from all four detectors of the multi-channel CW NIRS system.

Figure 8.9 plotted the fitted time constant values from the fast (τ_1) and slow (τ_2) component of $\Delta[HbO_2]$ increases, as shown in Fig. 8.6. Figure 8.9(a) shows the time constants from the well perfused/periphery region of tumor and is plotted in the logarithmic scale to display clear changes of τ_1 from day 0 to day 3 after CTX treatment. The values of τ_1 drop greatly at day 1 and 3 from that at pre CTX treatment, but followed by significant re-increases at day 5 (Fig. 8.9(a)). A decrease in time constant

implies an increase in blood flow velocity, and thus this set of data makes me conclude that the CTX treatment causes increases of tumor blood flow velocity. This conclusion can be supported by the fact that cyclophosphamide treatment, just like other antineoplastic agents, will cause the death of tumor cells accompanied by reduced capillary permeability, reduced interstitial water volumes, increased plasma volumes, and reduced vascular perfusion [165]. The reduced vascular perfusion after antineoplasic agent can be caused by the decrease of number of blood vessels in tumors even though the blood flow velocity increases. The increase of extracellular space in tumors implying the decrease of blood vessels in tumors is also reported [166] [167].

In particular, the increase in blood flow velocity could be expected since the reduction in interstitial water volume or fluid pressure may relieve the constriction of blood vessels, which in turn permits an increase in vessel diameters and in blood flow velocity. Even though both time constants are decreased after CTX treatment, τ_2 values are more or less stabilized at days 3 and 5 after a great decrease at day1, while τ_1 values show an even more significant drop at day 3. This could be possibly explained by the following considerations: the central region (or the poorly perfused region) of the tumor has already had 1) a much lower blood flow velocity, and 2) also a higher interstitial pressure than the tumor periphery. Both of these factors cause the central region of tumors to have a slow and sluggish blood flow. At day 5, τ_1 values increased largely from those at day 3, close to the values of τ_2 at day 5 (Fig. 8.9(b)). This match may imply that the blood flow velocities at the two different perfused regions become less distinct or more homogeneous than those before the treatment. The disappearance of bi-

phasic feature at day 5 (Fig. 8.6) explains the increase of A_1 and τ_1 values at day 5 since the double-exponential model in this case does not give rise to significantly distinct fitting parameters between A_1 and A_2, and between τ_1 and τ_2.

Figure 8.10 shows perfusion rate changes in the periphery (Fig. 8.10(a)) and central (Fig. 8.10(b)) region of the tumor (Tumor A in the single high dose group) after CTX treatment. The values of f_1 decrease after the treatment, while f_2 values initially increase at day 1 and then return to the pre-treatment level at day 3. The initial increase in f_2 could be explained by 1) more blood supply to the central region due to a decrease in peripheral perfusion and 2) reduction of interstitial pressure and water volumes induced by CTX [165]. However, once the perfusion at the central region of tumor increases, the tumor cells in the central region will be attacked better by CTX molecules, which in turn give rise to a significant decrease in f_2. The negative values of f_2 at day 5 are from the negative values of A_2 shown in Fig. 8.8(b).

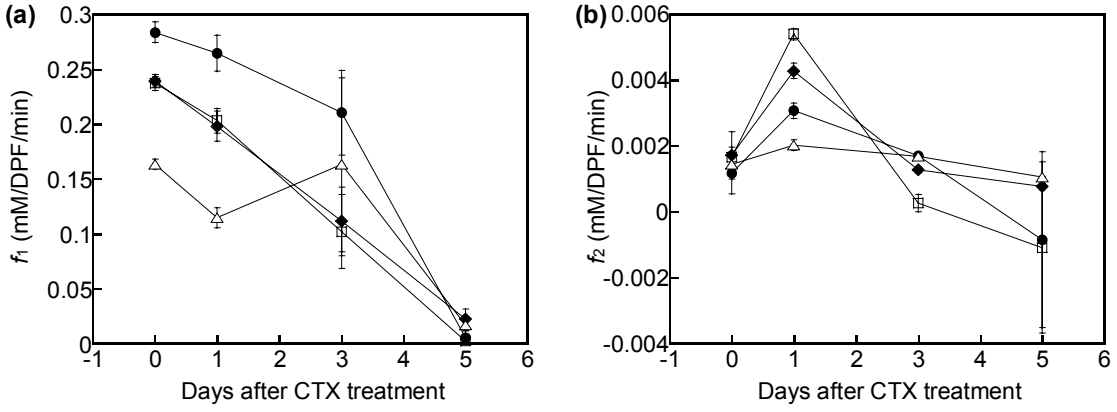

Fig. 8.10 Summary of the fitted parameters, f_1 (a) and f_2 (b), by using the bi-exponential model.

The ratios of A_1/A_2, τ_1/τ_2, and f_1/f_2 are shown in Fig. 8.11. Since both A_1 and A_2 values were decreased after CTX treatment (Fig. 8.8), the decrease in A_1/A_2 (Fig. 8.11(a)) must result from a more significant decrease in A_1, which represents the well perfused/periphery region of tumor. The conclusion is consistent with my earlier observation on Fig. 8.8, supporting my implication that tumor cells in the well perfused/periphery region were more treated by CTX than those in the poorly perfused/central region of tumor.

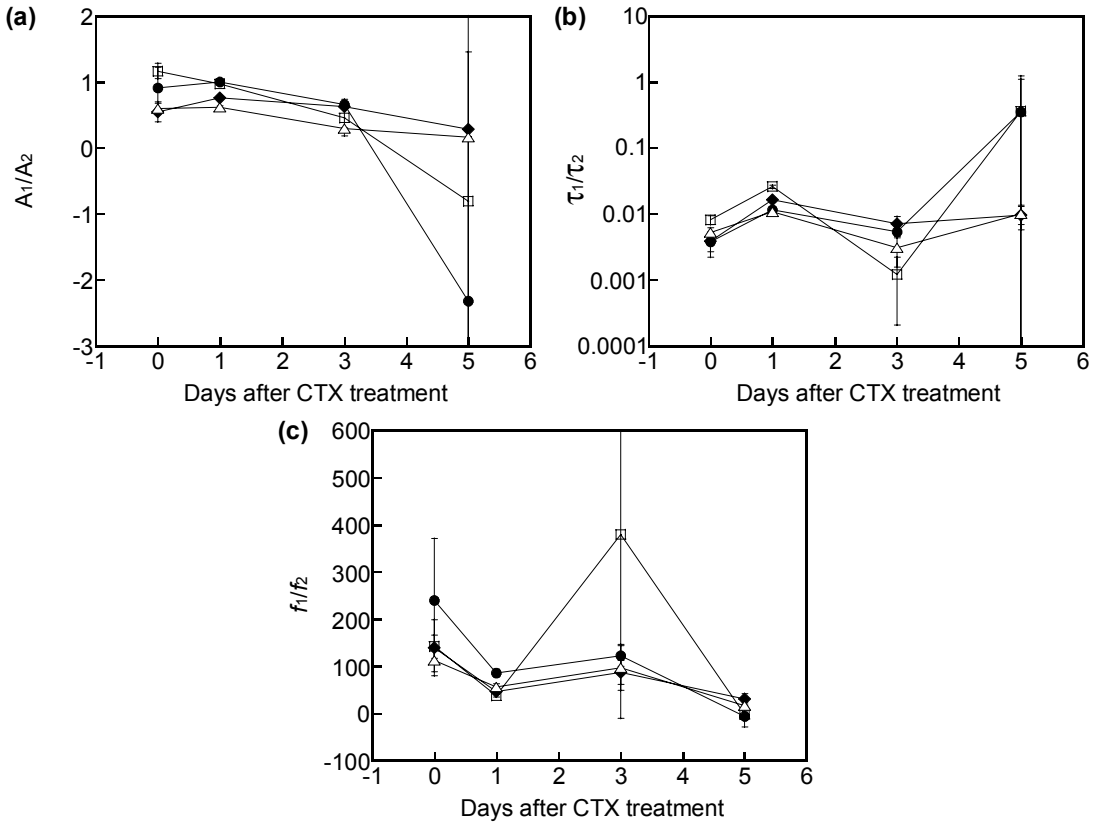

Fig. 8.11 Summary of the fitted parameters, A_1/A_2 (a), τ_1/τ_2 (b), and f_1/f_2 (c), by using the bi-exponential model.

Figure 8.11(b) shows changes in τ_1/τ_2 ratio after CTX treatment in a logarithmic scale. The ratio of τ_1/τ_2 is initially less than 0.01, meaning that there is a great difference in blood flow velocity between the well perfused and poorly perfused region of the tumor. However, an enormous increase of τ_1/τ_2 from two sections of the tumor at day 5 gives values of τ_1/τ_2 close to 1, suggesting that there is no significant difference in blood flow velocity between the well perfused and poorly perfused region of the tumor. Figure 8.11(c) shows the changes of f_1/f_2 after CTX administration. There is a great difference in perfusion rate at day 0 between the two distinct perfused regions in the tumor since the values of f_1/f_2 at all four channels are much larger than 1. However, 5 days after the treatment, I see much smaller values of f_1/f_2, suggesting that the perfusion rates within the tumor become more uniform and less distinct. In summary, all of these results indeed lead to the conclusion that the well perfused region of tumor is most likely to be affected first (Fig. 8.11(a)) after CTX treatment, and thus the corresponding blood flow velocity becomes closer to the value at the poorly perfused region of the tumor (Fig. 8.11(b)), resulting in less distinct perfusion rates within the tumor (Fig. 8.11(c)).

8.3.8 Correlations between tumor volume regressions and fitted parameters

Figure 8.12 shows correlations between the hemodynamic parameters and tumor volume decreases after CTX treatment. The data shown here include all of the measurements from the single high-dose (n=5) from all channels available. To find the correlations, at first, tumor volume changes from the CTX treated group were

normalized to the volume at day 0, as shown in Fig. 8.2(b). The second step was to normalize the maximum changes of $[HbO_2]$ during oxygen intervention ($\Delta[HbO_2]_{max}$) to the values of $[HbO_2]_{max}$ at Day 0. Figure 8.12(a) shows that there is a good correlation between the normalized $\Delta[HbO_2]_{max}$ and normalized tumor volume decrease after CTX treatment. This implies that when the tumor volume decreases due to the cytotoxic effects of CTX, there is a decrease in changes of tumor vascular oxygenation.

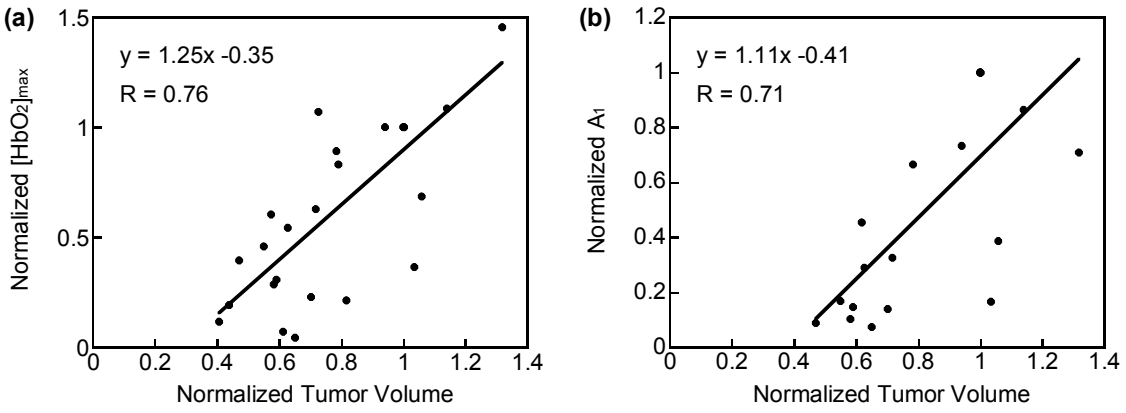

Fig. 8.12 Correlations between the normalized tumor volume changes and normalized $\Delta[HbO_2]_{max}$ (a) and normalized A1 values (b) during oxygen intervention after CTX treatment.

Figure 8.12(b) shows a correlation between the normalized A_1 values (from the well-perfused region) and normalized tumor volume decreases. It also has a relatively strong correlation. However, there is a weak correlation between the normalized A_2 values (from the poorly perfused region) and normalized tumor volume decreases (R = 0.54, data not shown). These results indicate that the decreases in tumor volume after CTX treatment are more associated or correlated with the therapeutic effects in the well

perfused/periphery region of the tumors, rather then in the poorly perfused region. In other words, the well perfused region of tumors is more likely to be affected by CTX, leading to deceases in tumor volume.

8.4 Discussions and conclusions

Changes of rat tumor volume show that CTX treatment is effective for this tumor type. For the control group, the average rat body weight gradually decreased during the entire time course of treatment, possibly due to the sickness of rats induced by the tumor growth (cachexia) or a frequent anesthesia. (At Day 10, the tumor volume was ~5 times as large as that at Day 0.) It is clear that there is different effectiveness of CTX treatment between the single high dose group (200mg/kg) and metronomic low dose group (20mg/kg for 10 days). Both of the CTX treatments delayed the tumor growth and even further reduced the tumor volume. However, a single high dose of CTX treatment caused the death of two rats, and the tumor volume was not decreased further 4 days after the treatment, while the metronomic low dose CTX treatment continued to provide tumor regression without causing severe sickness. From this observation, it is obvious that the metronomic low dose of CTX treatment is working much better than a single high dose for a rat mammary adenocarcinomas 13762NF tumor.

Earlier works by Liu *et al*. have used a single-channel NIRS system with one light source and one detector for global measurements of $\Delta[HbO_2]$ and $\Delta[Hb_{total}]$ in tumors during respiratory challenges [31] [33] [34]. Through those experiments, it has

been found that most tumors have a bi-phasic behavior in $\Delta[HbO_2]$ increase (i.e., a rapid increase followed by a slow and gradual increase) after switching the gas from air to carbogen/oxygen. To explain this bi-phasic behavior, Liu *et al.* have developed a mathematical model and formed a hypothesis that the bi-phasic behavior of $\Delta[HbO_2]$ during carbogen/oxygen inhalation results from two different vascular regions in tumor with two blood perfusion rates and vascular structures [31].

By giving oxygen intervention, tumor blood vessels are acutely subject to an increase of $[HbO_2]$ due to higher supply of oxygenated blood from artery compared to that with air breathing. However, due to the irregular vascular structure in tumor, the well perfused regions in tumor may have an increase in $[HbO_2]$ much faster than the other parts of tumor that are poorly perfused. Therefore, two time constants obtained from the tumor hemodynamic measurements during oxygen intervention allow revealing two blood flow/perfusion rates in tumor, more precisely, two different blood flow velocities within the tumor blood vessels. More recently, my study has shown that the bi-phasic increase in optical density occurs when there exist two different flow rates in dynamic tumor vascular phantoms [138], and it was also supported by a FEM simulation study [139]. The bi-phasic hemodynamic model is the basis of this chapter where I wish to detect any changes in vascular structures, hemodynamic features, or perfusion rate within a tumor after CTX treatment.

The amplitudes and time constants fitted from $\Delta[HbO_2]$ increase (Fig. 8.5) are summarized in Table 8.3 for single high-dose group, Tumor A. At day 0, A_1/A_2 is higher than 1, indicating that the measured signal results more from the well perfused

region than poorly perfused region. However, this ratio becomes less than 1 after injection of cyclophosphamide (Day 1 and 3). This may be explained by destruction of the well perfused vascular structure in tumor after chemotherapy. I expect that after a single high dose administration of CTX, the drug circulates in the blood vessels and is delivered to the tumor cells more in the well perfused region than in the poorly perfused region. This will lead to death of tumor cells in the well perfused region more effectively than that in the poorly perfused region, eventually resulting in decreases in tumor volume starting in the well perfused region followed by the tumor shrinkage in the poorly perfused region. Then, the tumor volume containing the well perfused regions will consequently decrease, so will the contribution of detected NIR signals from the well perfused region. In other words, a decrease in A_1/A_2 may indicate decease in well perfused tumor volume after the administration of CTX. This expectation is confirmed by the fitted parameters graphically shown in Figs. 8.8-8.9.

As shown in Table 8.3 and also in Fig. 8.11(c), the perfusion rate ratio, f_1/f_2, decreased after a single high dose of CTX administration. At Day 0, f_1/f_2 was very high, meaning that there was a big difference in perfusion rate between the well perfused and poorly perfused region in tumor. However, this ratio significantly decreased at Day 1 and 3 after CTX treatment, representing that the perfusion rate gap between the two distinct perfused regions became much smaller than that at Day 0. At Day 5, changes in $[HbO_2]$ during oxygen intervention do not show any bi-phasic behavior anymore, and it was fitted by a single-exponential model. This observation basically indicates that most of tumor cells and/or tumor vasculature in the well perfused region are possibly

destroyed by the effect of CTX, resulting in quite different hemodynamic behavior, i.e., converting a double-exponential feature to a single-exponential feature.

According to others [159] [167], an increase of perfusion was observed after CTX treatment, which is opposite to the results that I have obtained. However, there are a few differences between their results and mine that are shown in this chapter. Firstly, the treatment in their study showed a delay of tumor growth, and some viable tumor cells restarted to grow. However, in my study, the regression of tumor volume was observed after CTX treatment, and the regrowth of tumors was not found at least within the experimental period. Secondly, I have used rat mammary adenocarcinomas 13762NF, while radiation induced fibrosarcoma-1 (RIF-1) tumor was used in all of the referred studies. The dosages that the authors have used are 200 mg/kg [159] and 300 mg/kg [167], which do not differ much from the dosage that I have used (200mg/kg). Therefore, it may be possible that the tumor line used in this study has a greater susceptibility to CTX treatment than RIF-1 tumors that the other studies have used. In those studes, the authors have reported that the increase of perfusion/blood flow precedes the regrowth of viable tumor cells. Since there was no tumor regrowth during my study, I could expect a decrease in blood perfusion in tumors, which was also reported by Braunschweiger and Schiffer [165].

While the two different CTX treatment plans (i.e., single high dose and metronomic low dose) showed a few similar effects on tumor hemodynamics, it is noteworthy that the tumor hemodynamics at day 6 from the metronomic low dose CTX treatment (Fig. 8.4) still shows a bi-exponential feature and also a relatively high

maximum $\Delta[HbO_2]$ compared to that observed from a tumor at day 5 after a single high dose treatment (Fig. 8.5). This may imply that the metronomic low dose CTX treatment causes less disruption in tumor vasculature while it still give great therapeutic effects on rat breast tumors.

Tumor volume changes after CTX treatments were correlated well with some of the hemodynamic parameters (Fig. 8.12). It has been shown that there are strong correlations between tumor volume decreases and $\Delta[HbO_2]_{max}$ (R=0.76), A_1 (R=0.71), and f_1 (R=0.68) values (data not shown), respectively, while there are weak correlations between tumor volume decreases and A_2 (R=0.54), τ_1 (R=0.09), τ_2 (R=0.09), and f_2 (R=0.24).(data not shown). All of these results suggest that the decreases in tumor volume after CTX treatments are highly associated with the therapeutic effects of CTX in the well perfused/periphery region of the tumors, essentially causing a decrease in the well perfused tumor volume.

In conclusion, I have conducted the study in this chapter to show the possibility of using multi-channel NIRS to monitor tumor responses to CTX, which is one of the conventional chemotherapeutic agents, by comparing the changes in tumor vascular oxygenation before and after CTX treatment. The intratumoral and intertumoral heterogeneity of tumor vascular responses to CTX treatment were easily observed by quantifying the blood perfusion rate and vascular coefficients at four different locations of the tumor or taken from different tumors, respectively. Tumor hemodynamics has been significantly changed before and after CTX treatment compared to the saline-treated control group, showing high feasibility of using a multi-channel NIRS system as

a monitoring tool for cancer treatments. The future goal of my study will include the development of NIR imaging systems to obtain maps of tumor hemodynamic changes under therapeutic interventions or treatments from a whole tumor, allowing one to predict the efficacy of tumor treatment for better therapy outcome.

* This chapter was presented at Photonics West held by SPIE in 2005. This chapter is going to be prepared for a manuscript and is going to be submitted to the Neoplasia.

Jae G. Kim, Dawen Zhao, Ralph P. Mason, and Hanli Liu, "Chemotherapeutic (Cyclophosphamide) Effects on Rat Breast Tumor Hemodynamics Monitored by Multi-Channel NIRS.", *Proc. SPIE-Int. Soc. Opt. Eng.*, Optical Tomography and Spectroscopy of Tissue VI (ed: Chance et al) **, 5693**, 282-292 (2005).

CHAPTER 9

CONCLUSIONS AND FUTURE SUGGESTIONS

9.1 Conclusions

Two hypotheses and seven specific aims of my dissertation are reintroduced in this chapter with the conclusions drawn for each of the aims.

Hypothesis 1: The experimentally observed bi-phasic feature of $\Delta[HbO_2]$ increase in rat breast tumors during hyperoxic gas interventions is highly associated with two different perfusion rates within the tumor.

Aim 1: to modify and refine algorithms for accurate determination of oxygenated and de oxygenated hemoglobin concentrations in tumors. (Chapter 2)

Conclusion: the original algorithm that was used for a single-channel, frequency–domain, NIRS system was empirically modified for better accuracy to be used for tumor study. Later, I have found that the errors in the original algorithm were caused by data interpolation in hemoglobin extinction coefficients, which deviated from the correct values. I achieved an error analysis for possible variations in hemoglobin concentrations, which could result from discrepancies in hemoglobin extinction coefficients, and found that notable errors could be

caused by small discrepancies in hemoglobin extinction coefficients. Moreover, I performed a calibration experiment for a new NIR system that uses a white light source and a CCD-based spectrometer, and showed that a proper selection of two wavelengths can provide results as good as those derived from six-wavelength measurements using a multi-wavelength algorithm.

Aim 2: to develop a tumor vascular dynamic phantom to prove that the bi-phasic feature of $\Delta[HbO_2]$ increase in tumor during oxygen intervention is highly associated w ith two different perfusion rates within the tumor. (Chapter 3)

Conclusion: by either having two different diameters for the tubing with the same flow rate or having the same diameter tubing, but with two different flow rates, I could experimentally simulate, with India ink, the bi-phasic feature that was observed from the tumor oxygenation increase during hyperoxic gas intervention. This dynamic vascular phantom study of the transfer fuction proved that the bi-phasic feature can result from two different perfusion rates or two blood flow velocities within the tumor vasculature.

Aim 3: to support the tumor vascular dynamic phantom experiments by numerically simulating bi-phasic tumor oxygen dynamics using the steady state Finite Element Method with variable lengths of perfusion. (Chapter 4)

Conclusion: The finite element method was applied to simulate the results from the dynamic tumor vascular phantom and showed again that the bi-phasic increase

in $\Delta[HbO_2]$ could result from two different blood flow velocities in the tumor.

Hypothesis 2: NIRS is complementary with other techniques used to measure tumor oxygenation and can monitor cancer therapy effects by detecting changes in tumor vascular hemodynamics during respiratory challenges.

Aim 4: to demonstrate the consistency and correlation of NIRS results with those taken from needle pO_2 electrodes and MRI pO_2 readings. (Chapter 5)

Conclusion: NIRS measurements of $\Delta[HbO_2]$ are complementary to other techniques such as pO_2 needle electrodes and MRI pO_2 mapping. It was learned that increases in tumor tissue pO_2 during hyperoxic gas intervention depended highly on the baseline pO_2 level, while $\Delta[HbO_2]$ measured by NIRS always showed a significant increase, since the current NIRS instrument utilized only a single channel for global measurements. I concluded that NIRS imaging needs to be developed to correlate local blood oxygen level with a local pO_2 level in tumor tissues.

Aim 5: to monitor and investigate tumor vascular responses before and after administration of a vascular disrupting agent using NIRS. (Chapter 6)

Conclusion: A vascular disrupting agent (CA4P) caused a significant and acute drop in both blood volume and oxygenated hemoglobin concentration. By applying oxygen intervention, the changes in vascular hemodynamics were obtained and

fitted with the proved bi-exponential model. I have developed and performed novel data analysis on dynamic signals of $\Delta[HbO_2]$ and $\Delta[Hb_{total}]$ after CA4P administration. The fitted parameters revealed non-invasively the evolution and alternation of tumor vasculature and perfusion after the CA4P treatment, having great consistencies with other published reports. This study shows great promise for future applications of NIRS to serve as a monitoring tool for cancer therapy.

Aim 6: to monitor and quantify the heterogeneity of tumor vasculature using a multi-channel NIRS system with the proved mathematical model. (Chapter 7)

Conclusion: A three- or four- channel NIRS system was employed to investigate the heterogeneities in tumor hemodyanmics during hyperoxic gas interventions. The results clearly showed that the hemodynamic heterogeneities can be observed by a multi-channel NIRS and also suggested that a multi-channel NIRS could be a very useful tool to monitor tumors' heterogeneous response to cancer therapies.

Aim 7: to monitor responses of tumors before and after cyclophosphamide treatment using a multi-channel NIRS system, and to understand the therapeutic effects on tumor vasculatures. (Chapter 8)

Conclusion: This study proves again that NIRS can be used as a tool for monitoring tumor responses to cancer therapies in addition to a vascular disrupting agent. By employing a multi-channel NIRS, the heterogeneous responses to the therapy were observed intratumorally and intertumorally.

Overall, through my dissertation research, I have proved two hypotheses by accomplishing seven specific aims. A continuous wave NIRS is a relatively simple system that can monitor the changes in oxy-, deoxy-, and total hemoglobin concentration in isolated tissues. Hyperoxic gas intervention has been used to enhance the tumor blood oxygenation to make tumors more susceptible for cancer therapies. In addition, hyperoxic gas intervention can also serve as a contrast or a perturbation agent to introduce an acute hemodynamic signal and thus to enhance the NIRS signals significantly. A combination of the bi-phasic mathematical model and the acute NIRS signals measured during oxygen intervention provides a unique and excellent opportunity to non-invasively gain insight into the evolution and alternation of tumor vasculature and hemodynamic perfusion after drug treatment.

9.2 Future Suggestions

As mentioned in the discussion and conclusion sections of earlier chapters, there is a need for developing an NIR imaging system. A single-channel NIRS system used in Chapters 5 and 6 gave global changes in tumor oxygenation and also in blood volume during hyperoxic gas intervention. Later, my study extended to use 3- or 4- channel NIRS systems, as reported in Chapter 7 and 8, so that I could have local information detected from each detector to prove high heterogeneities in tumor vasculature and to reveal heterogeneous responses to chemotherapy. However, there is a limit of using a multi-channel NIRS system due to the finite size of experimental tumors, the light source, and the detectors. Currently, an NIR imaging system is being developed using a

CCD camera, which will provide spatial images of changes in tumor blood oxygenation and blood volume due to either oxygen intervention or therapeutic treatment. It could be correlated with pO_2 maps obtained from ^{19}F MR pO_2 mapping as it was suggested in Chapter 5.

An NIR imaging system could be combined with other optical imaging modalities such as fluorescence imaging and luminescence imaging, since all of these imaging modalities are CCD camera based systems. By employing optical fibers for NIR imaging, it could be compatible with CT, PET and MRI, which are being developed by others. NIR imaging cannot provide spatial resolution as well as CT or MRI due to its intrinsic characteristic of light diffusion in a highly scattering media, such as tissues. However, NIR imaging has a great sensitivity in detecting changes in hemoglobin concentrations and also has a high temporal resolution, both of which are essential for obtaining any functional change from tumor/cancer under therapy.

In chapters 6 and 8, I proved that NIRS can be a useful tool to detect tumor responses to cancer therapy. Therefore, I believe that it is worthwhile to apply an NIR imaging system to monitor tumor responses during and after regular cancer therapies such as radiation therapy, photodynamic therapy, and chemotherapy. Currently, many antiangiogenic or antivascular drugs are being developed for cancer treatments and under clinical studies, and NIRS/NIR imaging system could be a perfect tool to test these drugs' effects on tumor vasculatures non-invasively. With the current technologies available, a continuous wave NIRS can be made in a really portable, hand-held size, and it could be even smaller when MEMS technologies are matured in the

near future. I can imagine that a combination of the wireless technology and MEMS technology will make an attachable NIRS possible, which further opens up much more applications for biomedical research and clinical practice

Currently, the applications of NIRS/NIR imaging are mostly on the studies of cancers, brain function, and exercised muscles. However, I believe that there are more applications of NIRS/NIR imaging which one just need to explore and find.

APPENDIX A

THE EXTINCTION COEFFICIENT VALUES OF HUMAN HEMOGLOBIN

Appendix A1. The per equivalent extinction coefficients of deoxyhaemoglobin (unit: 0.25 $mM^{-1}cm^{-1}$)

Wavelength (nm)	Van Kampen (1965)	Van Assendelft (1970) (Takatani 1979)	Van Assendelft (1975)	Zijlstra (1987)	Wray (1988)	Mendelson (1989)	Cope (1991)	Zijlstra (1991)	Steinke (1992)	Zijlstra (1994)	Matcher (1995)	Prahl (1998)	Zijlstra (2000)
400												55.824	
402												59.047	
404												63.342	
406												67.637	
408												71.839	
410												75.989	
412												80.336	
414												85.649	
415													
416												90.962	
418												96.42	
420												101.89	
422												107.47	
424												115.3	
426												120.46	
428												125.21	
430												132.15	
431	140.1												
432												138.04	
434												138.04	
436												136.76	
438												125.39	
440												103.32	
442												90.81	
444												70.681	
446												59.306	
448												43.33	
450		14.5						13.51				25.823	13.48
452												15.66	10.58
454												9.0425	8.52
456												7.6747	7.022
458												6.4716	5.932
460		5.15										5.8472	5.131
462												5.2228	4.552
464												4.8152	4.12
466												4.5356	3.813
468												4.2564	3.602
470												4.0391	3.457
472												3.8275	3.366
474												3.7621	3.318
476												3.6982	3.297
478	3.31											3.6643	3.302
478.6									3.23				
480		3.34						3.35				3.6375	3.322
482												3.7203	3.353
484												3.8031	3.405
486												3.8859	3.465
488												3.9745	3.538
488.4									3.434				
490												4.171	3.633
492												4.3674	3.736
494												4.5639	3.861
496												4.7603	3.998
497.6									4.003				
498												4.9728	4.158

Wavelength (nm)	Van Kampen (1965)	Van Assendelft (1970) (Takatani 1979)	Van Assendelft (1975)	Zijlstra (1987)	Wray (1988)	Mendelson (1989)	Cope (1991)	Zijlstra (1991)	Steinke (1992)	Zijlstra (1994)	Matcher (1995)	Prahl (1998)	Zijlstra (2000)
500		4.09		4.31				4.34		4.34		5.2155	4.33
502												5.4582	4.525
504												5.7009	4.727
504.4									4.718				
506												5.9436	4.948
507		4.81							5.01				
508												6.1863	5.16
510		5		5.32						5.38		6.4434	5.383
512									5.523			6.7342	5.593
514												7.025	5.816
516												7.3158	6.025
517.4									6.107				
518												7.6066	6.249
520		6.27		6.4				6.48	6.424	6.48		7.8974	6.478
522		6.42										8.2128	6.737
524												8.5994	7.011
526												8.986	7.317
527.1									7.395				
528												9.3725	7.644
530				7.97						8.04		9.7591	8.01
532												10.146	8.411
534												10.522	8.866
534.1									8.815				
536												10.898	9.355
538										9.94		11.273	9.901
540		10.28	10.3	10.41				10.5		10.5		11.648	10.47
540.5									10.493				
541													
542		11		10.97				11.09		11.09		12.037	11.06
543													
544												12.427	11.62
545.3									11.849				
546												12.817	12.15
548												13.124	12.59
549		12.46											
549.4									12.604				
550				12.69				13.15		12.97		13.353	12.96
551.4									12.872				
552												13.52	13.21
554	13.04							13.35		13.34		13.63	13.35
555	13.04	13.04							13.081				
556	13.04											13.635	13.36
557.3									13.032				
558												13.541	13.29
560		12.54	12.7	12.72				13.09		13.09		13.447	13.11
562												13.069	12.88
562.4									12.376				
564												12.643	12.59
566									11.833			12.207	12.25
568				11.57				11.85		11.85		11.737	11.85
569		11.27											
570			11	11.04						11.44		11.268	11.42
570.9									10.758				
572												10.835	10.96
574												10.429	10.49
576			9.8	9.92				10.07		10.07		10.023	10.02
576.5													

Wavelength (nm)	Van Kampen (1965)	Van Assendelft (1970) (Takatani 1979)	Van Assendelft (1975)	Zijlstra (1987)	Wray (1988)	Mendelson (1989)	Cope (1991)	Zijlstra (1991)	Steinke (1992)	Zijlstra (1994)	Matcher (1995)	Prahl (1998)	Zijlstra (2000)
577		9.2											
577.7									9.087				
578								9.62				9.6169	9.564
579		8.86											
580				9.06						9.19		9.255	9.141
582												8.9191	8.734
584												8.5832	8.333
585.2									7.83				
586		7.23										8.2129	7.903
588												7.7688	7.422
588.2									7.044				
590				6.55				6.87		6.87		7.0811	6.875
592												6.3675	6.271
594												5.6437	5.629
594.5									5.08				
596												4.95	4.976
597.5									2.736				
598												4.2646	4.342
600		1.47		3.59				3.74		3.74		3.6693	3.759
602												3.4056	3.242
603									2.112				
604												3.1419	2.806
605		2.374											
606												2.8783	2.452
608												2.6194	2.169
609.6									1.913				
610												2.3609	1.946
612												2.1478	1.768
614												1.9405	1.627
614.3									1.606				
615		1.444											
616												1.8362	1.514
616.4									1.487				
618												1.7318	1.418
620												1.6274	1.336
621.7									1.304				
622												1.5483	1.27
624												1.4767	1.212
625		1.1											
626												1.405	1.163
626.6									1.176				
628												1.3417	1.12
630			1					1.09		1.06		1.2872	1.082
632												1.2327	1.022
633.4									1.063				
634												1.1827	0.996
635		0.949											
636												1.1506	0.974
638												1.1184	0.953
640												1.0863	0.936
640.2									0.971				
642												1.0542	0.92
644												1.0221	0.907
645		0.859											
646												0.99127	0.895
648												0.9644	0.884
650					0.9358		0.9338				0.9338	0.93753	0.873

Wavelength (nm)	Van Kampen (1965)	Van Assendelft (1970) (Takatani 1979)	Van Assendelft (1975)	Zijlstra (1987)	Wray (1988)	Mendelson (1989)	Cope (1991)	Zijlstra (1991)	Steinke (1992)	Zijlstra (1994)	Matcher (1995)	Prahl (1998)	Zijlstra (2000)
650.7									0.89				
651							0.9260				0.9260		
652							0.9182				0.9182	0.91066	0.864
653					0.9110		0.9104				0.9104		
654							0.9032				0.9032	0.88379	0.852
655		0.811					0.8960				0.8960		
656							0.8889				0.8889	0.85692	0.836
657					0.8865		0.8817				0.8817		
658							0.8746				0.8746	0.83005	0.828
659							0.8674				0.8674		
660		0.8			0.8605	0.86	0.8602	0.81		0.81	0.8602	0.80664	0.815
661							0.8516				0.8516		
662							0.8429				0.8429	0.78507	0.799
663					0.8315		0.8343				0.8343		
664							0.8248				0.8248	0.76349	0.782
665		0.789					0.8146				0.8146		
666							0.8044				0.8044	0.74192	0.763
667					0.7983		0.7941				0.7941		
668							0.7832				0.7832	0.72035	0.743
669							0.7723				0.7723		
670					0.7608		0.7614				0.7614	0.69878	0.721
671							0.7498				0.7498		
672							0.7380				0.7380	0.67721	0.699
673							0.7261				0.7261		
674					0.7198		0.7142				0.7142	0.65691	0.677
675		0.757					0.7022				0.7022		
676							0.6902				0.6902	0.6386	0.655
677					0.6783		0.6781				0.6781		
678							0.6663				0.6663	0.62029	0.633
679							0.6546				0.6546		
680							0.6428	0.61		0.62	0.6428	0.60198	0.612
681					0.6375		0.6312				0.6312		
682							0.6197				0.6197	0.58367	0.591
683							0.6082				0.6082		
684					0.5980		0.5968				0.5968	0.56537	0.571
685		0.699					0.5859				0.5859		
686							0.5751				0.5751	0.54706	0.551
687					0.5608		0.5643				0.5643		
688							0.5541				0.5541	0.52875	0.533
689							0.5443				0.5443		
690							0.5345				0.5345	0.51299	0.516
691					0.5270		0.5249				0.5249		
692							0.5164				0.5164	0.50012	0.5
693							0.5079				0.5079		
694					0.4975		0.4994				0.4994	0.48726	0.485
695		0.606					0.4916				0.4916		
696							0.4843				0.4843	0.47439	0.471
697							0.4769				0.4769		
698					0.4718		0.4698				0.4698	0.46152	0.459
699							0.4633				0.4633		
700							0.4568	0.44		0.45	0.4568	0.44857	0.447
701					0.4495		0.4503				0.4503		
702							0.4444				0.4444	0.43525	0.436
703							0.4387				0.4387		
704							0.4330				0.4330	0.42194	0.426
705		0.497			0.4300		0.4275				0.4275		
706							0.4222				0.4222	0.40862	0.416
707							0.4169				0.4169		

Wavelength (nm)	Van Kampen (1965)	Van Assendelft (1970) (Takatani 1979)	Van Assendelft (1975)	Zijlstra (1987)	Wray (1988)	Mendelson (1989)	Cope (1991)	Zijlstra (1991)	Steinke (1992)	Zijlstra (1994)	Matcher (1995)	Prahl (1998)	Zijlstra (2000)
708					0.4118		0.4116				0.4116	0.39588	0.406
709							0.4067				0.4067		
710							0.4018				0.4018	0.38512	
711					0.3948		0.3968				0.3968		
712							0.3919				0.3919	0.37435	0.387
713							0.3870				0.3870		
714							0.3821				0.3821	0.36359	0.379
715		0.407			0.3783		0.3773				0.3773		
716							0.3727				0.3727	0.35283	0.37
717							0.3680				0.3680		
718					0.3625		0.3634				0.3634	0.34207	0.361
719							0.3591				0.3591		
720							0.3549				0.3549	0.33147	0.353
721					0.3480		0.3507				0.3507		
722							0.3469				0.3469	0.32129	0.346
723							0.3433				0.3433		
724							0.3398				0.3398	0.31111	0.34
725		0.4655			0.3358		0.3364				0.3364		
726							0.3338				0.3338	0.30092	0.334
727							0.3312				0.3312		
728					0.3268		0.3287				0.3287	0.2882	0.33
729							0.3270				0.3270		
730							0.3257				0.3257	0.27555	0.327
731							0.3244				0.3244		
732					0.3215		0.3237				0.3237	0.27555	0.326
733							0.3238				0.3238		
734							0.3238				0.3238	0.27555	0.327
735		0.366			0.3215		0.3240				0.3240		
736							0.3257				0.3257	0.27544	0.329
737							0.3274				0.3274		
738					0.3268		0.3291				0.3291	0.27512	0.333
739							0.3319				0.3319		
740							0.3353				0.3353	0.27897	0.339
741							0.3386				0.3386		
742					0.3373		0.3424				0.3424	0.29041	0.346
743							0.3472				0.3472		
744							0.3520				0.3520	0.30185	0.355
745		0.404			0.3530		0.3567				0.3567		
746							0.3625				0.3625	0.31651	0.366
747							0.3684				0.3684		
748					0.3725		0.3743				0.3743	0.33331	0.377
749							0.3803				0.3803		
750							0.3864	0.39		0.37	0.3864	0.35131	0.388
751							0.3926				0.3926		
752					0.3935		0.3984				0.3984	0.37883	0.399
753							0.4036				0.4036		
754							0.4086				0.4086	0.38544	0.409
755		0.439			0.4110		0.4137				0.4137		
756							0.4162				0.4162	0.39012	0.415
757							0.4183				0.4183		
758					0.4195		0.4205				0.4205	0.39012	0.417
759							0.4204				0.4204		
760							0.4186				0.4186	0.38713	0.414
761							0.4169				0.4169		
762					0.4150		0.4142				0.4142	0.37711	0.407
763							0.4086				0.4086		
764							0.4030				0.4030	0.36489	0.396
765		0.41			0.3975		0.3974				0.3974		

Wavelength (nm)	Van Kampen (1965)	Van Assendelft (1970) (Takatani 1979)	Van Assendelft (1975)	Zijlstra (1987)	Wray (1988)	Mendelson (1989)	Cope (1991)	Zijlstra (1991)	Steinke (1992)	Zijlstra (1994)	Matcher (1995)	Prahl (1998)	Zijlstra (2000)
766							0.3896				0.3896	0.35263	0.381
767							0.3815				0.3815		
768					0.3713		0.3734				0.3734	0.34033	0.364
769							0.3647				0.3647		
770							0.3557				0.3557	0.32797	0.347
771							0.3467				0.3467		
772					0.3413		0.3378				0.3378	0.31561	0.33
773							0.3292				0.3292		
774							0.3206				0.3206	0.30325	0.314
775		0.335			0.3125		0.3120	0.29		0.32	0.3120		
776							0.3044				0.3044	0.29089	0.299
777							0.2968				0.2968		
778					0.2873		0.2892				0.2892	0.2787	0.285
779							0.2825				0.2825		
780							0.2763				0.2763	0.26886	0.273
781							0.2701				0.2701		
782					0.2665		0.2643				0.2643	0.25902	0.262
783							0.2593				0.2593		
784							0.2543				0.2543	0.24918	0.253
785		0.26			0.2498		0.2494				0.2494		
786							0.2455				0.2455	0.23934	0.245
787							0.2417				0.2417		
788					0.2370		0.2379				0.2379	0.23045	0.238
789							0.2346				0.2346		
790							0.2316				0.2316	0.2227	0.233
791							0.2286				0.2286		
792					0.2270		0.2258				0.2258	0.21495	0.228
793							0.2235				0.2235		
794							0.2211				0.2211	0.2072	0.223
795		0.241			0.2193		0.2188				0.2188		
796							0.2169				0.2169	0.20074	0.219
797							0.2150				0.2150		
798					0.2130		0.2131				0.2131	0.19559	0.216
799							0.2115				0.2115		
800							0.2100	0.2		0.21	0.2100	0.19043	0.215
801					0.2080		0.2085				0.2085		
802							0.2071				0.2071	0.18596	
803							0.2059				0.2059		
804							0.2047				0.2047	0.18427	
805		0.224			0.2040		0.2036	0.2			0.2036		0.204
806							0.2028				0.2028	0.18257	
807							0.2019				0.2019		
808					0.2010		0.2010				0.2010	0.18088	
809							0.2003				0.2003		
810							0.1997				0.1997	0.17927	
811					0.1990		0.1990				0.1990		
812							0.1985				0.1985	0.17796	
813							0.1980				0.1980		
814					0.1973		0.1976				0.1976	0.17665	
815		0.22					0.1972				0.1972		
816							0.1969				0.1969	0.17533	
817							0.1965				0.1965		
818					0.1963		0.1962				0.1962	0.17402	
819							0.1960				0.1960		
820							0.1959				0.1959	0.17344	
821					0.1955		0.1957				0.1957		
822							0.1955				0.1955	0.1734	
823							0.1954				0.1954		

Wavelength (nm)	Van Kampen (1965)	Van Assendelft (1970) (Takatani 1979)	Van Assendelft (1975)	Zijlstra (1987)	Wray (1988)	Mendelson (1989)	Cope (1991)	Zijlstra (1991)	Steinke (1992)	Zijlstra (1994)	Matcher (1995)	Prahl (1998)	Zijlstra (2000)
824					0.1948		0.1953				0.1953	0.17337	
825		0.208					0.1952				0.1952		
826							0.1952				0.1952	0.17333	
827							0.1951				0.1951		
828					0.1945		0.1951				0.1951	0.1733	
829							0.1951				0.1951		
830							0.1951				0.1951	0.17326	
831					0.1945		0.1951				0.1951		
832							0.1951				0.1951	0.17323	
833							0.1951				0.1951		
834					0.1943		0.1951				0.1951	0.17319	
835		0.205					0.1951				0.1951		
836							0.1951				0.1951	0.17316	
837					0.1943		0.1952				0.1952		
838							0.1952				0.1952	0.17312	
839							0.1953				0.1953		
840					0.1943		0.1954	0.19			0.1954	0.17309	0.19
841							0.1954				0.1954		
842							0.1955				0.1955	0.17305	
843							0.1956				0.1956		
844					0.1945		0.1957				0.1957	0.17299	
845		0.205					0.1958	0.19			0.1958		0.192
846							0.1960				0.1960	0.17294	
847					0.1950		0.1961				0.1961		
848							0.1963				0.1963	0.17288	
849							0.1964				0.1964		
850					0.1953		0.1965				0.1965	0.17283	
851							0.1968				0.1968		
852							0.1970				0.1970	0.17277	
853					0.1960		0.1973				0.1973		
854							0.1975				0.1975	0.17272	
855		0.205					0.1978				0.1978		
856							0.1981				0.1981	0.17266	
857					0.1970		0.1984				0.1984		
858							0.1987				0.1987	0.17311	
859							0.1991				0.1991		
860					0.1980		0.1994				0.1994	0.17358	
861							0.1998				0.1998		
862							0.2002				0.2002	0.17405	
863					0.1993		0.2006				0.2006		
864							0.2011				0.2011	0.17451	
865		0.205					0.2016				0.2016		
866					0.2008		0.2021				0.2021	0.17498	
867							0.2026				0.2026		
868							0.2031				0.2031	0.17545	
869					0.2025		0.2036				0.2036		
870							0.2041				0.2041	0.17646	
871							0.2047				0.2047		
872					0.2043		0.2053				0.2053	0.17749	
873							0.2059				0.2059		
874							0.2065				0.2065	0.17852	
875		0.212					0.2071				0.2071		
876					0.2060		0.2078				0.2078	0.17955	
877							0.2084				0.2084		
878							0.2090				0.2090	0.18058	
879					0.2083		0.2097				0.2097		
880							0.2103	0.2			0.2103	0.18161	0.2
881							0.2109				0.2109		

Wavelength (nm)	Van Kampen (1965)	Van Assendelft (1970) (Takatani 1979)	Van Assendelft (1975)	Zijlstra (1987)	Wray (1988)	Mendelson (1989)	Cope (1991)	Zijlstra (1991)	Steinke (1992)	Zijlstra (1994)	Matcher (1995)	Prahl (1998)	Zijlstra (2000)
882					0.2103		0.2116				0.2116	0.18246	
883							0.2122				0.2122		
884							0.2129				0.2129	0.1833	
885		0.208			0.2125		0.2136				0.2136		
886							0.2142				0.2142	0.18415	
887							0.2148				0.2148		
888					0.2145		0.2155				0.2155	0.18499	
889							0.2161				0.2161		
890							0.2167				0.2167	0.1859	
891					0.2165		0.2174				0.2174		
892							0.2180				0.2180	0.18681	
893							0.2186				0.2186		
894							0.2191				0.2191	0.18772	
895		0.221			0.2183		0.2197				0.2197		
896							0.2202				0.2202	0.18863	
897							0.2207				0.2207		
898					0.2200		0.2211				0.2211	0.18954	
899							0.2216				0.2216		
900							0.2220				0.2220	0.19046	
901					0.2213		0.2224				0.2224		
902							0.2228				0.2228	0.19126	
903							0.2231				0.2231		
904					0.2225		0.2234	0.21			0.2234	0.19186	0.213
905		0.224					0.2236				0.2236		
906							0.2238				0.2238	0.19245	
907					0.2230		0.2240				0.2240		
908							0.2241				0.2241	0.19304	
909							0.2241				0.2241		
910					0.2233		0.2242				0.2242	0.19364	
911							0.2241				0.2241		
912							0.2239				0.2239	0.19423	
913					0.2230		0.2238				0.2238		
914							0.2235				0.2235	0.1946	
915		0.231					0.2233				0.2233		
916					0.2223		0.2230				0.2230	0.19451	
917							0.2226				0.2226		
918							0.2221				0.2221	0.19443	
919							0.2217				0.2217		
920					0.2208		0.2211	0.21			0.2211	0.19434	0.208
921							0.2204				0.2204		
922							0.2198				0.2198	0.19426	
923					0.2188		0.2190				0.2190		
924							0.2181				0.2181	0.19416	
925		0.215					0.2173				0.2173		
926					0.2163		0.2164				0.2164	0.19309	
927							0.2153				0.2153		
928							0.2143				0.2143	0.19202	
929					0.2130		0.2132				0.2132		
930							0.2120				0.2120	0.19096	
931							0.2108				0.2108		
932					0.2090		0.2095				0.2095	0.18807	
933							0.2081				0.2081		
934							0.2066				0.2066	0.18439	
935		0.212			0.2048		0.2052				0.2052		
936							0.2036				0.2036	0.18072	
937							0.2020				0.2020		
938					0.1998		0.2004				0.2004	0.17704	
939							0.1986				0.1986		

Wavelength (nm)	Van Kampen (1965)	Van Assendelft (1970) (Takatani 1979)	Van Assendelft (1975)	Zijlstra (1987)	Wray (1988)	Mendelson (1989)	Cope (1991)	Zijlstra (1991)	Steinke (1992)	Zijlstra (1994)	Matcher (1995)	Prahl (1998)	Zijlstra (2000)
940		0.2				0.2	0.1969	0.18			0.1969	0.17336	0.183
941					0.1945		0.1950				0.1950		
942							0.1932				0.1932	0.16968	
943							0.1913				0.1913		
944					0.1888		0.1894				0.1894	0.16513	
945		0.189					0.1873				0.1873		
946							0.1853				0.1853	0.16027	
947					0.1823		0.1832				0.1832		
948							0.1810				0.1810	0.15541	
949							0.1789				0.1789		
950					0.1755		0.1767				0.1767	0.15056	
951							0.1746				0.1746		
952							0.1724				0.1724	0.14585	
953					0.1685		0.1703				0.1703		
954							0.1679				0.1679	0.14223	
955		0.176					0.1654				0.1654		
956					0.1613		0.1629				0.1629	0.13862	
957							0.1605				0.1605		
958							0.1581				0.1581	0.13501	
959					0.1540		0.1557				0.1557		
960							0.1533	0.14			0.1533	0.13139	0.136
961							0.1509				0.1509		
962					0.1468		0.1485				0.1485	0.12778	
963							0.1461				0.1461		
964							0.1436				0.1436	0.12384	
965		0.154			0.1395		0.1412				0.1412		
966							0.1387				0.1387	0.11833	
967							0.1363				0.1363		
968					0.1323		0.1339				0.1339	0.11283	
969							0.1315				0.1315		
970							0.1291				0.1291	0.10733	
971							0.1268				0.1268		
972					0.1253		0.1244				0.1244	0.10382	
973							0.1220				0.1220		
974							0.1196				0.1196	0.10057	
975		0.138			0.1183		0.1173				0.1173		
976							0.1149				0.1149	0.09732	
977							0.1126				0.1126		
978					0.1113		0.1103				0.1103	0.09374	
979							0.1081				0.1081		
980							0.1058				0.1058	0.08991	
981					0.1048		0.1037				0.1037		
982							0.1015				0.1015	0.08609	
983							0.0994				0.0994		
984					0.0985		0.0973				0.0973	0.08227	
985		0.106					0.0953				0.0953		
986					0.0925		0.0932				0.0932	0.07845	
987							0.0912				0.0912		
988							0.0892				0.0892	0.07463	
989					0.0868		0.0872				0.0872		
990							0.0852				0.0852	0.07081	
991							0.0834				0.0834		
992					0.0813		0.0815				0.0815	0.06698	
993							0.0797				0.0797		
994							0.0779				0.0779	0.06316	
995		0.093			0.0763		0.0762				0.0762		
996							0.0745				0.0745	0.05934	
997							0.0727				0.0727		

Wavelength (nm)	Van Kampen (1965)	Van Assendelft (1970) (Takatani 1979)	Van Assendelft (1975)	Zijlstra (1987)	Wray (1988)	Mendelson (1989)	Cope (1991)	Zijlstra (1991)	Steinke (1992)	Zijlstra (1994)	Matcher (1995)	Prahl (1998)	Zijlstra (2000)
998					0.0713		0.0710				0.0710	0.05552	
999							0.0694				0.0694		
1000								0.06			0.0678	0.0517	0.057
1001					0.0668						0.0663		
1002											0.0648		
1003											0.0633		
1004					0.0625						0.0619		
1005											0.0605		
1006											0.0591		
1007					0.0585						0.0577		
1008											0.0564		
1009											0.0552		
1010					0.0548						0.0539		
1011											0.0527		
1012											0.0515		
1013					0.0515						0.0504		
1014											0.0493		
1015											0.0482		
1016					0.0483						0.0471		
1017											0.0461		
1018											0.0451		
1019					0.0455						0.0441		
1020											0.0432		
1021											0.0422		
1022					0.0428						0.0413		
1023											0.0404		
1024											0.0396		
1025					0.0405						0.0388		
1026											0.0380		
1027											0.0373		
1028					0.0383						0.0365		
1029											0.0358		
1030											0.0351		
1031					0.0363						0.0343		
1032											0.0337		
1033											0.0330		
1034					0.0345						0.0324		
1035											0.0318		
1036					0.0328						0.0313		
1037											0.0307		
1038											0.0301		
1039					0.0313						0.0296		
1040											0.0290		
1041											0.0285		
1042					0.0300						0.0280		

Appendix A2. The per equivalent extinction coefficients of oxyhaemoglobin (unit: 0.25 $mM^{-1}cm^{-1}$)

Wavelength (nm)	Van Kampen (1965)	Van Assendelft (1970) (Takatani 1979)	Van Assendelft (1975)	Zijlstra (1987)	Wray (1988)	Mendelson (1989)	Zijlstra (1991)	Cope (1991)	Steinke (1992)	Zijlstra (1994)	Matcher (1995)	Prahl (1998)	Zijlstra (2000)
400												66.558	
402												71.056	
404												77.179	
406												88.552	
408												105.58	
410												116.71	
412												125.05	
414												131.07	
415	130.98												
416												130.47	
418												128.88	
420												120.09	
422												107.97	
424												94.059	
426												81.508	
428												70.778	
430												61.518	
431													
432												53.53	
434												41.333	
436												33.205	
438												29.785	
440												25.645	
442												23.195	
444												20.361	
446												19.081	
448												16.761	
450		17					16.2					15.704	16.2
452												14.716	14.9
454												13.388	13.8
456												12.374	12.81
458												11.874	11.96
460		11.26										11.12	11.17
462												10.33	10.5
464												9.9518	9.875
466												9.2683	9.333
468												8.7177	8.834
470												8.3023	8.399
472												7.905	7.993
474												7.5284	7.637
476												7.2127	7.303
478												6.9295	7.002
478.6									6.878				
480		6.84					6.72					6.6573	6.722
482												6.4254	6.482
484												6.2951	6.256
486												6.1674	6.073
488												6.0437	5.888
488.4									5.82				
490												5.9211	5.741
492												5.7717	5.595
494												5.6144	5.473
496												5.4626	5.353

Wavelength (nm)	Van Kampen (1965)	Van Assendelft (1970) (Takatani 1979)	Van Assendelft (1975)	Zijlstra (1987)	Wray (1988)	Mendelson (1989)	Zijlstra (1991)	Cope (1991)	Steinke (1992)	Zijlstra (1994)	Matcher (1995)	Prahl (1998)	Zijlstra (2000)
497.6									5.296				
498												5.315	5.254
500		5.05		5.18			5.15			5.15		5.2332	5.154
502												5.1491	5.07
504												5.1045	4.984
504.4									4.975				
506												4.9865	4.927
507		4.81							4.916				
508												4.999	4.882
510	4.76	4.76		4.92						4.88		5.0088	4.878
512									4.958			5.0376	4.921
514												5.1073	5.042
516												5.2504	5.235
517.4									5.49				
518												5.6274	5.548
520		5.88		6.05			5.98		6.065	5.98		6.0506	5.981
522		6.42										6.6126	6.579
524												7.3173	7.32
526												8.1241	8.23
527.1									8.968				
528												8.9975	9.25
530				10.39						10.35		9.9892	10.35
532												10.969	11.42
534												11.731	12.4
534.1									12.701				
536												12.438	13.22
538										13.9		12.928	13.9
540		14.27	14.3	14.24			14.32			14.32		13.309	14.32
540.5									14.485				
541	14.37												
542	14.37	14.37		14.41			14.52			14.52		13.323	14.52
543	14.37												
544												13.024	14.34
545.3									13.827				
546												12.467	13.83
548												11.665	12.99
549		12.46											
549.4									11.981				
550				11.87			12.01			12.01		10.754	12.01
551.4									10.919				
552												9.9188	11.02
554							10.07			10.17		9.2038	10.17
555		9							9.42				
556												8.6192	9.482
557.3									8.897				
558												8.364	9.015
560	8.47	8.47	8.5	8.72			8.77			8.77		8.1533	8.767
562												8.155	8.769
562.4									8.676				
564												8.4789	9.042
566									9.617			9.1238	9.614
568				10.49			10.5			10.5		10.043	10.5
569		11.27											
570			11.9	11.66						11.68		11.124	11.68
570.9									12.511				
572												12.293	13.05
574												13.327	14.37

Wavelength (nm)	Van Kampen (1965)	Van Assendelft (1970) (Takatani 1979)	Van Assendelft (1975)	Zijlstra (1987)	Wray (1988)	Mendelson (1989)	Zijlstra (1991)	Cope (1991)	Steinke (1992)	Zijlstra (1994)	Matcher (1995)	Prahl (1998)	Zijlstra (2000)
576			15.3	15.1			15.27			15.26		13.885	15.26
576.5													
577	15.37	15.37											
577.7									14.983				
578							15.36					13.682	15.36
579		13.73											
580				14.14						14.42		12.526	14.42
582												10.826	12.6
584												8.6599	10.28
585.2									7.922				
586		7.23										6.6501	7.938
588												4.9408	5.887
588.2									5.053				
590				4.16			4.26			4.26		3.6002	4.262
592												2.6171	3.062
594												1.9197	2.216
594.5									1.773				
596												1.4209	1.634
597.5									1.149				
598												1.1261	1.234
600		0.8		0.98			0.96			0.96		0.8	0.957
602												0.666	0.775
603									0.644				
604												0.532	0.641
605		0.465											
606												0.4473	0.539
608												0.4119	0.46
609.6									0.373				
610												0.3765	0.397
612												0.3411	0.346
614												0.3057	0.305
614.3									0.275				
615		0.288											
616												0.2775	0.271
616.4									0.248				
618												0.2565	0.242
620												0.2355	0.218
621.7									0.189				
622												0.2145	0.197
624												0.1935	0.18
625		0.183											
626												0.1769	0.164
626.6									0.155				
628												0.1647	0.15
630			0.2				0.11			0.14		0.1525	0.139
632												0.1403	0.129
633.4									0.124				
634												0.1281	0.12
635		0.122											
636												0.1197	0.114
638												0.1151	0.108
640												0.1105	0.104
640.2									0.102				
642												0.1059	0.101
644												0.1013	0.099
645		0.099											
646												0.0976	0.099

Wavelength (nm)	Van Kampen (1965)	Van Assendelft (1970) (Takatani 1979)	Van Assendelft (1975)	Zijlstra (1987)	Wray (1988)	Mendelson (1989)	Zijlstra (1991)	Cope (1991)	Steinke (1992)	Zijlstra (1994)	Matcher (1995)	Prahl (1998)	Zijlstra (2000)
648												0.0948	0.098
650					0.1265			0.0967			0.0967	0.092	0.098
650.7									0.052				
651								0.0948			0.0948		
652								0.0930			0.0930	0.0892	0.099
653					0.1198			0.0915			0.0915		
654								0.0900			0.0900	0.0864	0.099
655		0.085						0.0886			0.0886		
656								0.0874			0.0874	0.0838	0.098
657					0.1148			0.0863			0.0863		
658								0.0853			0.0853	0.0814	0.098
659								0.0844			0.0844		
660		0.08			0.1113	0.12	0.08	0.0837		0.1	0.0837	0.0799	0.1
661								0.0829			0.0829		
662								0.0824			0.0824	0.0785	0.101
663					0.1088			0.0819			0.0819		
664								0.0815			0.0815	0.0771	0.101
665		0.073						0.0811			0.0811		
666								0.0809			0.0809	0.0757	0.101
667					0.1075			0.0807			0.0807		
668								0.0805			0.0805	0.0745	0.102
669								0.0804			0.0804		
670					0.1068			0.0803			0.0803	0.0735	0.102
671								0.0803			0.0803		
672								0.0803			0.0803	0.0725	0.102
673								0.0804			0.0804		
674					0.1065			0.0804			0.0804	0.0714	0.103
675		0.072						0.0803			0.0803		
676								0.0802			0.0802	0.0705	0.103
677					0.1063			0.0802			0.0802		
678								0.0801			0.0801	0.0698	0.103
679								0.0800			0.0800		
680							0.09	0.0799		0.1	0.0799	0.0694	0.103
681					0.1058			0.0797			0.0797		
682								0.0795			0.0795	0.069	0.103
683								0.0793			0.0793		
684					0.1050			0.0791			0.0791	0.0686	0.103
685		0.068						0.0789			0.0789		
686								0.0788			0.0788	0.0682	0.103
687					0.1043			0.0785			0.0785		
688								0.0784			0.0784	0.0686	0.103
689								0.0782			0.0782		
690								0.0781			0.0781	0.069	0.103
691					0.1038			0.0780			0.0780		
692								0.0780			0.0780	0.0694	0.103
693								0.0781			0.0781		
694					0.1038			0.0781			0.0781	0.0698	0.103
695		0.07						0.0783			0.0783		
696								0.0785			0.0785	0.0705	0.104
697								0.0787			0.0787		
698					0.1040			0.0791			0.0791	0.0715	0.104
699								0.0795			0.0795		
700							0.09	0.0800		0.1	0.0800	0.0725	0.105
701					0.1053			0.0805			0.0805		
702								0.0811			0.0811	0.0735	0.106
703								0.0817			0.0817		
704								0.0824			0.0824	0.0745	0.106

Wavelength (nm)	Van Kampen (1965)	Van Assendelft (1970) (Takatani 1979)	Van Assendelft (1975)	Zijlstra (1987)	Wray (1988)	Mendelson (1989)	Zijlstra (1991)	Cope (1991)	Steinke (1992)	Zijlstra (1994)	Matcher (1995)	Prahl (1998)	Zijlstra (2000)
705		0.075			0.1068			0.0831			0.0831		
706								0.0838			0.0838	0.0757	0.108
707								0.0847			0.0847		
708					0.1088			0.0854			0.0854	0.0771	0.109
709								0.0863			0.0863		
710								0.0871			0.0871	0.0785	0.11
711					0.1110			0.0881			0.0881		
712								0.0891			0.0891	0.0799	0.112
713								0.0901			0.0901		
714								0.0910			0.0910	0.0813	0.113
715		0.082			0.1135			0.0920			0.0920		
716								0.0931			0.0931	0.083	0.115
717								0.0941			0.0941		
718					0.1165			0.0952			0.0952	0.085	0.116
719								0.0964			0.0964		
720								0.0975			0.0975	0.087	0.118
721					0.1195			0.0986			0.0986		
722								0.0997			0.0997	0.089	0.12
723								0.1009			0.1009		
724								0.1021			0.1021	0.091	0.122
725		0.092			0.1225			0.1033			0.1033		
726								0.1045			0.1045	0.0931	0.123
727								0.1058			0.1058		
728					0.1258			0.1070			0.1070	0.0953	0.125
729								0.1083			0.1083		
730								0.1096			0.1096	0.0975	0.127
731								0.1109			0.1109		
732					0.1293			0.1122			0.1122	0.0997	0.129
733								0.1135			0.1135		
734								0.1148			0.1148	0.1019	0.131
735		0.103			0.1330			0.1161			0.1161		
736								0.1175			0.1175	0.1047	0.133
737								0.1188			0.1188		
738					0.1365			0.1203			0.1203	0.1081	0.135
739								0.1216			0.1216		
740								0.1230			0.1230	0.1115	0.137
741								0.1244			0.1244		
742					0.1403			0.1258			0.1258	0.1149	0.139
743								0.1272			0.1272		
744								0.1287			0.1287	0.1183	0.141
745		0.12			0.1440			0.1301			0.1301		
746								0.1315			0.1315	0.1219	0.143
747								0.1329			0.1329		
748					0.1480			0.1344			0.1344	0.1257	0.145
749								0.1359			0.1359		
750							0.14	0.1374		0.15	0.1374	0.1295	0.148
751								0.1388			0.1388		
752					0.1520			0.1403			0.1403	0.1333	0.15
753								0.1418			0.1418		
754								0.1433			0.1433	0.1371	0.152
755		0.139			0.1560			0.1448			0.1448		
756								0.1464			0.1464	0.1405	0.154
757								0.1478			0.1478		
758					0.1603			0.1493			0.1493	0.1435	0.157
759								0.1508			0.1508		
760								0.1524			0.1524	0.1465	0.159
761								0.1539			0.1539		

Wavelength (nm)	Van Kampen (1965)	Van Assendelft (1970) (Takatani 1979)	Van Assendelft (1975)	Zijlstra (1987)	Wray (1988)	Mendelson (1989)	Zijlstra (1991)	Cope (1991)	Steinke (1992)	Zijlstra (1994)	Matcher (1995)	Prahl (1998)	Zijlstra (2000)
762					0.1645			0.1555			0.1555	0.1495	0.161
763								0.1571			0.1571		
764								0.1586			0.1586	0.1525	0.163
765		0.154			0.1688			0.1602			0.1602		
766								0.1617			0.1617	0.1557	0.166
767								0.1634			0.1634		
768					0.1730			0.1649			0.1649	0.1591	0.168
769								0.1665			0.1665		
770								0.1680			0.1680	0.1625	0.171
771								0.1696			0.1696		
772					0.1775			0.1712			0.1712	0.1659	0.173
773								0.1728			0.1728		
774								0.1743			0.1743	0.1693	0.175
775		0.171			0.1820		0.17	0.1759		0.18	0.1759		
776								0.1775			0.1775	0.1723	0.178
777								0.1791			0.1791		
778					0.1863			0.1807			0.1807	0.1749	0.18
779								0.1824			0.1824		
780								0.1840			0.1840	0.1775	0.183
781								0.1855			0.1855		
782					0.1908			0.1871			0.1871	0.1801	0.185
783								0.1887			0.1887		
784								0.1903			0.1903	0.1827	0.188
785		0.184			0.1953			0.1920			0.1920		
786								0.1936			0.1936	0.185	0.19
787								0.1952			0.1952		
788					0.1998			0.1969			0.1969	0.187	0.193
789								0.1985			0.1985		
790								0.2001			0.2001	0.189	0.196
791								0.2017			0.2017		
792					0.2043			0.2033			0.2033	0.191	0.198
793								0.2049			0.2049		
794								0.2066			0.2066	0.193	0.201
795		0.194			0.2088			0.2083			0.2083		
796								0.2098			0.2098	0.1966	0.203
797								0.2114			0.2114		
798					0.2130			0.2131			0.2131	0.2018	0.206
799								0.2147			0.2147		
800							0.2	0.2163		0.21	0.2163	0.204	0.208
801					0.2173			0.2179			0.2179		
802								0.2195			0.2195	0.207	
803								0.2211			0.2211		
804								0.2227			0.2227	0.209	
805		0.22			0.2215		0.21	0.2243			0.2243		0.207
806								0.2259			0.2259	0.211	
807								0.2276			0.2276		
808					0.2258			0.2291			0.2291	0.214	
809								0.2307			0.2307		
810								0.2323			0.2323	0.216	
811					0.2300			0.2339			0.2339		
812								0.2354			0.2354	0.218	
813								0.2369			0.2369		
814					0.2340			0.2385			0.2385	0.22	
815		0.22						0.2401			0.2401		
816								0.2416			0.2416	0.2218	
817								0.2432			0.2432		
818					0.2380			0.2447			0.2447	0.2254	

Wavelength (nm)	Van Kampen (1965)	Van Assendelft (1970) (Takatani 1979)	Van Assendelft (1975)	Zijlstra (1987)	Wray (1988)	Mendelson (1989)	Zijlstra (1991)	Cope (1991)	Steinke (1992)	Zijlstra (1994)	Matcher (1995)	Prahl (1998)	Zijlstra (2000)
819								0.2462			0.2462		
820								0.2478			0.2478	0.229	
821					0.2420			0.2493			0.2493		
822								0.2508			0.2508	0.2326	
823								0.2523			0.2523		
824					0.2458			0.2538			0.2538	0.2362	
825		0.238						0.2553			0.2553		
826								0.2568			0.2568	0.2391	
827								0.2583			0.2583		
828					0.2495			0.2598			0.2598	0.2413	
829								0.2612			0.2612		
830								0.2627			0.2627	0.2435	
831					0.2533			0.2641			0.2641		
832								0.2655			0.2655	0.2457	
833								0.2670			0.2670		
834					0.2570			0.2685			0.2685	0.2479	
835		0.249						0.2699			0.2699		
836								0.2713			0.2713	0.2503	
837					0.2608			0.2727			0.2727		
838								0.2741			0.2741	0.2529	
839								0.2754			0.2754		
840					0.2643		0.25	0.2768			0.2768	0.2555	0.248
841								0.2782			0.2782		
842								0.2796			0.2796	0.2581	
843								0.2808			0.2808		
844					0.2675			0.2821			0.2821	0.2607	
845		0.262					0.25	0.2835			0.2835		0.253
846								0.2848			0.2848	0.2625	
847					0.2710			0.2860			0.2860		
848								0.2873			0.2873	0.2635	
849								0.2887			0.2887		
850					0.2743			0.2899			0.2899	0.2645	
851								0.2911			0.2911		
852								0.2924			0.2924	0.2655	
853					0.2775			0.2936			0.2936		
854								0.2948			0.2948	0.2665	
855		0.267						0.2960			0.2960		
856								0.2971			0.2971	0.2682	
857					0.2805			0.2984			0.2984		
858								0.2995			0.2995	0.2706	
859								0.3007			0.3007		
860					0.2835			0.3018			0.3018	0.273	
861								0.3028			0.3028		
862								0.3039			0.3039	0.2754	
863					0.2865			0.3050			0.3050		
864								0.3061			0.3061	0.2778	
865		0.279						0.3071			0.3071		
866					0.2893			0.3081			0.3081	0.2796	
867								0.3092			0.3092		
868								0.3102			0.3102	0.2808	
869					0.2918			0.3112			0.3112		
870								0.3123			0.3123	0.282	
871								0.3132			0.3132		
872					0.2943			0.3141			0.3141	0.2832	
873								0.3150			0.3150		
874								0.3160			0.3160	0.2844	
875		0.285						0.3170			0.3170		

Wavelength (nm)	Van Kampen (1965)	Van Assendelft (1970) (Takatani 1979)	Van Assendelft (1975)	Zijlstra (1987)	Wray (1988)	Mendelson (1989)	Zijlstra (1991)	Cope (1991)	Steinke (1992)	Zijlstra (1994)	Matcher (1995)	Prahl (1998)	Zijlstra (2000)
876					0.2968			0.3177			0.3177	0.2857	
877								0.3186			0.3186		
878								0.3195			0.3195	0.2871	
879					0.2990			0.3204			0.3204		
880							0.28	0.3211			0.3211	0.2885	0.284
881								0.3219			0.3219		
882					0.3010			0.3227			0.3227	0.2899	
883								0.3234			0.3234		
884								0.3243			0.3243	0.2913	
885		0.292			0.3030			0.3250			0.3250		
886								0.3257			0.3257	0.2925	
887								0.3265			0.3265		
888					0.3048			0.3271			0.3271	0.2935	
889								0.3277			0.3277		
890								0.3284			0.3284	0.2945	
891					0.3065			0.3291			0.3291		
892								0.3297			0.3297	0.2955	
893								0.3302			0.3302		
894								0.3309			0.3309	0.2965	
895		0.297			0.3080			0.3316			0.3316		
896								0.3321			0.3321	0.2975	
897								0.3326			0.3326		
898					0.3095			0.3331			0.3331	0.2985	
899								0.3335			0.3335		
900								0.3341			0.3341	0.2995	
901					0.3108			0.3346			0.3346		
902								0.3351			0.3351	0.3005	
903								0.3355			0.3355		
904					0.3120		0.3	0.3359			0.3359	0.3015	0.297
905		0.302						0.3363			0.3363		
906								0.3367			0.3367	0.3023	
907					0.3130			0.3369			0.3369		
908								0.3374			0.3374	0.3029	
909								0.3377			0.3377		
910					0.3138			0.3378			0.3378	0.3035	
911								0.3382			0.3382		
912								0.3386			0.3386	0.3041	
913					0.3145			0.3388			0.3388		
914								0.3391			0.3391	0.3047	
915		0.305						0.3392			0.3392		
916					0.3150			0.3395			0.3395	0.3052	
917								0.3396			0.3396		
918								0.3397			0.3397	0.3056	
919								0.3396			0.3396		
920					0.3153		0.3	0.3397			0.3397	0.306	0.299
921								0.3400			0.3400		
922								0.3401			0.3401	0.3064	
923					0.3155			0.3401			0.3401		
924								0.3401			0.3401	0.3068	
925		0.307						0.3401			0.3401		
926					0.3158			0.3401			0.3401	0.3067	
927								0.3401			0.3401		
928								0.3400			0.3400	0.3061	
929					0.3158			0.3400			0.3400		
930								0.3399			0.3399	0.3055	
931								0.3398			0.3398		
932					0.3158			0.3397			0.3397	0.3049	

Wavelength (nm)	Van Kampen (1965)	Van Assendelft (1970) (Takatani 1979)	Van Assendelft (1975)	Zijlstra (1987)	Wray (1988)	Mendelson (1989)	Zijlstra (1991)	Cope (1991)	Steinke (1992)	Zijlstra (1994)	Matcher (1995)	Prahl (1998)	Zijlstra (2000)
933								0.3396			0.3396		
934								0.3394			0.3394	0.3043	
935		0.304			0.3155			0.3392			0.3392		
936								0.3389			0.3389	0.3039	
937								0.3387			0.3387		
938					0.3148			0.3386			0.3386	0.3037	
939								0.3383			0.3383		
940		0.3				0.29	0.29	0.3380			0.3380	0.3035	0.294
941					0.3145			0.3378			0.3378		
942								0.3376			0.3376	0.3033	
943								0.3372			0.3372		
944					0.3138			0.3367			0.3367	0.3031	
945		0.303						0.3363			0.3363		
946								0.3361			0.3361	0.3026	
947					0.3128			0.3357			0.3357		
948								0.3353			0.3353	0.3018	
949								0.3349			0.3349		
950					0.3120			0.3344			0.3344	0.301	
951								0.3339			0.3339		
952								0.3333			0.3333	0.3002	
953					0.3110			0.3328			0.3328		
954								0.3323			0.3323	0.2994	
955		0.299						0.3316			0.3316		
956					0.3098			0.3310			0.3310	0.2985	
957								0.3304			0.3304		
958								0.3300			0.3300	0.2975	
959					0.3083			0.3293			0.3293		
960							0.28	0.3286			0.3286	0.2965	0.283
961								0.3281			0.3281		
962					0.3065			0.3275			0.3275	0.2955	
963								0.3267			0.3267		
964								0.3261			0.3261	0.2945	
965		0.294			0.3050			0.3254			0.3254		
966								0.3249			0.3249	0.2933	
967								0.3242			0.3242		
968					0.3033			0.3232			0.3232	0.2919	
969								0.3225			0.3225		
970								0.3217			0.3217	0.2905	
971								0.3210			0.3210		
972					0.3013			0.3202			0.3202	0.2891	
973								0.3193			0.3193		
974								0.3184			0.3184	0.2877	
975		0.287			0.2993			0.3173			0.3173		
976								0.3164			0.3164	0.286	
977								0.3156			0.3156		
978					0.2973			0.3147			0.3147	0.284	
979								0.3137			0.3137		
980								0.3128			0.3128	0.282	
981					0.2950			0.3118			0.3118		
982								0.3108			0.3108	0.28	
983								0.3098			0.3098		
984					0.2925			0.3088			0.3088	0.278	
985		0.277						0.3076			0.3076		
986					0.2900			0.3065			0.3065	0.2756	
987								0.3055			0.3055		
988								0.3043			0.3043	0.2728	
989					0.2873			0.3033			0.3033		

Wavelength (nm)	Van Kampen (1965)	Van Assendelft (1970) (Takatani 1979)	Van Assendelft (1975)	Zijlstra (1987)	Wray (1988)	Mendelson (1989)	Zijlstra (1991)	Cope (1991)	Steinke (1992)	Zijlstra (1994)	Matcher (1995)	Prahl (1998)	Zijlstra (2000)
990								0.3022			0.3022	0.27	
991								0.3011			0.3011		
992					0.2845			0.2998			0.2998	0.2672	
993								0.2985			0.2985		
994								0.2973			0.2973	0.2644	
995		0.263			0.2815			0.2962			0.2962		
996								0.2947			0.2947	0.2616	
997								0.2933			0.2933		
998					0.2785			0.2924			0.2924	0.2588	
999								0.2909			0.2909		
1000							0.25				0.2894	0.256	0.251
1001					0.2758						0.2882		
1002											0.2869		
1003											0.2854		
1004					0.2723						0.2840		
1005											0.2825		
1006											0.2813		
1007					0.2690						0.2800		
1008											0.2784		
1009											0.2770		
1010					0.2655						0.2752		
1011											0.2737		
1012											0.2723		
1013					0.2618						0.2706		
1014											0.2690		
1015											0.2676		
1016					0.2583						0.2662		
1017											0.2645		
1018											0.2626		
1019					0.2545						0.2613		
1020											0.2594		
1021											0.2577		
1022					0.2508						0.2561		
1023											0.2543		
1024											0.2525		
1025					0.2470						0.2508		
1026											0.2493		
1027											0.2473		
1028					0.2430						0.2459		
1029											0.2435		
1030											0.2416		
1031					0.2390						0.2400		
1032											0.2379		
1033											0.2354		
1034					0.2350						0.2331		
1035											0.2317		
1036					0.2308						0.2300		
1037											0.2280		
1038											0.2261		
1039					0.2263						0.2236		
1040											0.2219		
1041											0.2196		
1042					0.2223						0.2168		

REFERENCES

1. Cancer facts and figures 2005, American Cancer Society, http://www.cancer.org/docroot/ STT/stt_0.asp

2. B. J. Tromberg, N. Shah, R. Lanning, A. Cerussi, J. Espinoza, T. Pham, L. Svaasand, J. Butler, "Non-invasive in vivo characterization of breast tumors using photon migration spectroscopy," *Neoplasia,* **2**, 26-40 (2000).

3. B. W. Pogue, S. P. Poplack, T. O. McBride, W. A. Wells, K. S. Osterman, U. L. Osterberg, and K. D. Paulsen, "Quantitative hemoglobin tomography with diffuse near-infrared spectroscopy: pilot results in the breast," *Radiol.*, **218**, 261-6 (2001).

4. S. Nioka and B. Chance, "NIR spectroscopic detection of breast cancer," *Technol. Cancer Res. Treat.*, **4**, 497-512 (2005).

5. M. S. Patterson, B. Chance, and B. C. Wilson, "Time resolved reflectance and transmittance for the noninvasive measurement of tissue optical properties**,"** *Appl. Opt*., 28, 2331-2336 (1989).

6. R. Aronson, "Boundary conditions for diffusion of light," *J. Opt. Soc. Am. A*, **12**, 2532-2539 (1995).

7. E. M. Sevick, B. Chance, J. Leigh, S. Nokia and M. Maris, "Quantitation of time- and frequency-resolved optical spectra for the determination of tissue oxygenation," *Anal. Biochem*., **195**, 330-351 (1991).

8. B. Gallez, C. Baudelet, and B. F. Jordan, "Assessment of tumor oxygenation by electron paramagnetic resonance: principles and applications", *NMR in Biomed*., **17**, 240-262 (2004).

9. L. Gray, A. Conger, M. Ebert, S. Hornsey and O. Scott, "The concentration of oxygen dissolved in tissues at time of irradiation as a factor in radio-therapy," *Br. J. Radiol*., **26**, 638-648 (1953).

10. E. E. Schwartz, "The biological basis of radiation therapy," Philadelphia, Lippincott (1966).

11. J. D. Chapman, C. C. Stobbe, M. R. Arnfield, R. Santus, J. Lee, and M. S. McPhee, "Oxygen dependency of tumor cell killing *in vitro* by light activated photofrin II", *Radiat*. *Res*., **126**, 73-79 (1991).

12. B. Teicher, J. Lazo, and A. Sartorelli, “Classification of antineoplastic agents by their selective toxicities toward oxygenated and hypoxic tumor cells”, *Cancer Res*., **41**, 73-81 (1981).

13. J. H. Kaanders, L. A. Pop, H. A. Marres, J. Liefers, F. J. van den Hoogen, W. A. van Daal, A. J. and van der Kogel, “Accelerated radiotherapy with carbogen and nicotinamide (ARCON) for laryngeal cancer,” *Radiother. Oncol.*, **48**, 115-22. (1998).

14. J. Overgaard and M. R. Horsman, “Modification of hypoxia-induced radioresistance in tumors by the use of oxygen and sensitizers,” *Semin. Radiat. Oncol.*, **6**, 10-21. (1996).

15. H. B. Stone, J. M. Brown and T. Phillips, “Oxygen in human tumors: correlations between methods of measurement and response to therapy,” *Radiat. Res.*, **136**, 422-434 (1993).

16. D. Zhao, A. Constantinescu, E. W. Hahn and R. P. Mason. “Tumor oxygenation dynamics with respect to growth and respiratory challenge: Investigation of the Dunning prostate R3327-HI tumor,” *Radiat. Res*., **156**(5), 510-520 (2001).

17. D. Cater and I. Silver, “Quantitative measurements of oxygen tension in normal tissues and in the tumors of patients before and after radiotherapy,” *Acta Radiol*., **53**, 23 3-256 (1960).

18. J. A. O' Hara, F. Goda, E. Demidenko and H. M. Swartz, “Effect on regrowth delay in a murine tumor of scheduling split-dose irradiation based on direct pO_2 measurement s by electron paramagnetic resonance Oximetry,” *Radiat. Res.,* **150**, 549-56 (1998).

19. D. Zhao, L. Jiang, and R. P. Mason, “Measuring changes in tumor oxygenation”, Imaging in Biological Research, Part B (P. Machael Conn ed.) *Methods in Enzymol.*, **386**, 378-418 (2004).

20. R. P. Mason, A. Constantinescu, S. Hunjan, D. Le, E. W. Hahn, P. P. Antich, C. Blum and P. Peschke, “Regional tumor oxygenation and measurement of dynamic changes,” *Radiat. Res.*, **152**, 239-249 (1999).

21. H. Liu, Y. Gu, J. G. Kim, and Ralph P. Mason, “Near infrared spectroscopy and imaging of tumor vascular oxygenation”, Imaging in Biological Research, Part B (P. Machael Conn ed.) *Methods in Enzymol.*, **386**, 349-378 (2004).

22. B. L. Horecker, “The absorption spectra of hemoglobin and its derivatives in the visible and near infrared regions”, *J. Biol. Chem.,* **148**, 173-183 (1943).

23. E. J. van Kampen and W. G. Zijlstra, "Determination of hemoglobin and its derivatives," *Adv. Clin. Chem.*, **8**, 141-187 (1965).

24. R. Benesch, G. Macduff, and R. E. Benesch, "Determination of oxygen equilibria with a versatile new tonometer," *Anal. Biochem.*, **11**, 81-87 (1965).

25. O. W. van Assendelft and W. G. Zijlstra, "Extinction coefficients for use in equations for the spectrophotometric analysis of hemoglobin mixtures," *Anal. Biochem.*, **69**, 43-48 (1975).

26. R. E. Benesch, R. Benesch, and S. Yung, "Equations for the spectrophotometric analysis of hemoglobin mixtures," *Anal. Biochem.*, **55**, 245-248 (1973).

27. W. G. Zijlstra, A. Buursma, and W. P. Meeuwsen-van der Roest, "Absorption spectra of human fetal and adult oxyhemoglobin, deoxyhemoglobin, carboxyhemoglobin, and methemoglobin," *Clin. Chem*. **37**, 1633–1638 (1991).

28. Y. Mendelson and J.C. Kent, "Variations in optical absorption spectra of adult and fetal hemoglobins and its effect on pulse oximetry," *IEEE Trans. Biomedical Eng*., **36**, 844-848 (1989).

29. W. G. Zijlstra, A. Buursma, and A. Zwart, "Molar absorptivities of human hemoglobin in the visible spectral range," *J. Appl. Physiol.: Respirat. Environ. Exercise Physiol*., **54**, 1287-1291 (1983).

30. M. Cope, "The application of near infrared spectroscopy to non invasive monitoring of cerebral oxygenation in the newborn infant," Ph.D. thesis, Appendix B, 316-323, University College London (1991).

31. H. Liu, Y. Song, K. L. Worden, X. Jiang, A. Constantinescu, and R. P. Mason, "Noninvasive Investigation of Blood Oxygenation Dynamics of Tumors by Near-Infrared Spectroscopy", *Appl. Opt.*, **39**, 5231-5243 (2000).

32. W. G. Zijlstra, A. Buursma, H. E. Falke, and J. F. Catsburg, "Spectrophotometry of hemoglobin: absorption spectra of rat oxyhemoglobin, deoxyhemoglobin, carboxyhemoglobin, and methemoglobin," *Comp*. *Biochem*. *Physiol*., **107B,** 161-166 (1994).

33. J. G. Kim, D. Zhao, Y. Song, A. Constantinescu, R. P. Mason, and H. Liu, "Interplay of Tumor Vascular Oxygenation and Tumor pO_2 Observed Using Near

Infrared Spectroscopy, an Oxygen Needle Electrode, and ^{19}F MR pO_2 Mapping," *J. Biomed. Opt*., **8**, 53-62 (2003).

34. Y. Gu, V. A. Bourke, J.G. Kim, A. Constantinescu, R. P. Mason, and H. Liu, "Dynamic Response of Breast Tumor Oxygenation to Hyperoxic Respiratory Challenge Monitored with Three Oxygen-Sensitive Parameters," *Appl. Opt.*, **42**, 2960-2967 (2003).

35. W. G. Zijlstra and A. Buursma, "Spectrophotometry of hemoglobin: a comparison of dog and man," *Comp. Biochem. Physiol*., **88B,** 251-255 (1987).

36. W. G. Zijlstra, A. Buursma, and O. W. van Assendelft, "Visible and near infrared absorption spectra of human and animal hemoglobin: determination and application," (The Netherlands: VSP publisher) 57-64, (2000).

37. S. Wray, M. Cope, D. T. Delpy, J. S. Wyatt, and E. O. R. Reynolds, "Characterization of the near infrared absorption spectra of cytochrome aa3 and hemoglobin for the non-invasive monitoring of cerebral oxygenation," *Biochim. Biophys. Acta,* **933,** 184-192 (1988).

38. S. J. Matcher, C. E. Elwell, C. E. Cooper, M. Cope, and D. T. Delpy, "Performance comparison of several published tissue near-infrared spectroscopy algorithms," *Anal. Biochem.,* **227,** 54-68 (1995).

39. S. A. Prahl, "Tabulated Molar Extinction Coefficient for Hemoglobin in Water," http://omlc.ogi.edu/spectra/ hemoglobin/summary.html (Compiled using data from: WB Gratzer, Med. Res. Council Labs, Holly Hill, London and N Kollias, Wellman Laboratories, Harvard Medical School, Boston), Oregon Health and Science University (prahl@bme.ogi.edu) (1998)

40. R. B. Barlow and M. L. Polanyi, "Absorption measurements for oxygenated and reduced hemoglobin in the range 0.6-1.88 microns," *Clin. Chem.* **8,** 67-71 (1962).

41. O. W. van Assendelft, "*Spectrophotometry of hemoglobin derivatives,"* PhD thesis Univ. of Groningen The Netherlands (1970).

42. R. Cubeddu, A. Pifferi, P. Taroni, A. Torricelli, and G. Valentini, "Compact tissue oximeter based on dual-wavelength multichannel time-resolved reflectance," *Appl. Opt*. **38,** 3670-3680 (1999).

43. E. Heffer, V. Pera, O. Schütz, H. Siebold, and S. Fantini, "Near-infrared imaging of the human breast: complementing hemoglobin concentration maps with oxygenation images," *J. Biomed. Opt.* **9,** 1152–1160 (2004).

44. A. Torricelli, V. Quaresima, A. Pifferi, G. Biscotti, L. Spinelli, P. Taroni, M. Ferrari, and R. Cubeddu, "Mapping of calf muscle oxygenation and hemoglobin content during dynamic plantar flexion exercise by multi-channel time-resolved near-infrared spectroscopy," *Phys. Med. Biol.,* **49,** 685–699 (2004).

45. J. R. Taylor, "An introduction to error analysis: the study of uncertainties in physical measurements," 2nd ed (Sausalito: University science books) 73-77 (1997)

46. H. Liu, A. H. Hielscher, F. K. Tittel, S. L. Jacques, and B. Chance, "Influence of blood vessels on the measurement of hemoglobin oxygenation as determined by time-resolved reflectance spectroscopy," *Med. Phys.*, **22,** 1209-1217 (1995).

47. Y. Yang, H. Liu, X. Li, and B. Chance, "A low cost frequency-domain photon migration instrument for tissue spectroscopy, oximetry, and imaging," *Opt. Eng.* **36,** 1562-1569 (1997).

48. S. Fantini, B. Barbieri, and E. Gratton, "Frequency-domain multichannel optical detector for noninvasive tissue spectroscopy and Oximetry," *Opt. Eng.,* **34,** 32-42 (1995).

49. L. Cordone, A. Cupane, M. Leone, and E. Vitrane, "Optical absorption spectra of deoxy- and oxyhemoglobin in the temperature range 300 -20 K," *Biophys*. *Chem*., **24,** 259-275 (1986).

50. J. M. Steinke and A. P. Shepherd, "Effects of temperature on optical absorbance spectra of oxy-, carboxy-, and deoxyhemoglobin," *Clin*. *Chem*. **38,** 1360-1364 (1992).

51. R. Sfareni, A. Boffi, V. Quaresima, and M. Ferrari, "Near infrared absorption spectra of human deoxy- and oxyhemoglobin in the temperature range 20-40oC," *Biochim. Biophys. Acta,* **1340,** 165-169 (1997).

52. M. Kohl, U. Lindauer, G. Royl, M. Kühl, L. Gold, A. Villringer, and U. Dirnagl, "Physical model for the spectroscopic analysis of cortical intrinsic optical signal," *Phys. Med. Biol.* **45,** 3749-3764 (2000).

53. J. H. G. M. Klaessens, R. G. M. Kolkman, J. C. W. Hopman, E. Hondebrink, K. D. Liem, W. Steenbergen, F. F. M. deMul, and J. M. Thijssen J M, "Monitoring cerebral perfusion using near-infrared spectroscopy and laser Doppler flowmetry," *Physiol. Meas.,* **24,** N35–N40 (2003).

54. J. P. Newman, D. M. Peebles, and M. A. Hanson, "Adenosine produces changes in cerebral hemodynamics and metabolism as assessed by near-infrared spectroscopy in late-gestation fetal sheep in utero," *Pediat. Res.,* **50,** 217-221 (2001).

55. N. R. Helledie and P. Rolfe, **"**Near Infra Red Spectroscopy: pH sensitivity of the absorbances of dilute haemoglobin solutions and suspended erythrocytes at four wauelengths," EMBS, Proceedings of the Twelfth Annual International Conference of the IEEE, 1540-1541 (1990).

56. E. W. Weisstein, "Moore-Penrose Matrix Inverse," From *MathWorld*-A Wolfram Web Resource. http://mathworld.wolfram.com/Moore-PenroseMatrixInverse.html (Checked in Nov. 10, 2005)

57. R. J. Gillies, P. A. Schornack, T. W. Secomb, and N. Raghunand, "Causes and effects of heterogeneous perfusion in tumors," *Neoplasia*, **1** (3), 197-207 (1999).

58. D. R. Tailor, H. Poptani, J. D. Glickson, J. S. Leigh, and R. Reddy, "High-resolution assessment of blood flow in murine RIF-1 tumors by monitoring uptake of H2 17O with proton $T1\rho$-weighted Imaging," *Magn. Reson. Med.*, **49**, 1–6 (2003).

59. J. C. Acker, M. W. Dewhirst, G. M. Honore, T. V. Samulski, J. A. Tucker, and J. R. Oleson, "Blood perfusion measurements in human tumors, evaluation of laser Doppler methods," *Int. J. Hypertherm*, **6**, 287-304 (1990).

60. J. Griebel, N. A. Mayr, A. de Vries, M. V. Knopp, T. Gneiting, C. Kremser, M. Essig, H. Hawighorst, P. H. Lukas, and W. T. Yuh, "Assessment of tumor microcirculation: a new role of dynamic contrast MR imaging," *J. Magn. Reson. Imaging*, **7**, 111-119 (1997).

61. T. Durduran, "Non-invasive measurements of tissue hemodynamics with hybrid diffuse optical methods," PhD dissertation, University of Pennsylvania (2004).

62. M. W. Dewhirst, C. Gustafson, J. F. Gross, and C. Y. Tso, "Temporal effects of 5.0 Gy radiation in healing subcutaneous microvasculature of a dorsal flap window chamber", *Radiat. Res.*, **112**, 581-591 (1987).

63. S. Hunjan, D. Zhao, A. Constantinescu, E. W. Hahn, P. Antich, and R. P. Mason, "Tumor oximetry: demonstration of an enhanced dynamic mapping procedure using fluorine-19 echo planar magnetic resonance imaging in the dunning prostate R3327-AT1 rat tumor," *Int. J. Radiat. Oncol. Biol. Phys*., **49**, 1097-1108 (2001).

64. M. Höckel, P. Vaupel, "Tumor hypoxia: definitions and current clinical, biologic, and molecular aspects", *J Natl Cancer Inst.,* **93**, 266–76 (2001).

65. B. Chance, S. Nioka, J. Kent, K. McCully, M. Fountain, R. Greenfield, and G. Holtom, "Time resolved spectroscopy of hemoglobin and myoglobin in resting and ischemic muscle," *Anal*. *Biochem*. **174**, 698-707 (1998).

66. H. B. Nielsen, N. H. Secher, O. Clemmesen, and P. Ott, "Maintained cerebral and skeletal muscle oxygenation during maximal exercise in patients with liver cirrhosis," *J. Hepatol.* **43**, 266-71 (2005).

67. S. Watanabe, C. Ishii, N. Takeyasu, R. Ajisaka, H. Nishina, T. Morimoto, K. Sakamoto, K. Eda, M. Ishiyama, T. Saito, H. Aihara, E. Arai, M. Toyama, Y. Shintomi, and I. Yamaguchi, "Assessing muscle vasodilation using near-infrared spectroscopy in cardiac patients," *Circ. J.* **69**, 802-814 (2005).

68. B. Chance, E. Anday, S. Nioka, S. Zhou, L. Hong, K. Worden, C. Li, T. Murray, Y. Ovetsky, D. Pidikiti, and R. Thomas, "A novel method for fast imaging of brain function non-invasively with light", *Opt. Express*, **2**(10), 411-423 (1998).

69. R. Wenzel, H. Obrig, J. Ruben, K. Villringer, A. Thiel, J. Bernarding, U. Dirnagl, and A. Villringer, "Cerebral blood oxygenation changes induced by visual stimulation in humans", *J. Biomed. Opt*., **1**(4),399-404 (1996).

70. T. Hoshino, K. Sakatani, Y. Katayama, N. Fujiwara, Y. Murata, K. Kobayashi, C. Fukaya, T. Yamamoto, "Application of multichannel near-infrared spectroscopic topography to physiological monitoring of the cortex during cortical mapping: technical case report," *Surg. Neurol.* **64**, 272-275 (2005).

71. R. G. Steen, K. Kitagishi, and K. Morgan, "In vivo measurement of tumor blood oxygenation by near-infrared spectroscopy: immediate effects of pentobarbital overdose or carmustine treatment", *J. Neuro-Oncol*., **22**, 209-220 (1994).

72. R. H. Thomlinson, and L. H. Gray, "The histological structure of some human lung cancers and the possible implications for radiotherapy", *Br. J. Cancer,* **9**, 539-549 (1955).

73. A. W. Fyles, M. Milosevic, R. Wong, M. C. Kavanagh, M. Pintile, A. Sun, W. Chapman, W. Levin, L. Manchul, T. J. Keane, and R. P. Hill, "Oxygenation predicts radiation response and survival in patients with cervix cancer", *Radiother. Oncol*., **48**, 149-156 (1998).

74. P. Bergsjo, P. Kolstad, "Clinical trial with atmospheric oxygen breathing during radiotherapy of cancer of the cervix," *Scand. J. Clin. Lab. Invest. Suppl*., **106**, 167-171 (1968).

75. H. D. Suit, N. Marshall, D. Woerner, "Oxygen, oxygen plus carbon dioxide, and radiation therapy of a mouse mammary carcinoma. Cancer," *Cancer*, **30**(5), 1154-1158 (1972).

76. S. S. Kety, “The theory and applications of the exchange of inert gas at the lungs and tissue,” *Pharmacol. Rev.,* **3**, 1-41 (1951)

77. Jae G. Kim, Mengna Xia, Hanli Liu, “Extinction coefficients of hemoglobin for near-infrared spectroscopy of tissue”, *IEEE Eng. in Med. & Biol. Magazine*, **24**, 118-121 (2005)

78. V. S. Kalambur, H. Mahaseth, J. C. Bischof, M. C. Kielbik, T. E. Welch, Å. Vilbäck, D. J. Swanlund, R. P. Hebbel, J. D. Belcher, G. M. Vercellotti, “Microvascular blood flow and stasis in transgenic sickle mice: Utility of a dorsal skin fold chamber for intravital microscopy,” *Am. J. Hematol*., **77**, 117-125 (2004).

79. P. Vaupel, O. Thews, D. K. Kelleher, and M. Höckel, "Current status of knowledge and critical issues in tumor oxygenation," In: Hudetz and Bruley (eds), Oxygen Transport to Tissue XX, 591-602 (Plenum Press, New York, 1998).

80. P. Vaupel, “Vascularization, blood flow, oxygenation, tissue pH, and bioenergetic status of human breast cancer,” In: Nemoto and LaManna (eds), Oxygen Transport to Tissue XVIII, 243-253 (Plenum Press, New York, 1997).

81. P. Vaupel, “Oxygen transport in tumors: Characteristics and clinical implications,” *Adv. Exp. Med. Biol*., **388**, 341-351 (1996).

82. P. Bergsjo and P. Kolstad, “Clinical trial with atmospheric oxygen breathing during radiotherapy of cancer of the cervix,” *Scand. J. Clin. Lab. Invest. Suppl*., **106**, 167-171 (1968).

83. H. D. Suit, N. Marshall, and D. Woerner, “Oxygen, oxygen plus carbon dioxide, and radiation therapy of a mouse mammary carcinoma. Cancer,” *Cancer*, **30**, 1154-1158 (1972).

84. T. J. Farrell, M. S. Patterson, and B. Wilson, “A diffusion theory model of spatially resolved, steady-state diffuse reflectance for the noninvasive determination of tissue optical properties *in vivo*”, *Med. Phys.*, **19**, 879-888 (1992).

85. R.A. Groenhuis, A.A. Ferwerda, and J. J. T. Bosch, “Scattering and absorption of turbid materials determined from reflection measurements. 1: Theory,” *Appl. Opt*., **22**, 2456-2462 (1983)

86. J. B. Mandeville, J.J.A. Marota, C. Ayata, G. Zaharchuk, M.A.Moskowitz, B. R. Rosen, and R. M. Weisskoff, “Evidence of a cerebrovascular postarteriole windkessel with delayed compliance,” *J. Cereb. Blood Flow Metab*., **19**, 679-689 (1999).

87. M. E. Brevard, T. Q. Duong, J. A. King, and C. F. Ferris, “Changes in MRI signal intensity during hypercapnic challenge under conscious and anesthetized conditions,” *Magn. Res. Imaging*., **21**, 995-1001 (2003).

88. Y. Gu, R. Mason, and H. Liu, “Estimated fraction of tumor vascular blood contents sampled by near infrared spectroscopy and 19F magnetic resonance spectroscopy,” *Opt. Express*, **13**, 1724-1733 (2005). http://www.opticsexpress.org/abstract.cfm?URI=OPEX-13-5-1724

89. M. Xia, R. P. Mason, and H. Liu, “A model of the hemodynamic responses of rat tumors to hyperoxic gas challenge”, Optical Tomography and Spectroscopy of Tissue VII, B. Chance, R. R. Alfano, B. J. Tromberg, M. Tamura, and E. M. Sevick-Muraca, eds., Proc. SPIE **5693**, 301-307 (2005).

90. D. A. Boas, G. Strangman, J. P. Culver, R. D. Hoge, G. Jasdzewski1, R. A. Poldrack, B. R. Rosen, and J. B. Mandeville, “Can the cerebral metabolic rate of oxygen be estimated with near-infrared spectroscopy?” *Phys. Med. Biol*., **48**, 2405–2418 (2003).

91. A. R. Padhani, A. Dzik-Jurasz, “Perfusion MR imaging of extracranial tumor angiogenesis,” *Top. Magn. Reson. Imaging*, **15**, 41-57 (2004).

92. A. Y. Bluestone, M. Stewart, J. Lasker, G.S. Absoulaev, and A. H. Hielscher, “Three-dimensional optical tomographic brainimaging in small animals, part1:hypercapnia,” *J. Biomed. Opt*., **9**, 1046-1062 (2004).

93. E. Rostrup, I. Law, F. Pott, K. Ide and G. M. Knudsen, “Cerebral hemodynamics measured with simultaneous PET and near-infrared spectroscopy in humans,” *Brain research*, **954**, 183-193 (2002).

94. R.B. Buxton, E.C. Wong, and L.R. Frank,”Dynamics of blood flow and oxygenation changes during brain activation: the balloon model,” *Magn. Reson. Med.*, **39**, 855-864 (1998).

95. K. J. Friston, A. Mechelli, R. Turner and C. J. Price, “Nonlinear Responses in fMRI: The Balloon Model, Volterra Kernels, and Other Hemodynamics,” *NeuroImage*, **12**, 466-477 (2000).

96. A. Mechelli, C. J. Price and K. J. Friston, “Nonlinear Coupling between Evoked rCBF and BOLD Signals: A Simulation Study of Hemodynamic Responses,” *NeuroImage*, **14**, 862-872 (2001).

97. Y. Zheng, J. Martindale, D. Johnston, M. Jones, J. Berwick, and J. Mayhew, "A Model of the hemodynamic Response and Oxygen Delivery to Brain," *NeuroImage*, **16**, 617–637 (2002).

98. R. B. Buxton, K. Uludağ, D. J. Dubowitz, and T. T. Liu, "Modeling the hemodynamic response to brain activation," *NeuroImage*, **23**, S220-S233 (2004).

99. K. Lu, J. W. Clark, Jr., F. H. Ghorbel, C. S. Robertson, D. L. Ware, J. B. Zwischenberger, and A. Bidani, "Cerebral autoregulation and gas exchange studied using a human cardiopulmonary model," *Am. J. Physiol. Heart. Circ. Physiol*., **286**, H584-H601 (2004).

100. R. K. Jain, "Determinants of tumor blood flow: a review," *Cancer Res*., **48**, 2641–2658 (1988).

101. R. K. Jain, "Barriers to drug delivery in solid tumors," *Sci. Am*., **271**, 58–65 (1994).

102. R. Mazurchuk, R. Zhou, R. M. Straubinger, R. I. Chau, and Z. Grossman, "Functional magnetic resonance (fMR) imaging of a rat brain tumor model: implications for evaluation of tumor microvasculature and therapeutic response," *Magn. Reson. Imaging*, **17**, 537-548 (1999).

103. Y. Song, A. Constantinescu, R.P.Mason, "Dynamic breast tumor oximetery: the development of prosgnostic radiology," *Tech. in Cancer Res. & Treatment*, **1**, 1-8 (2002).

104. E. L. Hull, D. L. Conover and T. H. Foster, "Carbogen-induced changes in rat mammary tumour oxygenation reported by near infrared spectroscopy," *British J. Cancer*, **79**(11/12), 1709-1716 (1999).

105. R. L. Fournier, "Oxygen transport in biological systems," Chap. 4 in Basic Transport Phenomena in Biomedical Engineering, 87-94, Taylor & Francis, Lillington (1999).

106. P. Peschke, E. W. Hahn, F. Lohr, F. Brauschweig, G. Wolber, I. Zuna and M. Wannenmacher, "Differential sensitivity of three sublines of the rat Dunning prostate tumor system R3327 to radiation and/or local tumor hyperthermia," *Radiat. Res.,***150**, 423-430 (1998).

107. E. W. Hahn, P. Peschke, R. P. Mason, E. E. Babcock and P. P. Antich, "Isolated tumor growth in a surgically formed skin pedicle in the rat: a new tumor model for NMR studies," *Magn. Reson. Imaging*, **11**, 1007-1017 (1993).

108. T. Y. Reynolds, S. Rockwell, and P. M. Glazer, "Genetic instability induced by the tumor microenvironment," *Cancer Res*., **56,** 5754-5757 (1996).

109. M. H. Friedman, "Gas Transport", Chap. 9 in Principles and models of biological transport, 240-242, Springer-Verlag, Berlin Heidelberg, (1986).

110. B. R. Barker, R. P. Mason, N. Bansal and R. M. Peshock, "Oxygen tension mapping by 19F echo planar NMR imaging of sequestered perfluorocarbon," *JMRI,* **4**, 595-602 (1994).

111. S. I. Fox, "Respiratory physiology," Chap. 16 in *Human Physiology*, 508-513, The McGraw-Hill companies, Inc., Boston (1999).

112. G. Brix, J. Debus, M. Mueller-Schimpfle, P. Peschke, P. Huber, H. J. Zabel and W. Lorenz, "MR-tomographische Quantifizierung struktureller und funktioneller Gewebeveraenderungen an stosswellen-therapierten Dunning-Prostata-Tumoren," *Z. Med. Phys.*, **3**, 76-82 (1993).

113. R. P. Mason, F. M. H. Jeffrey, C. R. Malloy, E. E. Babcock and P. P. Antich, "A noninvasive assessment of myocardial oxygen tension: 19F NMR sepectroscopy of sequestered perfluorocarbon emulsion," *Magn. Reson. Med*., **27**, 310-317 (1992).

114. J. Folkman, "Tumor angiogenesis: therapeutic implications," *New Engl. J of Med.*, **285**, 1182-1186 (1971).

115. D. W. Siemann, D. J. Chaplin, and M. R. Horsman, "Vascular-targeting therapies for treatment of malignant disease", *Cance*r **100**, 2491-2499 (2004).

116. D. W. Siemann, E. Mercer, S. Lepler, and A. M. Rojiani, "Vascular targeting agents enhance chemotherapeutic agent activities in solid tumor therapy," *Int. J. Cancer* **99**, 1-6 (2002).

117. C. B. Pattillo, F. Sari-Sarraf, R. Nallamothu, B. M. Moore, G. C. Wood, and M. F. Kiani, "Targeting of the antivascular drug combretastatin to irradiated tumors results in tumor growth delay," *Pharmaceut. Res.,* **22**, 1117-1120 (2005).

118. R. B. Pedley, S. A. Hill, G. M. Boxer, A. A. Flynn, R. Boden, R. Watson, J. Dearling, D. J. Chaplin, and H. J. Begent, "Eradication of colorectal xenografts by combined radioimmunotherapy and combretastatin A-4 3-*O*-phopsphate," *Cancer Res.* **61**, 4716-4722 (2001).

119. C. M. L. West and P. Price, "Combretastatin A4 phosphate" *Anti-Cancer Drugs* **15**, 179-187 (2004).

120. G. M. Tozer, C. Kanthou, and B. C. Baguley, "Disrupting tumor blood vessels," *Nature Rev. Cancer* **5**, 423-435 (2005).

121. P. E. Thorpe, D. J. Chaplin, and D. C. Blakey, "The first international conference on vascular targeting: meeting overview," *Cancer Res.* **63**, 1144-1147 (2003).

122. M. M. Cooney, J. Ortiz, R. M. Bukowski, S. C. Remick, "Novel vascular targeting/disrupting agents: combretastatin A4 phosphate and related compounds," *Curr. Oncol. Reports* **7**, 90-95 (2005).

123. E. El-Emir, G. M. Boxer, I. A. Petrie, R. W. Boden, J. L. J. Dearling, R. H. J. Begent, and R. B. Pedley, "Tumor parameters affected by combretastatin A-4 phosphate therapy in a human colorectal xenograft model in nude mice," *Eur. J. Cancer* **41**, 799-806 (2005).

124. Y. Sheng, J. Hua, K. G. Pinney, C. M. Garner, R. R. Kane, J. A. Prezioso, D. J. Chaplin, and K. Edvardsen K, "Combretastatin family member OXI4503 induces tumor vascular collapse through the induction of endothelial apoptosis," *Int. J. Cancer* **111,** 604–610 (2004).

125. G. M. Tozer, V. E. Prise, J. Wilson, M. Cemazar, S. Shan, M. W. Dewhirst, P. R. Barber, B. Vojnovic, and D. J. Chaplin, "Mechanisms Associated with Tumor Vascular Shut-Down Induced by Combretastatin A-4 Phosphate: Intravital Microscopy and Measurement of Vascular Permeability," *Cancer Res.* **61**, 6413–6422 (2001).

126. V. E. Prise, D. J. Honess, M. R. L. Stratford, J. Wilson, and G. M. Tozer, "The vascular response of tumor and normal tissues in the rat to the vascular targeting agent, combretastatin A-4-phosphate, at clinically relevant doses," *Int. J. Oncol.* **21**, 717–726 (2002).

127. G. M. Tozer, S. M. Ameer-Beg, P. R. Baker J. Barber, S. A. Hill, R. J. Hodgkiss, R. Locke, V. E. Prise, I. Wilson, and B. Vojnovic, "Intravital imaging of tumor vascular networks using multi-photon fluorescence microscopy," *Adv. Drug Deliv. Reviews* **57**, 135-152 (2005).

128. B. G. Siim, W. T. Laux , M. P. Rutland, B. N. Palmer, and W. R. Wilson, "Scintigraphic Imaging of the Hypoxia Marker 99mTechnetium-labeled 2,2′-(1,4-Diaminobutane)bis(2-methyl-3-butanone) Dioxime (99mTc-labeled HL-91; Prognox): Noninvasive Detection of Tumor Response to the Antivascular Agent 5,6-Dimethylxanthenone-4-acetic Acid," *Cancer Res.* **60**, 4582-4588 (2000).

129. R. J. Maxwell, J. Wilson, V. E. Prise, B. Vojnovic, G. J. Rustin, M. A. Lodge, and G. M. Tozer, "Evaluation of the anti-vascular effects of combretastatin in rodent tumours by dynamic contrast enhanced MRI," *NMR in biomed.* **15**, 89-98 (2002).

130. L. Bentzen, P. Vestergaard-Poulsen, T. Nielsen, J. Overgaard, A. Bjørnerud, Briley-Sæbø, M. R. Horsman, and L. Østergaard, "Intravascular contrast agent-enhanced MRI measuring contrast clearance and tumor blood volume and the effects of vascular modifiers in an experimental tumor," *Int. J. Radiat. Oncol. Bio. Phys.* **61**, 1208-1215 (2005).

131. D. Zhao, L. Jiang, E. Hahn, and R. P. Mason, "Tumor physiologic response to combretastatin A4 phosphate assessed by MRI," *Int. J. Radiat. Oncol. Biol. Phys.* **62**, 872-880 (2005).

132. S. Zhao, J. V. Moore, M. L. Waller, A. T. McGown, J. A. Hadfield, G. R. Pettit, and D. L. Hastings, "Positron emission tomography of murine liver metastases and the effects of treatment by combretastatin A-4," *Eur. J. Nucl. Med.* **26**, 231-238 (1999).

133. H. L. Anderson, J. T. Yap, M. P. Miller, A. Robbins, T. Jones, and P. M. Price, "Assessment of pharmacodynamic vascular response in a phase I trial of combreatastatin A4 phosphate," *J. Clin. Oncol.* **21**, 2823-2830 (2003).

134. G. M. Tozer, "Measuring tumor vascular response to antivascular and antiangiogenic drugs," *Br. J. Radiol.* **76**, S23-S35 (2003).

135. M. Kragh, B. Quistorff, E. L. Lund, and P. E. Kristjansen, "Quantitative estimates of vascularity in solid tumors by non-invasive near-infrared spectroscopy," *Neoplasia*, 3(4), 324-30 (2001).

136. M. Cope and D. T. Delpy, "A system for long term measurement of cerebral blood and tissue oxygenation in newborn infants by near infrared transillumination," *Med. Biol. Eng. Comp.* **26**, 289-294 (1988).

137. M. Kragh, B. Quistorff, M. R. Horsman, and P. E. Kristjansen, "Acute effects of vascular modifying agents in solid tumors assessed by noninvasive laser Doppler flowmetry and near infrared spectroscopy," *Neoplasia* **4**, 263-267 (2002).

138. J. G. Kim and H. Liu, "Investigation of breast tumor hemodynamics using tumor vascular phantoms and FEM simulations," in Biomedical Topical Meetings on CD-ROM (The Optical Society of America, Washington, DC 2004), WF16.

139. J. G. Kim and H. Liu, "Investigation of bi-phasic tumor oxygen dynamics induced by hyperoxic gas intervention: A numerical study," *Opt. Express*, **13**, 4465-75 (2005). http://www.opticsexpress.org/abstract.cfm?URI=OPEX-13-12-4465.

140. D. T. Delpy, M. Cope, P. van der Zee, S. Arridge, S. Wray, and J. Wyatt, "Estimation of optical pathlength through tissue from direct time of flight measurement," *Phys. Med. Biol*. **33** 1433-1442 (1988).

141. Y. Gu, R. P. Mason, and H. Liu, "Estimated fraction of tumor vascular blood contents sampled by near infrared spectroscopy and 19F magnetic resonance spectroscopy," *Opt. Express* **13** 1724-1733 (2005).
http://www.opticsexpress.org/abstract.cfm?URI=OPEX-13-5-1724

142. Y. Song, "Tumor oxygenation and physiology in response to therapeutic interventions investigated by 19F MRI and NIR spectroscopy," PhD dissertation, The University of Texas Southwestern Medical Center at Dallas (2001).

143. Q. Zhu, S. H. Kurtzman, P. Hegde, S. Tannenbaum, M. Kane, M. Huang, N. G. Chen, B. Jagjivan, and K. Zarfos K, "Utilizing optical tomography with ultrasound localization to image heterogeneous hemoglobin distribution in large breast cancers," *Neoplasia* **7** 263-270 (2005).

144. J. S. Maier, B. Barbieri, A. Chervu, I. Chervu, S. Fantini, M. A. Franceschini, M. Levi, W. W. Mantulin, A. Rosenberg, S. A. Walker, and E. Gratton, "In vivo study of human tissues with a portable near-infrared tissue spectrometer," *Proc. SPIE 2387,* R.R. Alfano, ed., 240-248 (1995).

145. N. Shah, A. E. Cerussi, D. Jakubowski, D. Hsiang, J. Butler, and B. J. Tromberg, "Spatial variations in optical and physiological properties of healthy breast tissue," *J. Biomed. Opt.* **9**, 534-540 (2004).

146. T. Durduran, R. Choe, J. P. Culver, L. Zubkov, M. J. Holboke, J. Giammarco, B. Chance, and A. G. Yodh, "Bulk optical properties of healthy female breast tissue," *Phys. Med. Biol.* **47**, 2847-2861(2002).

147. H. C. Thoeny, F. De Keyzer, F. Chen, Y. Ni, W. Landuyt, PhD, E. K. Verbeken, H. Bosmans, G. Marchal, and R. Hermans, "Diffusion-weighted MR Imaging in Monitoring the Effect of a Vascular Targeting Agent on Rhabdomyosarcoma in Rats," *Radiology* **234,** 756-764 (2005)

148. R. J. Maxwell, J. Wilson, V. E. Prise, B. Vojnovic, G. J. Rustin, M. A. Lodge, and G. M. Tozer, "Evaluation of the anti-vascular effects of combretastatin in rodent tumors by dynamic contrast enhanced MRI," *NMR in Biomed.* **15**, 89-98 (2002).

149. D. B. Jakubowski, A. E. Cerussi, F. Bevilacqua, N. Shah, D. Hsiang, J. Butler, and B. J. Tromberg, "Monitoring neoadjuvant chemotherapy in breast cancer using quantitative diffuse optical spectroscopy: a case study," *J. Biomed.. Opt*. **9**, 230-238 (2004).

150. G. Yu, T. Durduran, C. Zhou, H. W. Wang, M. E. Putt, H. M. Saunders, C. M. Sehgal, E. Glatstein, A. G. Yodh, and T. M. Busch, *Clin. Cancer Res.* **11**, 3543-3552 (2005).

151. G. Yu, T. Durduran, G. Lech, C. Zhou, B. Chance, E. R. Mohler III, and A. G. Yodh, **"**Time-dependent blood flow and oxygenation in human skeletal muscles measured with noninvasive near-infrared diffuse optical spectroscopies,**"** *J. Biomed. Opt.* **10**, 024027-1-024027-12. (2005)

152. T. Durduran, G. Yu, M. G. Burnett, J. A. Detre, J. H. Greenberg, J. Wang, C. Zhou, and A. G. Yodh, "Diffuse optical measurement of blood flow, blood oxygenation, and metabolism in a human brain during sensorimotor cortex activation," *Opt. Lett.* **29**, 1766-1768 (2004).

153. C. S. Parkins, A. L. Holder, S. A. Hill, D. J. Chaplin, and G. M. Tozer, "Determinants of anti-vascular action by combretastatin A-4 phosphate: role of nitric oxide," *Br. J. Cancer* **83**, 811-816 (2000).

154. D. A. Beauregard, R. B. Pedley, S. A. Hill, and K. M. Brindle, "Differential sensitivity of two adenocarcinoma xenografts to the anti-vascular drugs combratastatiin A4 phosphate and 5,6-dimethylxanthenone-4-acetic acid, assessed using MRI and MRS," *NMR in Biomed.* **15**, 99-105(2002).

155. D. A. Beauregard, S. A. Hill, D. J. Chaplin, K. M. Brindle, "The susceptibility of tumors to the anti-vascular drug combretastatin A4 phosphate correlates with vascular permeability," *Cancer Res.* **61**, 6811-6815 (2001).

156. J. H. Kaanders, J. Bussink, and A. J. van der Kogel, "ARCON: a novel biology-based approach in radiotherapy", *Lancet Oncol.*, **3**(12), 728-37 (2002).

157. J. Griebel, N. A. Mayr, A. de Vries, M. V. Knopp, T. Gneiting, C. Kremser, M. Essig, H. Hawighorst, P. H. Lukas, and W. T. Yuh, "Assessment of tumor microcirculation: a new role of dynamic contrast MR imaging," *J. Magn. Reson. Imaging*, **7**, 111-119 (1997).

158. R. G. Steen, K. Kitagishi and K. Morgan, "*In vivo* measurement of tumor blood oxygenation by near-infrared spectroscopy: Immediate effects of pentobarbital overdose or carmustine treatment", *J. Neuro-Oncol.,* **22**, 209-220 (1994).

159. S. Li, J. P. Wehrle, S. S. Rajan, R. G. Steen, J. D. Glickson, and J. Hilton, "Response of radiation-induced fibrosarcoma-1 in mice to cyclophosphamide monitored by in vivo 31P nuclear magnetic resonance spectroscopy," *Cancer Res.*, **48**, 4736-4742 (1988).

160. H. Poptani, N. Bansal, W. T. Jenkins, D. Blessington, A. Mancuso, D. S. Nelson, M. Feldman, E. J. Delikatny, B. Chance, and J. D. Glickson, "Cyclophosphamide treatment modifies tumor oxygenation and glycolytic rates of RIF-1 tumors: 13C magnetic resonance spectroscopy, Eppendorf electrode, and Redox scanning," *Cancer Res.*, **63**, 8813-8820 (2003).

161. D. Zhao, A. Constantinescu, E. W. Hahn, and R. P. Mason, "*In vivo* evaluation of metronomic chemotherapy on prostate tumors by MRI," CaPCure, New York, NY, November (2003).

162. D. B. S., Hoon, "Circlulating immune complexes in rats bearing 6-thioguanine-resistant variants of the 13762 mammary adenocarcinoma," *Cancer Res.*, **44**, 2406-2409 (1984).

163. A.R. Ahmed, S.M. Hombal, "Cyclophosphamide (Cytoxan). A review on relevant pharmacology and clinical uses," *J. Am. Acad. Dermatol*., **11**(6), 1115-1126 (1984).

164. P. Calabresi, B. A. Chabner, "Antineoplastic agents", In: A.F. Gilman, T. W. Rall, A.S. Niss, and P. Taylor (Editors), The Pharmacological Basis of Therapeutics, 8th ed. MacGraw-Hill, Singapore. (1992).

165. P. G. Braunschweiger and L. M. Schiffer, "Effect of dexamethasone on vascular function in RIF-1 tumors," *Cancer Res.*, **46,** 3299–3303 (1986).

166. P. E. Kristjansen, Y. Boucher, and R. K. Jain, "Dexamethasone reduces the interstitial fluid pressure in a human colon adenocarcinoma xenograft," *Cancer Res.*, **53,** 4764–4766 (1993).

167. H. Poptani, N. Bansal, R. A. Graham, A. Mancuso, D. S. Nelson, and J. D. Glickson, "Detecting early response to cyclophosphamide treatment of RIF-1 tumors using selective multiple quantum spectroscopy (SelMQC) and dynamic contrast enhanced imaging," *NMR in Biomed.*, **16**, 102-111, (2003).

BIOGRAPHICAL INFORMATION

Jae Gwan Kim was born in Pusan, South Korea in Feb. 1971. He stayed at Pusan until he graduated from Haewoondae High School. Since then he moved to Seoul and started his undergraduate study at Hanyang University in 1989. As to fulfill Korean Men's duty, he had served the army from Feb. 1991 to Aug. 1993. He returned to the school in spring 1994 and graduated with a Bachelor's degree in Metallurgical Engineering in Feb. 1996. He got a job at Samsung SDI, but realized the need for the further degree and continued his education at same place. During his graduate studies, his research area was in the development of a lithium microbattery. After the graduation with a master's degree in 1998, he had worked at LG-Caltex Oil Corp. in Yosu, South Korea for a year as an inspection and maintenance engineer. With the desire to study in new area, especially something that can help for the human, he came to the Texas, U.S. and started his graduate studies at joint program of biomedical engineering between the University of Texas Southwestern Medical Center at Dallas and the University of Texas at Arlington to achieve a PhD in Biomedical Engineering. His PhD research area was in the applications of near infrared spectroscopy to breast cancer research, and he was awarded for a three year of predoctoral fellowship from the Department of Defense

Breast Cancer Research Program in May 2003. After completion of his Ph.D., he will move to Irvine, CA to work as a postdoctoral scholar at the Beckman Laser Institute in the University of California at Irvine. He has been married to his wife for 7 years and they have two wonderful sons. He loves to sing a song and can play several musical instruments.

LIST OF PUBLICATIONS

PEER-REVIEWED JOURNAL

1) **Jae G. Kim**, Dawen Zhao, Yulin Song, Anca Constantinescu, Ralph P. Mason, Hanli Liu, "Interplay of tumor vascular oxygenation and tumor pO_2 observed using NIRS, pO_2 Needle Electrode and ^{19}F MR pO_2 Mapping", *J. Biomed. Opt.*, **8(1)**, 53-62 (2003).

2) Yueqing Gu, Vincent A. Bourke, **Jae G. Kim**, Anca Constantinescu, Ralph P. Mason, Hanli Liu, "Dynamic response of breast tumor oxygenation to hyperoxic respiratory challenge monitored with three oxygen-sensitive parameters", *Appl. Opt.*, **42(16)**, 2960-2967 (2003).

3) Hanli Liu, Yueqing Gu, **Jae G. Kim**, Ralph P. Mason, "Near infrared spectroscopy and imaging of tumor vascular oxygenation", Imaging in Biological Research, Part B (P. Machael Conn ed.) *Methods in Enzymol.*, **386**, 349-378 (2004)

4) **Jae G. Kim**, Mengna Xia, Hanli Liu, "Extinction coefficients of hemoglobin for near-infrared spectroscopy of tissue", *IEEE Eng. in Med.Biol. Magazine*, **24(2)**, 118-121 (2005).

5) **Jae G. Kim**, Hanli Liu, "Investigation of bi-phasic tumor oxygen dynamics induced by hyperoxic gas intervention: A numerical study", *Optics Express*, **13**, 4465-4475 (2005). http://www.opticsexpress.org/abstract.cfm?URI=OPEX-13-12-4465.

6) Yulin Song, **Jae G. Kim**, Ralph P. Mason, Hanli Liu, "Investigation of rat breast tumor oxygen consumption by near infrared spectroscopy," *J. Phys. D: Appl. Phys.*, **38**, 2682-2690 (2005).

PROCEEDINGS

1) **Jae Gwan Kim**, Yulin Song, Dawen Zhao, Anca Constantinescu, Ralph P. Mason, and Hanli Liu, "Interplay of Tumor Vascular Oxygenation and pO_2 in Tumors Using NIRS and Needle Electrode", *Proc. SPIE-Int. Soc. Opt. Eng.*, **4250**, 429-436 (2001).

2) Yulin Song, Yueqing Gu, **Jae G. Kim**, Hanli Liu, Anca Constantinescu, and Ralph P. Mason, "Correlation between total hemoglobin concentration and blood volume of breast tumors measured by NIR spectroscopy and ^{19}F MRS of PFOB", *Proc. OSA Biomedical Topical Meeting*, 241-243 (2002).

3) **Jae G. Kim**, Yulin Song, Anca Constantinescu, Ralph P. Mason, and Hanli Liu, "Investigation of tumor oxygen consumption and tumor vascular oxygen dynamics in response to pharmocological interventions by NIRS", *Proc. OSA Biomedical Topical Meeting*, 231-233 (2002).

4) Yueqing Gu, Vincent Bourke, **Jae G. Kim**, Mengna Xia, Anca Constantinescu, Ralph P. Mason, and Hanli Liu, "Breast tumor oxygenation in response to carbogen intervention assessed simultaneously by three oxygen-sensitive parameters", *Proc. SPIE-Int. Soc. Opt. Eng.*, **4955**, 416-423 (2003).

5) **Jae G. Kim**, Yueqing Gu, Anca Constantinescu, Ralph P. Mason, and Hanli Liu, "Non-Uniform Tumor Vascular Oxygen Dynamics Monitored By Three-Channel Near-Infrared Spectroscopy", *Proc. SPIE-Int. Soc. Opt. Eng.*, **4955**, 388-396 (2003).

6) **Jae G. Kim**, and Hanli Liu, "Investigation of breast tumor hemodynamics using tumor vascular phantoms and FEM simulations", in *Biomedical Topical Meetings on CD-ROM* (The Optical Society of America, Washington, DC, 2004), WF16.

7) **Jae G. Kim**, Dawen Zhao, Ralph P. Mason, and Hanli Liu, "Chemotherapeutic (Cyclophosphamide) Effects on Rat Breast Tumor Hemodynamics Monitored

by Multi-Channel NIRS.", *Proc. SPIE-Int. Soc. Opt. Eng.*, Optical Tomography and Spectroscopy of Tissue VI (ed: Chance et al) **, 5693**, 282-292 (2005).

PUBLICATIONS IN PREPARATION/SUBMITTED

1) **Jae G. Kim** and Hanli Liu, "Variation of haemoglobin extinction coefficients can cause errors in determination of haemoglobin concentration measured by near-infrared spectroscopy", *Phys. Med. Biol.*, under review.

2) **Jae G. Kim** and Hanli Liu, "Investigation of bi-phasic tumor oxygen dynamics induced by hyperoxic gas intervention: A dynamic phantom study", *Appl. Opt.*, ready to submit.

3) **Jae G. Kim**, Dawen Zhao, Ralph P. Mason, and Hanli Liu, "Acute Effects of Combretastatin on Breast Tumor Hemodyamics Monitored by Near-Infrared Spectroscopy," *Proc. Natl. Acad. Sci. (USA)*, ready to submit.

4) **Jae G. Kim**, Dawen Zhao, Ralph P. Mason, and Hanli Liu, "Noninvasive Monitoring of Tumor Response to Chemotherapy Using Near-Infrared Spectroscopy," *Neoplasia*, in preparation.

5) **Jae G. Kim**, Dawen Zhao, Ralph P. Mason, and Hanli Liu, "The Investigation of Heterogeneity in Tumor Vasculature By Using Near-Infrared Spectroscopy," *J. Biomed. Opt.*, in preparation.

6) **Jae G. Kim**, Vincent Bourke, Dheerendra Kashyap, Ralph P. Mason, and Hanli Liu, "Tumor vascular sO_2 distribution and the correlation with pO_2 investigated by using needle like optical probe and oxygen quenching fluorescence probe," *Phys. Med. Biol.*, in preparation.